On a Framework for more Automatic Design and Research in Sheet Metal Forming

A Case Study on Applied Automatic Optimisation of Process Simulations

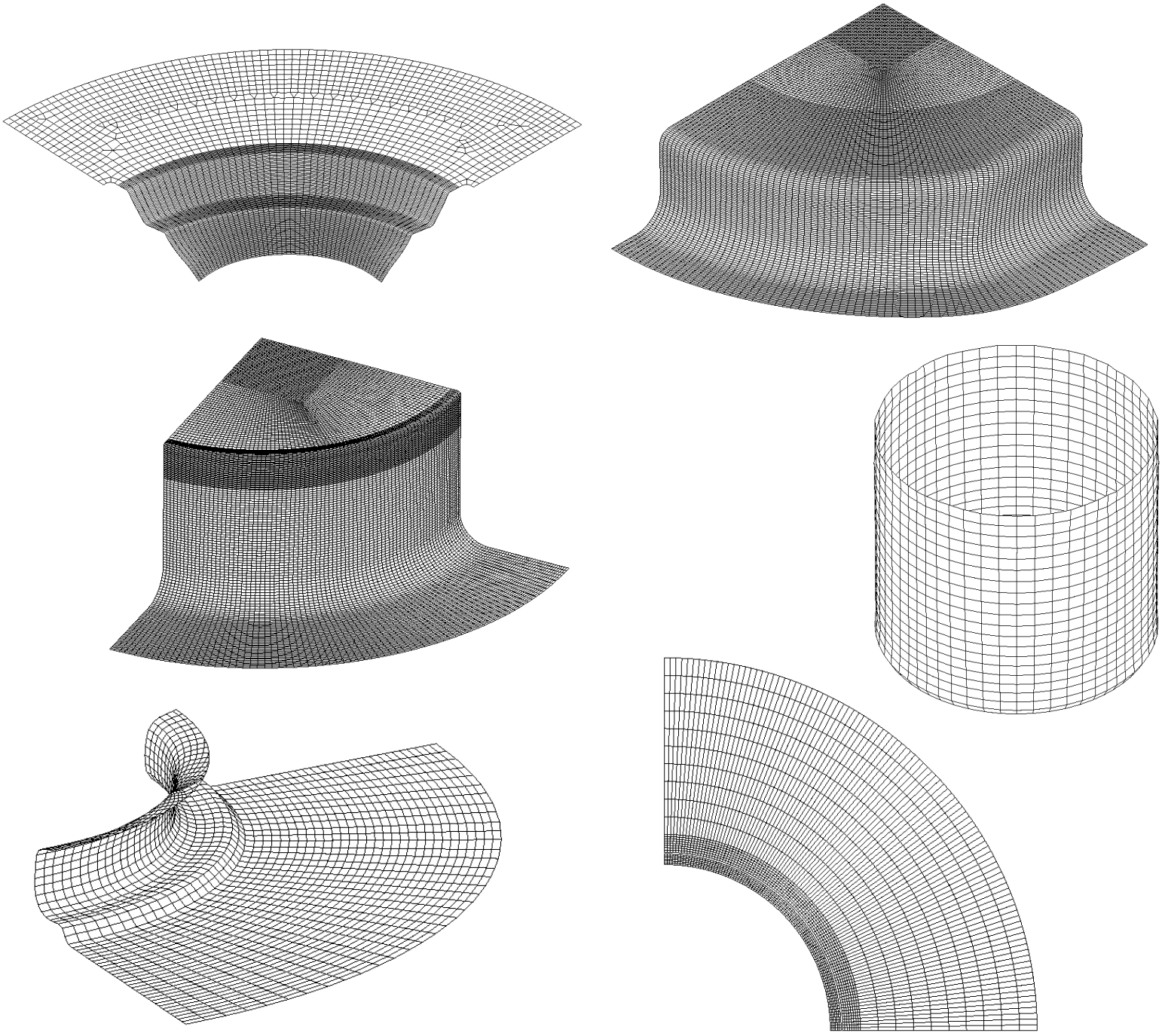

Claes Rubin Klose Dennis Bøjesen

Master's Thesis in Manufacturing Technology

Department of Materials and Production
Aalborg University

AALBORG UNIVERSITET

Aalborg University
Department of Materials and Production

Title:

On a Framework for more Automatic Design and Research in Sheet Metal Forming: A Case Study on Applied Automatic Optimisation of Process Simulations

Theme:

Master's Thesis

Project period:

1st of February - 1st of June 2018

Projectgroup:

Claes Rubin Klose

Dennis Bøjesen

Synopsis:

In the last couple of decades the development of numerical models and optimisation approaches has been of great academic interest. Similarly, the automotive industry are applying these approaches even more, due to the increased utilisation of high strength steels, which makes the forming operations more complex.
The aim of this project to develop an approach for formulating an automatic optimisation for sheet metal forming simulations. In order to achieve this, a framework consisting of five phases are proposed: Purpose, Process, Modelling, Optimisation and Results & Discussion.

The framework is throughout the report applied on 6 different sheet metal forming cases, for which a simulation and optimisation are constructed. The aim of the optimisations are improved tool geometry, springback, small radii etc. The optimisation problems are formulated using non-linear least square formulation and a gradient based optimisation algorithm.

Additionally, is an investigation of a new theory for reliving residual stresses, in metal formed parts, conducted and documented in a paper for a simple example. The method is later numerical tested on a deep drawn cup.

Supervisor:

Karl Brian Nielsen

Examiner:

Lars Erik Bräuner

Pages: 114

By signing this document, each member of the group confirms participation on equal terms in the process of writing the project. Thus, each member of the group is responsible for the all contents in the project.

Resumé

I gennem de seneste årtier har udviklingen af simulerings- og optimeringsværktøjer oplevet en enorm interesse akademisk, såvel som industrielt. Samtidig har bil-industrien øget deres anvendelse af disse værktøjer, grundet udfordringer med fremstilling af bildele af højstyrkestål, hvor mere komplekse bearbejdningsmetoder stiller store krav til processindstillingerne.
Denne rapport tager udgangspunkt i denne problemstilling, hvor fokus er at udvikle et udgangspunkt til et framework for automatisk optimering af pladeformgivningsprocessimuleringer. Dette framework tager udgangspunkt i en 5 trins fremgangsmåde, som består af: Formål, Proces, Modellering, Optimering og Resultat & Diskussion. For at udvikle og bestemme de vigtige egenskaber af disse 5 trin er rapporten konstrueret som et casestudy, med seks forskellige cases. For hver case er foretaget et litteratur studie, hvorefter en numerisk model er lavet, som bliver parametriseret og en optimering af modellen bliver anvendt.

De valgte cases igennem projektet vil blive præsenteret i det følgende:
Den først case er en industriel opgave stillet af Vestas Aircoil, som er en virksomhed placeret i Lem, der fremstiller varmevekslere. De har oplevet kvalitetsproblemer med deres fremstilling af kobber fin-plader. For at løse denne opgave er der konstrueret en flertrins numerisk model af den eksisterende følgeværktøjsproces, hvor det er bestemt at stemplet i den sidste process skal anvendes som design parameter til optimeringen.

Den anden case, omhandler optimering af en ny fremstillingsprocess, hvor det er muligt at opnå en relativ lille radius. Denne process foregår i to trin, hvor det første er en hydromekanisk dybtræk process og den anden er "Bulging-Pressing"-process. Da denne fremstillingsmetode er ny, er procesindstillingerne svære at bestemme, og derfor er der udviklet en optimering, hvor disse bliver bestemt.

Den tredje case, omhandler den samme process som den forrige case, men denne gang skal denne optimeringsmetode anvendes på en kompleks geometri. Denne geometri er et test emne til et måne fartøj, hvor små rundinger er et design krav.

Den fjerde case, har til formål at genere akademisk viden omkring en samlingsmetode indenfor varmeveksler-industrien, "hydraulisk expanded tube-tubesheet joint". Denne samling oplever kvalitets problemer ift. samlingens integritet, hvorved det her er ønskeligt at udvikle en optimering, hvor den optimale indstilling til en given samlingstilstand bliver fundet. Hertil er flydespænding varieret for både rør og tubesheet, samt spalten imellem disse.

Den femte case, tager udgangspunkt i fremstillingen af dørkarm-hjørne emner for en Airbus A380, hvor den nuværende proces oplever store problemer med tilbage-fjedring og brud i kritisk fortyndede områder. Til denne case blev den oprindelige fremstillingsmetode modelleret, hvor en ændring af hydroformgivningsformen blev foreslået. Denne nye form blev optimeret ift. tilbage-fjedringen, hvor det opnåede optimum forbedrede emnet.

Den sjette case, omhandler en eksotisk restspændings minimeringsmetode, hvor der i appendiks til dette projekt er lavet en artikel omhandlende denne behandlings metode på et simpelt emne. Denne case tager udgangspunkt i en dybtrukken kop, hvor der forefinder sig store restspændinger i kop væggen. For denne kop blev der foretaget en egenværdisanalyse, for at finde den frekvens mode, hvor restspændingerne blev påvirket mest. Evalueringsmetoden for denne proces er blevet diskuteret, hvor en FLSD viste hvorledes spændingstilstanden ændrede sig efter behandlingen. For denne case blev der ikke opbygget en optimering, men der blev foretaget en diskussion om, hvorledes sådan en skulle konstrueres.

Afslutningsvis blev det beskrevne framework evalueret, og nogle retningslinjer for hvorledes disse typer optimeringer skal udføres.

Preface

This report documents the master thesis composed by Claes Rubin Klose and Dennis Bøjesen at 4th semester of the master program Manufacturing Technology at Department of Materials and Production, Aalborg University. The project is performed in the period from the 1st of February and handed in the 1st of June 2018.

This project is completed under supervision of Professor Karl Brian Nielsen from Aalborg University. Throughout this project there are some people who has contributed/supervised additionally to this project, which we would like to send a thanks to:

- Benny Endelt, Associate Professor AAU: We would like to thank Benny Endelt for providing technical support and giving access to his developed optimisation code.
- Claus H. Ibsen, R&D Manager Vestas Aircoil A/S: We could like to thank Claus Ipsen, for providing the problem from Chapter 5, and giving feedback on this.

The purpose of this master thesis is to display the deployment of numerical models and gradient based optimisation upon a variety of cases, to show the large range of opportunities, when approaching a problem with this objective.

Reading Guide

Throughout this report, the sources are referred to by a number, which can be found in the bibliography on page 119, where the sources are ordered in the sequence of which they are referred to.

Figures and tables in the report are numbered according to the associated chapter and the order of appearance. Figures without any references are designed/composed by the authors.

Additional information for this report, can be found in the Appendix, beginning on page 129, which will be referred to accordingly. Furthermore, a zip file containing the keyword files, the optimisation inputs and videos of the simulations are uploaded.

Claes Rubin Klose & Dennis Bøjesen

Contents

Introduction and Theory 1

The focus of this project, is sheet metal forming, numerical modelling and optimisation, the following chapter will act as the problem analysis.

Sheet metal forming is widely used in the industry for the manufacturing of light-weight parts, where complex geometries can be achieved from thin metal sheets. In the recent decades various industries, e.g. the automotive industry [1], has focused on using high strength steel for manufacturing of parts. However, most high strength steel lack formability, which is why unconventional sheet metal forming solutions have to be further developed [2], such as hydroforming.
The constant necessity for improved products in regards to strength and weight are also requiring a fast development time, where the deployment of FEM has proven to be a massive enhancement factor for the automotive industry, where it is now being used earlier on in the product development phase [2]. The deployment of FEM in the product development phase has proven to have advantages in several branches of the development, where the industry used expensive try-outs to develop the tool geometries for new car components. Here it was found that by using the simulation tools a great improvement is achieved [3], both in terms of knowledge gained, but also minimising the lead time. The tool development and production time has already been improved by approximately 50%, by using simulation software and it is expected that this will continue to improve [4].
A. Makinouchi et al. [5] in 1998, visited different automotive companies in Europa, Japan and USA, they investigated their use of commercial FEM code for manufacturing development, all the companies used multiple codes for different phases in their development of tools. This proves the necessity of assessing the product/process development by utilising numerical modelling.

1.1 Sheet Metal Forming

Sheet metal forming is a branch of metal working and is characterised by a flat strip or coils, which are formed by a press, that plastically deforms the material into the desired shape. On figure 1.1, some examples of sheet metal formed parts from the Department of Materials and Production, AAU, can be seen.

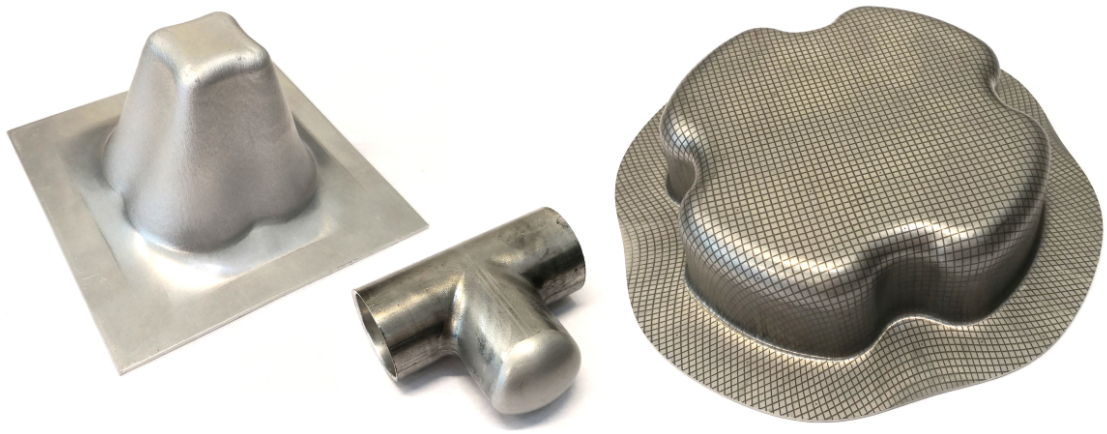

Figure 1.1. Sheet metal formed parts from the Department of Materials and Production, AAU.

In the following sections selected general terms, characteristics and processes regarding sheet metal forming will be presented, together with the forming defects and the materials formability and limits.

1.1.1 General Sheet Metal Forming Processes

There are some overall sheet metal forming processes, which will be presented in the following, and can also be seen on figure 1.2:

- **Shearing**: Is similar to cutting operations, where the sheet e.g. is pressed between a punch and a die, which causes large shear stresses that initiates fracture. The shearing process has several process parameters, such as the shape of the punch and die, speed of the operation and lubrication, etc. The process is often used for making the blanks used for later processing, but can also be used for making a holes.
- **Bending**: Is an operation where the sheet/blank is bend into a desired angle by either using rollers, punch and die, etc. The bending operation is very often influenced by the material parameters such as anisotropy and formability. These parameters influence several outcome measures, especially the springback, which is often compensated for by performing an over-bending.
- **Drawing**: Is an operation using die and punch, where the blank is forced into a die cavity by the punch. The part of the blank that is forced into the die is experiencing large tensile stresses, this causes the material to exceed its yield strength and thereby plastically deforms. These large tensile stresses either causes the material to stretch or forces the flange to draw-in additional material. This drawing causes the flange region to experience large compressive stresses, which can cause the material to wrinkle. Therefore the amount of draw-in is normally controlled by using a blank holder [6].
- **Hydroforming**: Is an operation, where either one or both sides of the blank is pressurised to a level which makes the material exceed its yield limit. This process can be performed where the blank is in direct contact with the fluid, which requires the setup to be sealed, or by having a rubber membrane being pressurised.

Hydroforming is often combined with the drawing operation, which can increase the formability of the process.

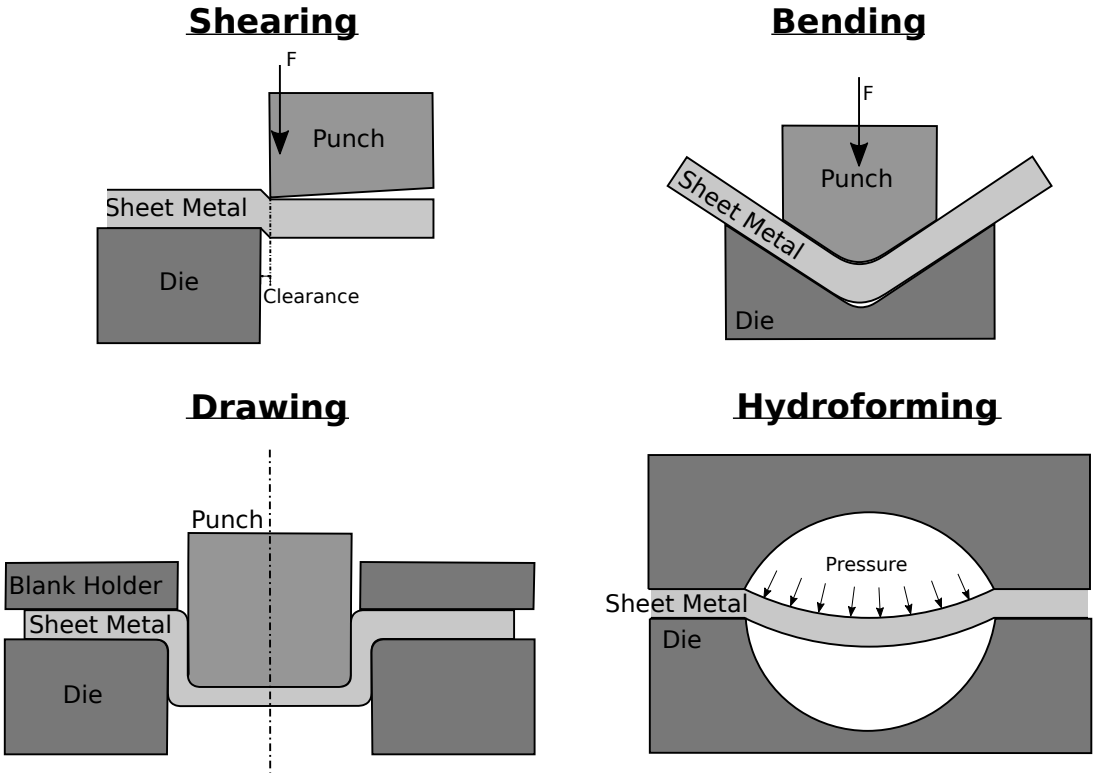

Figure 1.2. A graphical representation of four general sheet metal forming processes: Shearing, Bending, Drawing and Hydroforming.

All these processes can be combined to manufacture complex geometries, which is also called multi-step processing.

1.2 Defects

The tolerances of formed sheet metal parts can be influenced by a number of factors, which can vary from a deviation from springback to wrinkles or cracks.

1.2.1 Springback

The elastic recovery of a formed sheet metal part after unloading is known as springback, which can change the formed shape, illustrated on figure 1.3. Springback can cause shape error in the final product, if not accounted for and is therefore an important engineering subject [7].

The amount of elastic recovery is influenced by the size of the residual stress after unloading, the modulus of elasticity, and the degree of forming. Springback is furthermore affected by a number of factors such as material properties, anisotropy, bending radius, sheet thickness, temperature, etc.

In practice, springback is compensated for by using various strategies, a commonly used technique is over-forming. When doing over-forming, the amount of springback is predicted and the parts are formed further, this will cause the parts to springback into the desired shape. However, this is not always the case. By using this over-forming technique, it is necessary to have adequate knowledge of the springback pattern, where numerical simulation can be used for this purpose [8].

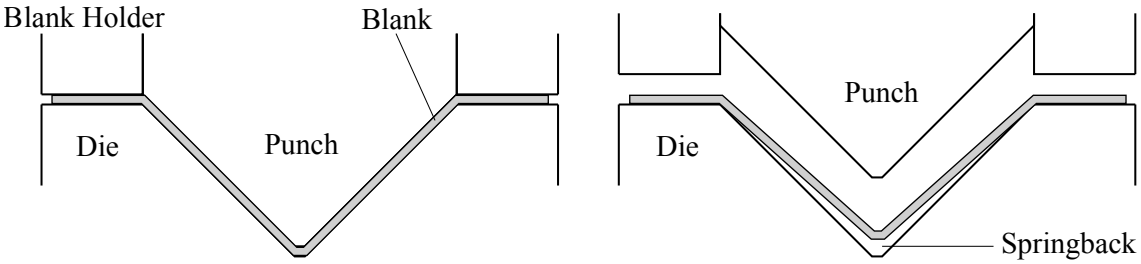

Figure 1.3. **Left:** Sheet metal forming during the final stage of the forming process, with the blank in black. **Right:** The springback can be seen as the gap between the blank and die, after removal of the punch.

In the industry, springback is still a big cost, where the U.S. automotive industry annually uses approximately $50 million (2014), on springback related errors [9]. Previously, springback corrections where compensated for with an experimental approach, for a single forming operation this would take approximately 5 weeks and cost 70000 €, and for a processes consisting of additional forming operations, this would take 10 weeks and cost 150000 €[10].

1.2.2 Formability

Formability in sheet metal forming can be defined as the ability to plasticity deform metal into a desired shape without undergoing localised wrinkles, thinning, necking or fracture.

Wrinkling

Wrinkling is a phenomenon where the sheet metal folds in waves, as show on figure 1.4. Wrinkles can be a result of high compressive stresses combined with a lack of sufficient supporting tool surfaces. Wrinkles appearing on e.g a cup wall can be difficult to avoid without redesigning the forming tools, while flange wrinkles can often be dealt with by increasing holding forces or adjusting the control system [11].

Figure 1.4. Wrinkles appearing on the flange of a deep drawn cup, due to too low blank-holder pressure.

Figure 1.5. Fracture of the cup, due to locally thinning.

Local Wall Thinning and Necking

Local wall thinning and necking is a phenomenon, where a small part section or band of a sheet is exposed to high strain concentrations resulting in large deformations. Strain concentrations can be a result of high resistant from wrinkles, lack of lubrication or contaminants on tool surfaces.

Fracture

Continued deformation applied to regions subject to necking or local wall thinning can result in fracture, a fracture defect can be seen on figure 1.5.

1.2.3 Other Defects

Other defects observed in sheet metal forming are blank misplacement, where the sheet metal is misplaced which may result is uneven forming, depending on the tool design and process, the sensitivity can vary. Another phenomenon influencing the tolerances is material anisotropy, a result of the steel stock production, the anisotropy of a material describes how the material parameters changes depending on the direction of production e.g. rolling.

1.2.4 FLD

Forming limit diagram (shown on figure 1.6) is an engineering tool that can be used to predict possible defects of a forming process. The diagram is split into different sections that describes the combination of the principal stains in the sheet. The forming limit diagram was first introduced by Keeler [12] in 1964 which through experiments defined the right side forming limit curve, Goodwin expanded the diagram with the left side in 1968 [13]. The diagram was later expanded to include wrinkles [14], which are of increasing concern as thinner sheets are used. The diagram is often used in combination with finite element software.

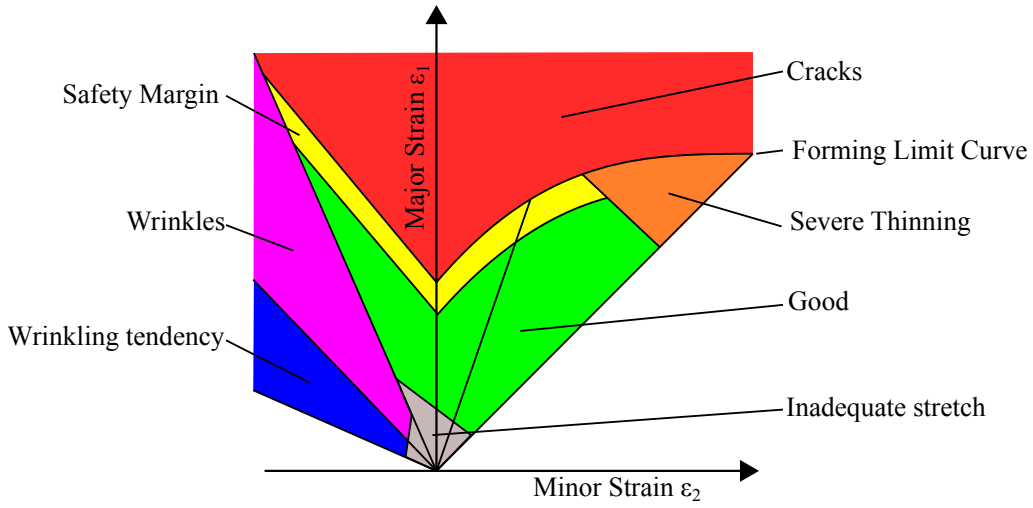

Figure 1.6. Forming limit diagram based on LS-DYNA naming, with inclusion of wrinkles, thinning and cracks.

The diagram is material specific, the exact material data is therefore required to ensure an usable result. The diagram can either be constructed analyticity or with experiments. The FLD is commonly used in the industry as a indicator for formability, however, this method is highly strain path dependent, and therefore it is not desirable to use for multi-stage forming [15].

1.2.5 FLSD

Forming limit diagrams (FLD) can be difficult to use in modern industrial manufacturing systems, with several stages of forming processes, because it is dependent on the strain path shape and the strain history of the sheet [16, 17]. A path independent stress-based FLD alternative, to the strain dependent limit diagram was proposed by Pelkkikangas et al. in 1977 supported by experimental data [18]. In 1982 Arrieux et al. rediscovered the path independence of a stress-based limit diagram, and proposed it as an alternative for multi-stage forming operations [19, 16, 18]. Strain path independence makes it possible to use forming limit stress diagrams to predict the forming limits of multi-stage forming processes [20].

Another advantages was found by Kolasangiani et al. [21], they concluded that no changes in the FLSD curve could be observed with changes in sheet thickness, whereas the FLD increased with increasing sheet thickness, based on results from numerical analysis and experiments.

1.3 Formability and Limits

The demand for light-weight structures and parts with increased strength are growing in many industries, illustrated by the automotive industry where the demand for high safety and fuel economy are resulting in use of less ductile light-weight materials. A common method of increasing strength and decreasing weight of a part simultaneously, is to use thin plates and optimised complex shapes [22, 23, 24].

Design of complex shapes either to add strength, stiffness or of design purposes can add critical regions. Critical regions are areas that require excessive stretching of the sheet into or drawing around sharp corners, small radii or depths that exceeds the materials formability, resulting in fracture. High strength steels will generally have a negative influence on formability, due too the lower ductility and higher springback, making complex shapes harder to achieve.

1.3.1 Multi-Step forming

Conventional one-step drawing process is fast and efficient, however, the complexity of the parts which can be made are limited, do to less control over the material flow. Lack of control can lead to: local thinning, gaps, or wrinkles, this is illustrated on figure 1.7. In some cases it may be impossible to obtain the desired shape with an one-step process. By splitting the process up into multiple steps and/or utilising hydroforming it is possible to manipulate the material to increase the formability. Hydroforming is a forming technique commonly used, to allows the material to move more freely than conventional punch and die drawing resulting in a more uniform thickness distribution and higher formability [22].

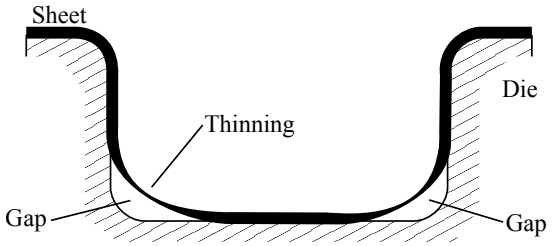

Figure 1.7. Illustration showing the principal of a forming process which is unable to achieve the desired shape, resulting in a gap and local thinning.

Multi-step drawing operations allows control over the material flow, and permit a higher degree of formability. In order to reach the complex shapes in a final step, the intermittent steppes must be designed correctly. The purpose of the intermittent step is to pull more material into the die area, the extra material can in the final step be drawn into the final shape. In order to manipulate the material optimally, the used of FEM is often recommended, both to ensure the thickness distribution throughout the sheet, and to minimise the amount of prototypes which have to be conducted [25].

Many different multi-step drawing configuration philosophies have been documented. The method patented by S. F. Golovashchenko [23] and presented by Golovashchenko et al. [24], is centered around the philosophy of backward drawing and introducing bulges adjacent to the critical regions in the intermittent steps, show on figure 1.8. Extra material is drawn into the die in the first step, the bulge, is then in the second step pushed out into the corner. The result is the ability to draw complex shapes which is impossible with an one-step operation, and the thickness distribution is more uniform.

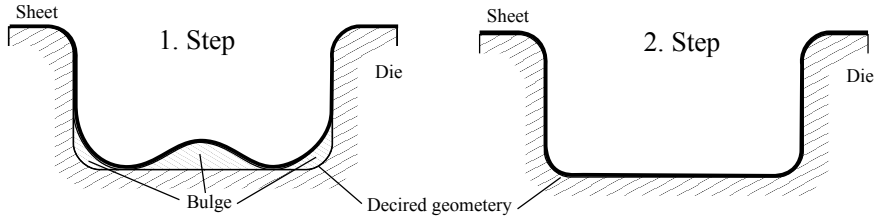

Figure 1.8. Multi-step forming process with the bulge configuration and the desired shape.

1.3.2 Deep Drawability

Deep drawing is a process which has been the subject of researches through a number of years, therefore many aspects of the process and the process parameters have been well documented. The major parameters which influence the drawability of a deep drawing operation are listed as following, the lists are split into three subjects: Material properties, Geometric and Equipment and Tooling [26, 27]. Although the parameters are presented for deep drawing the theory behind can be applied to other similar sheet metal forming processes.

Material properties

- Strength coefficient, K
- Strain-Hardening coefficient, n
- Normal anisotropy, r
- Planar anisotropy, Δr

Geometric properties

- Punch corner radius
- Die radius
- Punch-die clearance
- Blank diameter
- Blank thickness

Equipment and Tooling

- Lubrication/Friction
- Pressing speed
- Blank-holder

1.4 Residual Stresses

The presence of residual stresses in sheet metal forming operations are caused by inhomogeneous deformations[28], and is defined as the stress in a material without any

acting external forces. The residual stresses in sheet metal forming are highly affecting springback and failure [29]. There has been examples of deep-drawn cups, which has experienced corrosion cracking caused by the residual stresses, see figure 1.9. One of the problems with residual stresses is the ability to predict its influence or even the magnitude, and most methods for evaluation is by destructive testing, e.g. hole-drilling technique [30].

Figure 1.9. Deep drawn cup which has experienced corrosion cracking.

It is desirable to limit the amount of residual stresses in the forming operation, this can be done by several approaches, but mainly by making the forming process in to a more homogeneous deformation. This could for instance be to change the tool geometry as Joachim Danckert [28] did in his article regarding a circular cup deep drawing operation. The most common approach for removing the residual stresses is by annealing the formed part, and thereby recrystallise the material. This process is often undesirable, since it requires longer lead-time for the product, but also the fact that the residual stresses can cause the formed part to distort during annealing, which creates geometrical instability.

1.5 Numerical Simulation

The following section will describe the reason for modelling a manufacturing process, the development of numerical models, the solvers used for these models and the material modelling.

The purpose of a numerical model can vary, depending on the objective, e.g. error minimisation of an existing process, or development of new equipment for a future process. Generally numerical models are never fully accurate, however, the models can be used to estimate phenomenons close to reality. Depending on the application, the model can be validated for an accurate result, or only used for rough estimating.

Development of Numerical Models

Development of numerical models for sheet metal forming problems began in the 1960s and early 1970s, where the codes developed were considered very complicated and time consuming to develop and use. The models developed were 2D formulated and very often not consistent. However, the development continued through the 1980s and experienced

high activity, which lead to increasing stability of the models, but the applicability of the codes were not at a desired level yet, since the calculation time were too long.
From the beginning of the 1990s, the automotive industry drastically increased the use of numerical models for modelling their sheet stamping processes [31]. A. Makinouchi [32] did an investigation upon, the application of the numerical models in the industry, where the application of these models showed to improve the development of product and minimising defects. The area of numerical modelling of sheet metal forming is still of great interest today, where the automotive industry remains a large driving force in the development of increasingly accurate models, since computational power are getting faster, more efficient and cheaper.

Numerical Solvers

The motivation for modelling sheet metal forming processes is the high level of non-linearity and complexity [11]. These metal forming models has to cope with large deformation, non-linear material behaviour, computationally costly contact definitions, etc. In order to calculate this in an efficient way, different methods has been utilised through the history, where the advantages of the explicit method has proven to be more effective than the implicit method [11].
The implicit method is characterised by assuming the system to be quasi-static, and solves each step by iteratively solving the system of equations. This method is unconditionally stable and great at large time steps, however, this method requires large amounts of memory and long calculation time [33].
The explicit method is an inertia based method, where the system is considered to be influenced by the dynamics in the model. The method is initially developed for impact, explosion, etc. simulations, where the model duration is relatively short, approximately milliseconds, whereas the sheet metal forming processes has larger process duration. Therefore, to utilise the benefits of the explicit method, the velocities of the system is increased and thereby minimising the real-life processes time, into a much shorter simulation time. Literature states that the velocities of an explicit system can be increased by a factor of 10-50 without influencing the model considerately [31].
One of the areas where the explicit solver is lacking efficiency, is the ability to estimate springback of deformed part. The springback behaviour is an elastic release that can be estimated to be quasi-static, which is more accurate estimated with the implicit solver. Therefore a method, where the implicit and explicit solvers are combined was proposed by M. J. Finn et. al [34], where the forming operation is solved with an explicit solver and the last time steps are solved using an implicit. This switching method is very efficient for simulations, where springback is of great importance.

Material Modelling

In sheet metal forming the plastic deformation is one of the most important areas [33], which is why the material modelling is extremely important in order to estimate this deformation correctly. The mechanical behaviour of a material can normally be interpreted as a uni-axial tensile test, where the yielding condition describes the switching from elastic deformation into plastic deformation until an ultimate tensile strength is reached, and fracture occurs.

In sheet metal forming the loading conditions are often more complex than the uni-axial example, which makes the yielding condition more complex due to the evaluation of the equivalent stress condition. Another factor which has an influence in sheet metal forming, is the anisotropic behaviour of the material. Anisotropic describes the materials change in mechanical properties in different directions, which is caused by the manufacturing of the sheet metal stock, where the rolling direction causes the mechanical properties to vary depending on direction [27]. The anisotropic behaviour has been of large interest for a long time, where different material models has been proposed [35, 36, 37], e.g. Hill48-93, Barlat89-97, BBC2000-2005. Each of these models require different amount of material data inputs, which is necessary to determine experimentally.
Acquiring this data can be time consuming and are varying for each batch (Coil), therefore another approach is to estimate the material to be isotropic, which means that the material has same properties in all directions. This can be expressed by linear hardening, Hollomons Hardening, etc. These models require fewer inputs and are often less computationally costly to use.

Generally, the use of a anisotropic model is most desirable, but it requires correct material data, since these are difficult to estimate, it is more recommended to use an isotropic material model, instead of estimating a wrong anisotropic behaviour.

1.6 Optimisation

Automatic optimisation is a mathematical tool for finding a given problems minima or maxima, by modifying a set of design parameters. For optimisation problems in sheet metal forming, the implementation of FEM software has affected the use of optimisation enormously, previously the method of trial-and-error was the main method for improving processes [32]. With the use of FEM a digital twin of the current process can be established and an visual inspection of the forming behaviour can be made and modification can be tested. The method of visually inspecting the FEM output and making knowledge based improvements are very dependent on the skills of the personal using this. This method can also be classified as manual optimisation. Examples of this type of optimisation can be found in [38] and [28].
The method of automatic optimisation is of greater interest, since the user only has to have knowledge about basic optimisation and modelling techniques, which can be applied on several modelled processes. However, the method of automatically optimising a FEM based problem, proposes a few challenges: First of all the mathematical optimisation techniques are based on analytical problems, where the cost function is well-known, while a FEM models result is qualitatively. In order to use the mathematical techniques on the FEM model, the results has to be quantified into a cost function, such an improvement of the model results in a decrease of the cost function. When setting up an optimisation, it is important to emphasis the necessity of choosing the correct design variables for the optimisation. Bonte et. al. [39], proposed to perform a screening before selecting the design variables for the specific optimisation problem, which would support the selection of design variables.

There are a clear distinction between direct and inverse problems for FEM problems [40]. Direct problems are defined as the final results from a FEM model, since all the input

parameters are predefined and the only unknown is the result from the model. Inverse problems are defined by a desired results, where the input to the model is the design parameters. When making optimisation in sheet metal forming, the problems are defined as inverse problems.

1.6.1 Inverse Problems

There exist two categories for which desired parameters are to be found for inverse problems [40]. These are listed beneath.

- Parameter Identification
- Shape/Process Optimisation

Parameter Identification is used when a given experimental data set is compared a FEM model, and modifications to the constitutive parameters are performed in order to minimise the error between the experimental results and the FEM results. The purpose of doing this type of optimisation is to improve the precision and accuracy of the existing model. An example of this is Endelt et al. [41], who made an inverse modelling of a deep drawn square cup, to determine the constitutive parameter to the Barlat 2D criteria.
Shape/Process Optimisation is used, when the settings for a forming operation is unknown, but the desired component is. For this type of inverse problem, the pressure curve, tool geometry, etc. can be optimised in order to achieve e.g. the desired component. Here the error between the desired component and the FEM model can be compared to form the cost function. An example of this is Bonte et. al. [39], where they optimised a hydroforming process, with the punch displacement and the internal pressure curve as design parameters.

1.6.2 Optimisation Methods

There are three branches of overall optimisation methods for sheet metal forming, which can be seen listed beneath:

- Evolutionary Algorithms
- Surface Approximation Methodology (RSM)
- Gradient Based Algorithms

Evolutionary algorithms, are based on the theories by Darwin, "Survival of the fittest", it gives a random input to the optimisation, which are then calculated and evaluated. This method requires a lot of function evaluations, and are generally a more expensive optimisation method than the gradient based method [40]. The algorithm is great for determining the robustness of a process, since a large variation of the inputs are tested, and its applicability in sheet metal forming has increase since computational power has become less expensive [40].
The Surface Approximation Methods are commonly used as an experimental approach, where a set of design experiments are executed and a regression analysis is performed to fit the data to a predetermined model. By this fitted model a surface of the experimented region is approximated and a path of the steepest descent is calculated to find a direction for the optimisation. When the new region of interest is determined, a new regression

analysis is performed, this continuous until an optimum is reached. This method is very good at determining process robustness, since this method often performs a factorial experiment, however, this method requires a lot of function evaluations [42].
The Gradient Based algorithms are the most commonly used methods in sheet metal forming, due to potentially less function evaluations needed. There exists a large number of gradient methods, which are based on the same two principles: **1:** Determine a descent direction and **2:** Determine the step size. The main idea by using gradient based optimisation in FEM is to approximate the gradients in order to determine in which direction, of the design parameter, the minima can be reached. However, when using gradient based optimisation one of the pitfalls is possibility of ending up in a local minima. This problem is also known as the local vs. global problem, which is illustrated on figure 1.10. The evolutionary algorithms are on the other hand very robust in finding the global minima for any problem.

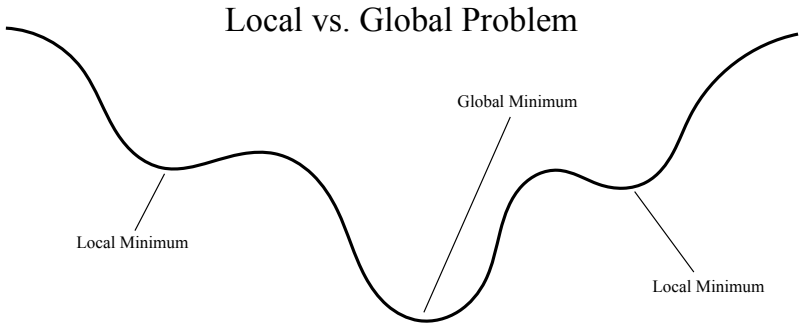

Figure 1.10. A graphical representation of the problem with finding the global minima.

1.7 Summary

In this section, a summary of the findings from Chapter 1 will be presented. This summary will be used for the later problem statement and solution strategy.

- **Sheet Metal Forming**: In the automotive industry, the focus for sheet metal forming operations, has been on development of methods for forming light-weight high strength steel components. This means a lot of unconventional forming operations are increasingly used, such as hydroforming.
- **Springback**: Is of large interest, both by the industry and the academic environment, its influence in sheet metal forming operations are difficult to predict. This is normally compensated for by over-forming.
- **Defects** The general defects in sheet metal forming is wrinkling, thinning/necking and fracture. These defects can be determine by using a Forming Limit Diagram (FLD), where the major and minor strain are used to predict these defects, this approach is often used in industry, but is not adequate for all processes. FLSD is recommended for multi-stage forming operations, because it is strain path independent.
- **Formability**: The defects in sheet metal forming can be avoided by increasing the formability in the forming operation. This can be done by several method e.g. by changing or increasing the forming steps.

- **Residual Stresses**: The residual stresses in sheet metal formed components are very important to consider, since these can cause corrosion cracking and influences the springback. The current methods for minimising the residual stresses are to thermally treat the part or to change the tool geometry to make a more homogeneous deformation.
- **Numerical Models**: Increasingly used in the automotive industry to model the sheet metal forming operations. An explicit solver has proven to be more beneficial, but a combination of the implicit and explicit is great at determining the springback.
- **Optimisation**: The use of automatic optimisation tools for inverse sheet metal forming problems are profitable, for development of parameter identification and shape/process settings. The use of Gradient based algorithms are beneficial compared to the Surface Response Method and Evolutionary algorithms, since the number of function evaluations are far less.

Based on this chapter, it can be concluded that sheet metal forming has seen a large development in recent years, which is partly due to the development of simulation tools. These simulation tools has made it possible to predict the challenges within the area of estimating, springback, defects and formability. This is still of increasing interest, due to the increasing computational power, but also the increasing use of high strength steel. Based on the use of high strength, the manufacturing processes has larger requirements, in order to achieve the attributes of the desired component. This increasing requirement to the manufacturing processes, causes the development time and man-power to increase as-well. The automatic optimisation techniques is utilised in many academic studies to minimise the man-power needed. However, the formulation of these optimisation problem are still an area of large research interest.

Problem Statement 2

In the area of sheet metal forming, a tremendous development has been carried out in the last couple of decades. Especially in the area of, development of simulation tools and utilisation of automatic optimisation techniques, has proven to be a feasible method to achieve increased product quality, process stability and efficiency. However, there are still used an enormous amount of man-power on research and development into product design and to reach stable manufacturing processes.
The aim of this project is to develop an initial framework, that makes the research and development phase of sheet metal forming faster and more effective, by utilising process simulation in combination with automatic optimisation techniques. Based on this the problem statement is formulated as follows:

How should an automatic optimisation for sheet metal forming simulations be constructed, in order to improve process design and aid research?

Solution Strategy

In this section, the solution strategy for the problem statement is presented. The framework will be developed through case studies, these cases cover a range of processes and challenges, which are based on previously published scientific papers or existing industrial challenges from former AAU projects.

These cases will demonstrate the advantages by setting up the problem in a suitable way, such automatic optimisation can be applied. Chapter 3 and 4, contains a presentation of the software used for making and solving the numerical models and for constructing the optimisation. The software selection is based on previous obtained experiences and existing knowledge at Aalborg University.
The outline of the framework, proposed in this project, is presented on figure 2.1, which consists of five parts: Purpose, Process, Modelling, Optimisation and Results & Discussion.

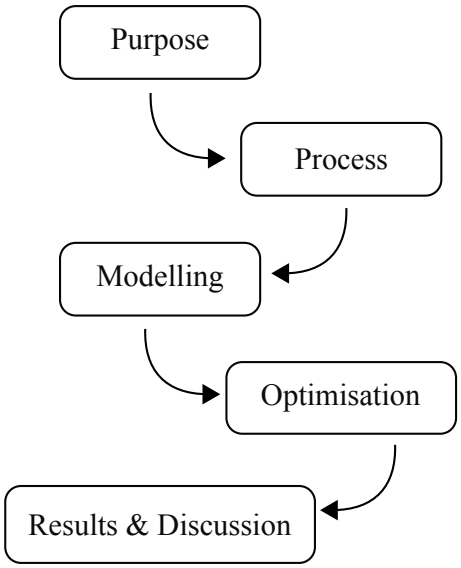

Figure 2.1. The framework structure formulated for this project, which will be used in all the six cases.

A thorough presentation and discussion of the finished framework will be presented in Chapter 11, where the knowledge obtained from each case are included. The structure of the framework outline, will be used in all the different cases, in order to determine the important attributes for each component. The six cases are presented in the following:

Case 1: Fins Manufacturing at Vestas Aircoil A/S

The aim of this case is to develop an approach for tool geometry optimisation, by taking offset in an industrial case, where the current outcome of the existing process has proven to not achieve the correct product geometry. The current operation is a multi-stage forming operation, which is fairly complex to understand with regard to the impact of each step, thus automatic optimisation is of large interest.

Case 2: Small Radius Cup

The aim of this case is to take offset in a newly developed forming process that can achieve relatively small radii, near complete corner fill. The current knowledge foundation is relative small, which is why the development of an automatic optimisation approach is desired, in order to achieve the optimal process settings for obtaining the smallest possible radii.

Case 3: Small Radii - Lunar Rover Test Piece

This case is similar to Case 2, since this is based on the same new forming process(Bulging-Pressing Compound Forming), however, this case aims to utilise the same developed approach, on a radius only 2.7 times the blank thickness, on a complex geometry.

Case 4: Hydraulic Expanded Tube-Tubesheet Joint

The case takes offset in an old joining process, where the academic development expands over a century, but the process still experiences quality challenges. Therefore this case aims to develop an automatic optimisation formulation, which will provide the optimal setting for a simplified model, and with this model develop a research approach which can extend the current knowledge base.

Case 5: Manufacturing of Airbus A380 Door Frame Corner

The case takes offset in two published papers about the manufacturing of a door frame corner piece for the Airbus A380, the world largest mass produced super-jumbo. This case aims to utilise automatic optimisation in the process design phase in order to achieve the desired product attributes, by minimising springback.

Case 6: VSR - Deep Drawn Cup

This case aims to utilise the exotic residual stress relieving process of Vibrational Stress Relieving (VSR). An investigation of the stress relieving behaviour is numerically tested on a deep drawn cup, in order to develop the foundation for a future optimisation.
An initial study for proving the relieving behaviour is documented in a paper, in Appendix A, where a simple example is devised.

3 LS-DYNA

The selected simulation software used in this project is LS-DYNA, which is a advanced general purpose multi-physics solver. The software code has been used at Aalborg University since 1991, where the Sheet Metal Forming Group began licensing LS-DYNA. This code has since than been the favourite FEM code for different forming operations, where in the resent years it has been applied for thermal coupled simulations, e.g. Laser Welding/Cutting.

3.1 History of LS-DYNA

The first version of the LS-DYNA, DYNA3D, was developed by John Hallquist at the Lawrence Livermore National Laboratory (LLNL), University of California and was released in 1978 as public domain. The code was initially developed for the purpose of simulating the FUFO nuclear bomb impact for low altitude release, which no 3D simulation software could at the time. In 1977 the nuclear FUFO bomb project was cancelled, but the development continued [43].
The development at LLNL continued until 1989, where John Hallquist resigned and started the company: Livermore Software Technology Corporation (LSTC). The code became more and more a commercial code, until the mid-nineties, where the public access to the code was limited. By 1992, it was one of the best non-linear FEM codes available with an explicit solver, which later on proved to be great for multi purpose simulations, which could delivers complex coupled solutions[43].

3.2 Syntax

The work flow of using LS-DYNA is very different than using other simulation software packages, where the model can be built, solved and evaluated is the same program. This is not the case for LS-DYNA which is only consisting of a solver and nothing more. This structure makes the LS-DYNA solver very simple to use, as it can be initiated with only one command line, that can be seen below.

```
- dyna_s i=Master.k ncpu=16 memory=20M
```

The command line specify that the single precision solver is used, the input file is Master.k, which is enough to run a simulation. To speed up the computational time, the number of

CPU's used can be increased, in this case is 16 specified, and the memory is set to 20MB to ensure sufficient memory allocation.

The input file for the LS-DYNA solver have to be made using a separate program, likewise is a separate program need to analyse the result of the simulation. For this is LSTC offering LS-PrePost free of charge, LS-PrePost is a program used for pre-processing and post-processing. The work-flow of how LS-DYNA is used with LS-PrePost, can be seen on figure 3.1

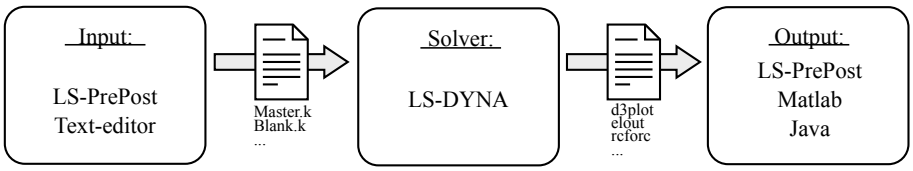

Figure 3.1. Work-flow of using LS-DYNA solver, and separate programs for the input files and analyse the output result.

The input, and most of the output files for LS-DYNA, is formatted in ASCII, this makes it possible to use, not only LS-PrePost, but a number of programs to built the input and analyse the output. On figure 3.2 an example of an input file can be seen, which can be edited using standard text-editor.

```
1  *MAT_POWER_LAW_PLASTICITY_TITLE
2  Copper
3  $#     mid        ro         e        pr         k         n       src       srp
4            18.96000E-9  118000.0      0.34     315.0      0.54       0.0       0.0
5  $#    sigy        vp      epsf
6           0.0       0.0       0.0
```

Figure 3.2. Keyword specifying a copper alloy material using Power Law Plasticity material model. Specified are: ID, mass density, Young's modulus, Poisson's ratio, strength coefficient and Hardening exponent.

LS-DYNA allows the user to select which unit set is used, this is not done directly, but instead selected e.g. when a geometry is drawn and the material properties are specified. The unit set used in this report can be seen in table 3.1.

Table 3.1. Unit set used in the simulations.

Name	Unit
Length	Millimeter
Time	Second
Mass	Tonne
Force	Newton
Pressure	MPa

Optimisation - Non-Linear Least Square

4

In this project the optimisation formulation of Non-linear Least Square is used, based on the beneficial formulation for FEM. The coding, formulation and implementation was performed by Benny Endelt for his Ph.d. Thesis [44]. The optimisation algorithms used in this project are all gradient based, and will be presented shortly in the next section.

4.1 Least Square Formulation

The general purpose for an optimisation is to minimise an objective function, in order to improve the current situation, by changing the selected design variables. This methodology has to some extend been applied to sheet metal forming, e.g. Benny Endelt Ph.d. Thesis [44]. His thesis focuses upon the application of a non-linear least square formulation of the objective function. The least square formulation can be seen in equation 4.1, which consists of a summation of the residual vector, which can be seen in equation 4.2. The residual vector is an error estimate between two data sets, which can be compared to a comparison between an empirical and simulated data set.

$$f(\mathbf{x}) = \frac{1}{2}\sum_{j=1}^{m} r_j^2(\mathbf{x}) = \frac{1}{2}\cdot r^T(\mathbf{x})\cdot r(\mathbf{x}) \tag{4.1}$$

$$r_j(\mathbf{x}) = \hat{y}_j - y_j \tag{4.2}$$

The purpose for using this formulations is the ability of quantifying the difference between two data sets into a positive number. This objective formulation is very generic and can therefore be applied for various problems, including numerical models.
A common approach for determining the search direction in optimisation is to use a gradient based approach, where the search direction is the opposite direction of the largest gradient. However, when applying this approach to optimisation on numerical models, the analytical expressions for the optimisation is not given and therefore it is necessary to estimate. For the least square formulation a Jacobian can be constructed for this purpose, see equation 4.3, and thereby make an estimate of the Jacobian by using a finite difference approximation, see equation 4.4. This Jacobian can then be used for constructing the

gradient, see equation 4.5.

$$J(\mathbf{x}) = \left[\frac{\partial r_j}{\partial x_i}\right] \tag{4.3}$$

$$\hat{J} = \frac{\partial r_j}{\partial x_i} = \frac{r_i(\mathbf{x} + \Delta x_j) - r_i(\mathbf{x})}{\partial x_i} \tag{4.4}$$

$$\nabla f(\mathbf{x}) = J(\mathbf{x})^T r(\mathbf{x}) \tag{4.5}$$

The determination of the Hessian can be seen on equation 4.6 and 4.7. The Hessian is used for the second order derivatives of the optimisation, which can be used to determine the curvature for objective function. The Hessian is constructed by the Jacobian, which is constructed on first-order information, and by the second order part which consists of a summation of the residual vector and the second order derivatives. This second order part can for some problems be very computational expensive to calculate, which is why some optimisation algorithms assumes the second order derivatives to be negligible.

$$H = \nabla^2 f(\mathbf{x}) = J(\mathbf{x})^T \cdot J(\mathbf{x}) + \sum_{i=1}^{m} r_i(\mathbf{x}) \cdot G_i(\mathbf{x}) \tag{4.6}$$

$$G_i(\mathbf{x}) = \nabla^2 r_i(\mathbf{x}) \tag{4.7}$$

With the defined objective function and the formulation for approximation of the gradient, only the selection of the specific optimisation algorithm is remaining. The selection of algorithms are very problem dependent, and will not be of interest in this project, since the focus is on application of the optimisation algorithms. In the following section, the selected method for setting up the sub-problem will be presented.

4.2 Trust Region

The method for solving gradient based optimisation problems are by changing the parameters values in the direction opposite to the gradient. The determination of the next design parameters are determined by the current design parameters added with the step size, s_i, see equation 4.8. The determination of this step size is also referred to as solving the sub-problem.

$$x_{i+1} = x_i + s_i \tag{4.8}$$

Solving the sub-problem can be done with different methods e.g. line-search. For this project, the method of Trust Region is used, which is a simple method where a trustworthy region is determined and the step is regulated by this. A representation of this can be seen on figure 4.1, where the trust region is represented as a circle, for a problem with two design parameters.

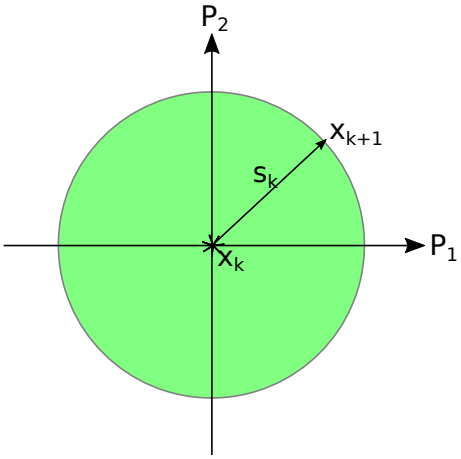

Figure 4.1. Illustration of the trust region, the green area, where the current parameters, x_k, is the center and the step, s_k gives the next parameters, x_{k+1}. This is all represented in the design space. Here it is can be seen that the trust region, sets the bound for the step size.

The trust region is calculated before each step, and is based on gradient and Hessian properties, this will not be further elaborated. A important thing to note is that when the optimisation algorithm proposes a new design parameters set, and the these estimated design parameters does not minimise the objective function, the trust region decreases and a new set of design parameters are proposed. Similarly, the trust region can also increases if the objective function decreases. This can be seen on figure 4.2.

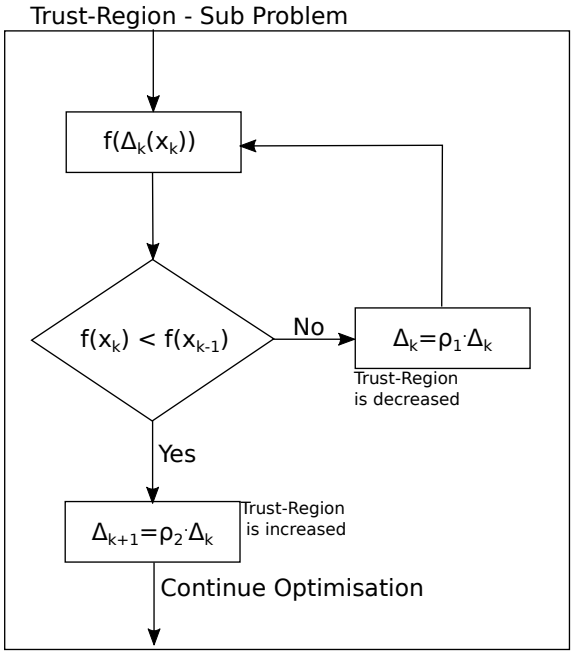

Figure 4.2. A simplified flow diagram of the trust-region method, where the object function is evaluated in order to increase or minimise the trust-region. The gain factors for the increasing and decreasing can be modified, by setting the trust-region control parameters.

4.3 Automatic Optimisation Structure

The overall structure for the automatic optimisation used in this project can be seen on figure 4.3, where each step will be elaborated on the following list:

- **Initial Parameters**: The first step of the optimisation, where the initial parameters guess are set by the user.
- **Numerical Simulation**: These initial parameters are then implemented into the numerical model, which is performed with the shell script *nativein*(see Appendix C.3).
- **Calculate Object Function**: This steps takes place when the simulation is terminated, and the data required from the simulation is extracted, also performed with the shell script *nativein* and *Cutter.sh* (see Appendix C.3 and C.4), the data is then used for calculating the defined Least Square Objective function, defined in the java script: *ObjectFunction.java*. This objective function value is then compared to the first stopping criteria ϵ_1 to determine if the optimisation should terminate. Else the optimisation continues to the next step.
- **Simulate Finite Difference**: For this step, the simulations required in order to make a finite difference approximation is initiated. The amount of simulations required in this step is equal to the number of the design parameters in the optimisation problem.
  These simulations can be run simultaneously, and thereby minimising the time required for this step [44].
- **Calculate Search Direction**: The data from the prior step is extracted and the Gradient and the Hessian is calculated, depending on the selected optimisation algorithm. The gradient is in this step evaluated in order to determine if the gradient is smaller then the second stopping criteria ϵ_2, else a new search direction is calculated and an initial step length.
- **Trust-Region - New Step**: The previously determined search direction and the step length is modified by the trust-region, and a new step is calculated. In this step, the trust-region size is evaluated in order to determine if the step length is too small compared to the third stopping criteria ϵ_3.
- **Numerical Simulation**: The new step is simulated in order to determine the data needed for the objective function calculations.
- **Calculate Object Function**: The simulation data is extracted and the objective function is calculated. The objective function is evaluated according to the trust-region, where an increase in the objective function will result in a decrease of the trust-region, and a decrease in the objective function will results in an increase of trust region for the next step. A decrease of the objective function will results in a comparison with the first stopping criteria, if this is not met, then the iteration number is increased by one and the optimisation continues with estimating the finite difference.

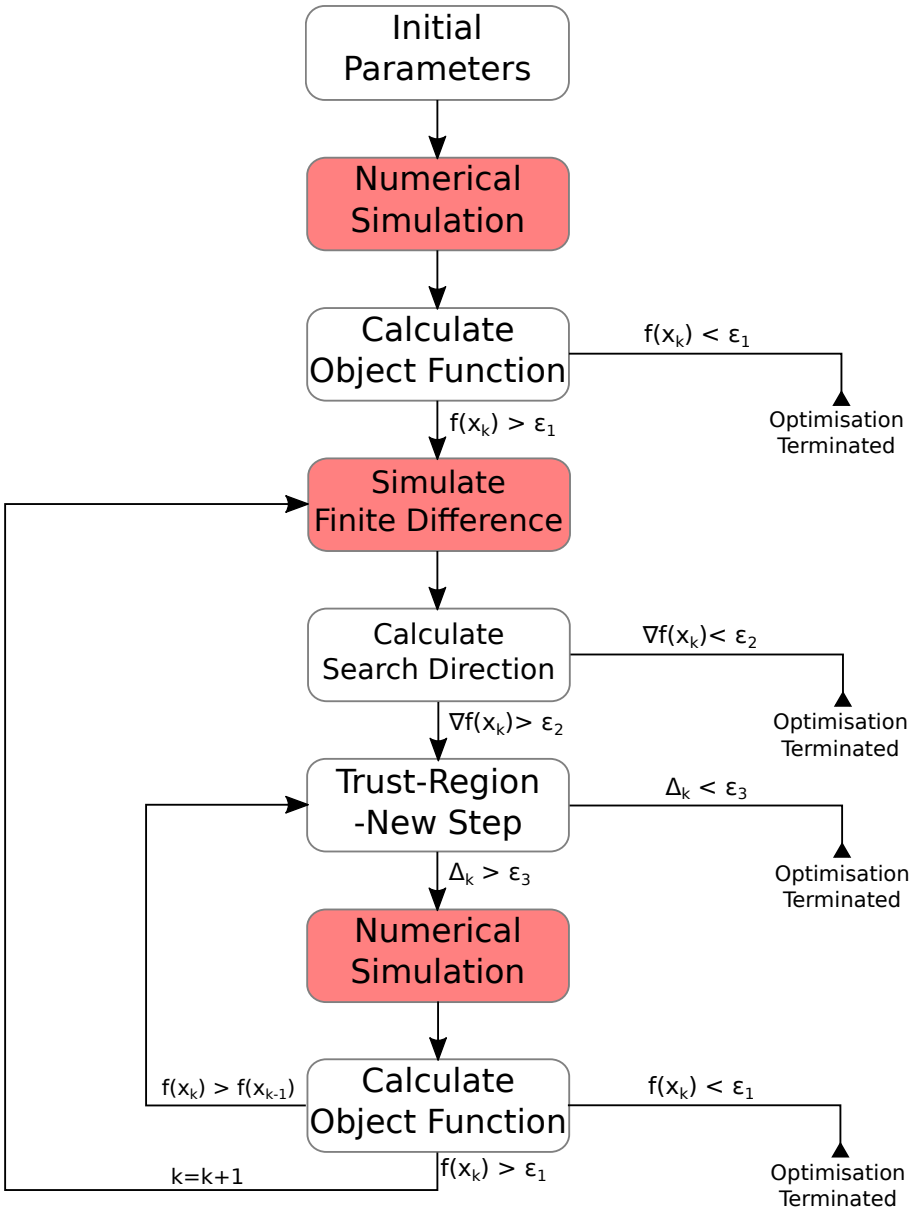

Figure 4.3. A flow diagram of the automatic optimisation procedure used in this project, the red boxes illustrate when a simulation is performed.

The files used for setting up the optimisation will not be presented in the report, but can be found in the Appendix C, where the files *lsopti.in*, *ObjectiveFunction.java*, *nativein* and *Cutter.sh* are presented.

Case 1: Fins Manufacturing at Vestas Aircoil A/S

5

In this chapter, the modelling and optimisation of a multi-step forming operation will be presented and tool geometry and process parameter optimisation will be performed. The model constructed in this section, takes offset in the fins manufacturing at Vestas Aircoil A/S, who is as customised heat exchanger manufacturer. The fin manufacturing process, is a 7 step forming process, where the main challenges are achieving the correct geometry and the secondary challenges is to introducing new sheet materials in the process. This process is then modelled and an automatic optimisation is performed on the final step, in the multi-step forming process, where the punch radius and displacement are the design parameters.

In Appendix D, additional information regarding: simulation, keyword and optimisation data, can be found.

5.1 Purpose

The purpose is presented in bullet points underneath, the first objective is to demonstrate the modelling approach for multi-step forming operations, together with the optimisation formulation for such a model.
The second purpose is to formulate a general approach for tool geometry optimisation, where focus is on a robust formulation method for defining geometries.

- Modelling and optimisation of multi-step forming operations
- General approach for tool geometry optimisation

5.2 Process

Vestas Aircoil A/S, located in Lem Denmark, is a manufacturer of customised heat exchangers used in the e.g. container ship industry. An air to water heat exchanger can be simplified as presented on figure 5.1, which shows the primary components with names. This example will take offset in the manufacturing of the heat exchanger fins.

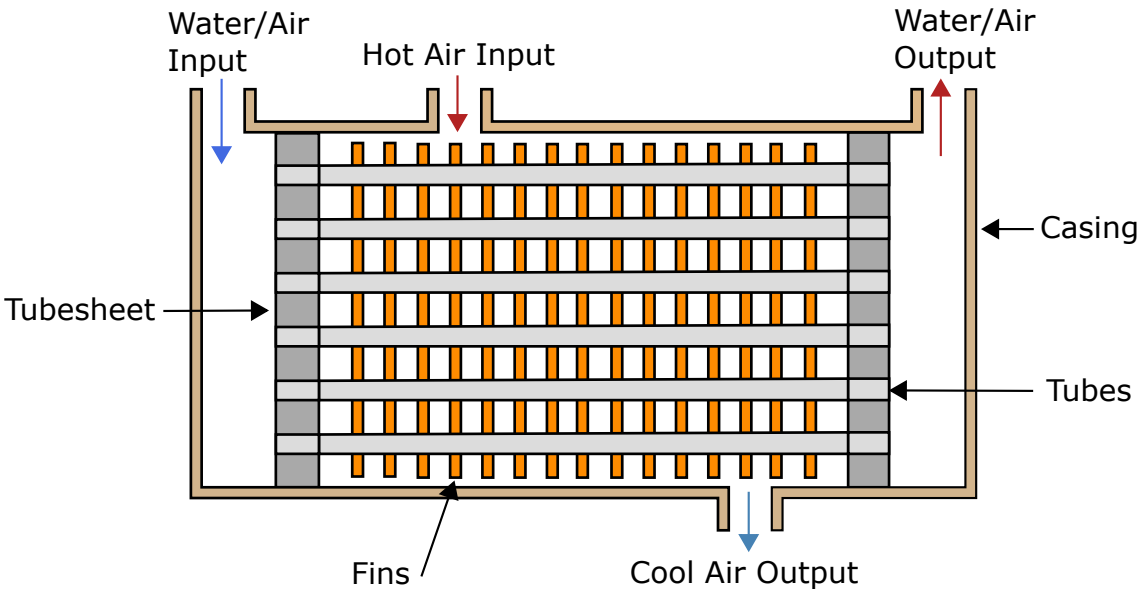

Figure 5.1. A graphical representation of the components in a heat exchanger from Vestas Aircoil A/S. (Source: [45])

The purpose of the heat exchanger fins are to assure an effective heat transfer, by controlling the heat flow from, tube to fins and fins to air. The fins are mounted in the heat exchanger, by stacking the manufactured fins onto tubes, that are inserted in the fins holes, this can be seen on figure 5.2. The tube-fin assembly are afterwards secured in the tubesheets, this process is called a tube-tubesheet joint.
The fins are designed for the stacking, where the vertical part of the fins assure the distance between the fins and are used to obtain a firm contact for a later expansion of the tube, which joins the tube and fins to make an efficient heat transfer connection, this process is called bullet expansion.

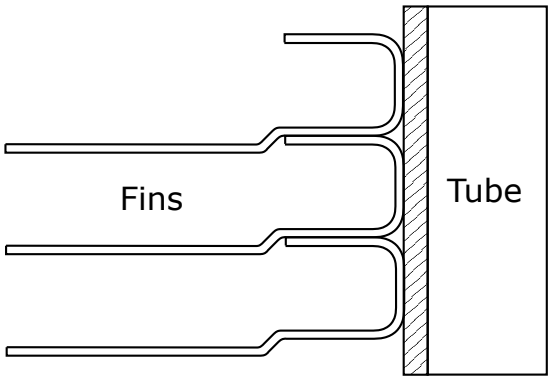

Figure 5.2. The stacked fins and the tube.

Figure 5.3. Copper alloy fin before it is mounted in the heat exchanger.

The fins' material is a copper alloy, CuTe alloy (SM0300), which is feed from a coil to the fin production line.

5.2.1 Manufacturing Process

The fins are manufactured by a multi-step progressive sheet metal forming process. The process consists of seven steps, which are illustrated on figure 5.4, the process description is based on the former student project by Barlo at al. [46] made in collaborations with Vesta Aircoil A/S.

The process is performed by moving the top die, downwards and thereby pushing the spring tensioned blankholder down and deforming the copper plate against the punches at a pre-set depth. On the figure it can be seen that some of the dies are connected and displaced the same distance, and the blankholder is controlled by a preloaded spring. The punches can be adjusted manually in height, but are fixed in position during the manufacturing.

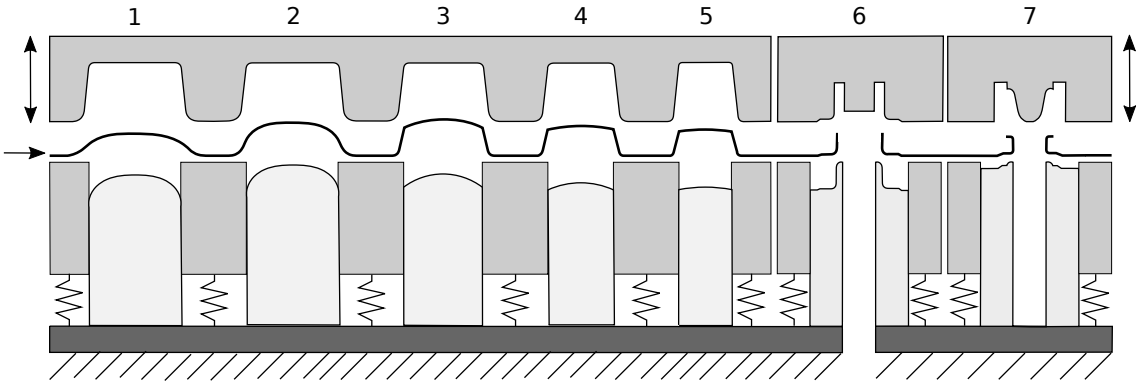

Figure 5.4. An illustration of the 7 steps in the manufacturing of the fins, where the plate material is fed from the left and the top part is moved downwards, which deforms the material. The first 5 steps are drawing operations, where the material is deformed into a cup-like shape. The 6. step performs a cutting operations and straightens the vertical part, also called dimpling, and in the 7. step the vertical part is formed into a open hem.

The first five steps are drawing operations, which purpose is to draw-in material, these multiple redrawing steps helps to minimise the thinning compared to a single step drawing. The first two steps are consisting of the same size die and punch, the three following steps the dies and punches are gradually decreased, before the dimpling operation in step 6. The dimpling process can be divided into two operations, the first is a shearing operation, where the center part is punched out, the second operation is straightening where the vertical parts are created on the fins. The final step, step 7, forms the vertical part into an open hem.

5.2.2 Challenges with the Process

The current set-up was constructed in 2007 by a subcontractor, specifically for making copper alloy fins. At Vestas Aircoil A/S they have observed cracking in the open hem edge, for some of the fins. They initiated an investigation upon this problem by hiring a company to perform 3D scans of the different steps in the fins manufacturing. It was observed that the final shape of the fins where not completely similar to the ones defined

by the CAD drawing. Therefore Vestas Aircoil A/S expresses interest in obtaining an improvement of this process, in order to obtain the desired fin shape.

In addition, some of the heat exchanger customers are demanding that the fins are made in stainless steel, instead of the copper alloy used in the current design, due to environmental requirements. The change in material has been tested by some initial experiments, fracture of the plate material was observed early on in the drawing part of the manufacturing process. Therefore Vestas Aircoil A/S also expresses a desire to determine the optimal setting for the stainless steel fin production, in order to obtain the geometry specified on the CAD drawing.

When developing a multi-step forming process, an Expert System is used, where the desired geometry is inputted and a process plan is proposed. However, these system are often based on simplified plasticity theory, which is why these system often should be modelled to determine the process limitations [47].

5.3 Modelling

The punches and dies model geometries used in the first six steps, and die used in the seventh step, was constructed by Barlo et al. [46], and reused in the simulation and optimisation in this case.

When modelling multi-stage processes, there are some general challenges that have to be considered, such as springback between the steps and keeping track of the residual stresses [48]. In order to keep track of these, two modelling methods are proposed: Either each process stage is modelled in their individual simulation, which would mean that this method should consists of 7 simulation. The advantage by modelling it like this, is that the debugging is fairly simple, since the calculation time is relatively short, and one simulation can be debugged individually. The disadvantages is the handling of deformed parts between the different simulations, which requires extra care when positioning and moving the parts.
The other approach is to model all the stages in one simulation, where the continuity of the process is included. The advantages is the possibility of keeping track of the deformable part, e.g. tracking the plastic strain in one element. The disadvantage is the long calculation time, which is undesirable for the modelling and debugging phase.

A combination of these two methods are used For the fin manufacturing model. This model will be divided into two simulations; the first 5 and a half steps, and the last one and a half steps, which splits the 6. step into two halfs. The purpose for dividing the process in such manner, is the shearing operation. In LS-DYNA shearing can be modelled with a function called `Define_Curve_Trim`, which can only be performed at the start of a simulation, time-step 0.0 sec. A graphical representation of the modelling approach can be seen on figure 5.5. Here it can be seen that the forming operation is modelled with a simulation time of 0.015 sec and the repositioning of the blank is done in 0.005 sec, before the next forming operation is initiated at time 0.02 sec.

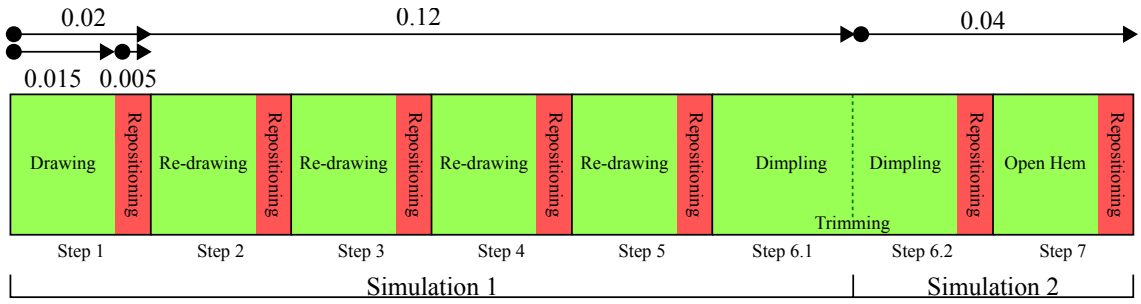

Figure 5.5. A graphical representation of the multi-step simulation, where the models are divided at the dimpling step (step 6), because of the trimming operation defined in LS-DYNA.

All steps on figure 5.5, are modelled the same way, which consists of a die, punch, two blank holders and the blank. This is illustrated on figure 5.6. For all the steps, the die is moved down and up with a S-curve at a fixed displacement, where the blank is moved with the die down to the punch and deformed. The punch is fixed in space and are placed in a predefined position corresponding with the 3D scans received from Vestas Aircoil A/S. In order to control the blank in the downward movement, the lowest blank holder is modelled with an acting load, that increases with the displacement of the blank holder, which corresponds to a spring. When the forming is done, the blank is repositioned, by moving the blank upwards. It was observed with some initial investigations that the blank is containing a large amount of inertia, which forces the blank to continue the upward movement after repositioning. Therefore a second blank holder is implemented and fixed in space, and keeps the blank positioned at the same initial position.

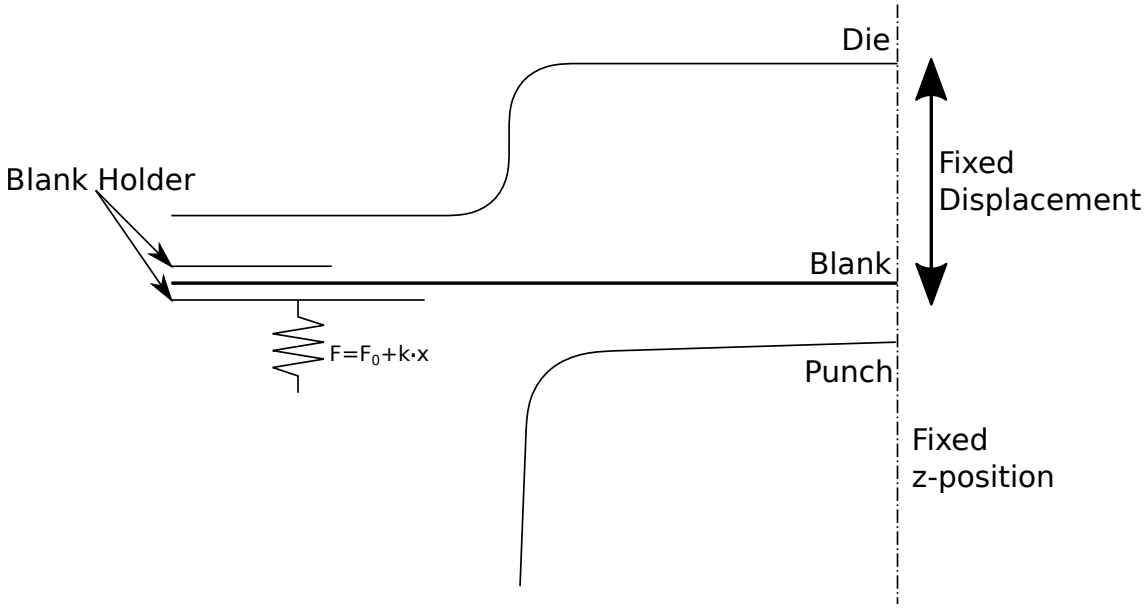

Figure 5.6. A graphical representation of the forming set-up for the model.

The fixed displacement and the deformation from the model can be seen on figure 5.7,

where the first simulation from figure 5.5 is the one shown here. The different positions of the punches are influencing the drawing depth/height. The blue line is the displacement of the non-deformed part of the blank and the red part is the middle part of the blank, which is the point on the blank with the largest drawing depth/height.

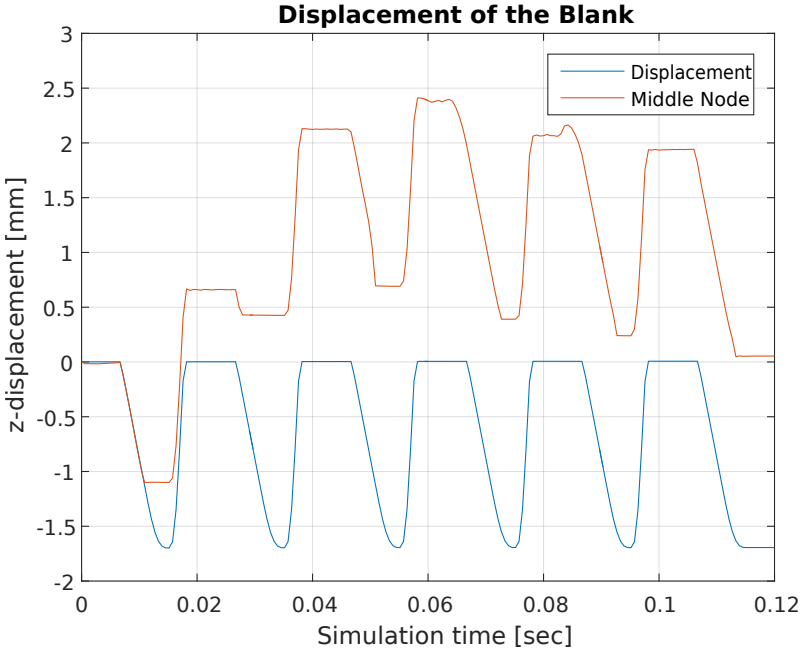

Figure 5.7. The z-axis displacement of the blank and the middle node, which represents the height of the deformed blank. It should be noted, that the blank is moved to the fully displaced position for the final step.

The model which best replicates the 3D scanned fin geometry from the current production, is presented on figure 5.8, where the blank's geometry after each step is presented. Here it can be seen that the blank is starting with two steps of wide drawing, and thereafter the geometry is gradually minimised in the y-axis.

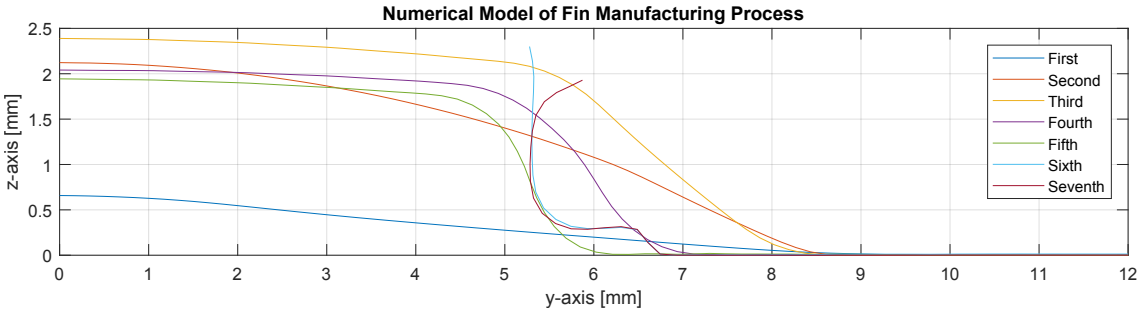

Figure 5.8. The blank's geometry after each of the seven steps.

The blank's material is simplified to be pure deformable copper [27], the material parameters can be seen in table 5.1. This material is not the same as the one used at Vestas Aircoil A/S, since it has not been possible to acquire the specific material data.

The material model used is an isotropic plasticity model, which is based on the power law hardening rule [35], LS-DYNA material model no. 18.

Table 5.1. The material parameters used for the copper fins simulation. Parameters from S. Kalpakjian et al. [27].

Input Parameters		LS-DYNA unit	Copper
Density	ρ	[tons/mm^3]	8.96e-9
Young's Modulus	E	[MPa]	118e3
Poission's ratio	ν	[-]	0.3
Strength coefficient	K	[MPa]	315
Hardening exponent	n	[-]	0.54

The blank is modelled as shell elements with the Belytschko-Tsay element formulation with 7 integration points through the thickness [49].

5.4 Optimisation

The tool geometry will be optimised in order to achieve a more desirable fin geometry. The application of FEM optimisation for improving a multi-step forming operation, by changing the tool geometry was also performed by Z. Zimniak [25], where his objective was to achieve a more uniform thickness distribution. However, in order to achieve an uniform thickness for this case, the entire model has to be parameterised, which is undesirable for the initial investigation of this process, where the correct fin geometry is of interest.
Tang et al. [50], performed an optimisation in regards to the later bullet expansion process, to optimise the geometry of the fins to obtain the best contact. However, this optimisation focuses on obtaining the correct geometry, defined by the CAD drawings.

The objective function is formulated by defining the fin geometry, as a horizontal plane and a vertical plane, where the objective function is calculated as the error between the current node set and the planes. This can be seen on figure 5.9. Through the development of this optimisation another objective was found in order to assure the nodes in the horizontal plane to be better levelled. The level objective is formulated by including the rotation of a node through the process, and making sure that it is rotated 180°, as is also presented on figure 5.9.

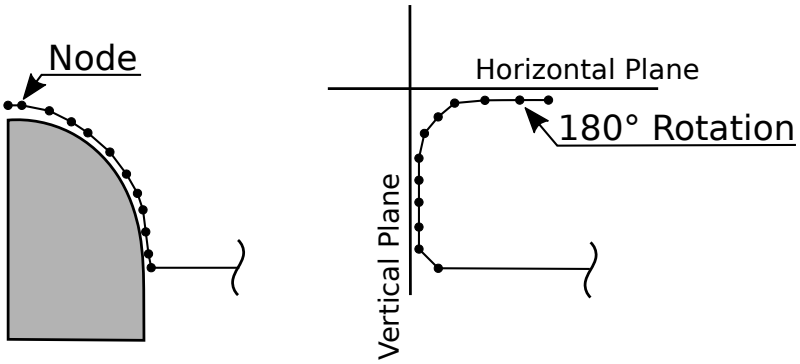

Figure 5.9. Illustrates the formulation of the objective function, which consists of two planes and a nodes rotation.

The horizontal plane is redefined for each optimisation run, since the height of the hem is not of interest for this optimisation, therefore the node tracked for the 180°rotation, is defining the z-coordinate for the objective function. The purpose of defining the objective like this is to achieve a squared open hem.

5.4.1 Design Parameters

This optimisation will focus upon the tool geometry as one of the design parameters. Therefore the important features of the tool geometry is decided to be the radius, see figure 5.10, and the displacement of the tool during the forming process. In order to implement these parameters properly, the tool geometry is constructed using Block Mesher (a short description of Block Mesher can be found in Appendix B) and the displacement is parameterised in the keyword file.

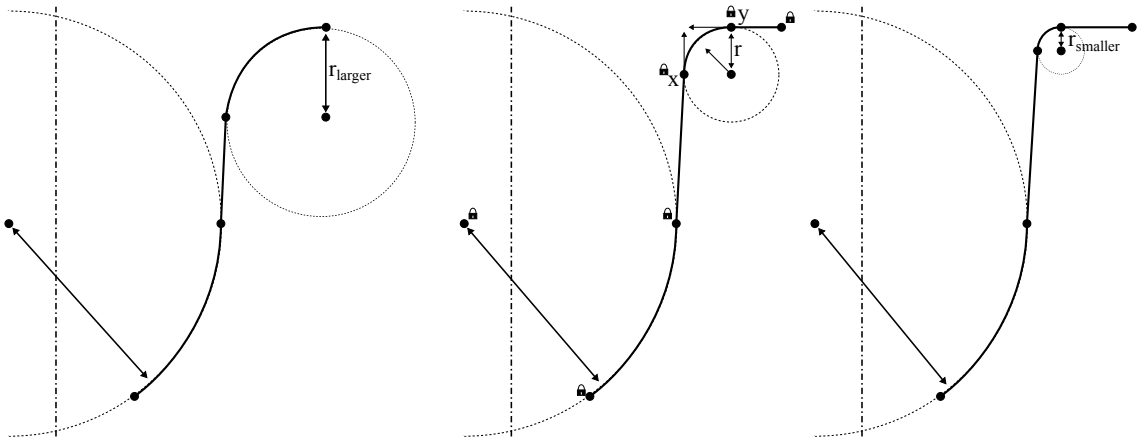

Figure 5.10. The parameterised tool geometry, where the punch inner radius is the only parameters that is to be changed, without affecting the entire geometry. Therefore the two point presented in the middle, are locking individually, such the radius always consists of a 90°curve.

There are some bounds, for these design parameters, that are necessary to apply, in order to limit the possibility of creating unrealistic solutions or possible error terminations for

the numerical model. Therefore, both the displacement and the radius are bounded as can be seen in table 5.2.

Table 5.2. The prescribed parameter bounds for the optimisation, together with the initial guess.

	Radius	Displacement
Upper Bound	1.2 mm	10 mm
Lower Bound	0.2 mm	7 mm
Initial Guess	0.8 mm	8.5 mm

It should be noted that by applying bounds to the parameters, the solution space in decreased and the steps, which will be calculated by the optimisation algorithm, will be smaller due to a prescribed bounded step size, this is generally undesirable to have these kinds of bounds, but in this case it is necessary.

5.5 Results and Discussion

In this section the results from the optimisation will be presented and discussed. For this optimisation, the scaled factorized Broyden-like method is used, the initial trust region is determined by the half of the pure newton step, however, the step size is highly influenced by the bounds applied to the problem. The cost function and design parameters for each iteration can be found in Appendix D.4.
The optimal settings found from the optimisation is summarised in table 5.3 and 5.4. For this type of problem where the move-limits are relatively short, the solution is highly dependent on a qualified initial guess. One of the things worth noting is the size of the cost function, which for this problem is fairly small, this is due to no penalties applied and only 9 nodes are included for the objective function.

Table 5.3. The optimum settings for the optimisation of the fin geometry.

Type	Radius [mm]	Displacement [mm]	Cost Function
Initial Guess	0.7	8.5	0.37
Optimum	0.60	8.73	0.14

In table 5.4, some of the specifics regarding the optimisations performance can be seen. It should be noted that the optimisation terminated due to a too small step size, because the trust region was decreased a lot for the final iteration.

Table 5.4. The function evaluation, trust region evaluation and the number of iterations performed.

	Function Evaluation			Trust Region		
Type	Total	Cost	Jacobian	Increase	Decrease	Iterations
Optimum	24	12	12	4	6	6

The cost function for each iteration in this problem can be seen on figure 5.11, where it can be seen that the optimisation reaches a minimum for the last two steps. It should also be noted that the optimisation is allowed to increase the objective function for one step, in order to limit the possibility of getting stuck in a local minimum. On figure 5.12, the parameter setting for each iteration can be seen. Here it is noteworthy that the punch displacement seems to have a linear convergence and that the radius is more non-linear.

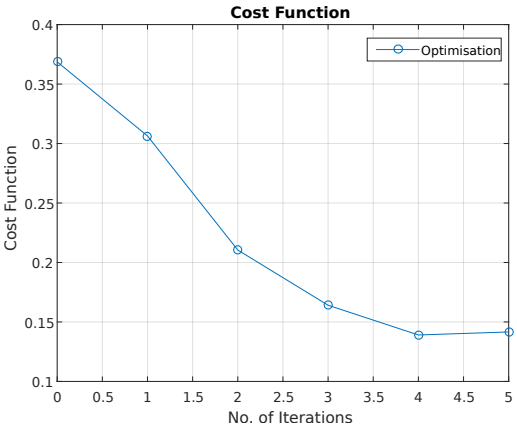

Figure 5.11. The cost function for each iteration.

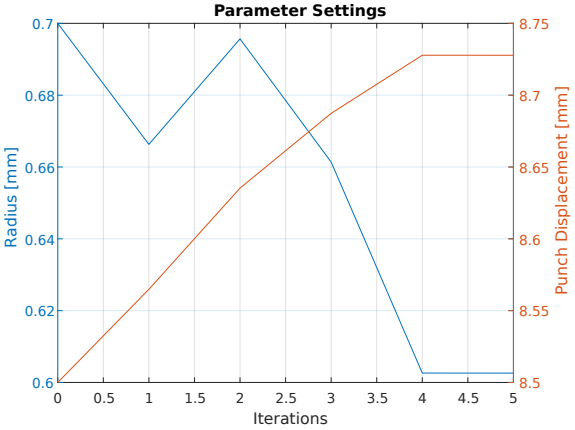

Figure 5.12. The parameter settings for each iteration.

The objective for this optimisation has been to achieve an improvement of the current geometry. This is done by making an objective function replicating a horizontal and vertical plane. The geometry for the initial guess, optimum, current geometry and the objective geometry, can be seen on figure 5.13. Here it can be seen that the improved design, achieves a 90 °bend, in relation to the vertical and horizontal plane.

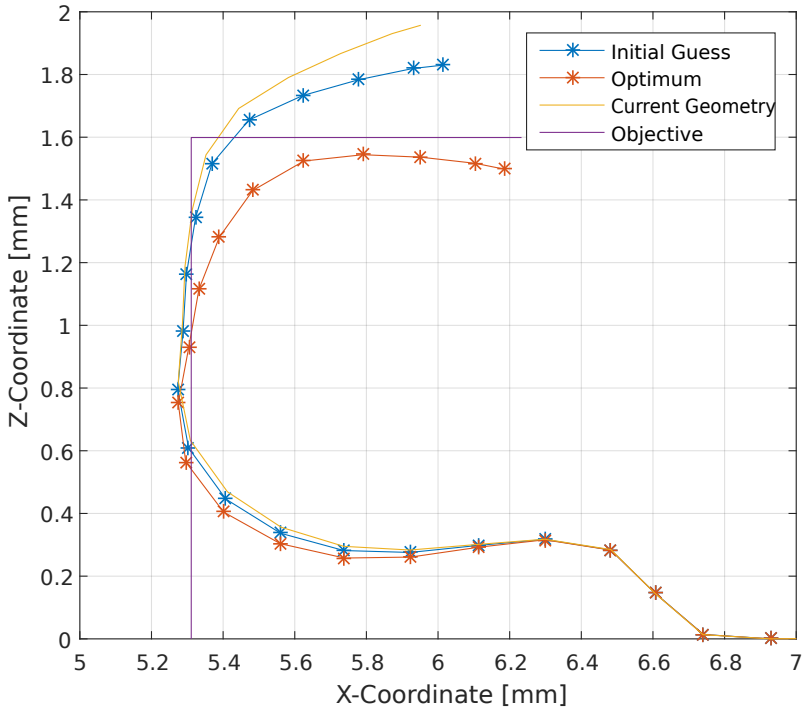

Figure 5.13. A plot of the fin geometry, the initial guess, optimised, current and objective are illustrated.

On figure 5.13, it can also be seen that a geometry with larger z-coordinate height, can only be achieved by increasing the height of the material delivered to the trimming operation, if the open hem width should be preserved. Therefore it can concluded, that if the objective is to get a higher open hem, then optimisation should be performed on the 5 previous drawing steps.

From the results of the optimisation, in table 5.3, it can be seen that the radius has converged to the value of 0.6 mm, and since this value is not at the boundary, the result can be conclusive. However, it should be noted that the parameters are a bit connected, since a smaller radius would require a larger displacement to achieve contact and vise versa.

5.6 Sub-conclusion

This chapter is based on a case, from the manufacturing of fins at Vestas Aircoil A/S, which are manufactured with a multi-step forming process. The main focus for this numerical model is to keep track of the residual stresses during the simulation time, where the 7 steps process has been divided into two simulation, since the LS-DYNA trimming operation requires this to be done at timestep 0.0 sec.
The objective function of the fins geometry were determined to consist of a vertical and a horizontal part with a 90°bend. The design parameters were determined to be the radius on the final punch and its displacement. The punch was parameterised using the Block Mesher in LS-PrePost, and the optimum was found to be a radius of 0.6 mm and a displacement of 8.73 mm.

If a higher open hem is desired, then the five first forming operation has to be included in the optimisation as design parameters, these steps were not included due to high computational costs, but it would be beneficial in order to create a larger solution space.

Case 2: Small Radius Cup 6

In this chapter, the development of a model which can achieve a very small radius will be made. The model is based on a two stage forming process, consisting of a hydromechanical deep drawing and a bulging-pressure compound step, which is based on a published paper [51]. The optimisation made for the model is based on a multi-objective function: including the sum of thickness and geometrical error. The geometrical objective aims for a sharp edge and the thickness's aims is to minimise the thickness strain. The design parameters are the two punch displacements and the pressure curve in the final stage. The results from the optimisation are very depending on the size of the initial trust region, which influences the magnitude of the final pressure in the oil-pressure path, therefore three different optimisation where deducted.

In Appendix E, additional information regarding: simulation, keyword and optimisation data, can be found.

6.1 Purpose

The purpose for this case is presented in bullet points underneath, where the first objective is to develop a model for making a cup that can get the smallest possible radius, this model will then be optimised in order to achieve the minimal radius. The objective function formulation for this optimisation, should be some what generic, in terms of being applicable for other models. Furthermore, this case will also focus on the formulation of process settings as the design parameters for the optimisation, where the formulation of such will be generalised.

- Develop a model and an optimisation for obtaining the smallest possible radius
- General formulation of process settings optimisation

6.2 Process

The following will present the radius limitations for conventional forming method. Recommendations for conventional deep drawing states that the minimum punch radius should not exceed 10 times the sheet thickness for aluminium, and 5 times the sheet thickness for stainless steel [26]. The punch nose corner radius is critical, and may cause local thinning and cracks do to high friction if the radius is too small. Punch nose friction

can be lowered by using hydro-mechanical deep drawing which will increase the limited draw ratio [52]. In Hydro-mechanical deep drawing the die is replaced by a pressurised draw bed which allows increased process control. Smaller punch nose radius may be possible to achieve with Hydro-mechanical deep drawing, but there is still a limit which is far form a perfect corner fill.

In tube hydroforming is corner filling and small radius's likewise a topic of research, which share similar defects and challenges as hydro-mechanical deep drawing. Elyasi et al. [53, 54] used a method, for expanding a tube out in a die with shape corners, where the part of the die, which form one side of the corner, is moved during hydroforming, after an initial bulging process. By moving the die towards the final shape, and pressurising the inside of the tube, was it possible to feed material, instead of stretching the material into the corner. The better material flow and decreased friction allowed the corner to be completely filled in contrary to the conventional die design where the corner was only partial filled.

Wang et al. [55] proposed a method, named bulging-pressing compound forming, for achieving a very small radius deep drawn cups, by using a two step process, which consist of a hydro-mechanical deep drawing operation followed by a moving die/punch bulging pressing operation. Bulging-pressing compound forming was further investigated by Wang et al. [51]. The second step is similar to the moving die tube hydroforming process, with the purpose of feeding the material into the corner instead of stretching, resulting in optimal corner fill and uniform thickness distribution throughout the corner.

The process of bulging-pressing compound forming, illustrated on figure 6.1, consists of a two step forming operation. The first step is a hydro-mechanical deep drawing, where the blank is deep drawn, by a punch, into a pressurised draw bed. The second is bulging-pressing compound, where the opposite side of the blank is pressurised and a punch is moved down from the top to feed the material out into the corner.

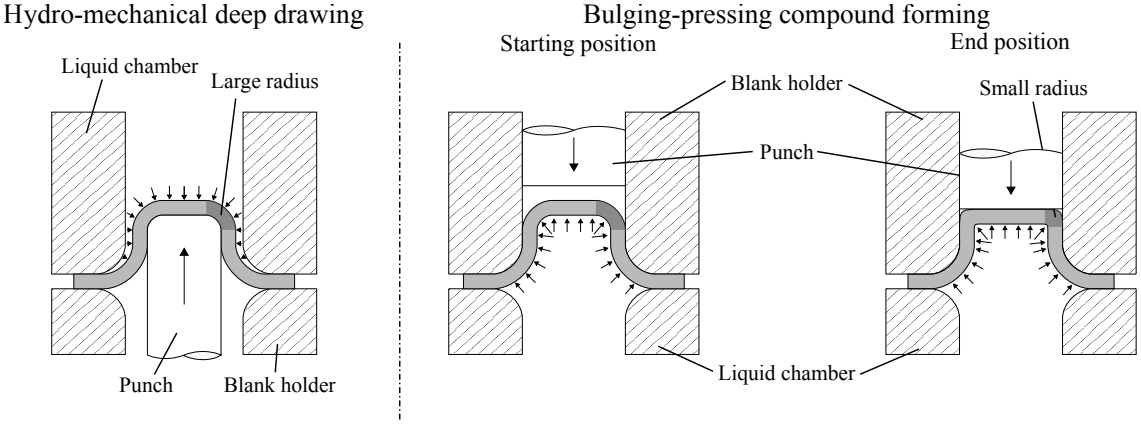

Figure 6.1. Bulging-pressing compound forming, which consist of two steps. The first step is hydro-mechanical deep drawing, the second step is bulging-pressing compound forming where the large radius is formed into a smaller radius limited by the sheet thickness.

This process has some different parameters in order to achieve the desired thickness

distribution and minimal radius. For both steps the pressure curve has a large influence upon the final product, together with initial punch position for the first stage, and the punch velocity for the second stage [51].

6.3 Modelling

The modelling of the bulging-pressing compound forming process is modelled as one simulation, containing the two steps. The model is constructed with the parts, that can be seen on figure 6.2. The model is based on the parts from Wang et al. [51], but for this model, the liquid chambers also acts as blank holders.

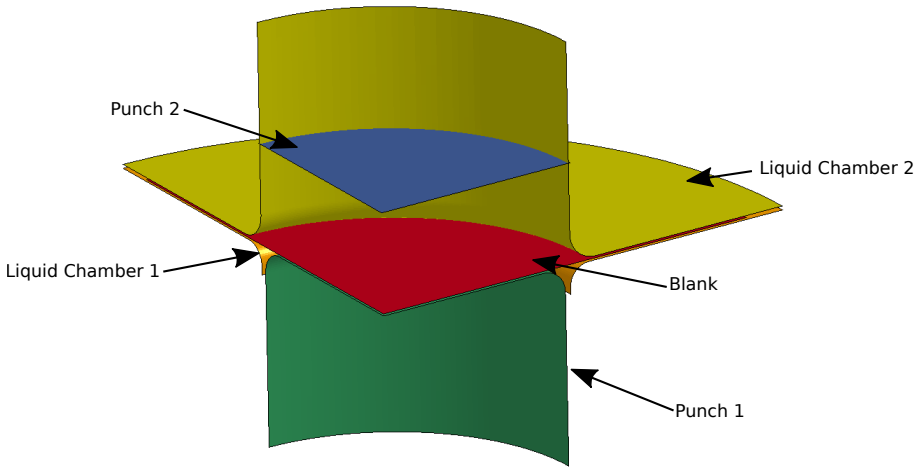

Figure 6.2. The numerical model for the bulging-pressure compound forming process. The dimension of the parts can be seen in table 6.2.

All the parts are constructed as shell elements, where the tool- and die-parts are modelled as rigid. The blank is modelled with fully integrated shell element modified for higher accuracy(ELFORM = -16) and with 5 integrations points[49] throughout the thickness. This element formulation is selected based on the applied implicit step in the final 0.001 sec of the simulation(from 20-21 ms), which requires the shell elements to be fully integrated[49]. The implicit step is used for including the springback in this geometrical optimisation, as was proposed by Finn et al. [34].
The material model used for the blank is Hill's 1948 planar anisotropic material with 3 R values[35], the material data is based on Wang et al. [51]. The material data and the geometrical measurements can be seen in table 6.1 and 6.2.

Table 6.1. Material parameters of aluminium alloy 2024-O for the blank [51].

Component	Value	Unit
Mass density	2.7e-9	t/mm^3
Yield strength	224	MPa
Tensile strength	425	MPa
Strength coefficient (K)	306	MPa
Strain exponent (n)	0.24	
Posson's ratio	0.3	
Young's modulus (E)	71	GPa
Anisotropy coefficient r_0	0.70	
Anisotropy coefficient r_{45}	0.65	
Anisotropy coefficient r_{90}	0.60	

Table 6.2. Dimensions of modelled tools and blank, data from Wang et al.[51].

Component	Value [mm]
Punch diameter	100
Punch nose radius	6
Liquid chamber diameter	103
Liquid chamber nose radius	7
Blank holder diameter	103
Blank holder nose radius	5
Blank diameter	200
Blank thickness	1

One of the biggest challenges with multi-step models is the initiation and timing of the different forming operations. This process consists of two steps, as describes earlier, the first is a hydromechanical deep drawing, where the punch one is moved a prescribed distance while a hydraulic pressure is applied, for the second step the process is similar but reversed. The pressure curves and the punch displacements for each of these steps can be seen on figure 6.3 and 6.4. The contact between the blank and the punches are also very important, since the second step can move below the end position of punch 1. Therefore the contact has a predefined birth and death time, which initiates and eliminates the contact to avoid problems.

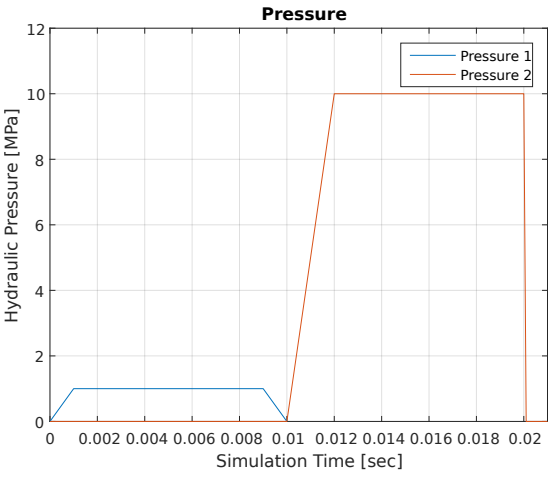

Figure 6.3. The pressure curve for the two phases.

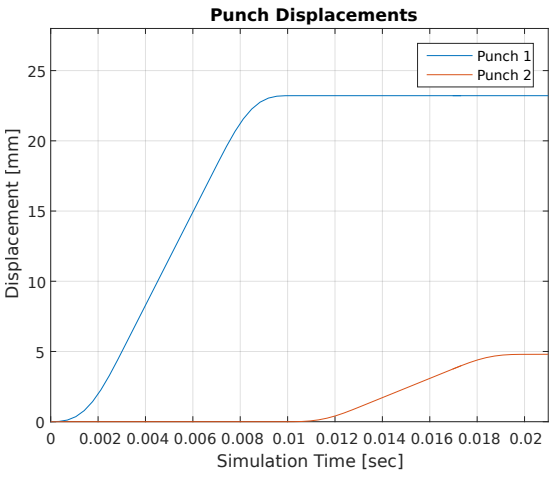

Figure 6.4. The punch displacement for each punch.

For applying the pressure on the blank as in the real-life process, the pressure is prescribed to the plate in a predefined circle in the region where there are no contact between blank and blank holder. This can be seen on figure 6.5.

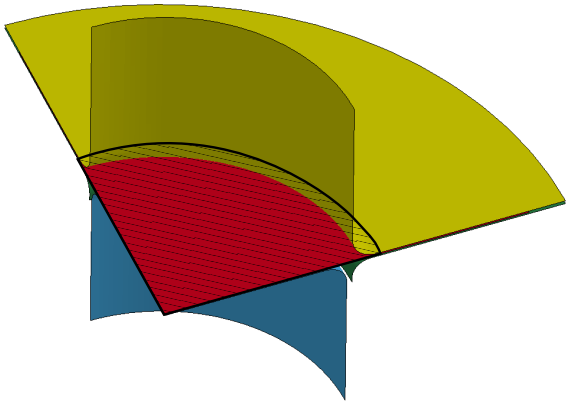

Figure 6.5. The pressure is applied to the blank elements within the shaded area, the element list is update during the simulation. The area is projected infinitely in the Z-direction.

A challenge of building a simulation that include very small radii, is having enough elements around the bends, this is shown on figure 6.6. If the elements are too large a limit can be reached where the corner is performed around one element, and the radius can not be decreased.

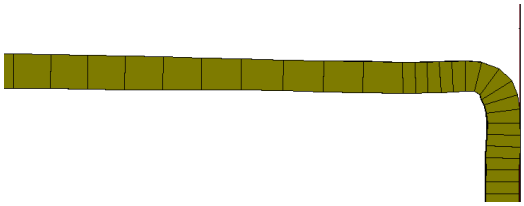

Figure 6.6. A sharp corner, which shows the challenge of having enough elements around sharp bends, the elements in the figure is shell elements with prescribed thickness added.

Based on the objective for the optimisation of achieving a very small radius, the mesh shown on figure 6.7 is made, that include a region with smaller elements. The small element region is placed at what becomes the corner in the final geometry, the element size is selected to have at-least four elements around the radius. In the remainder for the plate larger elements are used to archive better computational times.

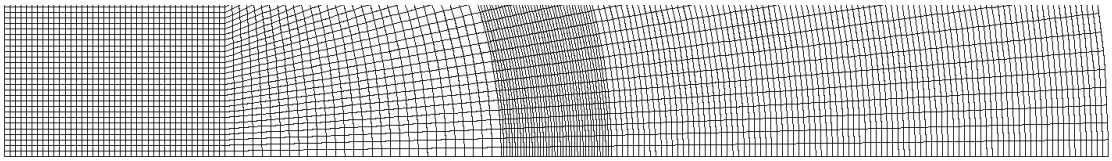

Figure 6.7. Mesh used with region where elements are smaller to allow a sharp bend.

6.4 Optimisation

The objective of this optimisation is to determine the optimal process settings for achieving as small a corner radius as possible. This can, however, be achieved fairly easy, without any

constraints or other objective by e.g. increasing the pressure tremendously and stretching a small section the material to fit the corner. This is highly unwanted therefore a second objective is determined, to achieve as uniform a thickness distribution.

The formulation of a multi-objective function on least square form, can be seen on equation 6.1, the two different residual vectors are constructed for two objectives.

$$f(x) = \frac{1}{2}\sum_{j=1}^{m} r_j^2(x) + \frac{1}{2}\sum_{i=1}^{n} r_i^2(x) \tag{6.1}$$

The general challenge with multi-objective optimisation is the weighting of the objectives. Weighting can for the least square formulation be controlled by applying scaling parameters, or by observing the magnitude of the different objective functions. For this objective function, no scaling is applied in the two objectives, since the magnitude of the thickness objective is far smaller, than the geometrical, the geometric will be considered as the primary objective and the thickness the secondary, as wanted.

6.4.1 Geometrical Objective

For the formulation of the geometrical objective function, there are a couple of problems which is necessary to keep in mind, such as the possible defects. The defects which have to be considered, show on figure 6.8, is the top gap defect where the roof of the cup is no longer in contact with the punch, and cup side slip defect where a bulged is formed a the flange of the cup.

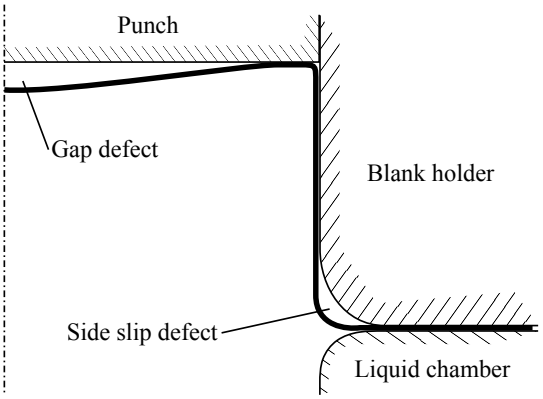

Figure 6.8. The two main defects which have to be avoided, the top gap and side slip.

The geometrical defects, has to be included in the geometrical objective function, therefore a method of setting up the desired geometric as a top plane and a cylinder is applied, see figure 6.9.

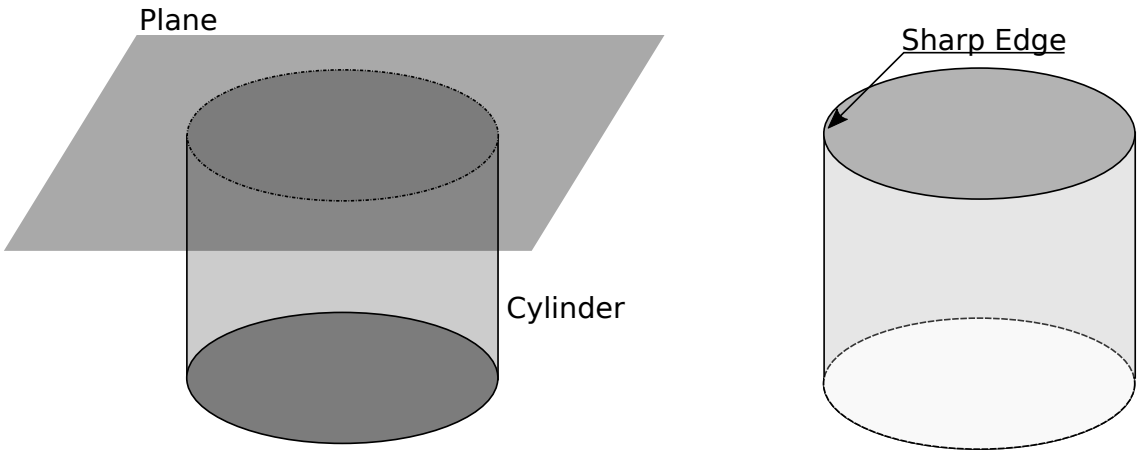

Figure 6.9. A geometrically representation of the geometrical objective.

By defining the optimal geometry this way, the model is forced to converge towards a final geometry, where the cup top has to be similar to the top plane, and the cup side is forced to be a straight vertical section.
The main purpose of the geometrical objective function is to achieve as small a corner radius, for this purpose the plane and cylinder formulation is still valid. On figure 6.9, it can be seen how the edge will be described as a 90°corner. The geometrical assessment in 2D of the corner region can be seen on figure 6.10, where the shortest distance to either, the plane or the cylinder, is selected as the nodal component in the residual vector.

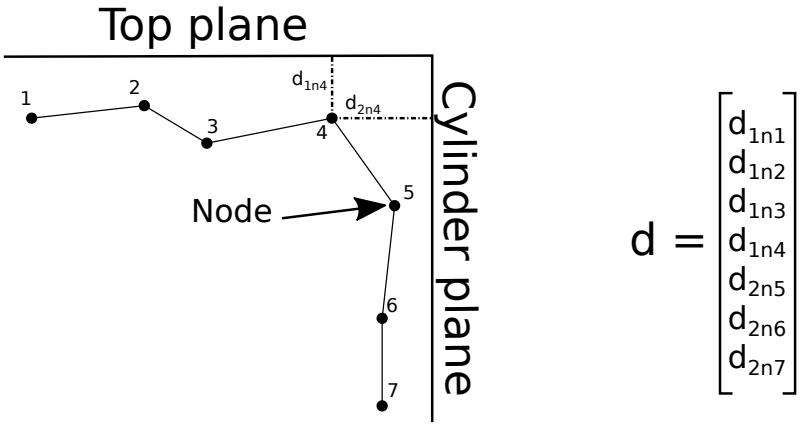

Figure 6.10. Illustration of the geometrical objective, where the shortest distance to either the plane or cylinder, is sorted and used in the residual vector(d).

In order to evaluate the final geometry, post-processing of the simulation is important. A set of nodes are predetermined to be within the region of interest, especially the region near the corner edge, and are dumped in the *nodout* file. The X, Y and Z coordinate data is afterwords cut out and stored in separate files for use in the optimisation script. The Z data is used, when assessing the distance to the top plane and the X and Y are used for determining the radius, which is compared to the cylinder radius. On figure 6.11, the selected node points can be seen, which are selected based on the final geometry.

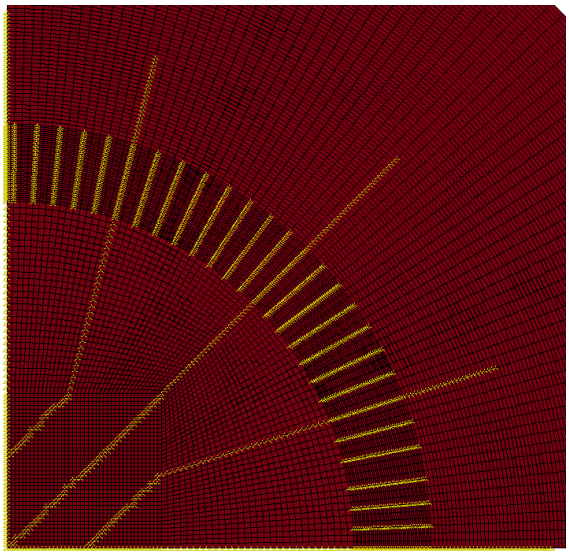

Figure 6.11. Selected nodes on the blank are selected to be within the regions of interest in the final shape. Origo is located in the bottom left.

6.4.2 Uniform Thickness Objective

The second objective for this optimisation is to achieve an uniform thickness distribution. The reason for setting this requirement is to limit the possibility of fracture due to local thinning. This is formulated by extracting the element thickness local strain (ϵ_{zz}) from the *elout* file. By using the strain formulation no additional calculations are required, since the objective can be formulated as the thickness strain, where a minimising would mean that the strains should converge towards zero.

In the *elout* file the strain is divided into two segments, one for the distance between the top point and middle point of the element, and one for the middle point and bottom point, as illustrated on figure 6.12. Therefore the thickness strains for each element is averaged for the sake of simplification.

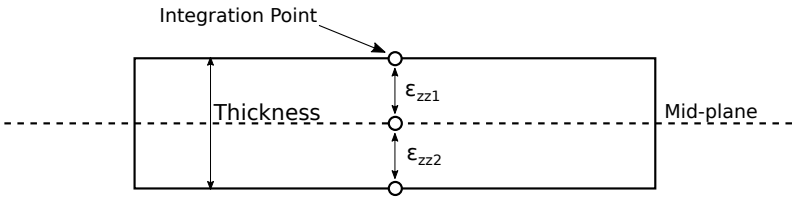

Figure 6.12. Illustrates the location of the thickness strains for a shell elements.

The selected set of shell elements, which are dumped in the *elout* file, are based on the anisotropic behaviour in the model. The selected elements can be seen on figure 6.13.

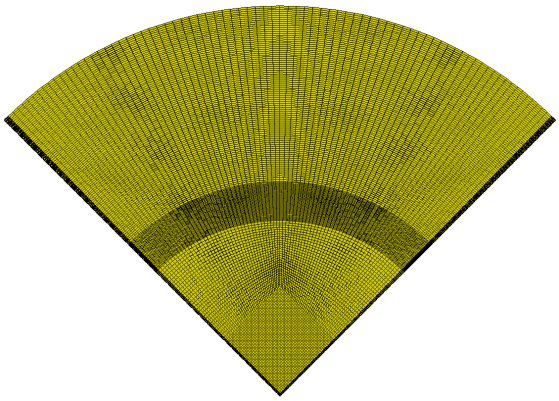

Figure 6.13. The selected elements, outlined in black along the symmetry lines.

6.4.3 Design Parameters

The design parameters in this model are inspired by the one from Wang et al. [51], which divided the problem into two simulations, where the pressure curve were the main design parameters. The chosen design parameters for the optimisation are:

- Displacement of the first punch.
- Displacement of the second punch.
- Pressure curve of the second forming operation, discretised into 4 points/parameters.

The pressure curve of the first forming operation is not set as a parameter, due to limited influence on the final geometry. These design parameters can be seen on figure 6.14, where it is also shown that Punch 2 is placed 2 mm above the final position of punch 1, in order to avoid penetration and to limit the influence from the variations in the gap between these punches.

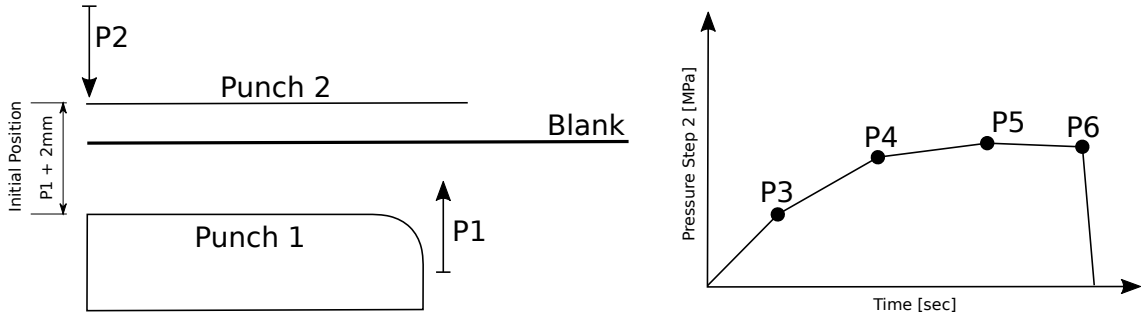

Figure 6.14. Illustrates the six parameters used for this optimisation, where the first two is punch displacements and the last four parameters are use for describing the pressure curve.

The initial parameters settings are as follows: P1=20 mm, P2=3 mm, P3=10 MPa, P4=10 MPa, P5=10 MPa and P6=10 MPa. The initial geometry, for these parameters, can be seen on figure 6.15, the desired geometry is included as-well, where the height is set to be 20 mm.
On figure 6.16, the desired thickness for the objective function and the initial thickness

distribution is presented. The object function is calculated to be 2427.61 with the initial parameter settings.

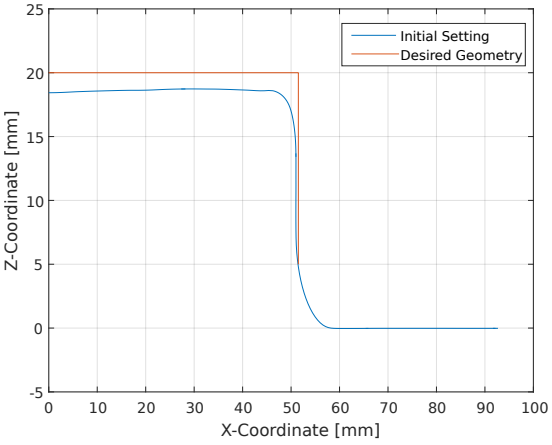

Figure 6.15. A plot of a cross section from the numerical model, where the cup geometry for the initial setting can be seen and the desired geometry, which is formulated as the objective for the optimisation.

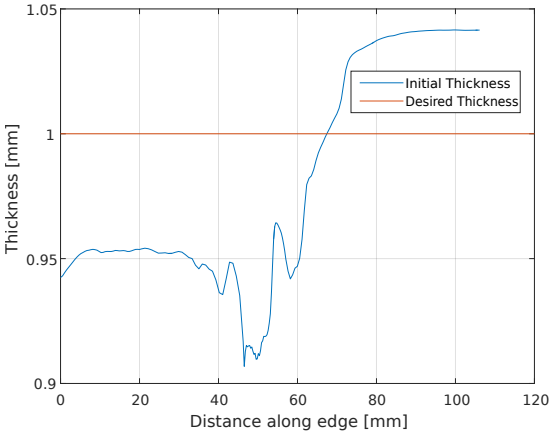

Figure 6.16. A plot of a cross section from the numerical model, where the thickness distribution can be seen for the initial setting, and compared to the desired thickness.

6.5 Results and Discussion

In this section the results from the optimisation will be presented and discussed. In order to determine the validity of the results, three optimisation results will be presented, where the convergence for the parameters will be examined. The cost function and six design parameters for each iteration can be found in Appendix E.4.

The totally structured secant method is used as the algorithm for the three optimisation runs, the initial trust region size are the only setting varied for each of the optimisations. The reason for varying this setting is based on the findings from the first optimisation run, which can be seen in table 6.3 and 6.4, where the pressure curve's parameter P6 is increasing a lot. Therefore the initial trust region was forced smaller in the two other optimisation runs, which resulted in a smaller value for P6, and a smaller cost function value. The cost function for each iteration for the individual optimisation run can be seen on figure 6.17.

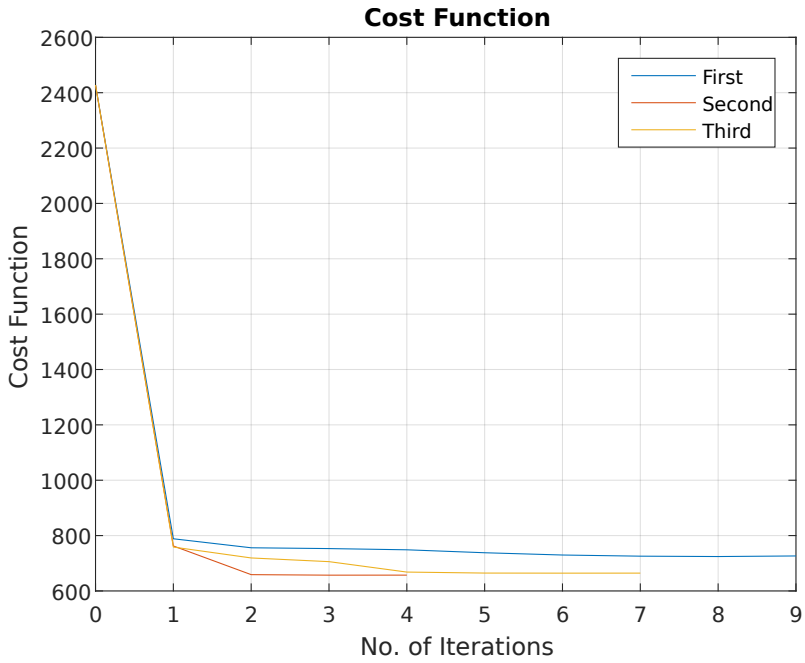

Figure 6.17. The cost function for the three optimisation runs.

Table 6.3. Shows the parameters, cost function and smallest edge radius for the initial setting, and for the different optimisations which has been performed.

Run	P1 [mm]	P2 [mm]	P3 [MPa]	P4 [MPa]	P5 [MPa]	P6 [MPa]	Cost Function	Radius [mm]
Initial	20.0	3.0	10.0	10.0	10.0	10.0	2427.61	3.93
First	23.22	4.80	9.14	8.62	29.57	199.41	726.40	0.70
Second	23.11	4.60	9.40	2 0.87	21.93	23.14	657.13	0.84
Third	23.09	4.56	9.24	28.37	26.24	56.35	664.39	0.64

Table 6.4. Shows the optimisation data for each of the optimisation runs, which are the number of function evaluations and the type, together with the trust region increases, decreases and initial size, and finally the number of iterations.

Run	Function Evaluation			Trust Region			Iterations
	Total	Cost	Jacobian	Increase	Decrease	Initial size	
First	82	22	60	6	12	372.21	10
Second	42	12	30	2	7	40.00	5
Third	69	21	48	4	13	104.58	8

The main objective for the optimisation is to minimise the possible corner radius, on figure 6.18, the radius development through the simulation time can be seen.

It is important to note that the pressure parameters, as the design parameters, is applied starting from 0.01 sec, before that the punch 1 displacement is the only design parameter which is affecting the radius.

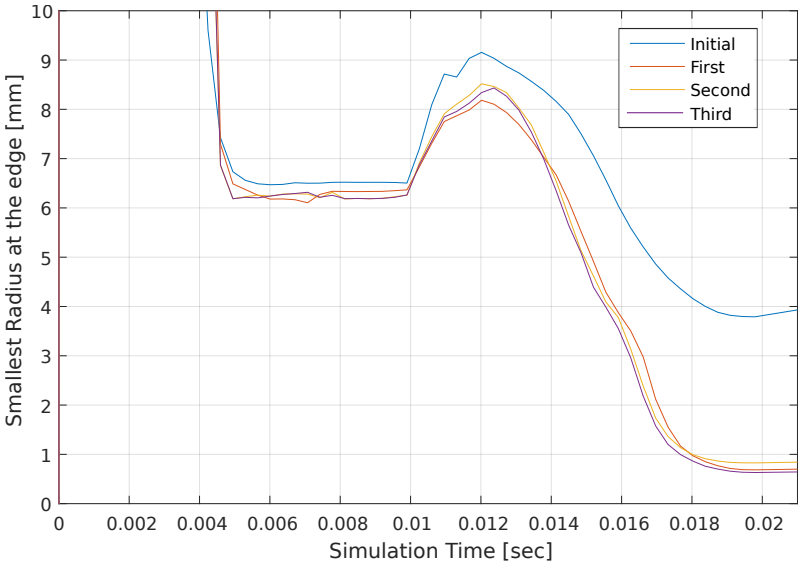

Figure 6.18. The radius development through the simulation time.

The final geometry for the three optimisation runs, can be seen on figure 6.19, together with the initial setting. For the first optimisation run, the edge part of the cup fits the desired shape fairly great, but at the middle of the cup, a larger deviation can be observed. The large increased height in the middle section, is due to the springback, which is affected by the large pressure in the first optimisation run. Similar behaviour can be seen for the two other optimisations, where the middle part is elevated due to the springback.

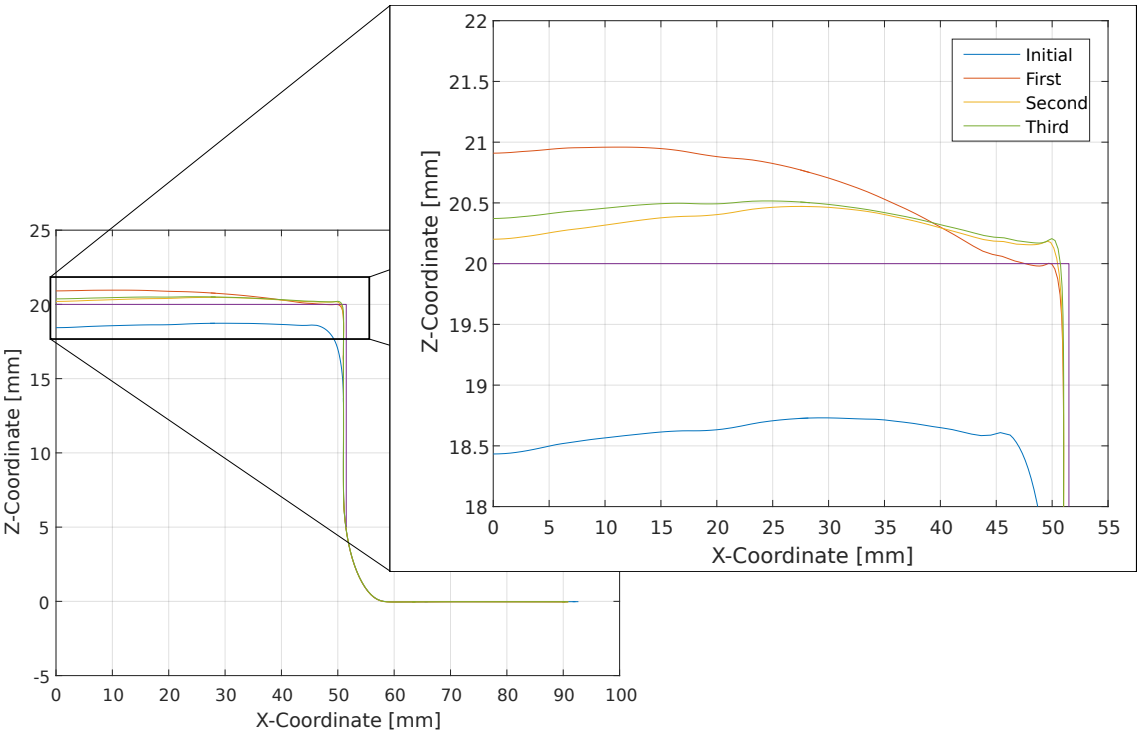

Figure 6.19. The final geometry for the three optimisations after springback, with focus on the top part of the cup.

The thickness distribution for the different optimisation runs are presented on figure 6.20, the thickness peak is located directly at the corner. All the optimisations experiences a decreased thickness, compared to the initial in the inner 30 mm of the part, and increased thickness for approximately 75 mm and outwards. This can be a sign of larger draw-in and more stretching, which can be caused by the larger punch 1 displacement.

The region between 40-60 mm, experiences the largest difference between each optimisation run. In this region the thickness increases significantly in the first and the third optimisation, this is due to the large increase in pressure, which forces the material to fill out the corner significantly, which causes the material from approximately 40-50 mm, to stretch towards the corner.
Compared to the second optimisation run, the thickness distribution is more uniform, since it experiences less thickness deviations, smaller peak, even though the radius achieved is smallest of the three optimisations.

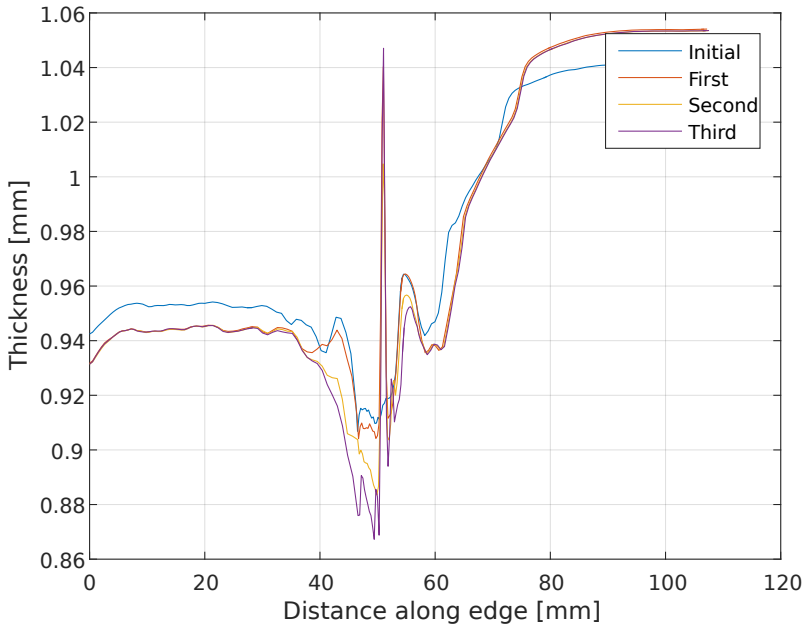

Figure 6.20. Shows the thickness distribution of the initial condition and for the three optimums.

6.6 Sub-conclusion

This chapter is based on a case of a the bulging-pressure compound forming method, which make it possible to achieve a very small radius and nearly perfect corner fill. The model was inspired from Wang et al. [51], where a blank is first hydro-mechanical deep drawn, and thereafter the bulging-pressure compound forming method is used to force the material to fill the corner and thereby obtaining a very small corner radius.

The goal of the optimisation is to achieve a small corner radius, using the bulging-pressure compound forming method, the objective function, for achieving this, is formulated as a top plane and a cylinder, which creates a cup with a perfect square corner.
The design parameters for the optimisation are selected to be the pressure curve for the second step and the two punch displacements. The optimisation results are highly

influenced by the initial trust region size, the result is improved by prescribing a smaller initial trust region for the problem. The smallest radius found for the optimisation is 0.64 mm, where the smallest thickness is 0.87 mm, the blanks initial thickness is 1 mm.

The final design parameters in the pressure curve has an significant influence upon the springback of the bottom of the cup, where a high value causes large hardening in the corner, which forces the top section to springback.

Caes 3: Small Radii - Lunar Rover Test Piece

7

In this chapter, the developed optimisation method and model from Chapter 6 is tested on a more general test piece described by Wang et al. [51]. For this complex test piece, the formulation of the thickness objective function is further tested, in order to investigate if the region experiencing the largest thinning will be improved if it is included in the objective function. The design parameters for this optimisation are the two punch displacements and the two hydraulic-pressures applied in the first and second operation. Finally, the results from this optimisation is compared to experimental data from Wang et al. [51].

In Appendix F, additional information regarding: simulation, keyword and optimisation data, can be found.

7.1 Purpose

The purpose of this case is to test the general object function method developed in Chapter 6, using the same manufacturing principal and material on a test piece with higher complexity. Furthermore, the results will be compared with experiments conducted, by Wang et al. [51], on the test piece to evaluate the optimisation results.

- Optimisation of bulging-pressing compound forming of complex test piece.
- Test of general object function formulation method.
- Experimental result comparison.

7.2 Process

The geometry used in this case is the second presented in Wang et al. [51] and Wang et al. [55], which is a test piece used to investigate manufacturing methods for China's first lunar rover which name is translated to "Jade Rabbit". The test piece can be seen on figure 7.1. The part is similar to the round cup used in Chapter 6 with the addition of two flat sides, and a material thickness of 1.5 mm.

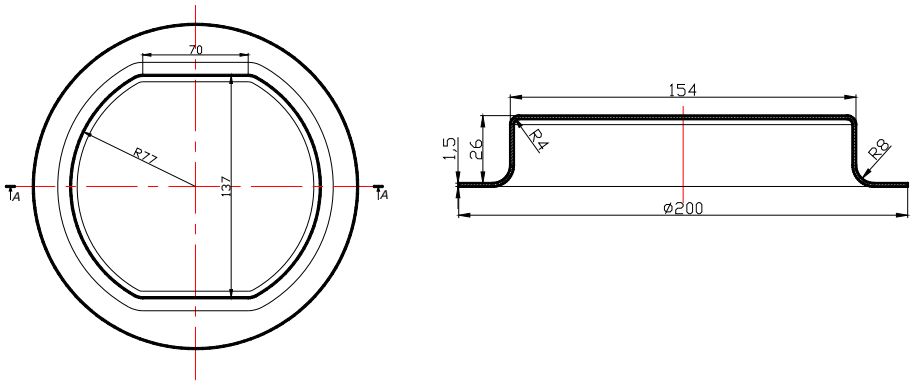

Figure 7.1. Test piece with flat sides and key dimensions (unit: mm) [51]

In this case the requirements to the final geometry increased as the height of the cup is 26 mm and the radius's is 4 mm, only 2.7 times the blank thickness, and 8 mm at the shoulder radius in the first draw. The cup is made in the same material as in Chapter 6, aluminium alloy 2024-O, which material parameters are presented in table 6.1 on page 42.

The test piece is manufactured with the multi-step bulging-pressing compound forming process, in this case a radius is added to the second punch, illustrated on figure 7.2, in contrary to the totally flat punch used in Chapter 6. The punch radius is set to 4 mm in order to achieve the wanted cup radius of 4 mm measured on the outside. To account for the blank thickness of 1.5 mm the radius measured in LS-DYNA should be approximately 3.25 mm, since the thickness is offset from the mid-plane of the shell element.

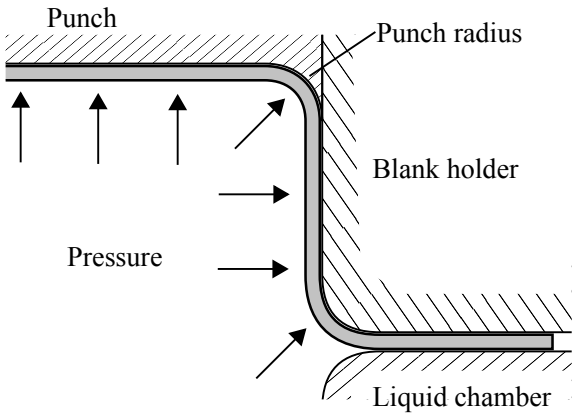

Figure 7.2. Illustration of the bulging-pressing compound forming setup used to manufacture the test piece.

7.3 Modelling

The simulation is modelled using the same procedure as the model in Chapter 6. The simulation consists of a hydro-mechanical deep drawing operation followed by a bulging-pressing compound forming operation. The model is constructed with the parts shown on figure 7.3, where the liquid chamber and blank holder is used in both operations. The radius between the straight wall and round wall is 4 mm on the blank holder. Punch 1's nose radius is set to 8 mm, based on the punch used by Danckert in the NUMISHEET'93

benchmark for square cup deep drawing [56]. The blank is modelled with even sized element in most of the part, the element size is selected to allow several elements around the corner radius region.

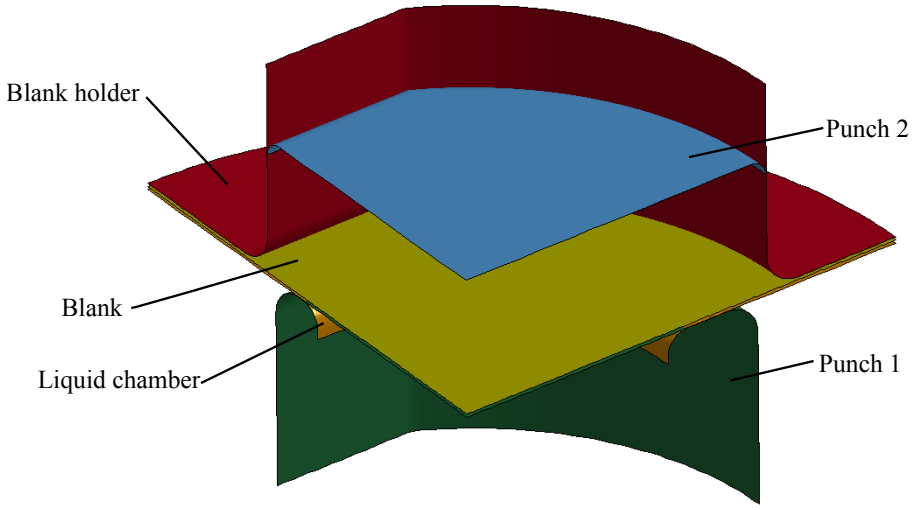

Figure 7.3. Test piece optimisation model. The dimension of the model can be seen in table 7.1.

The blank is modelled with fully integrated shell element modified for higher accuracy(elform=-16) with 5 integration point through the thickness, the tool parts are modelled with rigid shell elements. To include springback of the deformed blank, the simulation is switched to implicit in the final 0.001 sec of the simulation time, which is the bases for the blank element selection. The material model for the blank is, MAT_122_HILL_3R, as for Chapter 6.

Table 7.1. Dimensions of modelled tools and blank.

Component	Value [mm]
Punch 1 diameter	74.5
Punch 1 nose radius	8
Punch 2 diameter	77
Punch 2 nose radius	5.5
Liquid chamber diameter	77 (68.5)
Liquid chamber nose radius	8
Blank holder diameter	77 (68.5)
Blank holder nose radius	8
Blank diameter	220
Blank thickness	1.5

The gap between the die and punch 1 is set to 2.5 mm, this measurement is not presented in the papers documenting the test piece [51, 55], therefore the settings from the following papers are used as a recommendation:

Gavas et al. [57], recommends a gap between 1-1.3 mm for deep drawing operations.
In the experiments conducted by Zhang et al. [52] on hydromechanical deep drawing was

a gap size of 1.11 mm used, with a blank thickness of 1 mm.
Zhang et al. [58] used a 1 mm gap on a 0.9 mm thick hydromechanical deep drawn blank. A 1.45 mm gap was used by Danckert et al. [59] on a deep drawing operation on a approximate 1 mm blank thickness.

7.4 Optimisation

The purpose of the optimisation is to find the optimal settings for the multi-step forming operation, in order to achieve the desired geometry. This case uses the same formulation method as presented in Chapter 6, which consists of geometrical and a thickness contribution to the objective function.

The optimisation will be formulated on the least square form, with no scaling of the different objectives. Therefore it is only the data extracted from the FEM model and loaded into the Java optimisation script which is changed, along with the specific formulation of the geometrical objective.

7.4.1 Geometric Objective

The geometric part of the objective function is constructed using the same approach as in Chapter 6.3, where a cylinder is used for the round side, a flat plane for the top of the cup and a vertical flat plane for the flat side, this can be seen on figure 7.4. The top plane height is 26 mm the radius of the cylinder is 76.25 mm and the side plane is 67.75 mm from the center. Furthermore it is noteworthy, that by modelling the geometrical objective function with sharp edges, then the objective function will never become zero.

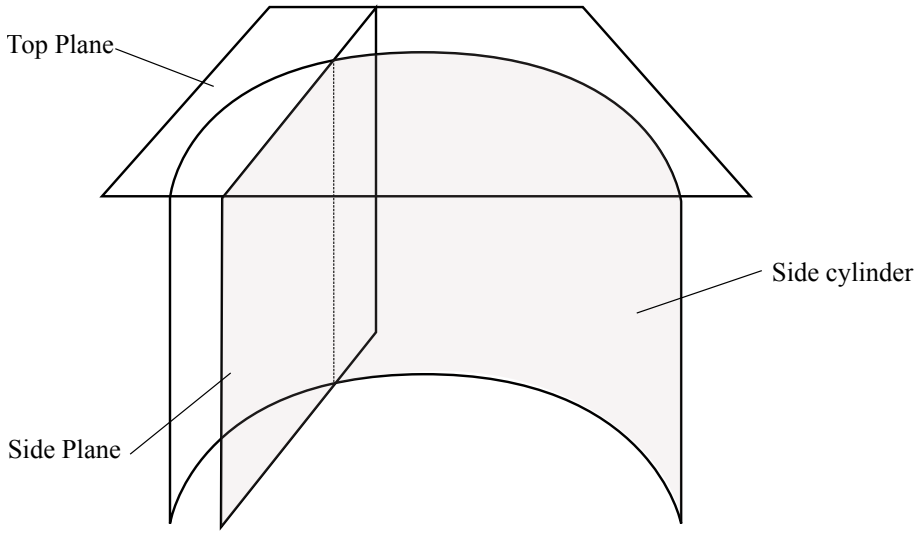

Figure 7.4. Three part geometric objective function, top plane, side plane and side cylinder.

The node set used for this optimisation is less than the previous small radii optimisation, this was to test if a acceptable result could be generated from a lower dataset. The selected node set allowed larger flexibility in the placement of the nodes in the final geometry. The only requirement for the node set is that the nodes located in border between the cylinder wall side and flat was side is included, the node set can be seen on figure 7.5

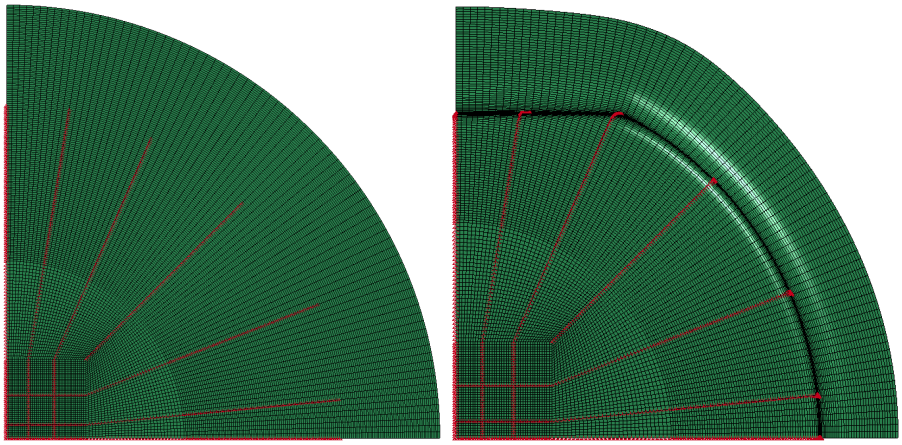

Figure 7.5. Node set shown on the initial blank and the formed blank.

7.4.2 Thickness Objective

The second part of the objective function serves to achieve an uniform blank thickness, which is formulated as in Chapter 6. The flat wall side of the geometry invalidate the assumption of axis symmetry thickness distribution. The most critical area is located at the boarder between the flat wall side and round wall side, shown on figure 7.6. Therefore a set of elements in this region, the red circle on figure 7.6, is added to the element list, which also included the elements along the two symmetry sections.

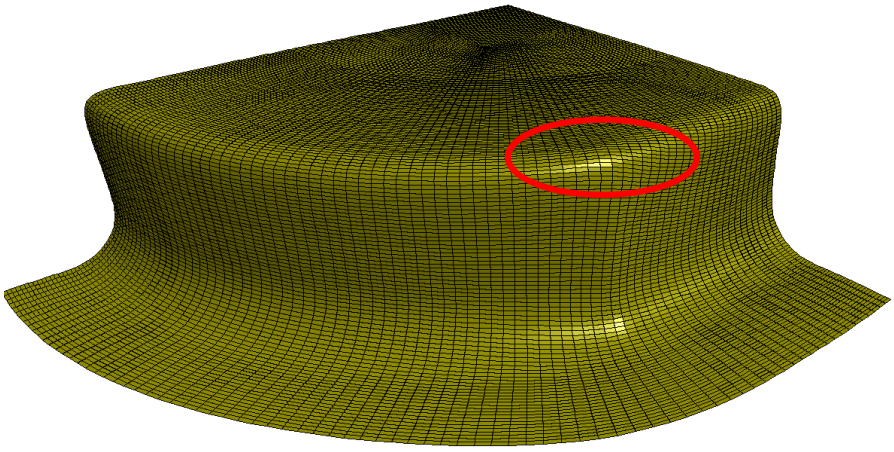

Figure 7.6. The formed cup, where the elements in red circle are included in the thickness objective, since this is the critical thinning area.

7.4.3 Design parameters

The design parameters in this optimisation are selected based on the results of the small radii optimisation. The parameters are:

- Displacement of punch 1. (P1)
- Displacement of punch 2. (P2)

- Pressure curve of second forming operation, where the parameterisation is similar to figure 6.14 on page 47, where the two final points are P5. (P3 - P5)
- Pressure of first forming operation, where this parameter is a scale factor. (P6)

The final pressure curve of the second forming operation is discretised into 3 points, furthermore the pressure of the first forming operation is added to investigate if this parameter has an influence on the thickness distribution.

The initial parameter settings are: Displacement of punch 1=20 mm, displacement of punch 2=5 mm, pressure of first forming operation=10 MPa, and the second forming operations pressure curve, the three points are set to=1 MPa.

7.5 Results and Discussion

In this section the results of the optimisation will be presented and discussed. First a comparison between the two element sets will be presented, to determined how large the influence of the corner elements are. Afterwards the parameters and the different objectives will be presented and discussed.

As presented, the element set from Chapter 6 is updated to include the elements in the corner region which is exposed to the most thinning. Two optimisation runs are conducted, in order to evaluate the influence of the extra elements. The two are identical except form the element sets and the final settings. On figure 7.7 the result of the two runs can be seen, where the blank thickness along the corner section (see figure 7.9) is plotted. The purpose of using the element set which include the corner is to increase the thickness in the upper corner, it can be seen that the two runs have the same thickness at this point. This may be a result of only a small amount of thinning in the first place, do to the capability of bulging-pressing compound forming. If the amount of thinning is higher in the corner region, then this would have weighted higher in the objective function.

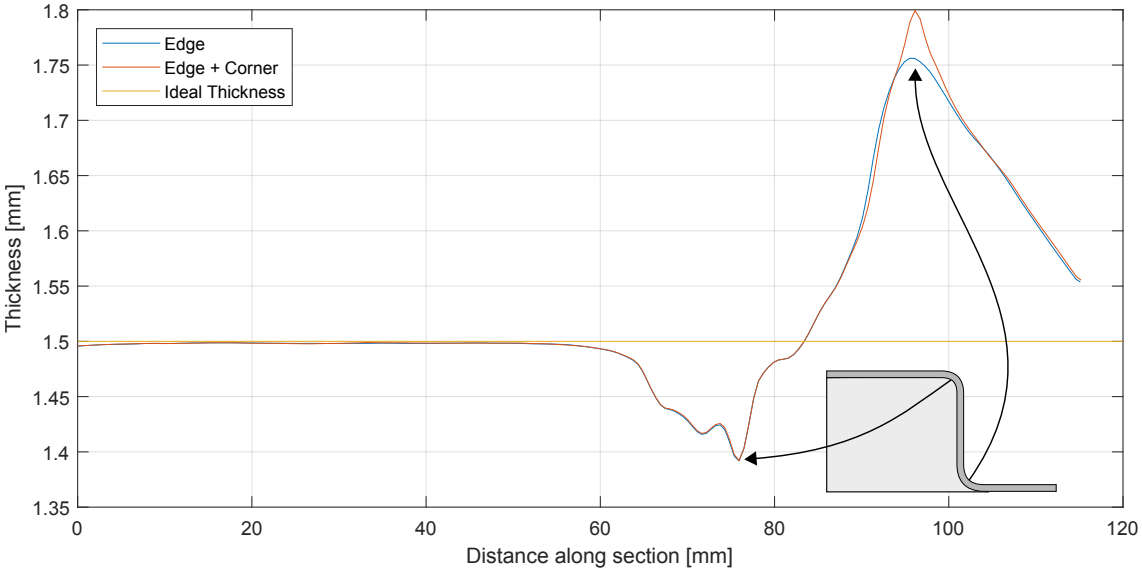

Figure 7.7. Thickness distribution of the two element sets.

In table 7.2 the optimised parameters of the two optimisation runs with different element sets are presented, along with the initial parameter settings. The parameter: P6, which is the pressure of the first forming operation, is almost zero in both sets, and can therefore almost be considered as a conventional deep drawing operation instead of a hydro-mechanical deep drawing.

The cost function and the six design parameters through each iteration, are documented in Appendix F.

Table 7.2. The optimised parameters for the two element sets, and the initial parameter settings. The radius is measured in the middle of the element and is influenced by the element thickness.

Run	P1 [mm]	P2 [mm]	P3 [MPa]	P4 [MPa]	P5 [MPa]	P6 [MPa]	Radius [mm]
Initial	20	5.0	1.0	1.0	1.0	1.0	3.32
Edge element set	29.879	5.426	0.979	0.994	3.082	0.002	3.23
Corner element set	30.609	6.162	1.142	1.010	3.316	0.002	3.23

7.5.1 Geometry

The first objective of the optimisation is to achieve the desired geometry of the cup, in figure 7.8 the final geometry of the two optimisation can be seen, and the result of a simulation with the initial setting is likewise included.

The final cup top reached the desired height of 26 mm, a slight waviness can be seen from the top corner edge towards the center, the extend of the waves is in the range of 0.23 mm. The side wall of the cup likewise reached the desired shape, a wave along the wall height can be observed, the extend af the wave is below 0.20 mm depending of the measurement points.

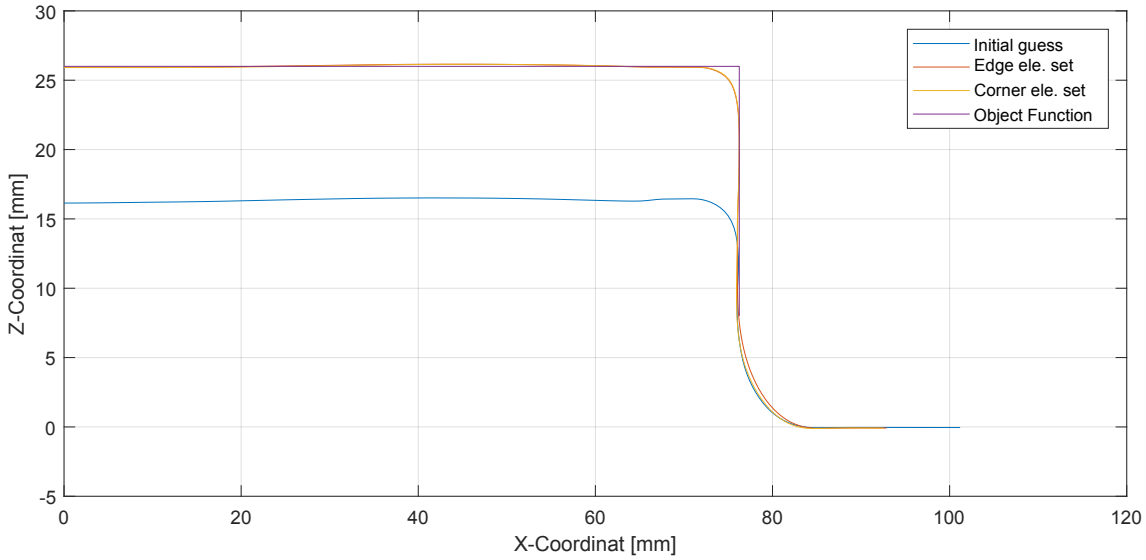

Figure 7.8. Side view of the final geometry of the two optimisation runs, and the initial settings.

A small side slip defect can be observed in the final optimisation with the edge element set, which can be a result of too low pressure, this defeat is not included in the object function for the lowest nodes. This defeat may be removed by including nodes which lay further away from origo.

7.5.2 Thickness Distribution

The second objective of the optimisation is the thickness distribution. The cup is evaluated at three sections, these are shown on figure 7.9, the sections are: x-axis, y-axis and a section from the origo through the side corner.

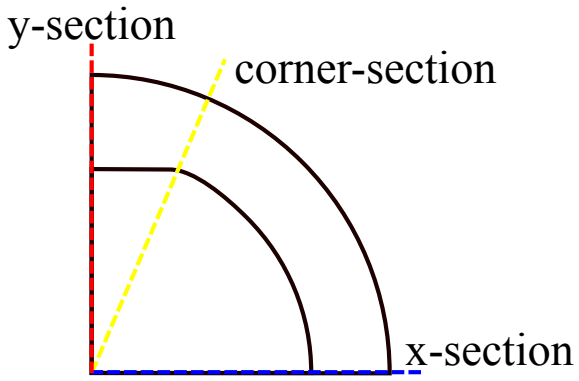

Figure 7.9. The three sections at which the thickness is evaluated.

To evaluate the thickness of the optimisation using the element set including the corner, the thickness distribution in the section are presented on figure 7.10, and are compared to the data presented by Wang et al. [51]. The data is extracted from the paper's figure 29, some extraction error should be expected.

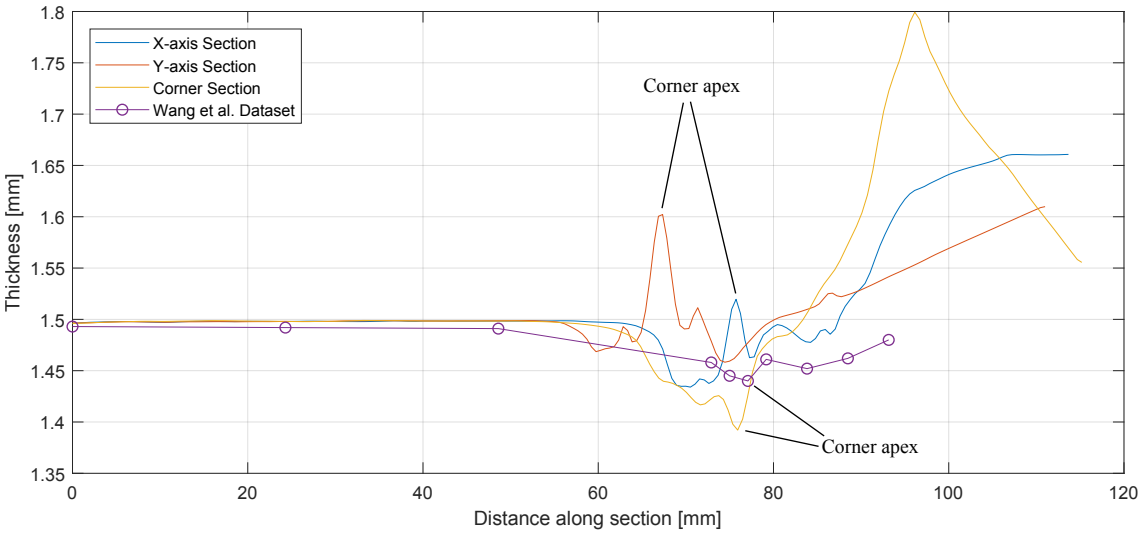

Figure 7.10. Thickness measurement from the optimisation with corner element set along the section presented on figure 7.9, Wang et al. [51] thickness dataset (x-axis section) is included for reference.

The sections along the x- and y-axis experiences a thickness increases at the corner apex, and slight thinning before and after the corner apex, which is likewise observed in the optimisation in Chapter 6. The width of the peak in this optimisation is much wider which is a product of a larger corner radius. If the Wang et al. [51] thickness dataset (x-axis) is compared to the result along the x-axis, the same thickness increases peak can not be observed.

A thickness increase peak can not be observed on the corner-section, where thinning occurs along the entire corner radius. The thinning indicate that the process of rolling the material into the corner is not successful, and if the cup is drawn deeper this is the region where fracture is likely to occur. This problem might be corrected if the thickness is weighted more in the object function, which may happen naturally to some degree if a higher lever of thinning is experienced.

7.5.3 Radius Development

The corner radius objective of 4 mm was not directly included in the objective function, but indirectly prescribed through the fixed punch 2 radius. The corner radius development of the three sections as a function of time, is presented on figure 7.11. As the radius is measured in the nodes, where the element thickness is off-setted in both direction, the final thickness is influencing the result. The corner section reached a final radius of 3.54 mm, and the two other section reached a final radius of 3.23 mm.

If a thickness estimate of 1.5 mm is used, the final outside radius 3.98 mm for the two side section, and 4.29 mm for the corner section.

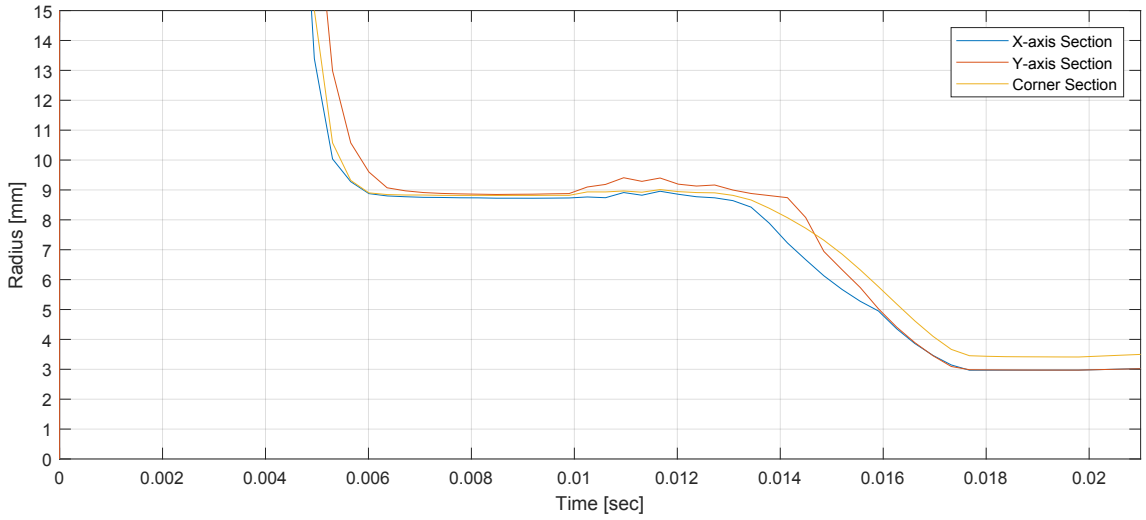

Figure 7.11. The corner radius of the three sections, hydro-mechanical deep drawing is performed from time 0-0.01 sec, bulging-pressing compound forming 0.01-0.02 sec and springback in the remaining time.

7.6 Sub-conclusion

The optimisation presented in this chapter uses the methods and techniques presented in Chapter 6, to manufacture a lunar rover test piece. The test piece is a flat top cup, with both round and straight wall sides. Both hydro-mechanical deep drawing and bulging-pressing compound forming are used to manufacture the cup. The optimisation uses a extended version of the object function formulated in Chapter 6. The cup is based on measurement presented by Wang et al. [51].

The first goal of the optimisation is to achieve the desired shape, that included a outer corner radius of 4 mm, which is only 2.7 times the blank thickness (1.5 mm). The second goal is to achieve a uniform thickness distribution throughout the blank. The design parameters are selected to be the displacement of the two punches, the pressure of the first forming operation and the pressure curve of the second forming operation. The optimal settings for the parameters are found, that fulfilled the geometry requirements while achieving a somewhat uniform thickness distribution.
Two optimisations were devised in order to achieve a better thickness distribution in the corner, which observed a more severe thinning, by including elements in the corner part. This did not improve the results of the optimisation, however, this is assumed to be because of the magnitude of the thickness objective. Furthermore, this severe thinning region experiences more stretching and does not increase in thickness as other edges.

Case 4: Hydraulic Expanded Tube-Tubesheet Joint

8

In this chapter, the hydraulic expanded tube-tubesheet joint process is investigated by modelling a plane strain model with rotational symmetry, where the tubes is expanded into the tubesheet and subsequently unloaded. The objective is to achieves as high a tube-tubesheet contact force as possible, which indicates higher integrity of the joint. The design parameter is the applied pressure in the inner tubewall, and the objective function is based on the contact force after forming and unloading. In order to use least square optimisation on an maximisation problem, the contact force is inverted, which means that a increase in the contact force would minimise the objective function. By this model and optimisation formulation, seven different optimisations are devised with different yield stresses and clearances for the tube and tubesheet in order to determine their individual influence on the contact force.

In Appendix G, additional information regarding: simulation, keyword and optimisation data, can be found.

8.1 Purpose

For this case, the purpose is presented in bullet points underneath, the first objective is to develop a model, which can be used for various parameters, e.g. different materials, different geometries. This will the ease the development of finding the optimal setting. The second objective is to formulate a maximisation problem using least square formulation, which would give a robust function evaluation.

- Develop a robust model, which can be used for academic studies
- Formulate a maximisation problem using the least square formulation

8.2 Process

Research of the tube-tubesheet process has been carried for a long time, where in the 1940's Goodier et al. [60] investigated the residual pressure after expansion, with a plane-stress model, and its relation with the expansion degree. During the same period Grimison et al. [61] did a parameter study, that established the process fundamentals. In the 1990's

Kalnins et al. [62] did mathematical studies upon the different process parameters, which are still the leading standards in the tube-tubesheet joining industry.

The tube-tubesheet joint is mainly used in the heat exchanger industry, e.g. Vestas Aircoil A/S, where the joint consists of a tube that is inserted into the tubesheet hole, and thereafter the tube is expanded into the tubesheet to make a leak proof joint. The tube's and tubesheet's position in a heat exchanger can be seen on figure 5.1 on page 28. Theory states, one of the challenges with the process is the ability to perform an expansion, where the tubesheet does not plastically deform, since this causes the performance of the joint to decrease. The advantages of using this joining method, is the low unit price per joint, and its non-affecting behaviour on corrosion properties of the materials, compared to welding. The expansion method can be performed in two way, by mechanical roller expansion or by hydraulic expansion. The mechanical roller expansion is performed with 3-5 rollers, which are rolling on the inside wall of the tube, and are moved outwards by a conical mandrel, which forces the pipe to plastically deform and reach the tubesheet wall. For the hydraulic expansion, a hydraulic tool is inserted into the tube, and then expands the tube radially into the tubesheet, this can be seen on figure 8.1. For this case, the hydraulic expansion method is selected, since this is less computationally costly to model, than the roller expansion due to the long contact distance.

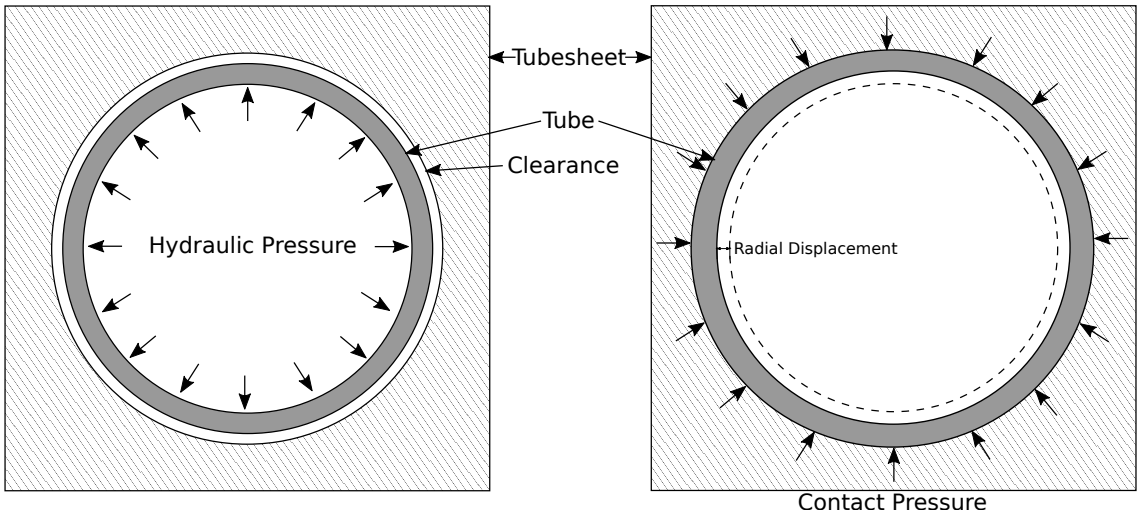

Figure 8.1. On the left is the initial situation in the tube-tubesheet joint by hydraulic expansion and to the rigt is the final situation, where the elastic release of the tubesheet material acts on the expanded tube, which gives a contact pressure.

The current method for evaluating the integrity of the joint is done in two ways, destructive and non-destructive. The destructive method is by performing a pull-out test on the joint, where the tube is pulled-out of the tubesheet hole. This method is used for estimating the contact pressure between the tube and the tubesheet. The non-destructive method is by measuring the tubesheet hole diameter before expansion, tube inner and outer diameter, and the tube inner diameter after expansion. From these measures, equation 8.1 can be made in order to estimate the apparent wall reduction %WR, where the u_r is the radial displacement, c is the clearance between the tube and tubesheet, and t is the thickness of

the tube, these can also be seen on figure 8.1. Kalnins et al. [62], found that the optimal contact pressure is reached in the region from 3% and 6%WR for stainless steel.

$$\%WR = \frac{u_r - c}{t} \cdot 100\% \tag{8.1}$$

One of the problems with the %WR is that this varies for each material combination, therefore when changing tube or tubesheet material, the settings for the process has to be changed. It is of great interest to formulate a more robust method to forecast the contact force and the determine process settings, instead of performing a series of experiments with destructive testing.
Additionally, leak proof testing of the joints can also be perform as a non-destructive testing method, however, this method is poor at locating the critical joint, since a heat exchanger consists of hundreds of tube-tubesheet joints. This method does not test the contact pressure, and thereby not the joint integrity.

8.2.1 Applied Pressure vs. Contact

The contact pressure is of large interest for the process, and therefore an initial study upon this behaviour has been conducted in order to verify this phenomenon. On figure 8.2, 12 simulations are used to detect the optimal pressure setting in order to obtain the largest contact force. For this initial study, the material AISI 304L is used for both the tube and tubesheet, the optimal setting is found to be in the region of 150-400MPa.

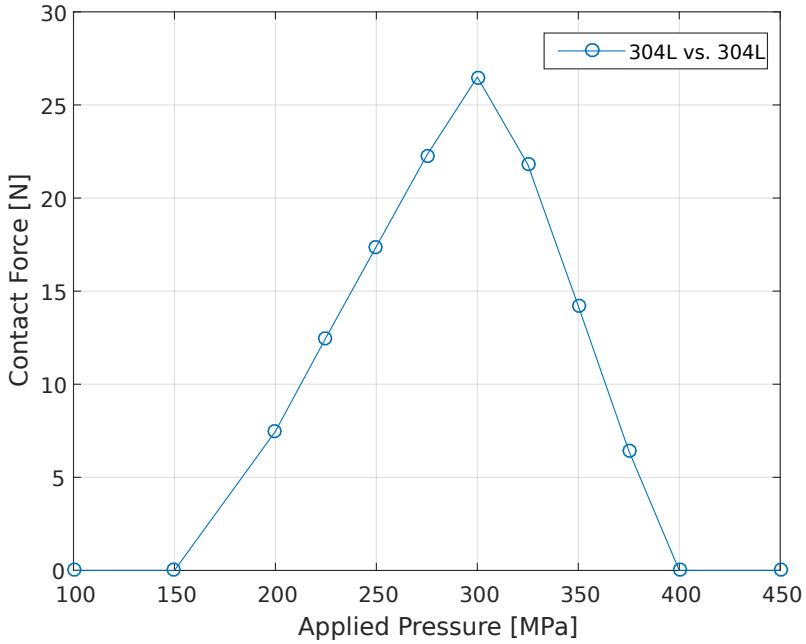

Figure 8.2. Here is the contact force for 12 simulations with varying internal pressure, the tube and tubesheet is both AISI 304L.

For this case, the %WR will not be used as an indication of quality, but only the contact force, since this is more valid for the joint integrity. Ma et al. [63] observed similar behaviour for their experimentally hydraulically expanded joints, and for the experiments they found an optimal pressure in the region of 160-300 MPa, but they did not reach as high a degree of over-expansion.

Based in these initial studies on the applied pressure and the contact obtained, a series of optimisation will be performed, in order to investigate the yield stresses effect on the tube and tubesheet obtained contact force. Furthermore, the effect of the clearance will be investigated in order to determine the effect of %WR.

8.3 Modelling

The hydraulic tube-tubesheet expansion modelling is based on the modelling approach from Alexouli et al. [64], where the model is assumed to be plane strain, since this deformation does not strongly affect the axial displacement [65]. By only making the model one solid element in height and constraining the top and bottom nodes in the z-direction, the plane strain assumption is implemented. The difference between the model made by Alexouli et al. [64] and this one is the possibility for axisymmetric, since the force acting on the inner tube wall is the even distributed pressure. Therefore the model is constructed as can be seen on figure 8.3, the boundary conditions are also illustrated.

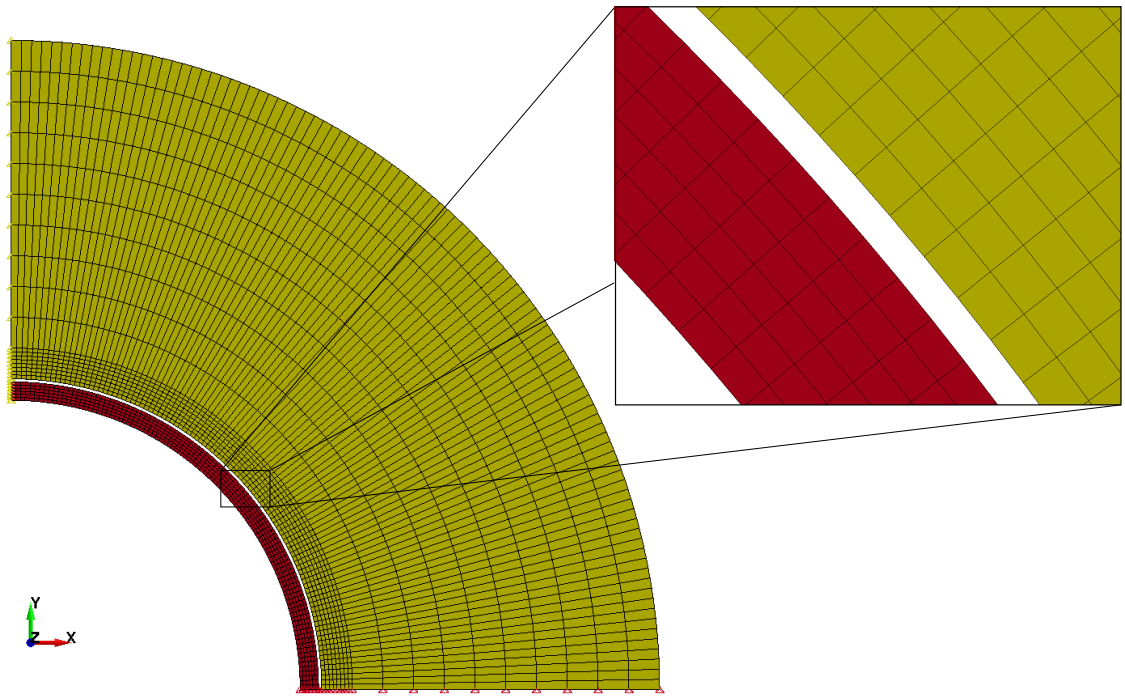

Figure 8.3. A view of the numerical model, the red part is the tube and the yellow is the tubesheet. The model is only one element in height and the mesh is modelled to be aligned, which improves the contact calculations.

The aim for this model is to estimate the integrity of the joint, and therefore some requirement for the contact stability is imposed. Klose et al. [45] constructed a model of the roller expansion process, which experienced large amount of contact penetration, that caused the estimation of the joint integrity to be unstable. In order to make this models contact more stable various aspects and contact models have been tested, the best is found to be *CONTACT_AUTOMATIC_SURFACE_TO_SURFACE_MORTAR, which requires an implicit solver [66]. This contact model calculates the contact

interactions by the Lagrange method, which for this case has proven to be fairly stable. This model is simulated as quasi-static in contrast to the others cases in this project.

The hydraulic pressure is applied on a segment set at the inner tube wall, on the inner solid elements surfaces. For these segments, a load curve is defined, see figure 8.4, where a steady state phase is included in the time period 0.015-0.018 sec, and then the loading is phased out, which allows for springback to occur.

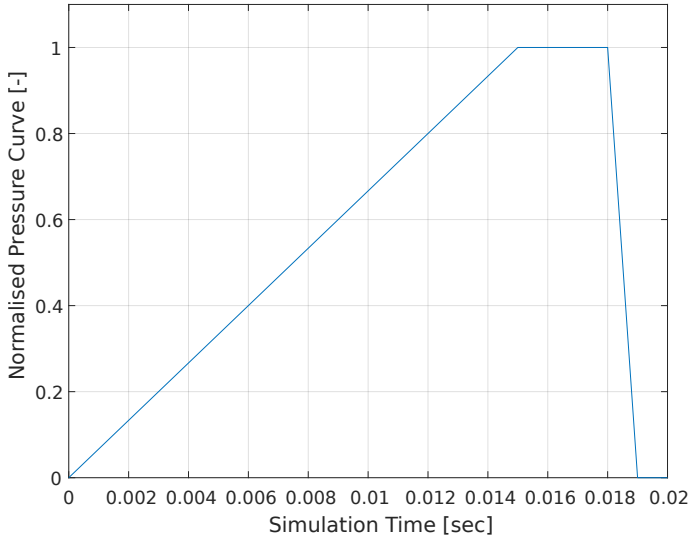

Figure 8.4. The profile of the pressure curve used in the simulation, which includes a loading phase from 0-0.015 sec, a steady state phase at 0.015-0.018 sec, and the final unloading and relaxation phase.

One of the aims is to evaluate the material parameters influence upon the joint integrity. Therefore the material parameters are given as bi-linear material data, see table 8.1, and the material model selected is MAT_PLASTIC_KINEMATIC. This material model is suited for isotropic and kinematic hardening plasticity, and are perceived as a cost effective material model[35], the isotropic hardening is used. The current used materials for tube and tubesheet is AISI 304L and AISI 316L[65], respectively, this case will focus on the AISI 304L.

Table 8.1. The material parameters from Madsen et al. [65] for both AISI 304L and AISI 316L.

Input Parameters		LS-DYNA units	AISI 304L	AISI 316L
Density	ρ	[tons/mm^3]	7.85e-9	7.85e-9
Young's Modulus	E	[MPa]	193e3	193e3
Poission's ratio	ν	[-]	0.3	0.3
Yield Stress	σ_y	[MPa]	325	516
Tangent Modulus	E_t	[MPa]	2200	1800

The geometries of the modelled parts can be seen in table 8.2, where the tube geometry and the tubesheet hole are similar to the ones from Klose et al. [45].

Table 8.2. The geometries for the numerical model.

Tube		Tubesheet	
Thickness	0.6 mm	Hole diameter	10.2 mm
Outer diameter	10.0 mm	Outer diameter	42.2 mm

In order to increase the robustness of the model, some sensor parameters has been included, to minimise the possibility for simulation error termination. This sensor parameter detect the displacement for one of the outer nodes in the tubesheet, if the displacement is larger than 1 mm, the contact and the load is shut off, which will result in zero contact force. This is implemented due to the influence upon the optimisation if an error termination occurs, where the optimisation package does not check for normal or error termination.

8.4 Optimisation

The objective for the optimisation is to find the optimal setting for the pressure level, for which the contact force is highest. For this optimisation problem, there are some difficulties in order to find the optimal solution. The first of the challenges are to maximise the contact force, where the least square formulation is constructed to find a specific setting or to approach zero. Therefore the formulation for the residual vector is devised, see equation 8.2, where F is the contact force, and to avoid the possibility of obtaining zero in the denominator, the absolute value is used here and added with one. For this formulation a higher contact force will make the vector approach zero, which makes this formulation well suited for maximisation where the maximum value is not known.

$$r(x) = \frac{1}{1 + |F|} \tag{8.2}$$

From this formulation of the maximisation problem, the data from figure 8.2 are plotted to evaluate the design space, see figure 8.5. Form the figure, it is clear thatin the vicinity of the optimum, the objective function values are fairly small, which causes the gradients to be similarly small.

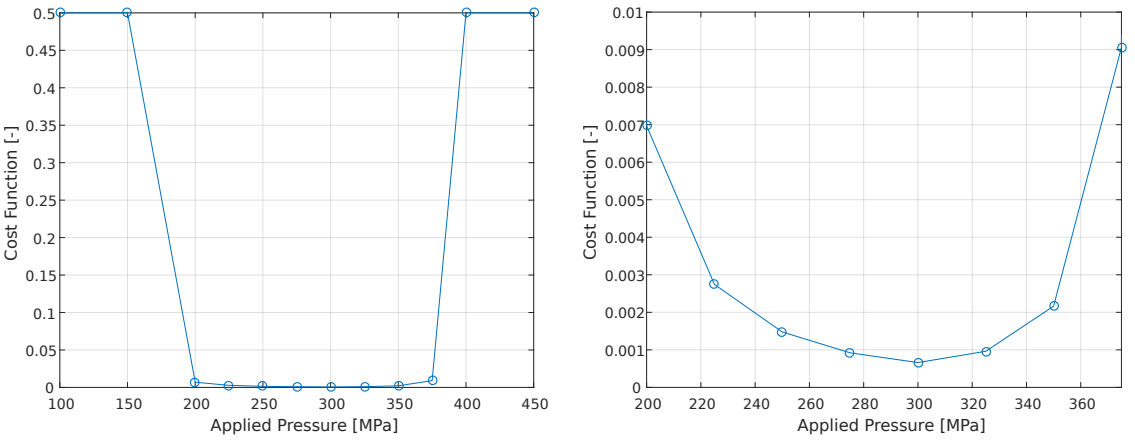

Figure 8.5. To the left is the design space plotted for the case on figure 8.2 with the equation 8.2. To the right, the region from 200-380 MPa is zoomed in.

The other challenge with this problem is to select the correct starting point. From figure 8.2, it can be seen that a regions under and above the optimal setting has a value of zero. The sensitivity analysis depends on reaching a point which is non-zero, else the gradient will be zero. Therefore selecting a feasible starting point, non-zero, is crucial in order to reach an optimal solution.

The extracted data for this problem is the ASCII file *rcforc*. This ASCII file stores the contact forces for both the slave and master side, where the component values are the same, but with opposite sign, this is however not an issue for this problem, since the absolute value of the contact force is used in the objective function. The contact force extracted is the dump at the final time step in the simulation. The resultant contact force for one of the simulations can be seen on figure 8.6, here the final part of the simulation is steady state, if contact is reached, then this part will be larger than zero.

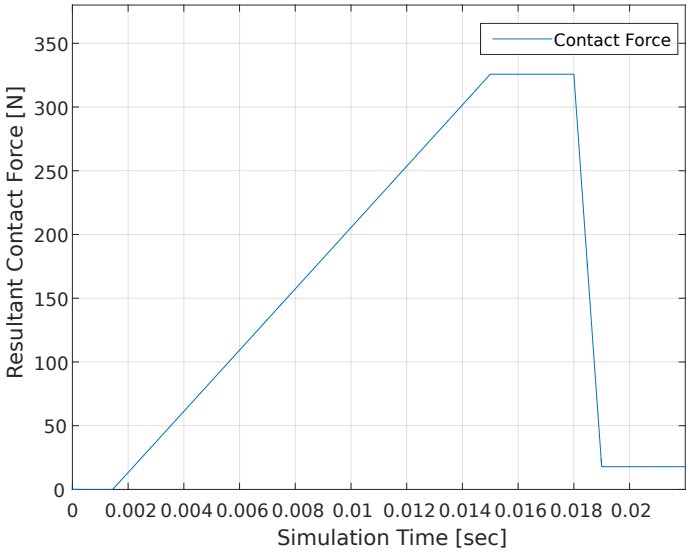

Figure 8.6. An example of the contact force through the simulation, the last part is the relaxed part of the simulation, where the contact is existing after unloading.

The aforementioned sensor's implemented in the simulation, is modelled to remove the contact force obtained, if a failure conditions is met, such the contact force goes to zeros, which for the optimisation algorithm would mean that the problem is not at a minimum.

8.5 Results and Discussion

In this section, the results from the tube-tubesheet expansion optimisation will be presented. Several different tube and tubesheet materials has been tested in order to find the optimal applied pressure and to evaluate the material combinations.
In order to evaluate if the optimisations has reached the optimum, an optimisation has been applied to the presented initial study from figure 8.2. Here the Totally Structured Secant Method is applied with an initial trust region of 500, estimated by some initial investigations. The optimisation data can be seen in table 8.3.

Table 8.3. The optimisation data for the case where both the tube and tubesheet has the material model resembling AISI 304L.

Test	Parameter [MPa]		Objective Function		Contact Force [N]		No.
	Initial	Optimal	Initial	Optimal	Initial	Optimal	Iterations
	200	304.48	7e-3	6.55e-4	7.47	26.8	9

For this initial optimisation problem, it is possible to illustrate the convergence behaviour. This is evaluated by plotting both the objective function and the contact force, this can be seen on figure 8.7 and 8.8. From these two figures, it can be seen that the optimisation are converging from each side of the optimum.

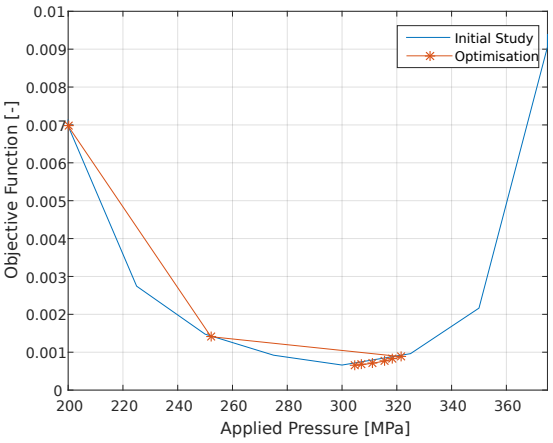

Figure 8.7. The objective function for each iteration in the optimisation.

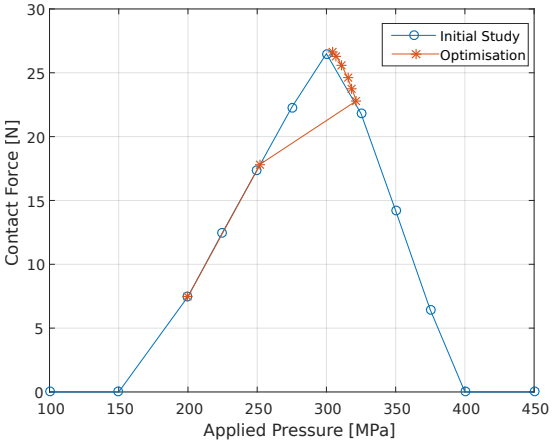

Figure 8.8. The contact force for each iteration in the optimisation.

Based on the initial verification of the optimisation, an research plan is devised, where the yield stress of the two parts, tube and tubesheet, are of interest. This parameter will be varied in three levels for the two parts, which will result in the following array:[0.8 1 1.2], and by using the material model for the tube, where the yield stress is 325 MPa, therefore the array is structured like this: [260 MPa 325 MPa 390 MPa].

8.5.1 Tubesheet Yield Stress

The tubesheet will be varied at three different yield stresses, while the tube yield stress is kept constant at 325 MPa, where the optimal contact force and the applied pressure is of interest. The results for the optimisation can be seen in table 8.4, where the initial optimal setting for the design parameter and the contact force can be seen. All the optimisations are performed with the same optimisation algorithm, as the one used for table 8.3. It should be noted that the initial parameter setting are different for each of the optimisations, since this proved better convergence behaviour.

Table 8.4. The results from the optimisation of the three different yield stresses for the tubesheet.

Yield Stress [MPa]		Parameter [MPa]		Contact Force [N]		No.
Tube	Tubesheet	Initial	Optimal	Initial	Optimal	Iterations
325	260	180	249.68	3.39	16.28	12
325	325	200	304.48	7.47	26.80	7
325	390	220	324.91	11.55	28.53	6

The optimisation results for the three different settings are represented on figure 8.9 for each iterations, the settings for the σ_y =325 MPa are similar to the one on figure 8.8. It can be observed the three optimisations shows similar slope for the region of 180-275 MPa, which might indicate that the slope is dependent on Young's Modulus and the peak is determined by the yield point.

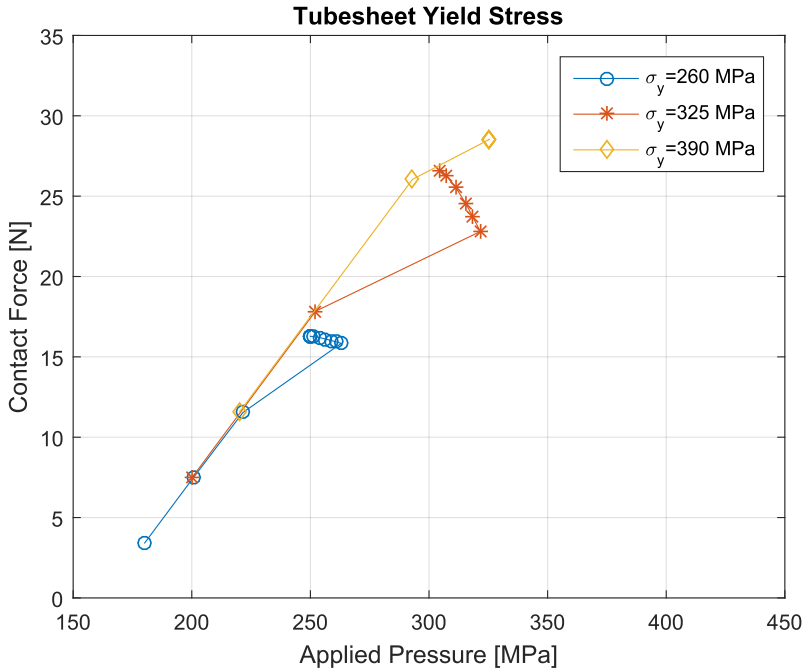

Figure 8.9. The three optimisations for the tubesheet yield stress for each iterations, which are summarised in table 8.4.

Based on the optimal settings found, the following two plots, figure 8.10 and 8.11, are made, where the contact force reached and applied pressure are shown, respectively. It is noteworthy, that the relation of the settings are not linear, and might indicate that an possible optimum for tubesheet can be found based on the decrease of the slope between the three yield stress settings. The results are similar to the ones found by Kalnins et al. [62], they found that an increase in yield stress for the tubesheet would result in an increase of the contact force. It is also found that this increase is not a linear relation, and therefore an optimum might be of interest in order to find the optimal setting for the tubesheet yield stress.

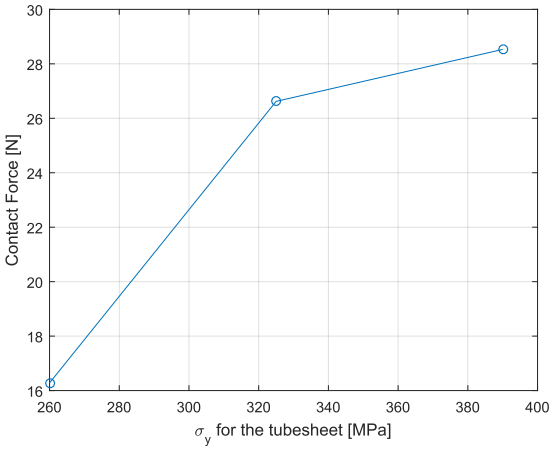

Figure 8.10. The optimal contact force for the three tubesheet yield stresses.

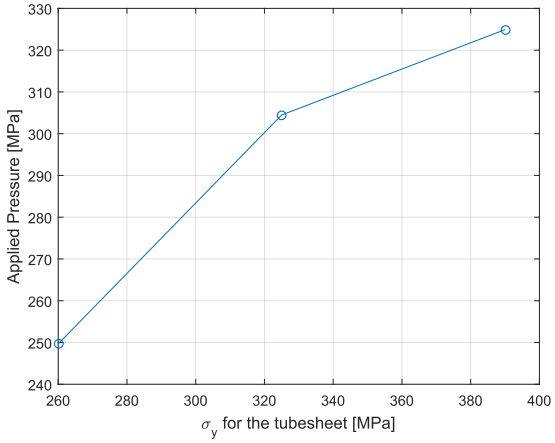

Figure 8.11. The optimal applied pressure for the three tubesheet yield stresses.

The optimal conditions found are in the following compared to the radial displacement and the plastic strain through the thickness, which can be seen on figure 8.12 and 8.13, receptively. On the two figure, it is observed that the hypothesis of avoiding plastic strain in the tubesheet, in order to achieve the optimal contact force is not confirmed. The other hypothesis is regarding the apparent wall reduction, which for the radial displacement is calculated to be close to 10% for the low and middle yield stress level, where for the high yield stress level it is close to 4%, for the optimal settings. Based on these results it would be obvious to declare the %WR to be an incomplete measure to determine if the joint quality is desirable. However, the plastic strain through the tubesheet is an evidence for deformation at the free edge of the tubesheet, this would under some conditions be very undesirable if a nearby tubesheet hole could become deformed.

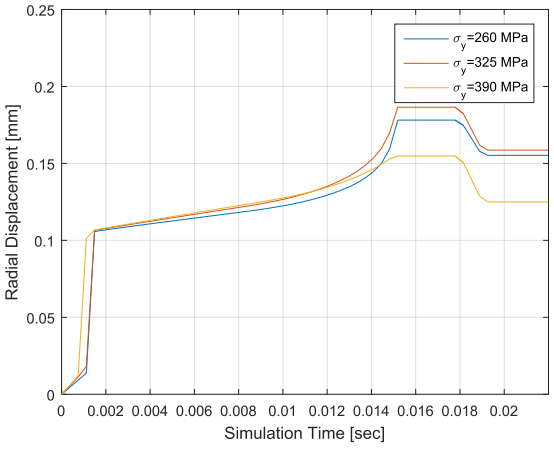

Figure 8.12. The radial displacement of the three optimal conditions of tubesheet yield stress variation.

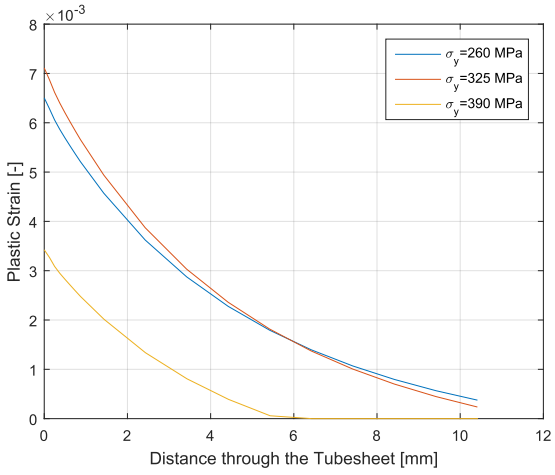

Figure 8.13. The plastic strain through the tubesheet for the three optimal conditions of tubesheet yield stress variation.

8.5.2 Tube Yield Stress

The tube is varied at three different yield stresses, where the optimal setting is of interest. The results from the optimisations can be seen in table 8.5.

Table 8.5. The results from the optimisations of the three different tube yield stresses.

Yield Stress [MPa]		Parameter [MPa]		Contact Force [N]		No.
Tube	Tubesheet	Initial	Optimal	Initial	Optimal	Iterations
260	325	200	267.84	13.73	22.38	7
325	325	200	304.48	7.47	26.80	7
390	325	220	309.14	5.24	21.94	10

Similar to the tubesheet yield stress variations, figure 8.14 illustrates the contact force for the three tube yield stress settings for each iteration. There seems to be no similar slope behaviour as for the tubesheet yield stress variations, but the optimum for the 325 MPa and 390 MPa has similar applied pressure setting.

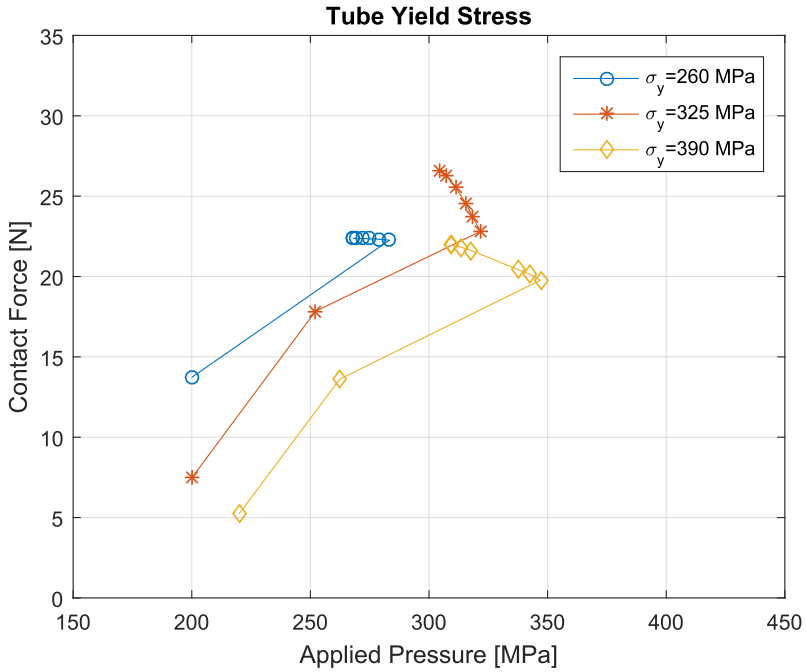

Figure 8.14. The three optimisations for the tube yield stress for each iterations, which are summarised in table 8.5.

Based on these optimal settings, the following two plot for the contact force and the applied pressure, on figure 8.15 and 8.16 respectively, are made. It indicates that the setting with the tube yield stress at 325 MPa results in the largest contact force, but it is also noteworthy, that the obtained contact force for the two other settings are not as low as for the lowest contact force obtained found for the tubesheet setting with 260 MPa. The applied pressure for the optimal settings, indicates that a higher yield stress needs a higher applied pressure, however, the increase in applied pressure for the higher yield stress is relatively low.

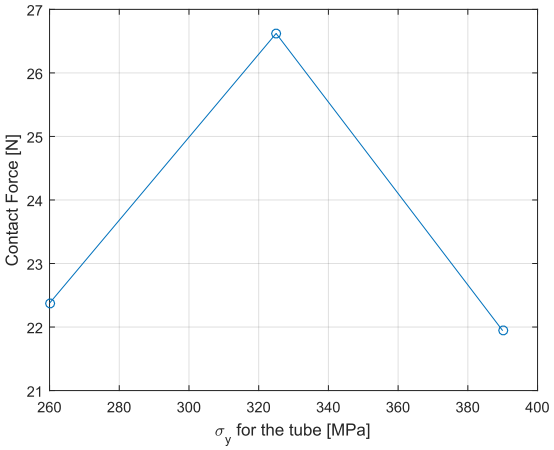

Figure 8.15. The optimal contact force for the three tube yield stresses.

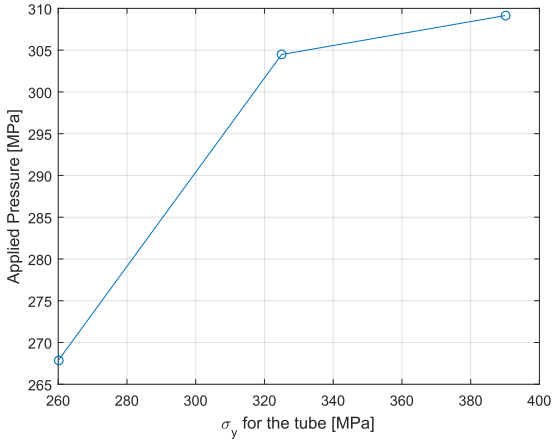

Figure 8.16. The optimal applied pressure for the three tube yield stresses.

The radial displacement and the plastic strain through the tubesheet, for the three tube yield stress optimal settings, are plotted on figure 8.17 and 8.18, respectively. For the 390 MPa and 325 MPa yield stress settings, the radial displacement are higher than the low settings. This is also visible in the plastic strain through the tubesheet, where these two settings shows plastic strain throughout the tubesheet, which is undesirable, as aforementioned. The tube with the lower yield stress, reaches a similar level as the one with the high tubesheet yield stress, where the %WR is around 3.5%, the two other tube yield stresses are at approximately 10%.

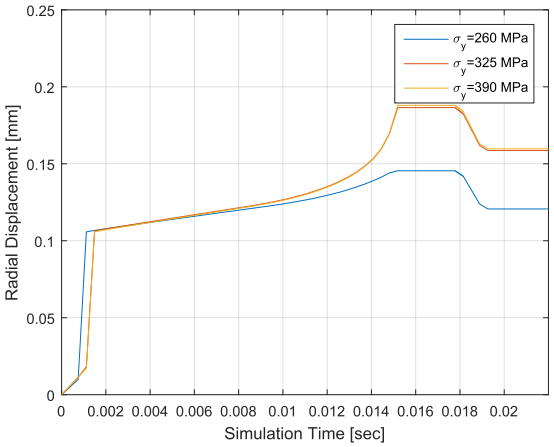

Figure 8.17. The radial displacement for the three optimal conditions.

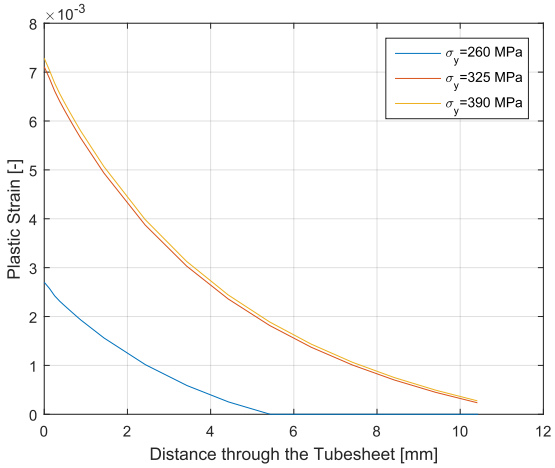

Figure 8.18. The plastic strain through the tubesheet for the three optimal conditions.

8.5.3 Discussion of Yield Stress Influence

Based on the five optimisations with different yield stresses, some conclusions can be drawn. By observing only the contact force obtained, the optimal conditions would be to utilise a high yield stress for the tubesheet. This seems to be valid, when comparing the

results to the ones found in the literature, see [62], but there are some factors which has to be taken into account. However, these results indicates that there are a relation between the tube and tubesheet yield stress and the contact force, based on results in the optimal condition, a higher yield stress for the tubesheet than the tubes would be most desirable. The optimal condition is very model dependent, where this model allows the tubesheet outer part to expand, which is not always possible or even desirable. However, the reason for allowing this expansion makes the model act more robust and thereby improves the convergence of the optimisation. A possible method for improving the applicability of these results is to utilise a more realistic tubesheet shape, where the stiffness of tubesheet is not necessary rotational symmetric. This could e.g. be to model the tubesheet as Alexouli et al. [64], where the tubesheet geometry for a representative cell is similar to the one on figure 8.19. For their case the nearby tubesheet holes were not allowed to deform in any way, which could be utilised in the optimisation as a penalty parameter for the objective function.

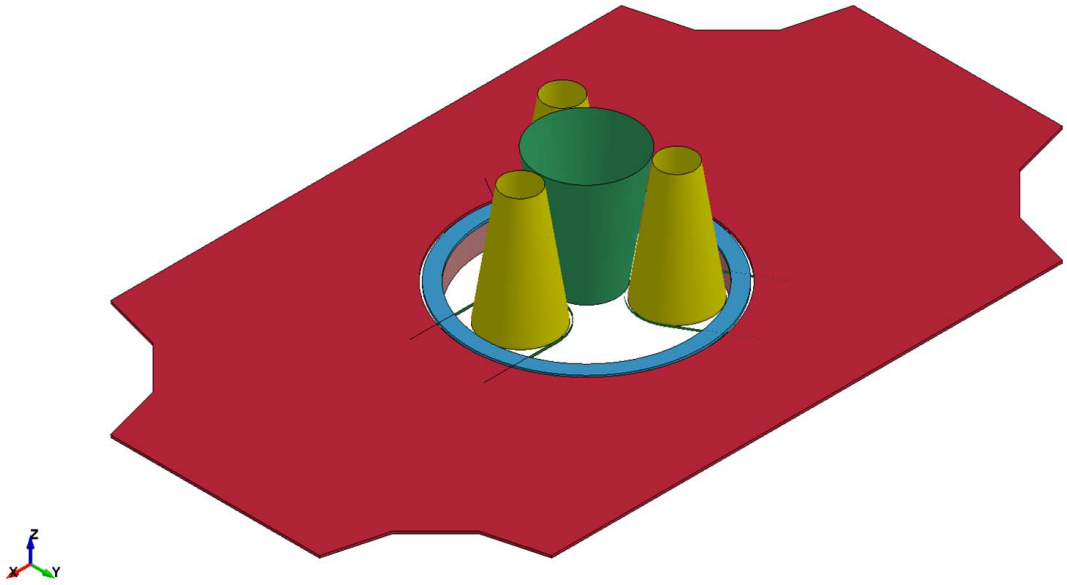

Figure 8.19. The model made by Alexouli et al. [64], where the real-life tubesheet geometry were included(The red part). (Source: [64])

Through the literature study for the tube-tubesheet joint process, the application of optimisation to find the optimal conditions are very rare(it was not possible to find any), the general approach is to determine the parameters influence by utilising statistical method. The advantage of using an optimisation approach is the ability to find the optimal setting, whereas an statistical approach would only find a region for which the optimum could be within. For this case it also important to note that the optimisation is only beneficial if the initial parameter setting is within the region where contact is obtained, else the optimisation will terminate quickly and not find the optimum.

8.5.4 Clearance Effect

In this section, the clearance (c) between the tube and tubesheet is varied in three levels of 0.05 mm, 0.10 mm and 0.15 mm. The clearance variations are constructed by changing the inner diameter of the tubesheet hole and the outer diameter of the tubesheet, such the tubesheet thickness is kept constant. Therefore the tube dimension is constant through this test series, together with the material parameters, all conditions are similar to the based model (Tube: σ_y=325 MPa, Tubesheet: σ_y=325 MPa). The results for the three optimisations can be seen in table 8.6.

Table 8.6. The results from the optimisation of the three different clearance settings.

Clearance [mm]	Parameter [MPa]		Contact Force [N]		No.
	Initial	Optimal	Initial	Optimal	Iterations
0.05	200	303.55	8.72	28.18	12
0.10	200	304.48	7.47	26.80	7
0.15	200	298.29	0	24.94	5

On figure 8.20, the contact force for each of the optimisations are illustrated. It seems that the slope of the three optimisations are similar to the observations made for the tubesheet yield stress, but here they are shifted towards a lower applied pressure limit for a smaller clearance and visa versa. Another observation which can be made is that the maximal obtained contact force between there different optimisations are not that big, and are with in the same region as applied pressure.

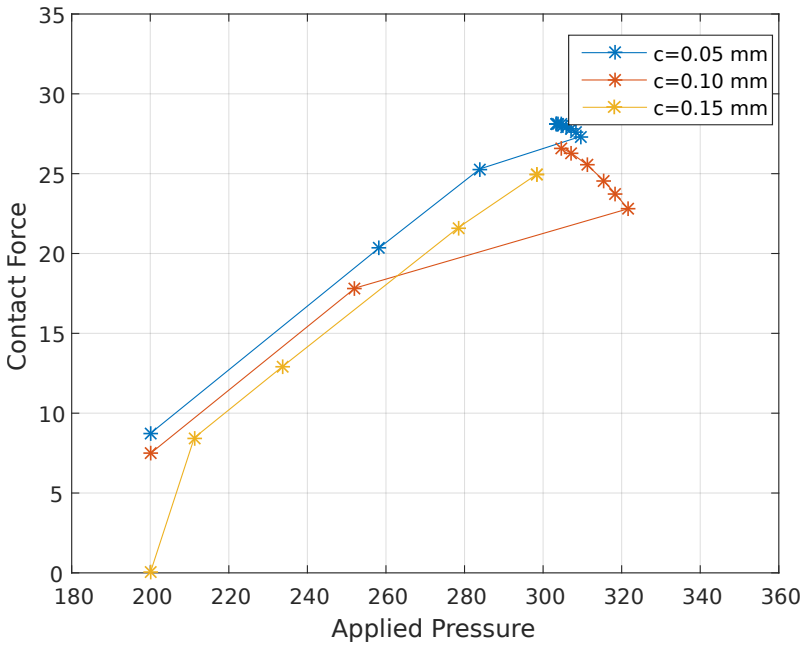

Figure 8.20. The three optimisation for the clearance effect for each iteration, which are summarised in table 8.6.

As described earlier, the normal non-destructive evaluation procedure for tube-tubesheet joints are to measure the apparent wall reduction (%WR), which is expected to be affected

the clearance. On figure 8.21, the apparent wall reduction through the simulation can be seen for the three optimisations. The smaller and bigger clearances' %WR are both smaller than the mean clearance, at a value of 7.67% and 6.99%, respectively. The obtained apparent wall reduction are for both cases compensated for by increasing the radial displacement, as can also be seen on figure 8.20, where the applied pressure is only shifted a small amount.
On figure 8.22, the plastic strain through the tubesheet can be seen, it can be seen that both the smaller and bigger clearance has a smaller plastic strain development, however, it is indicated that a smaller clearance results in a increase in the plastic strain.

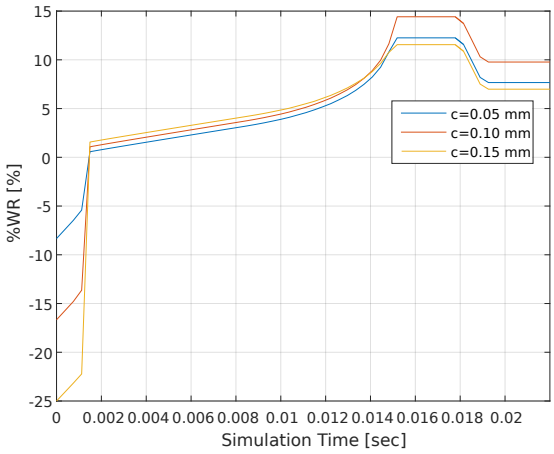

Figure 8.21. The %WR for the three optimisations, which is calculated based in equation 8.1.

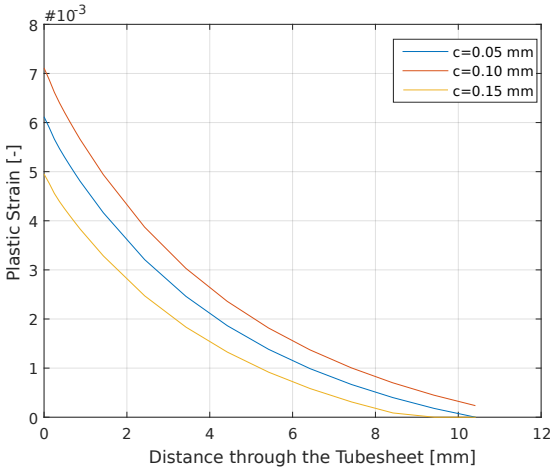

Figure 8.22. The plastic strain through the tubesheet for the three clearance optimisation runs.

Based on this study upon the clearance effect, it is concluded that the clearance does not strongly affect the obtained contact force. Furthermore, it is also found that the %WR is not affected by the increase or decrease in the clearance.

8.6 Sub-conclusion

This chapter's subject is on the case of hydraulically expanded tube-tubesheet joint, the main objective was to achieve as high a contact force as possible. The modelling approach was to use a plane strain assumption, recommended by Madsen et al. [65], and the geometries were modelled as rotational symmetric. The main challenge with the model was to achieve a uniformly distributed and numerical robust contact force, therefore a implicit contact model using the Lagrange method was used to improve the robustness of the model output.
The optimisations objective was to maximise the contact force, but in order to use the least square formulation this had to be reformulated into a minimisation problem. The only design parameters selected was the applied pressure in the inner tubewall.
By this optimisation approach five optimisations with different yield stresses for the tube and tubesheet were devised, and the optimal condition were found for each and compared to each other. Here the optimal condition were estimated to depend on the relation

between the tube and tubesheet yield stress, where a higher tubesheet yield stress would result in an increased contact force.

Case 5: Airbus A380 Door Frame Corner

9

In this chapter, a springback optimisation of the manufacturing of an corner piece for an Airbus A380's door frame is presented. The corner piece is manufactured in a five step process, where critical springback is experienced after the final operation. The modelling of the processes are based on the documentation by Wang et al. [51, 67]. In order to minimise the springback an optimisation of a new hydroforming die is developed and parameterised, the geometric parameters are used as the design parameters, together with the hydroforming pressure. The optimisation lead to a reduced springback, but did not remove it entirely. The thinning was likewise minimised, even though it was not included in the objective function.

In Appendix H, additional information regarding: simulation, keyword and optimisation data, can be found.

9.1 Purpose

The purpose of this case is summarised in bullet points below. The first objective is to build a simulation of the corner piece manufacturing for a Airbus A380 door frame, based on the limited information accessible [68, 67] . This model has to be robust regarding determination of a realistic springback, for a later optimisation. The second objective is to analyse the springback behaviour, and develop a method which might minimise the springback. This model should be parameterised, such that optimisation can be used to find the optimal conditions. Finally, the optimised model will be evaluated in order to determine the feasibility of the reached optimum.

- Develop a simulation of the manufacturing of the Airbus A380 corner piece including a robust springback analysis.
- Analyse the springback behaviour and develop an optimisation schedule which minimises the springback.
- Determine the feasibility of the optimal settings.

9.2 Process

The Airbus A380 is the world largest mass-produced airplane. This super-jumbo requires four jet engines to achieve lift, and six doors to allow the up to 853 passengers and crew, to enter and exit the double-decks comfortably [69].

The history of aeronautics demonstrates the importance of properly designed and manufactured window and door corners, which in 1954 was the cause for a number of disasters, that promoted the use of round windows and doors [70]. Therefore this corner pieces is very important, not only allow the door to close and seal properly, but also to ensure safety.

The corner door frame of the A380 is designed as one piece which is produced separately and then assembled into a complete door-frame, the corner frame part can be seen on figure 9.1. The corner piece shown on the figure is the focus of this case, where the figure shows the finished shape after trimming it is the steps prior, that are of interest in this case.

Figure 9.1. CAD drawing, corner piece of the A380 door frame [67].

The process of manufacturing the corner part can be split into six steps, the steps are illustrated on figure 9.2, and the key dimensions and part names are presented on figure 9.3. The process flow of the corner part production are based on a Paper by Lang et al. [68, 67]

Hydroforming 1 The rough blank is given a double curvature by a hydroforming operation. In this operation the blank is oversized, and held in place along the edges.

Trimming 1 The curved oversized blank is trimmed to obtain a blank that is smaller in length and width, and containing rounded corners. Furthermore the middle pattern is cut out in the blank, see figure 9.2, to increase formability in the following steps.

Hydroforming 2 In the second hydroforming operation, the blank corner 1 and 2 is formed. Due to the limitations of hydroforming the corners are oversized to 4 mm in radius for the first corner and 6 mm for the second corner, the third corner is not form in this operation. Due to the hole in the middle of the blank, a dummy blank is used, which are placed on top of the blank, at which the pressure is applied.

Stamping This stamping operation is carried out in two steps, the blank is not removed from the tool in between. It is after this stamping operation, that the crucial springback is observed.

- In the first stamping operation the corners 1 and 2 are formed to the final measurement of 1.58 mm and 2.54 mm which correlate to 1/16 in and 1/10 in.
- In the second step, the third corner is formed to the final measurement of 1.58 mm.

Trimming 2 After stamping the blank is parted into four corner pieces and trimmed to the final measurements.

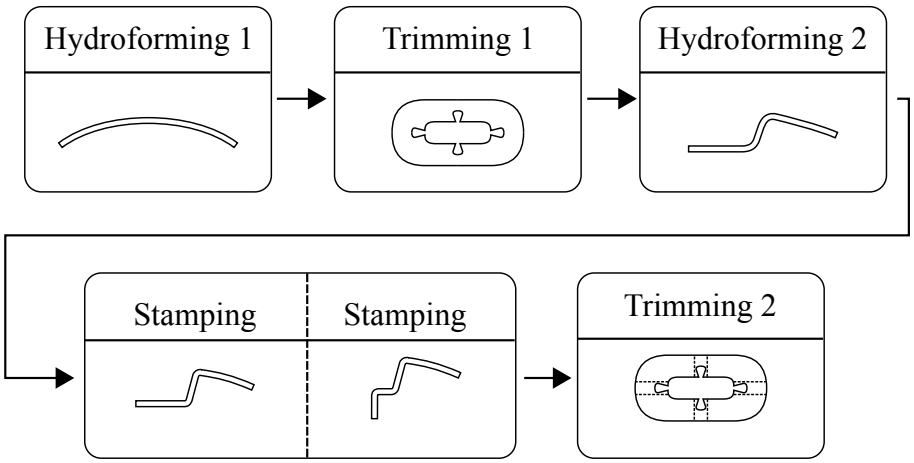

Figure 9.2. Process flow of as described by Lang et al. [68, 67]

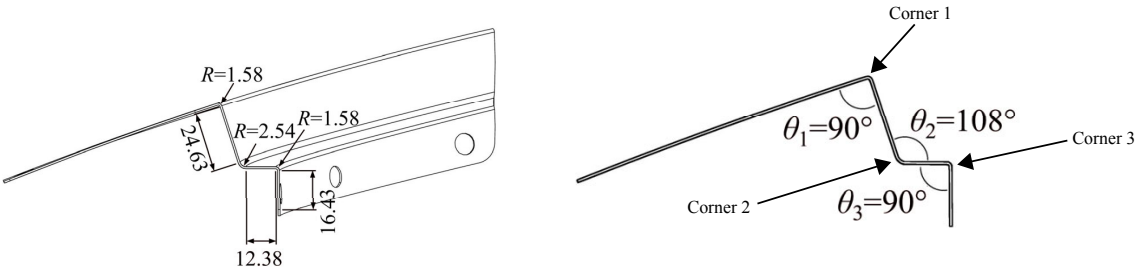

Figure 9.3. Dimensions of the finished door frame corner [68]

Photos from the production facility in Tianjin, China, can be seen on figure 9.4.

The corner part is produced in SUS321 following the Japanese standard for stainless steel. SUS321 has good formability, with the downside of requiring higher pressure during forming and springback is more severe compared to more conventional stainless steel types. SUS321 material is used on airplanes, due to its good thermal and fatigue properties. The materiel properties used in the simulation and optimisation are documented in table 9.1.

Table 9.1. SUS321 material parameters [67] (Strength coefficient [71]).

Input Parameters		LS-DYNA unit	SUS 321
Density	ρ	[tons/mm^3]	7.850e-9
Young's Modulus	E	[MPa]	198e3
Poission's ratio	ν	[-]	0.28
Yield Stress	σ_y	[MPa]	270
Strength coefficient	K	[MPa]	1372
Hardening exponent	n	[-]	0.44

The main challenge experienced during the manufacturing of the corner piece, is springback after the second hydroforming operation and after the stamping operation, which causes the last vertical section to stick out. Furthermore, the springback is not uniform along the curvature, where more springback is experienced at the edges compared to the middle of the corner part.
The second challenge during production is fracture, the critical area is located at the vertical sections edges, which can be seen on figure 9.4. The extent of this problem is not known and is only observed on some of the documentation from the production facility, which can not be presented in this report.

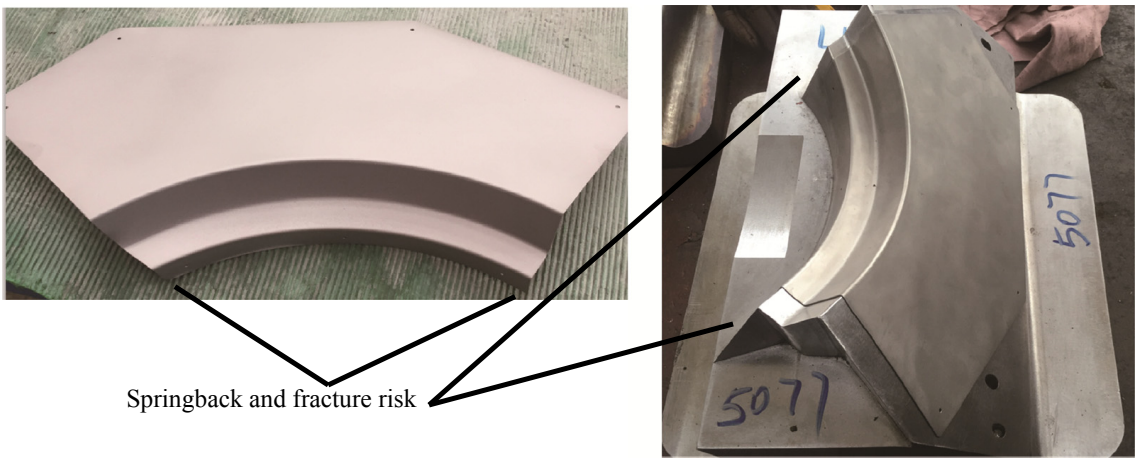

Figure 9.4. Photos from the production facility in Tianjin, China. [67]

9.3 Modelling

During modelling of the frame corner tooling parts, it was decided to de-feature the design to simplify the optimisation and the automatic part generation scripts. Four main features are removed or simplified on the design:

- The straight section is removed, see figure 9.5, this allows the die and punches to be rotational symmetric.
- The corner of the blank cutout is made as a large radius instead of a straight section and a smaller radius.

- The curvature of the blank is removed along with the first hydroforming operation, this is shown on figure 9.6, as the measurements of the double curvature is not known. Therefore the angle of the first bend is changed from 90° to 108°.

Drawings of the blank and stamping die, with measurements can be found in Appendix H.5.

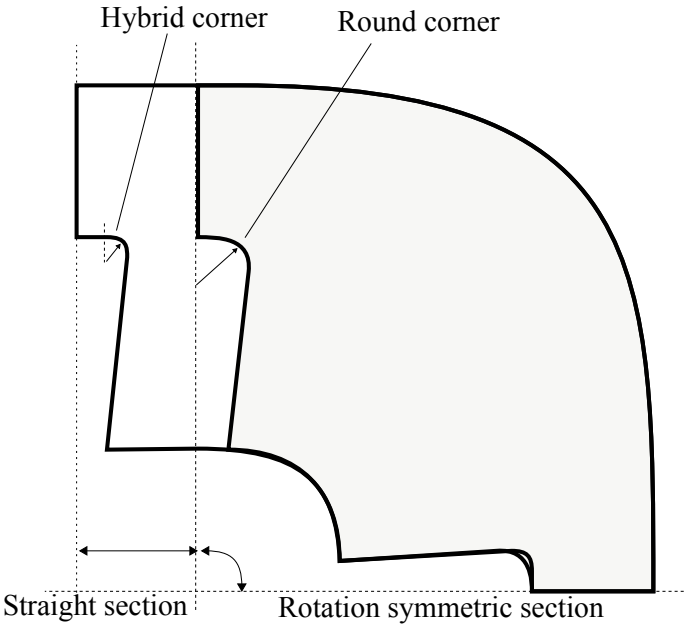

Figure 9.5. A rough illustration of the Airbus blank design and the simplified blank design in gray.

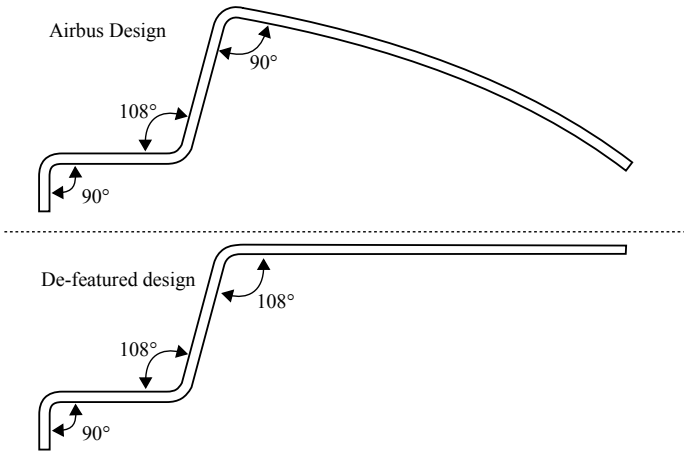

Figure 9.6. Illustrations of the profile view for the Airbus design and the de-featured design used in the simulation.

The process is modelled in one continuous simulation, the operations included are: the second hydroforming operation and the two step stamping operation. The parts modelled can be seen on figure 9.7, where the hydroforming parts are shown on the left, and stamping parts on the right, and the blank holder is used during the entire forming time. In order to switch between the two operations, the contact between the right parts are turned on

and off during the simulation. The hydroforming operation is modelled with a dummy blank as used in the production, the hydraulic pressure is prescribed to the dummy with a pressure curve similar to how it is done in the tube-tubesheet joint case, shown on figure 8.4 on page 67.

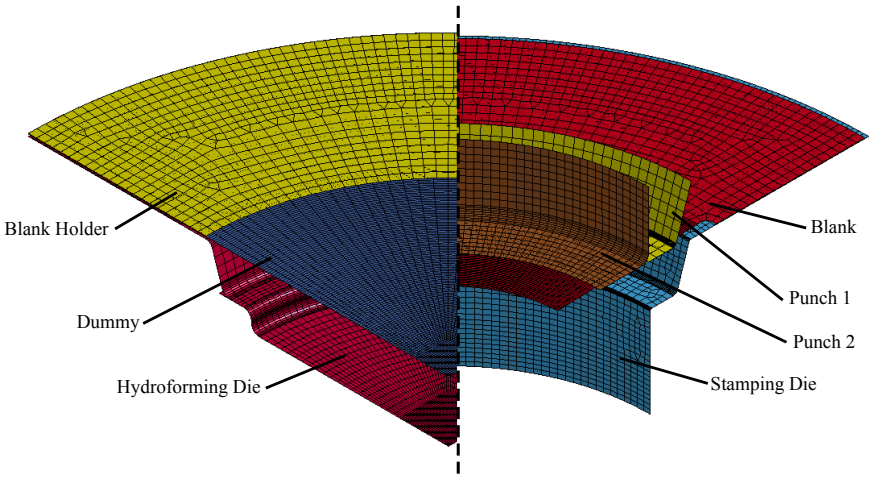

Figure 9.7. Parts included in the simulation, the parts of the hydroforming operations is on the left, and the stamping parts on the right. The blank holder and blank is used in both operations.

The parts are modelled with shell elements, element formulation elform=-16 based on the implicit time-period for the blank, and elform=2 for the remaining parts. The blank and dummy are specified with material model: *018-Power_Law_Plasticity with the material parameters presented in table 9.1. Contacts are defined using: Forming_Surface_To_Surface with both static and dynamic friction set to 0.1, viscous contact damping is set to 70%. Termination time is set to 0.040sec, allowing for 0.01sec for hydroforming, 0.01sec for each stamping operation and 0.01sec for explicit springback/damping, afterwards an implicit springback method is used.

9.3.1 Springback modelling

If the same springback modelling methods used in previous cases was used, a stable springback will not be reached, and the final springback position will be random. This is due to the shape of the blank, where the trimmed sides causes the blank to act like a large cantilever beam, which causes vibrations in the free end. The vibrations of the blank are evoked when the contact to the punches and blankholder are turned off, and counteracts the vibrations and results in a random springback position, therefore a number of actions are taken.

- Damping is added to the blank, at the time-step the stamping operation is done and unloading is initiated. The damping is slowly decreased during a time period, to avoid excessive locking of the blank.
- Instead of turning off the contact between the blank and punches, they are moved backward to slowly release the contact force. This is primarily done based on the high contact force between punch 2 and the blank.

- The termination time is increased from 0.03 sec to 0.04 sec allowing the blank to settle explicit before switching to implicit. A long resting period likewise ensures the kinetic energy lower before switching to implicit.
- The blank flange is locked in z direction, to avoid the blank from rotating during implicit springback and to avoid vibrations in flange.
- A different implicit springback method is used: `Seamless Springback Method` which is an implicit method that is performed after the explicit time. With the seamless method the implicit timestep is automatically adjusted, and 10 non-linear springback steps are used [72].

Material Model for Springback Purposes

The accuracy of a springback simulation is strongly dependent on the constitutive material model selected for the blank. Material models which include the Bauschinger effect and cyclic hardening characteristics will result in a more accurate springback, due to better description of the elements hardening history [73, 74, 75, 76, 77].

The material model selected (*018-Power_Law_Plasticity) does not include this and will therefore not simulate the springback as accurately, this type of material model is, however, known to underestimate the springback [74, 76]. A material model that would give better results, could be the Yoshida-Uemori material model [77], which is made to improve simulated springback for sheet metal formed parts. The challenge of using this model is the seven material parameters required, besides the anisotropic parameters. The material parameters known for SUS321 is not sufficient for using Yoshida-Uemori material model, therefore *018-Power_Law_Plasticity is used instead. Springback is still a very challenging topic in the automotive industry.

9.3.2 Optimisation Hydroforming Die

In order to minimise the springback, a test with two different hydroforming dies were modelled, one for the preliminary investigation of the process, and one for the optimisation, shown on figure 9.7. The original die included the two first bends and a flat bottom, the die used in the optimisation included a bottom cavity. By changing the die geometry, the blank is more plastically deformed, which seems minimise the springback.

9.4 Optimisation

The objective of this optimisation is to reduce or compensate for the springback, the blank thickness thinning in the critical areas is considered as a secondary objective. This is not included, as the thinning in the original design is maximally 0.15 mm on a 0.8 mm blank. Furthermore, the result of the optimisation showed less thinning than the original design, which further solidifies the decision for not including element thickness in the object function.

The formulation methods presented in earlier cases are reused. It is decided to approach the problem as a tool optimisation case, with focus on the hydroforming operation, as this process have a higher degree of freedom compared to the stamping operation. With

the current hydroforming die design and process, the number of design parameters which influence the third bend is limited to the hydraulic pressure.

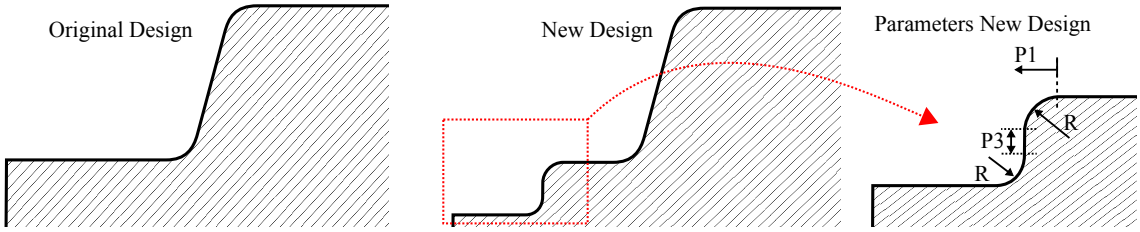

Figure 9.8. Illustrations of the original design, the new design and the parameters defining the new design

Therefore it is chosen to redesign the hydroforming die to included a bend related to the third bend in the final geometry. The approach is based on Roll et al. [10], which suggested it is possible to minimize springback with additional foldings and higher stretching. The new die design is shown on figure 9.7 and figure 9.8.

9.4.1 Geometrical Objective

The objective, which is purely geometrical, is formulated using the cylinder surface method, as used before. The z-axis is used as the center of the cylinder, the radius is set to 124.3 mm which is estimated from Airbus design as this measurement is not specified, the radius includes half the starting element thickness.

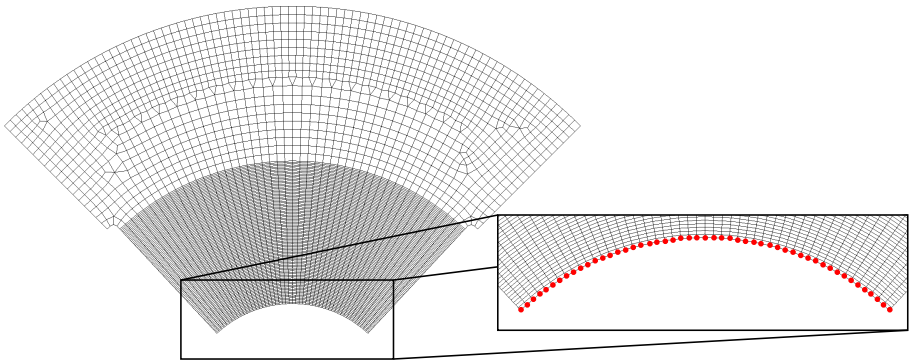

Figure 9.9. Node shown with red dots, is used to evaluate the springback.

The nodes used to evaluate the springback, can be seen on figure 9.9, these nodes experience the largest displacement during springback. When only including the bottom nodes and only specifying one geometric shape objective, there is a risk that springback in the other parts of the blank are increasing. It is observed that the springback change in the other parts are negligible, it is therefore not included.
Another approach could be to formulate objective function as the geometrical deviation for the entire part, such approach was used by Endelt et al. [78] for a tube hydroforming process.

9.4.2 Design Parameters

The design parameters for this optimisation are focused on the hydroforming operation, as changes to the stamping operation would require large amount of changes to both the die and punching tool and maybe the hydroforming die. The design parameters are:

- The distance P1, which is the placement of the new bend in relation to the third bend in the stamping operation.
- Radius of the new die profile, see figure 9.8.
- The distance P3, which is the distance between the two new radii.
- Maximal hydroforming pressure.

The parameters are applied bounds from 0.001 to inf. to avoid problems with the tool generation script, which fails if surfaces are missing, the lower limit for the distance P1 is set to 0.

9.5 Results and Discussion

The results of the optimisation will be presented in this section, along with a discussion of the results. The convergence of the four parameters and the developed objective function is documented in Appendix H. The results which will be presented is: Springback, thickness, final parameters and hydroforming die shape.

The optimisation algorithm used for this case is the totally structured secant method, where the step size is regulated by the Dog-Leg method and the initial trust region is set to 50, based on previous cases [44]. The initial parameter settings and the the final settings are presented in table 9.2, the optimisation data is documented in table 9.3.

Table 9.2. Initial settings, optimum settings and the cost function.

Run	P1 [mm]	Radius [mm]	P3 [mm]	Pressure [MPa]	Cost Function
Initial	1	5	1	100	124
Optimum	0.000497	10.813	0.8256	35.517	96

Table 9.3. Data for the optimisation, number of function evaluations and the type, together with the trust region increases, decreases and initial size, and number of iterations.

Function Evaluation			Trust Region			Iterations
Total	Cost	Jacobian	Increase	Decrease	Initial size	
335	15	20	1	10	50	4

The optimal hydroforming die based on the optimum parameters can be seen on figure 9.10, On the figure, the original die is shown with a dashed line, and the blank with the optimal pressure (22.52 MPa) applied is shown with blue. The hydroforming die is built

as two parts in LS-PrePost which is why the corner 2 have a extra flat piece, this does not influence the simulation.

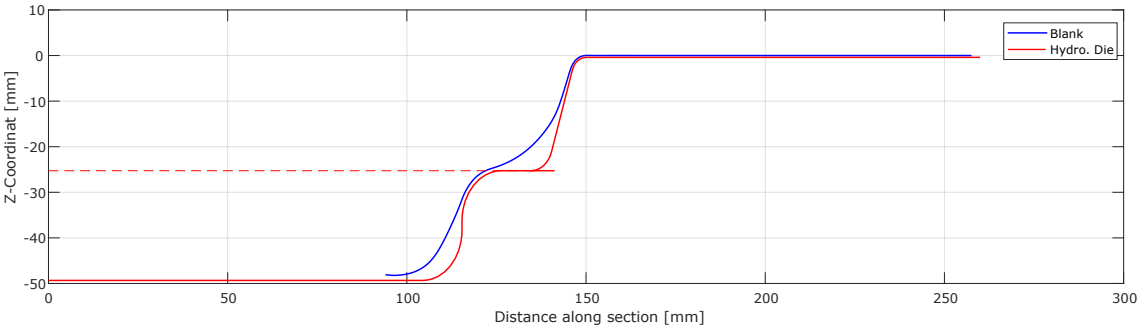

Figure 9.10. The optimised hydroforming die (red) , original hydroforming die (dashed red) and the blank with 22.52 MPa pressure in the optimised hydroforming die.

9.5.1 Springback

The main objective for the optimisation is to reduce springback of the third bend after unloading of the punches, in the stamping operation, and before the final trimming. The part is simplified to be symmetric around a center line, therefore springback is evaluated at two sections, a section through the center of the part and a section from origo to the flange edge, through the center cut-out corner. The evaluated sections are shown on figure 9.13, these two sections are used as they represent where there are the least springback (center section) and where springback is most severe (edge section).

On figure 9.11 the result of the optimised design can be seen, along with the part made from the original design, and the objective cylinder (124.3 mm) shape. In the original design the springback measured at the tip is 1.3 mm, in the optimised design in the springback was reduced to 0.7 mm at the center section section.

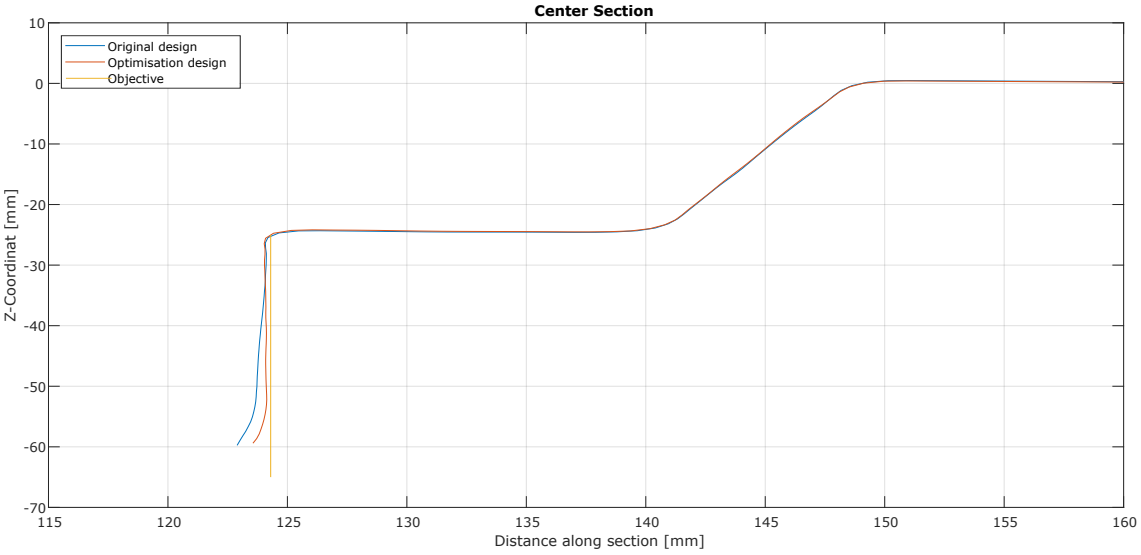

Figure 9.11. Springback of the original design and the optimised design, at the center section.

On figure 9.12, the results from the edge section can be seen. Springback of the part with the original design is 5.1 mm at the tip and for the optimised design the springback is reduced to 3.3 mm.

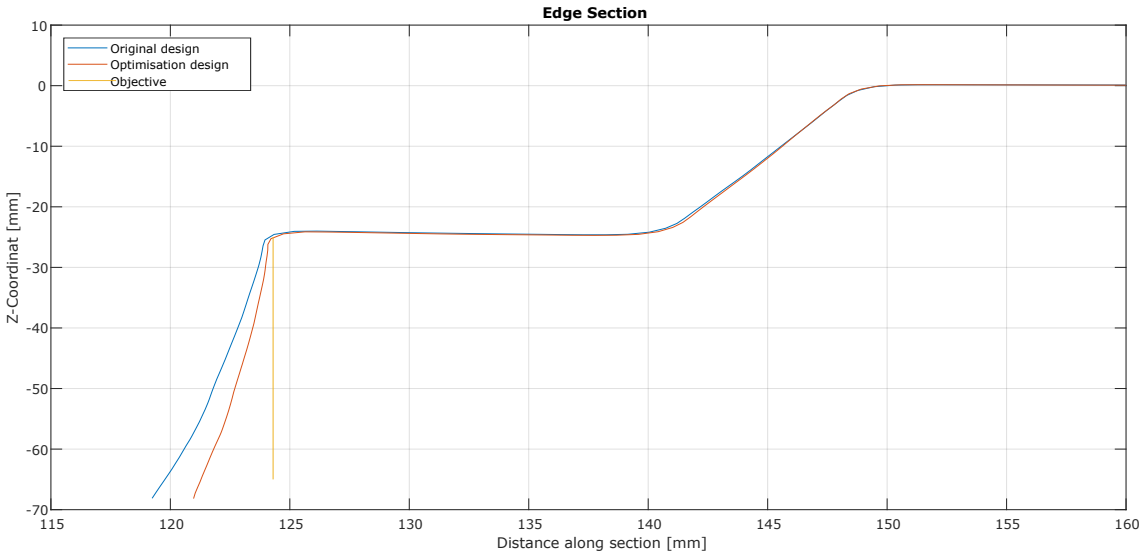

Figure 9.12. Edge section springback for the original design and the optimised design.

From the optimisation the springback is reduced, but is not fully removed. This can either be the adopted springback reduction method, or it can be result of the poor material model selected.

The material model can be improved by used a model which utilises the Bauschinger effect, which better reflects the hardening history of the elements. The adopted springback reduction method introduce a higher degree of complexity to the model, as multiple different forming operation are used, this further imply the need of a better material model.

The new hydroforming design is a possible solution strategy, which is not guaranteed to solve the problem, and better springback results may be generated by increasing the number of design parameters to include e.g. the stamping punches and die geometry, the cut-out design or by adding a new stage. This would greatly increase the model complexity and computational time.

9.5.2 Fracture

The secondary challenge which is not included in the objective function is the risk of fracture. Risk of fracture is very complex to evaluate, therefore it is selected to compare the blank thickness from the two die designs to get an estimate if the change of avoiding fracture improves the thinning.

On figure 9.13, the blank thickness of the original design can be seen. On this part there are two critical areas, below the third bend and center of the vertical wall, where photos from the factory showed fracture in the area below the third bend.

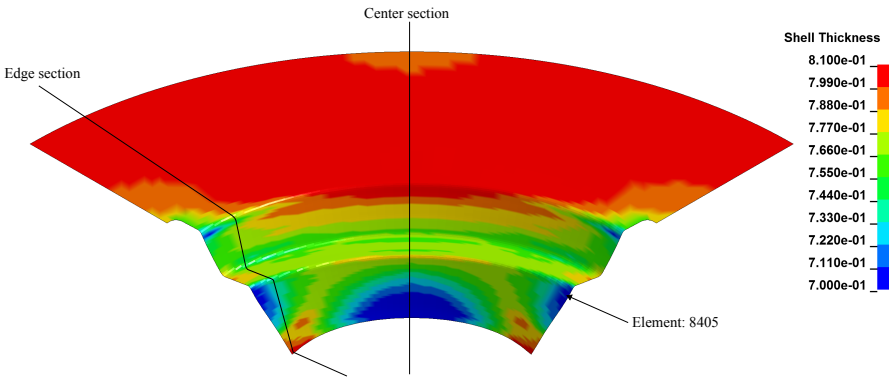

Figure 9.13. Blank thickness distribution with the original design, the starting blank thickness is 0.8 mm.

On figure 9.14, the blank thickness from the optimised hydroforming die can be seen, where the thickness is shown with the same scale as figure 9.13. The thickness reduction below the third bend is greatly reduced, which will decrease the risk of fracture. The thickness reduction of the vertical wall is likewise improved. The most thinned element (8405), located at the third bend with the original design, thickness is 0.701 mm, the thickness of this element is increased to 0.743 mm with the new design.

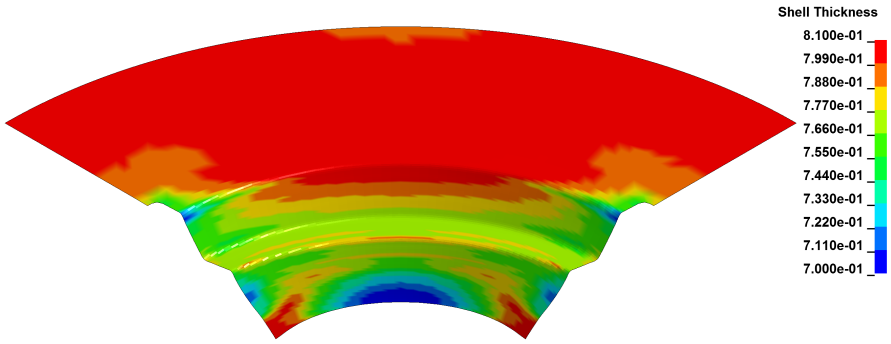

Figure 9.14. Blank thickness distribution of part produced the optimised hydroforming die design, the scaled is identical to figure 9.13.

Based on these thickness evaluations it can be seen that the new die design, has increased the thickness in the critical areas, while minimising the springback.

9.6 Sub-conclusion

In this chapter, a part of a door frame corner for a Airbus A380, the largest mass produced super-jumbo in the world, is utilised for performing a springback optimisation. The corner part is produced in a five step process, that involves trimming, hydroforming and stamping. The part was after stamping plagued by springback especially at the third corner and photos from the production shows that fracture is likely to occur at this bend likewise.

In order to improve the springback behaviour, an optimisation approach is devised, where the die used in the second hydroforming operation, is redesigned with a extra bend,

where the size of the bend is used as design parameters in the optimisation. The design parameters defined for the optimisation is the hydroforming pressure, radius of the new die section, along with placement and depth.

With the optimised hydroforming operation, the springback at the center is reduced from 1.3 mm to 0.7 mm and at the edge from 5.1 mm to 3.3 mm. It is expected that higher accuracy can be achieved by using a better material model made for springback analysis. Thickness reduction is likewise minimised in the overall plate, and in the critical region the thickness is increased from 0.701 mm to 0.743 mm. Based on the optimised solution, it is assessed, that the solution increases the feasibility, but the springback can still to be improved further.

Case 6: VSR - Deep Drawn Cup 10

In this chapter, the Vibrational Stress Relieving (VSR) process is applied for a deep drawn cup containing large residual stresses. Initial investigation on the VSR process is documented in an Paper in Appendix A, where the process is virtually tested on some simple examples. The forming of a deep drawn cup is modelled as in a previously publication by Danckert [28]. Based on the deformed cup, an eigenvalue analysis is used in order to locate the frequency modes at which the areas containing the largest residual stresses are affected. Two modes are used for further investigations, where a discussion upon development of an optimisation for this process and a forming limit stress like diagram (FLSD) [11] is constructed in order to investigate the two frequency modes influence in the stress relieving.

- *It may be beneficial to read the Paper in Appendix A, before this chapter.*

In Appendix I, additional information regarding: simulation and keyword can be found.

10.1 Purpose

The purpose with this case, are listed beneath, is to develop a VSR optimisation approach, such the largest residual stresses can be minimised. This case focuses upon applying this method for complex geometries, the fundamentals of the process is documented in a presented Paper(See Appendix A).

- Locate the largest residual stresses and the resonant frequency mode for relieving these, on a complex geometry.
- Develop a possible optimisation approach for the VSR treatment of complex geometries.

10.2 Process

Vibratory stress relief (VSR) is an non-thermal alternative to thermal heat treatment, for relieving residual stresses and ensure geometry stability in welded or cast metal structures. The method has in the recent years gained the public's interest, due to the promising possibility in saving both time, equipment and cost, especially for very large structures which normally require special care.

VSR is performed by applying a cyclic load to the construction at a specific frequency, with the purpose of redistributing residual stress peaks. The frequency selected is an eigenfrequency or near an eigenfrequency of the construction, this ensures that a small load can be used, to achieve very high amplitude stresses in the construction [79, 80].

In preparation of doing this case a preliminary study of VSR is conducted and documented in a Paper, which can be found in Appendix A. The residual stresses of a hole plate is treated, and the conclusions of the study is that VSR has potential and relived the residual stresses, but the selected eigenfrequency mode are important along with the boundary conditions imposed on the treated part. The eigenfrequency mode used decides where the residual stresses are removed, if the mode does not accumulate amplitude stresses in an area, the residual stresses in this area is not removed, this can be seen on figure 10.1 and 10.2.

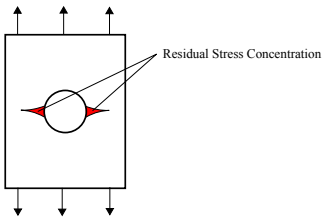

Figure 10.1. Hole plate, plasticity loaded to cause residual stress, where shown.

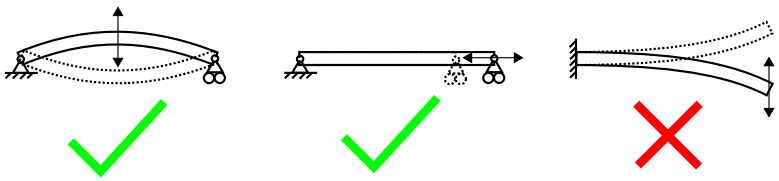

Figure 10.2. The three mode investigated in the paper (Appendix A), the two first mode was found the reduce residual stress peaks, the last mode resulted in new residual stresses.

Even though VSR have been studied since 1943 [81] the validity and advantages of VSR is not fully agreed upon. It have been claimed that compared to thermal treatment savings up to 90% can be made [82] depending on the set-up.

Studies have concluded that VSR have potential to effectively reduce residual stress peaks, if the correct eigenfrequency mode and load are selected [83, 84, 85, 86]. Furthermore studies concluded that VSR has a positive effect on fatigue life [87, 88].
Other studies have concluded limited success with VSR, where the result were either very small, it only worked on simple geometry or it was too dependent on the boundary conditions and amplitude[89, 90, 91]. Simulations of VSR have proved that if the correct eigenfrequency mode, load and boundary conditions, are selected it is possible to reduce residual stress in complex structures and welds [92, 93].

10.3 Modelling

For this VSR treatment of a deep drawn cup, two models are build, one for making the deep drawn cup and one for performing the stress relieving operation.

10.3.1 Deep-Drawn Cup

In order to prove the applicability of the VSR treatment, a Paper upon minimising the residual stresses in a deep drawn cup was used as inspiration. Danckert [28], devised an example where residual stresses were minimised by changing the ironing die shape. For this case the minimising of the residual stresses will be caused by the VSR treatment, and therefore only the first two deep drawing steps from his article will be devised. The dimensions of the different parts can be seen in table 10.1 and table 10.2.

Table 10.1. Tool dimensions of the two drawing stages [29].

	First draw	Second draw
Punch diameter	99.61 mm	83.23 mm
Punch nose radius	7 mm	2.41 mm
Die profile radius	8.5 mm	7 mm
Die clearance	1.9 mm	1.9 mm

Table 10.2. Blank parameters and frictions coefficient [29].

Blank material	AISI 304	
Blank diameter	108.78	mm
Blank thickness	1.5	mm
Young's modulus	196	GPa
Possion's ratio	0.3	
Strength coefficient	1367	MPa
Strain exponent	0.42	
Friction Blank - Punches	0.10	
Friction Blank - Die/Blank holder	0.80	

The model can be seen on figure 10.3, it can be seen that the forming operation is performed continuously, by moving the punches downwards with a constant velocity. For the two forming steps, there are two dies and punches, where the punches are moved downwards together, for the second forming operation the contact between the first punch and the blank is shut off. All the parts are modelled with shell elements, the tooling is modelled as rigid and the blank is modelled with the material model no. 18 (Power law plasticity, see parameters in table 10.2) and element formulation 2 (Belytschko-Tsay) with 7 integration points through the thickness.

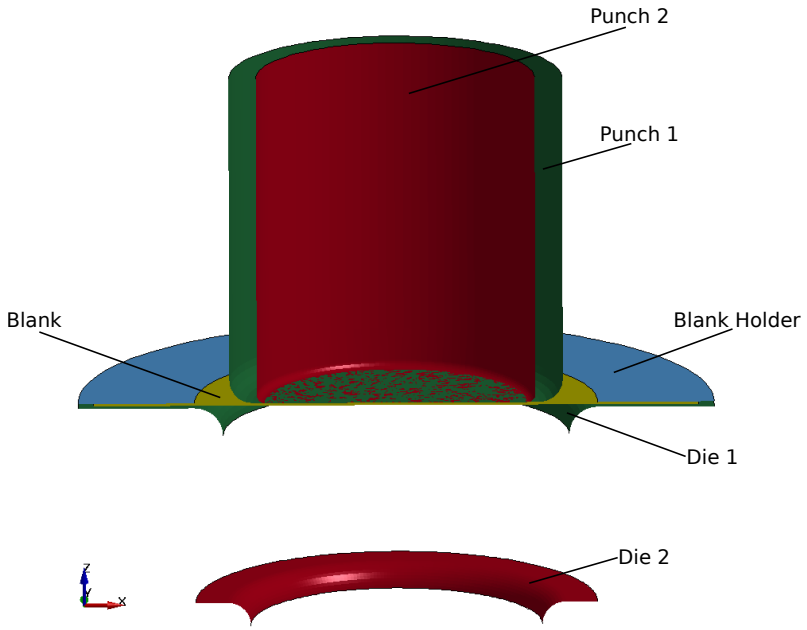

Figure 10.3. The numerical model for the deep-drawn cup is presented, the green parts are the punch and die for the first operation, the red are for the second drawing, the blue is the blank holder and the yellow for the blank.

In the final phase of the simulation, the model is switched to an implicit solver, which brings the cup into a steady state phase, which allows the cup to perform springback. Hereafter the cup is saved in a dynain file, which will be used for the VSR treatment, this file contains the deformed cup together with the stresses and strains.
This model is constructed without any symmetry conditions, since the cups frequency modes would be influenced by these.

Residual Stresses in Deep Drawn Cup

In order to perform the desired VSR treatment, an initial investigation upon the location and magnitude of the residual stresses are performed in this section. There are three stress components, which are interesting to investigate: The axial-, hoop- and radial stresses. The magnitude of these residual stresses in the cup wall can be seen on figure 10.4. It is clear that the radial stress are negligible, since the magnitude of the hoop and axial stresses are significantly higher(If elements were vertical, the stress should be identical zeros due to the use of shell elements). The region with the highest stresses are located in the top half of the cup wall, which is the region that are most desirable to stress relief.

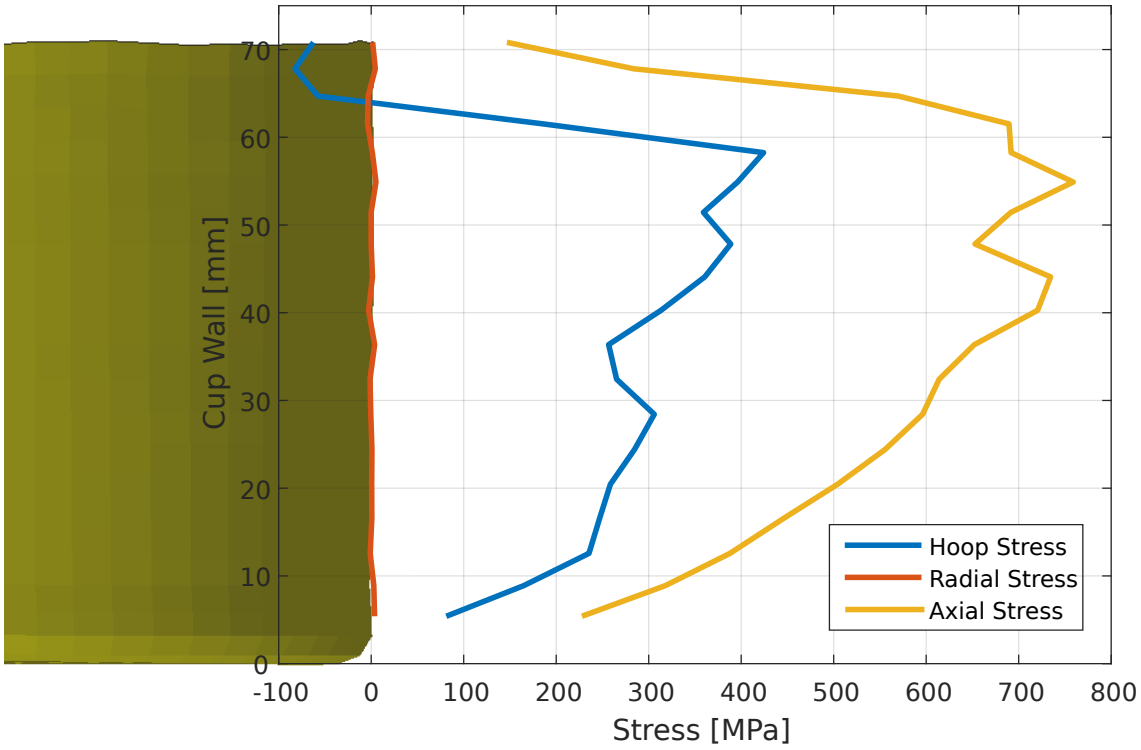

Figure 10.4. The stress components, Hoop, Radial and Axial, for the cup walls middle integration point.

10.3.2 VSR Model

It is desired to find the eigenfrequency of the cup, in order to achieve the benefits of the resonance. Therefore an initial eigenvalue analysis is performed, where the 100 lowest eigenvalues are found. Each eigenvalue mode are investigated in order to find the one most suited for relieving the highest residual stresses. The criteria are to affect the cup rotationally symmetric and to reach the highest stress peaks in the region with the highest axial and hoop stresses.

In order to minimise the number of possible eigenfrequencies that affects the cup wall, some boundary conditions are applied on the cup. The bottom and the associated first 5 mm in the bottom of the cup wall are all locked in x, y and z translation, based on previous experience with the model. Based on the analysis, two eigenvalues are selected for the initial VSR treatment. The modes can be seen on figure 10.5 and figure 10.6, the eigenvalue are $16\,023\,\mathrm{s}^{-1}$ and $18\,700\,\mathrm{s}^{-1}$, respectively.

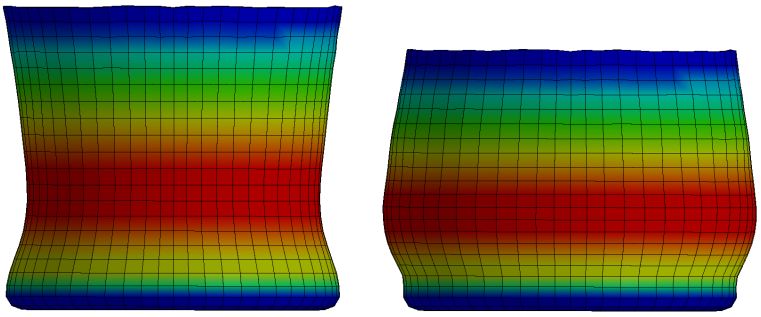

Figure 10.5. No. 41 eigenvalue mode found from the eigenvalue analysis. The red part has the largest equivalent stresses and the blue part is approximately zero.

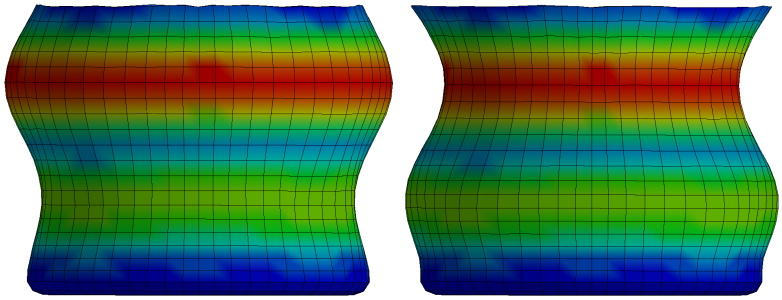

Figure 10.6. No. 55 eigenvalue mode found from the eigenvalue analysis. The red part has the largest equivalent stresses and the blue is approximately zero.

For these initial tests the model is applied a cyclic load, the VSR treatment, which is performed with an explicit solver, which allows the system to accumulate the amplitudal stresses. When this phase is done, the loading is terminated, and when the the system relaxed(By some applied mass-damping), it is switched to an implicit solver, where the velocities of the system is forced to zeros, and the system reaches a steady state level. When the system is at steady state, then the residual stresses are evaluated.
The loads are applied to the model with the loading function, which can be seen in equation 10.1, where F_0 is the load and F_t is the applied load at the given time.

$$F(t) = F_0 \cdot \sin(2\pi \cdot 16023 \cdot s^{-1} \cdot t) \tag{10.1}$$

10.3.3 Eigenvalue: 16023

For this initial investigation, the load F_0 has been tested for three cases,30 N, 25 N and 20 N, where the load is applied on the top nodes. The hoop and axial stresses are examined, in order to determine their influence. This can be seen on figure 10.7 and 10.8. It can be seen that the region where the largest stresses are applied, approximately 50-20 mm, the stresses are minimised the most. By looking at the hoop stresses, the load at 30 N are causing the tensile hoop stresses to become compressive, and for the two other cases the tensile stresses are minimised and approaching zero. For the axial stresses, the three loading cases minimises the residual stresses in the region of the largest stresses, but for

the 25N and 30N loads the maximal axial residual stress are increases after the VSR treatment, which is highly undesirable.

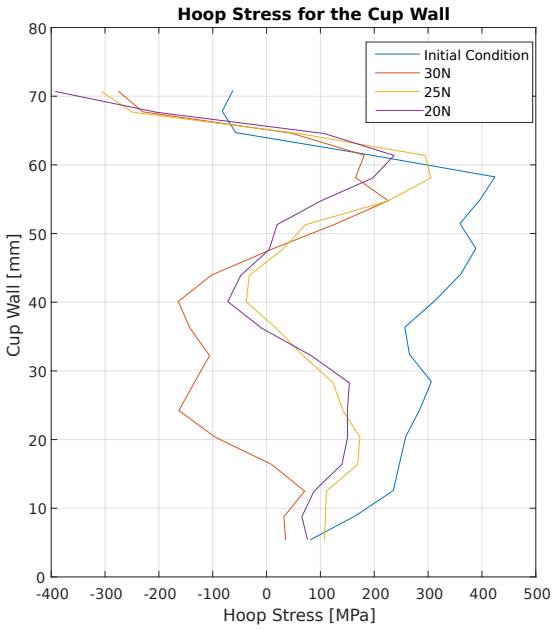

Figure 10.7. Hoop Stress for the cup wall for the three loads.

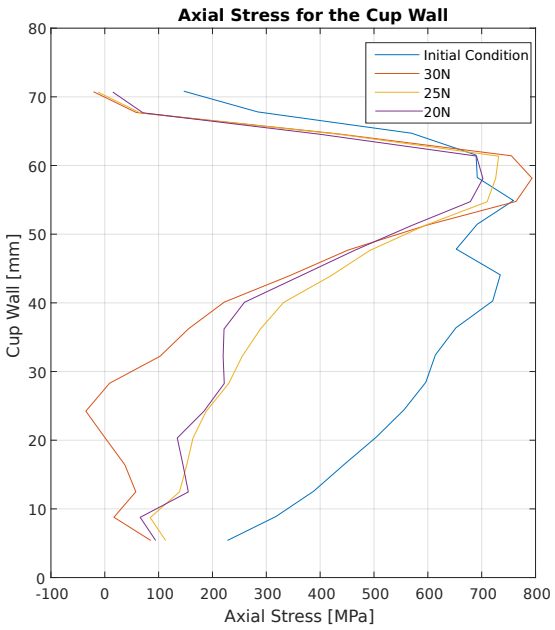

Figure 10.8. Axial Stress for the cup wall for the three loads.

Based on the initial study, it can be observed that the VSR treatment are minimising the residual stresses in the region with the largest stress amplitudes, see figure 10.5. However, for some of the largest tested load, the maximal residual stress found in the cup are increased, and therefore the most critical stresses in only limited reduced. This indicates that a too large applied load can cause an worsening of the residual stress condition. Therefore it is clear that the load is very important, our initial studies has also shown that the no. of cycles is an important factor as well, especially when the resonant VSR treatment is applied, due to the growth of the vibrational amplitudes (Appendix A).

10.3.4 Eigenvalue: 18700

For this eigenvalue, relating to figure 10.6, the loads are applied in a set of elements in the bottom half of the cup. This is done, since the top nodes in this mode are displaced and rotated, and therefore the loading would be extremely difficult to model. For this mode the largest stress fluctuations are experienced in the top half of the cup, where the largest residual stresses initially are located. Therefore the hypothesis is that the residual stresses would be minimised in this region.
For this case the hoop and axial stresses will be examined and three different loading is applied as-well, however, for this loading, the load is applied on shells sets, and therefore the applied value is a pressure, therefore the three loads are as follows 15 MPa, 20 MPa and 25 MPa. For these three load cases, the hoop stresses and axial stresses can be seen on figure 10.9 and 10.10, respectively. It should be noted, that this applied loading is quite large, but similar studies has been performed for loading at 10 MPa, which showed small

influence, this could be due to the vibrational amplitude growth periode, which where too short for this loading.

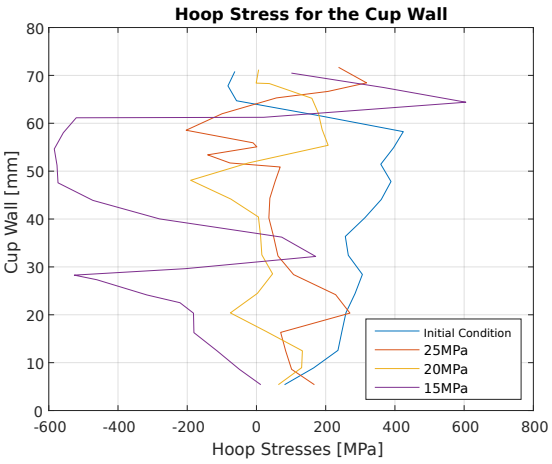

Figure 10.9. Hoop Stress for the cup wall for the three loads.

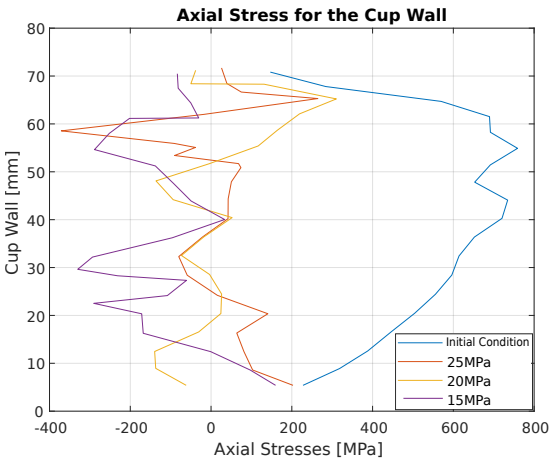

Figure 10.10. Axial Stress for the cup wall for the three loads.

10.4 Optimisation Approach

Optimisation of the VSR treatment is not a common approach in the academic community, however, this case has been made in an effort to develop a method to obtaining the optimal conditions. For this case, a previously defined frequency mode is selected, and will as such not be one of the design parameter. Because, the search for resonant frequency modes will be challenging for the optimisation algorithm. Therefore the aforementioned eigenvalue analysis is utilised, and used to determine the mode at which the highest residual stresses are affected the most.

10.4.1 Objective Function

The objective for this optimisation is to minimise the residual stresses in the cup wall. By observing figure 10.4, it can be seen that the axial stresses have the highest stress levels, and therefore these should be used for the residual vector. 19 shell elements with 7 integrations points along the height on both sides of the cup are used for the objective function, which mean that the residual vector consists of 238 values. By formulating the objective function as such, the initial function will be in the magnitude of billions, which will result in large gradients, which might affects the algorithms negatively.
Therefore another approach would be desirable, in order to evaluate the entire stress condition and get a lower cost function value.

10.4.2 Design Parameters

The number of cycles are one of the important factors in this process, together with the load applied on the part. These two components are to be selected as design parameters.

10.5 Results and Discussion

In this section, the two different frequency modes will be further examined, and discussed in terms of which are most desirable and how this can be evaluated.

As presented earlier in this project, sheet metal forming operations are normally evaluated by using a FLD for the formed component, which can described the different conditions in the formed part e.g. wrinkling or thinning. This method is also consisting of some pitfalls, such as strain path dependence, where a FLSD, Forming Limit Stress Diagram, are more suited for the purpose of this case. The FLSD is well suited for showing the current stress state for the cup, and therefore a comparison between the initial state and after the VSR treatment are very interesting. For the following FLSDs, all the elements in the cup are included, the maximal principal stress and the second principal stress are extracted from the d3plot file and plotted in Matlab, since the FLSD function does not exist in LS-PrePost.
In table 10.3, the mean FLSD results are summarised for the 6 different tests and for the initial conditions. On figure 10.11, 10.12 and 10.13, the FLSD is presented for the frequency mode with the eigenvalue at 16023 for the loading 20 N, 25 N and 30 N, respectively. The frequency mode with the eigenvalue at $18\,700\,\mathrm{s}^{-1}$, the FLSD is presented on figure 10.14, 10.15 and 10.16, for the loading at 15 MPa, 20 MPa and 25 MPa, respectively.
From table 10.3, it can be seen that the initial condition is experiencing a bi-axial tensile stress condition.

Table 10.3. The mean values from the FLSD's for the 6 different VSR treatments are summarised and compared with the initial conditions mean FLSD.

VSR Treatment	Major Stress	Minor Stress
Initial Condition	302.63 MPa	146.01 MPa
20 N	315.39 MPa	39.96 MPa
25 N	242.82 MPa	49.11 MPa
30 N	238.56 MPa	45.22 MPa
15 MPa	125.52 MPa	−6.81 MPa
20 MPa	139.24 MPa	2.73 MPa
25 MPa	159.39 MPa	−10.07 MPa

The frequency mode with the eigenvalue at $16\,023\,\mathrm{s}^{-1}$, the three different loading condition can be seen on the following figures, 10.11, 10.12 and 10.13. Generally for this frequency mode, the points are minimised in the minor stresses, and therefore moves towards the major axis. This indicates that the cup is changing from a multi-axis tension condition towards uni-axial tension. Another interesting observation is that 0n figure 10.11, the major stress is hardly changed, which shows that the points are moving towards the zero minor stress. For the two higher loadings, figure 10.12 and 10.13, the points are similarly minimised in the minor stress, but are also starting to be minimised in the major stress. This might indicate that this frequency mode are affecting the relieving behaviour for the minor stress. This can also be seen in the mean value for FLSD's in table 10.3, and on the figures, where the change in the means values are represented with a green arrow.

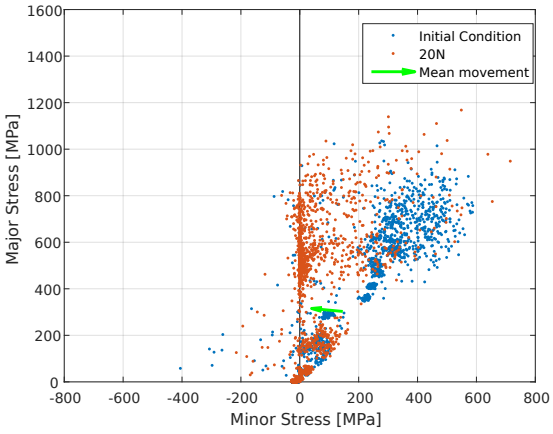

Figure 10.11. The FLSD for the initial condition of the cup and after the VSR treatment for the frequency mode with the eigenvalue at $16\,023\,\mathrm{s}^{-1}$ and load of 20 N, the green arrow represents the change in the mean values.

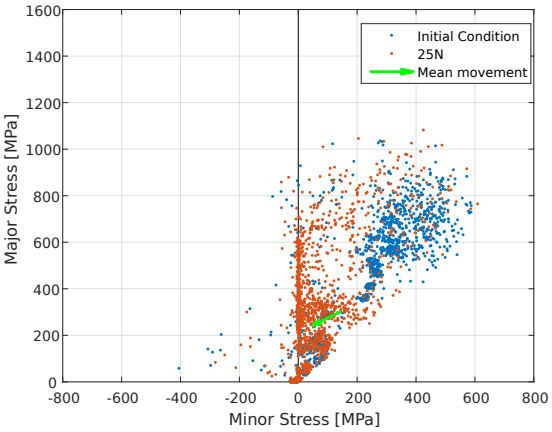

Figure 10.12. The FLSD for the initial condition of the cup and after the VSR treatment for the frequency mode with the eigenvalue at $16\,023\,\mathrm{s}^{-1}$ and load of 25 N,the green arrow represents the change in the mean values.

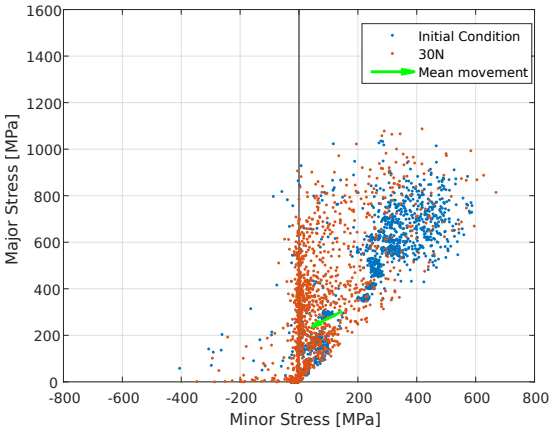

Figure 10.13. The FLSD for the initial condition of the cup and after the VSR treatment for the frequency mode with the eigenvalue at $16\,023\,\mathrm{s}^{-1}$ and load of 30 N, the green arrow represents the change in the mean values.

The frequency mode with the eigenvalue at $18\,700\,\mathrm{s}^{-1}$, the three different loading conditions can be seen on the following figures, 10.14, 10.15 and 10.16. Generally for this frequency mode, the points in the FLSD are moving towards zeros for both the minor and major stress, which can also be seen on the mean values, see table 10.3. However, by comparing the FLSDs for this frequency mode to the other frequency mode, the points at this mode are moved into the negative minor stress, which indicates that the elements are moved from being in tension towards being in compression. By introducing compressive stresses, the possibility of obtaining wrinkling like behaviour in the cup is more likely, however, it is still unknown if the magnitude of the loading is the cause of this increase in elements experiencing compressive stresses, but this might be worth investigating.

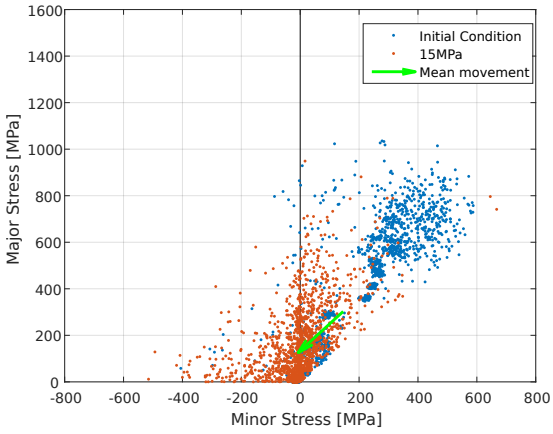

Figure 10.14. The FLSD for the initial condition of the cup and after the VSR treatment for the frequency mode with the eigenvalue at $18\,700\,\mathrm{s}^{-1}$ and load of 15 MPa, the green arrow represents the change in the mean values.

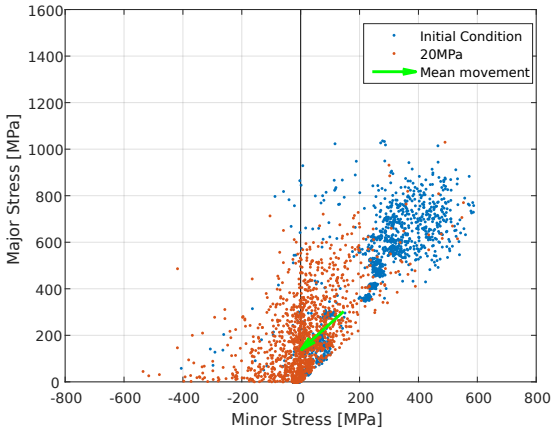

Figure 10.15. The FLSD for the initial condition of the cup and after the VSR treatment for the frequency mode with the eigenvalue at $18\,700\,\mathrm{s}^{-1}$ and load of 20 MPa, the green arrow represents the change in the mean values.

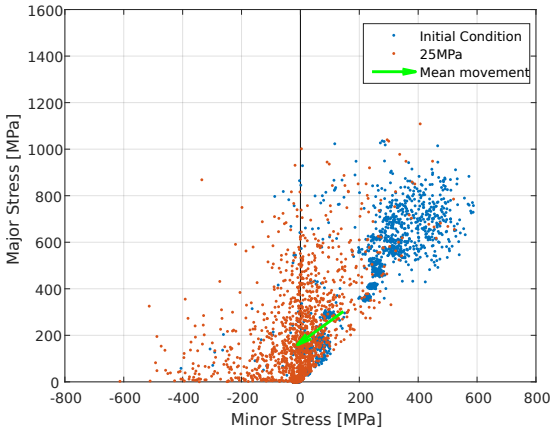

Figure 10.16. The FLSD for the initial condition of the cup and after the VSR treatment for the frequency mode with the eigenvalue at $18\,700\,\mathrm{s}^{-1}$ and load of 25 MPa, the green arrow represents the change in the mean values.

It was observed for this last frequency mode, that the cup geometry changed during the treatment, the bottom half of the cup was deformed such it moved inwards, which can be seen on figure 10.17. This could be caused by different behaviours, such as the magnitude of the loading or the introduction of compressive stresses, but the specific cause is not determined.

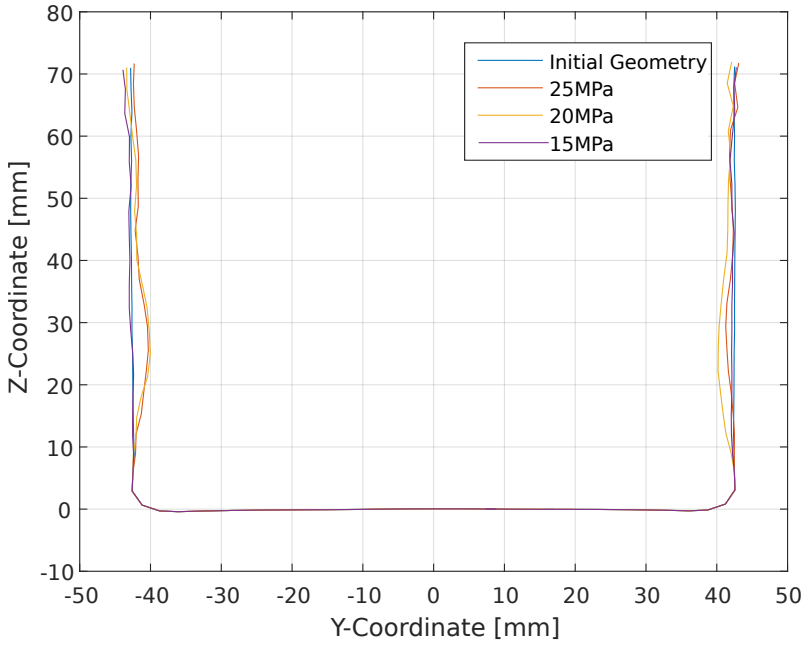

Figure 10.17. The geometrically change in the VSR treated cup at the frequency mode with the eigenvalue at $18\,700\,\mathrm{s}^{-1}$, it can be seen that the two highest loadings are making the bottom half of the cup wall move inwards.

10.6 Sub-conclusion

This chapter is based on applying the Vibrational Stress Relieving (VSR) process on a complex deformed part, based on the Paper in Appendix A. A deep drawing example by Danckert [28], was used for making a part which contains large residual stresses. This deep drawing operation is then modelled and a deformed cup containing residual stresses are produced, the largest residual stresses are located in the top half of the cup.
Based on the Paper in Appendix A, it was concluded that the selection of frequency mode is crucial for relieving the desired residual stresses. Two frequency modes were found by using a build-in eigenvalue analysis in LS-DYNA. The load were varied in order to determine their individual influence, for these two modes. A FLSD was constructed, in order to determine how the residual stresses are influenced by these modes and loads. From the FLSDs it was observed that these could be used to determine the general relieving pattern for the process.
The boundary conditions applied to this cup are relative unrealistic. In the Paper in Appendix A, it was found that the correct boundary conditions are crucial for the stress relieving behaviour, in order to achieve the desired mode.

it is very desirable to develop an optimisation approach in order to determine the optimal settings for this process. It is concluded that the design parameters for the process should be the number of cycles for the treatment, and the applied load. It is further discussed that using the optimisation for determining the correct frequency mode will be very difficult and should therefore be determined the by engineer.
The main challenge with applying optimisation to this problem is the formulation of the objective function, the current idea is to sum up all the stresses in a section which is desired to relief. Another approach, which has not been tested, could be to formulate the

objective function using the FLSD approach.

11 Framework

Six cases has been devised in order to develop and determine the important attributes of the proposed framework(see figure 2.1 on page 16). The proposed framework consists of five parts: Purpose, Process, Modelling, Optimisation and Results & Discussion. These five parts will be presented in each individual section in this chapter, where the acquired knowledge and experience from the cases are used to formulate, some guidelines and considerations that are important when deploying this approach. The revised framework is presented on figure 11.1.

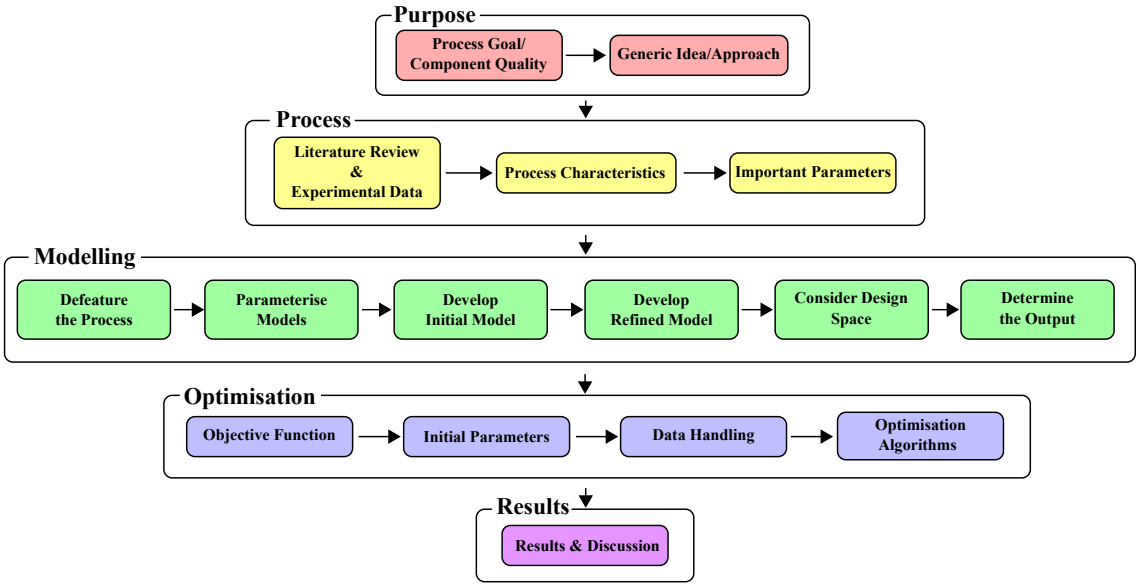

Figure 11.1. The revised framework, based on the knowledge found through the six cases.

11.1 Purpose

The initial phase, for this framework, is to determine the purpose of modelling and optimising the given problem. This part is possibly the most important part, since the subsequently stages are highly influenced by the formulated purpose. The different stages of defining the purpose, are presented on figure 11.2, and will be explained in the sections to follow.

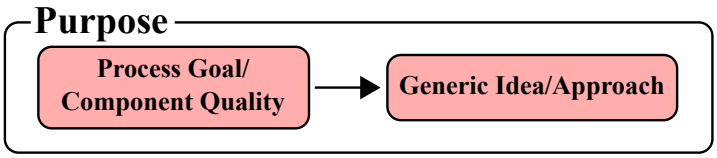

Figure 11.2. Sub-framework of the purpose section, split into two boxes.

Process Goal or Component Quality

Exploring the solutions space, and selecting the correct process goal or component quality identifier, is a critical decision which has to be made. If the correct purpose and focus of the remaining work is identified the following phases will be more targeted, resulting in finding the correct solution, parameters and/or process. If the incorrect process goal or quality identifiers are selected´, the result can be rather useless.

Generic Idea/Approach

Before resources are put into literature reviews or experiments are conducted, it is useful to formulate a generic approach to solving the challenge. A generic idea/approach can be formulated as a quick evaluating of the process or component in question, where the known knowledge is documented before a thorough study is conducted. By documenting what is known, and what is unknown, it is possible to target the literature review and explored solution space on a focused topic or subset of processing methods. It also worth considering if an optimisation approach will improve the current state, or another approach is more feasible.

It is extremely important to not limit the reviewed process or solution space to what is already known, and ensure that new and experimental technology/methods are also considered.

11.2 Process

This section will present an approach for understanding the selected process. It is in this phase, where the solution strategy is formed, and the ideas are generated in order to solve the problems. The different steps, presented on figure 11.3, will be elaborated in the following sections.

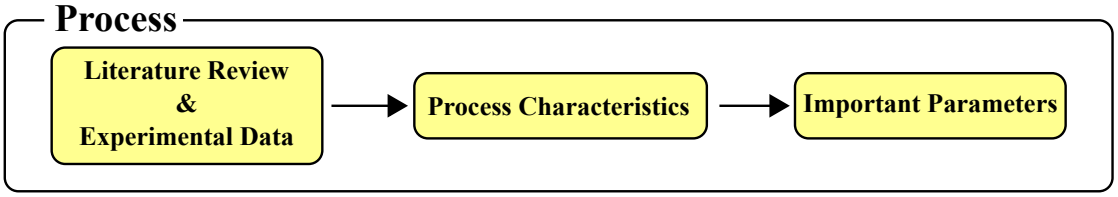

Figure 11.3. Sub-framework of the process section, split into three boxes.

It is important to keep in mind, that if the previous academic work, or experimental work, for the current process is not sufficient, then this phase can require that the desired

knowledge is created, such as for the VSR part in this report, see Appendix A for the paper.

Literature Review and Experimental Data

The duration of this phase is highly dependent on the previous knowledge about the selected process. If this is a new process, this phase should be fairly thorough, but if the process is similar to previously obtained knowledge, this phase can be less cumbersome. However, no matter the previous knowledge, it is important to determine if a similar optimisation is documented and what are the results and approach. This method is utilised in the presented cases, in Chapter 6 a publication by Wang et al. [51] was used and a similar optimisation was performed, this was used as offset for that case.
If any experimental data is acquired/obtained, this can be used for a validation of the numerical model. Furthermore, if the literature review does not give sufficient data, a structured experimental approach can be beneficial.

Process Characteristics

Based on the literature review and/or experimental data, the process characteristics can be pinpointed. The aim with this part is to locate the advantages and limitations of the process, and thereby evaluate if the defined purpose can be achieved with the selected process. By assessing this early in the process development phase, it is possible to modify the process selection, to a more suited one.
This method was used in Chapter 9, the Airbus A380 door corner piece, where a hydroforming process is used on the blank for an area, which is not fully enclosed. Therefore a dummy blank is introduced, such this process can be achieved.

Locate Important Process Parameters

After determining the process characteristics, a similar phase for establishing the important process parameters shall be performed. The aim of this phase is to locate possible design parameters of the process, which can be adjusted to change the process outcome. Bonte et al. [39], proposed a screening process, where e.g. the input parameters for the numerical model are tested to find the ones which influence the desired output.
This phase is used in all cases, either by finding the parameters through the literature review or by initial tests with the model. It is important to establish both the parameters which improve the process and the ones that can worsen it.

11.3 Modelling

When modelling a sheet metal forming operations, there are different modelling approaches to consider, depending on the desired output. Whether the model should be calculated explicit, implicit or even a combination, which contact models are best suited, how the tool should be modelled, etc. Theses are all decision, which has to be made in order to develop a valid model. All the modelling decisions made throughout this project is based on recommendations from the literature, guidance from professors and experience with process modelling. In this section, some of the experiences with modelling simulations for

optimisation are presented as guidelines, for setting up such problems. On figure 11.4, the approach for constructing a numerical model, which should be used for optimisation, is shown. These six steps are elaborated in the following sections.

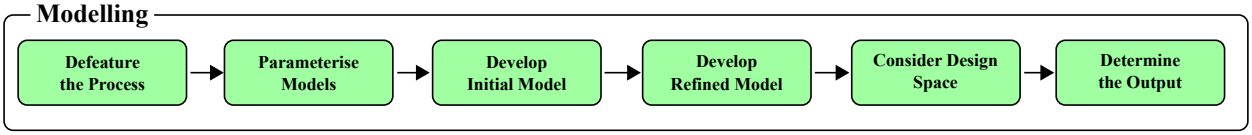

Figure 11.4. Sub-framework for modelling, consisting of six boxes.

A common and recommended stage in process modelling is verification, in the cases presented this is not performed. When utilising process simulations and optimisation this step is a must, before major decisions are made about a manufacturing setup on the bases of the simulation results. Verification should be performed in conjunction with development of the initial/refined model and on the optimised parameters, if possible.

Defeature the Process

A general practise is to defeature the process, such only the important feature are present in the simulation, hence the importance of considering the desired output. Defeaturing reduces the amount of parts, which have to be modelled, parts that can cause problems and will generally lower the computational time.
A technique used in all presented cases, is to assume that tooling parts are rigid and that the processes can be modelled as a quarter with symmetry axis, except the VSR cup. Over defeaturing, has to be considered when evaluating the results of the simulation as information and process effects can get lost, if too much of the process is removed.

Parametrise Geometries

After defeaturing the process, modelling of the geometries has to be performed. It is recommended to draw the different parts, using a parameterised method, e.g. a auto-generation script. Scripts makes remodelling easier, if a tool optimisation is desired or errors have been made, as the geometries are already formulated with variables.

The LS-PrePost drawing/meshing tool, Block Mesher, was used for the parts which could be symmetrically defined. The Block Mesher made it possible to ensure that a part had the desired mesh and number of elements/nodes, that in the cases where this element/node data was exported, was formulated correctly. A guide/description of the Block Mesher tool is located in Appendix B, along with a script used for the last punch in the Fins Manufacturing case.

Develop Initial Model

When starting out building a numerical model, it is highly recommended to start-out with a fairly simple model, also known as a debug model. This model has to act as a trial-and-error model, where the calculation time is relatively short, and the element mesh are relative coarse. This method has been used in the development phase for all the

cases, where e.g. in Chapter 5 a coarse model was developed, in order to modify the die positioning, since changing the previous step could affect the following process.
A recommendation is to used the **include* function in the keyword file, which makes it easier for a later refinement of the different parts.

Develop Refined Model

When a model is considered to be debugged, a refinement of the "blank"-part can be performed. Hereafter a couple of things has to be further evaluated, first of all, it is important to examine the influence from the mass-time-step scaling upon the new blank. If the mass is drastically changed, the model might change its response, and therefore corrections has to be made. It should also be assessed, if the selected refinement improves the output desirably, compared to the increased calculation time.

Consider Design Space

It is very important to consider all the possible solution for the numerical model, before setting up the optimisation. This is especially necessary when using the tool geometry or punch displacement as design parameters, since a proposed change in these might result in initial penetration, which can lead to unrealistic result or error termination. In Chapter 6, this consideration was implemented for the two punch displacements, where a constant distance between the two parts were applied.
Another example of applying limitations to the design space was in Chapter 8, where a sensor-switch was implemented to increase the robustness of the model.

When considering the design space, it is important not to limit the feasible design space, but only remove the infeasible region. The aim is to increase the models robustness in an optimisation, and not to limit the possible solutions.

Determine the Output

The final stage before setting up the optimisation, is to determine the desired output from the numerical model. It is important to select the correct sampling rate, and the desired output format.

11.4 Optimisation

The construction of an optimisation for a numerical model is in this project done with a non-linear least-square formulation, and a java-script to perform the calculations. The proposed framework for the optimisation part can be seen on figure 11.5, and are elaborated in the following.

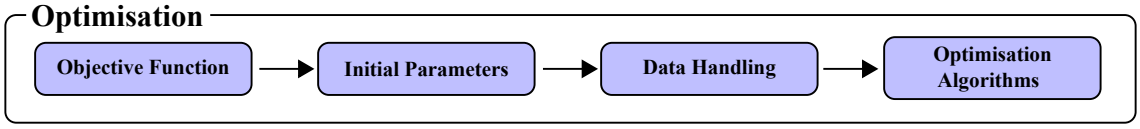

Figure 11.5. Sub-framework for optimisation, which contains the four step done when formulation an optimisation.

Objective Function

When defining an objective function, the most important attributes to consider is whether or not an improvement is actually represented in the objective function. It can be beneficial to test the objective function, by testing the model at two or more different settings and determine if the improvement is represented in the objective function value. If not, a reformulation is necessary.

Throughout the six cases, three different objective function types has been deployed, geometrically, thickness and contact force.
The **geometrically objective** is constructed as the shortest distance to a desired surface, for the extracted nodes in the numerical model. Each nodal points distance to a given surface is calculated and stored in the residual vector, so when the distance becomes shorter, the objective function decreases. A pitfall with this formulation is when using shell elements, the thickness offset is important to take into account, which is half the shell thickness.
The **thickness objective** has been applied as a way to minimised the possibility of fracture, and achieving a more uniform thickness distribution. This objective function is achieved by extracting the thickness strain from the element data, based on the desired region of interest. In the cases where this objective is used, the desired thickness is formulated as the initial thickness, which implies that the thinning should be as small as possible.
The **contact force objective**, was used as a maximisation problem. In order to formulate this problem as a minimisation, the contact force is inverted, and to avoid the possibility of obtaining a denominator which is zeros, one is added to the denominator.

The three presented objective functions types are throughout this report combined as needed to optimise the desired aspects of the given problem.

Start Parameters

The start parameters has through this project proved to be a very important setting for the optimisation. In Chapter 8, the hydraulically expanded tube-tubesheet joint, the importance of selecting the correct start parameter is very demonstrable. Where a selected starting point outside the obtained contact region (contact force equal to zero), would cause the optimisation to terminate.
It is impossible to setup a specific guideline for selecting the proper start parameter values, the selection is often based on engineering intuition[94]. It is always desirable to select a the start parameters for a known feasible region, but for some optimisation it can be a poor selection, if the optimisation gets stuck in a local minimum. It can be necessary to

change the starting parameters if the optimisation terminates or if the reached optimum is suspected to be non-feasible or a local minimum.

Data Handling

In order to control the input and output data from the simulation, it is vital that data handling is performed in a robust manner. This is especially important when using automatic optimisation, where the input and output is not visually inspected by the user.
The used optimisation code is an external Java based script, which has to interact with the LS-DYNA/LS-PrePost syntax. The input parameters to the model is formatted in the Java script, in order to achieve the correct syntax, which is inserted in the keyword file. This method is generally robust, but for the tool optimisation it is necessary to generate a script, which calculates the coordinates for the different points/section. These points are inserted in a .cfile script which is run with LS-PrePost to build the new geometry.

Regarding the output from the simulation, the extraction method is influencing the robustness of the optimisation. The final state in the simulation is used as the evaluation value, therefore the data extracted is always in the bottom of the output file. Papers discuss the used of filters on the output data, in order to minimise any numerical errors or instabilities. The application of data filtering is a often used approach in optimisation of sheet metal forming processes [44, 95], this is either used to limit the amount of numerical noise or for inverse modelling approaches where noise is present on the empirical data. This filtering approach is often vital for curve fitting, e.g. where the punch forces for deep drawing is used, the filter method is great for improving the convergence behaviour of the optimisation algorithm. Filtering has not been utilised, for this project, due to the cases presented, but it is important to consider, when setting up an optimisation.

Algorithms

In this project, the optimisation algorithms are used as a tool for performing the optimisations, the theory behind these algorithms are not the main scope and is therefore not discussed in depth. This part is mainly used as a "black box" approach, where the main objective is to setup the optimisation and not formulate/programme the algorithms. The utilised algorithms are all gradient based, due to the developed Java code[44]. This means that this projects approach is not only applicable for gradient based algorithms, but can also be applied on other algorithms, since it is the formulations of the problems and the modelling approaches, that are crucial for the optimisation.
However, the importance of robust algorithms should not be neglected, since a specific algorithm can have different behaviour for different problems. This also relates to the settings for the algorithms, where for some cases, an initial trust-region had to be set or as for Chapter 8, hydraulically expanded tube-tubesheet joint, the optimisation criterion had to be change, due to the magnitude of the objective function.

11.5 Results and Discussion

When the optimisation is terminated and an optimum is found, it is necessary to evaluate if the obtained results are actually the desired results. There are various methods to asses the outcome from the optimisation. First of all, the cause for the termination, has to be assessed if the optimisation is caught in a local minimum, or if the objective function is converged. If the optimisation behaviour seems to be stuck, the algorithm has to be modified or the start parameter values has to be changed. If the optimisation is converged to what looks like a global minimum, it should be check if the optimised simulation seems to be realistic, and are there any non-physical phenomenons.
The feasibility of the optimum design has to be checked. The method to check if the reached optimum is possible is very process dependent, the most common approach throughout this report has been to evaluate the thickness, and asses the thinning. However, it is also possible for one step forming operations to use FLD, or for multi-step forming operations to use FLSD, to determine if the solution would result in any defects.

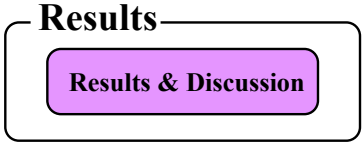

Figure 11.6. Sub-framework of the results and discussion section.

12 Conclusion

The main purpose of this project is to develop the foundation, which can be expanded by others, of a framework for automatic optimisations of sheet metal forming simulations, in order to improve the efficiency of research and process design. Six individual cases has been conducted, with the aim to develop a numerical model and perform an automatic optimisation of this. Based on these cases, the following framework, consisting of Purpose, Process, Modelling, Optimisation and Results & Discussion, is proposed:

Purpose

This is the initial phase, where the problem is defined and the desired goal is described. This phase emphasis on the generic idea/approach, where the general feasibility and opportunities are evaluated.

Process

The second phase is about acquiring as much knowledge on the selected process, where a literature review/ experimental data is very important. This will be the foundation for determining the process characteristics and the possible design parameter for the optimisation.

Modelling

When modelling for an optimisation, it is found to be very important to defeature the process to only consists of the things, which are of interest in the optimisation. A initial parameterisation is required, for developing an initial coarse debugging model which can later be refined. It is important to consider the solution space of the optimisation, in order to improve the robustness of the model, to avoid possible simulation technical error. Finally, the output from the numerical model should be considered, and determine if it represents the results.

Optimisation

In this project the least-square formulation is utilised, and three different objective functions are developed throughout this project: A geometrical, a thickness distribution, and a contact force. It is important to consider if the objective function represents an improvement by minimising the objective function. Hereafter the initial parameters has

to be selected, it is recommended to select those in a known feasible region based on engineering intuition. Data handling is to be considered, in order to utilise the correct syntax and evaluate the data in a robust manner. Finally, the desired optimisation algorithm should be selected.

Results & Discussion

This final phase emphasis on evaluating the reached optimum, by checking the feasibility of the solution, together with the termination criteria. It is important to asses the optimum, in terms of: If the reached optimum desirable and feasible?

The six cases conducted is this project, can be divided into two categories: Research and Process Design, and will be elaborated in the following.

Research

Two cases are used for developing research: Hydraulically Expanded Tube-Tubesheet Joint and VSR treatment of Deep Drawn Cup.
The aim of the Hydraulically Expanded Tube-Tubesheet Joint case, were to utilise the framework to develop research. The automatic optimisation tool was used to find the optimum for a 7 different settings, where the yield stress relation between the tube and tubesheet was found to be highly influencing upon the resulting contact force.
For the VSR treatment of Deep Drawn Cup case, the process fundamentals are described in a Paper in Appendix A, it was found that the residual stresses can be relieved by resonant vibration treatment, when the stress amplitudes reaches the materials yield stress. This theory are then applied on a deep drawn cup, where different eigenfrequency modes are tested and evaluated using a forming limit stress diagram inspired approach, this evaluation method looks promising, for possible optimisation.

Process Design

Two optimisation approaches are used for the process design, where either the tool or the process settings are optimised. A tool optimisation was deployed in the Fins Manufacturing at Vestas Aircoil A/S and the Airbus Corner Piece cases.
In the Fins Manufacturing case, the radius of the punch is optimised to achieve a more flat flange, and in the Airbus Corner Piece case a new hydroforming die is developed and optimised, in order to minimise the springback.
The hydraulic pressure and the two punch displacement was used as the design parameters, in the two bulging-pressuring compound forming cases. This process showed great potential for achieving radii far smaller then what is possible with conventional hydromechanical or deep drawing processes.

13 Perspectives

This chapter, contain reflections upon the work conducted in the report in relation to possible future work.

Fins Manufacturing at Vestas Aircoil A/S

It would be of great interest, for this case, to develop an optimisation approach for the five first steps in the fin manufacturing, which would possibly be able to increase the formability and freedom of the final fin geometry. The objective could be to increase the height of the final bulge before the trimming operation, together with an objective of minimising the thinning of the blank. The design parameters for an initial approach could be the vertical position of the five punches.

Small Radii Cup

In the bulging-pressing compound forming process for producing the small radii cup, it would be interesting to increase the desired depth of the cup, and thereby investigate if this would affect the optimisation and/or the manufacturing process. This will also be the bases for a investigation upon the process limitations, for determining if there are pitfalls e.g. for the draw depth of the cup.

Small Radii - Lunar Rover Test Piece

It would be interesting to develop an approach of improving the thickness distribution of the formed cup. This could be by changing the die and/or punch geometries, such the material flow would improve. It could also be by further investigating the applied pressure in the first hydromechanical deep drawing operation, where the optimisation found the pressure to be negligible/zero.

Hydraulic Expanded Tube-Tubesheet Joint

The tubesheet geometry was modelled as a rotationally symmetric, it would be interesting to investigate how the tubesheet geometry influences the obtained contact force. This could be investigated by utilising the correct tubesheet geometry presented by Alexouli

et al. [64], and then apply a penalty into the objective function, where any change in the nearby tubesheet holes are penalised.

Airbus A380 Door Frame Corner

Springback of the corner part was minimised by introducing a new hydroforming die, however, the corner piece still experiences springback. Therefore a parameterisation of the punches in the final stamping process, could be used as additional design parameters for the optimisation.

VSR - Deep Drawn Cup

It would be interesting to develop and perform an optimisation, upon the deep drawn cup. The proposed design parameters would be used, the main challenge would be to develop an objective function, which would be able to evaluate the treatments relieving behaviour. An objective function formulation could be to utilise the FLSD like approach presented, and use the mean value as the objective to be minimised. Furthermore, it should be considered whether the geometrically change, caused by the treatment, should be included in the objective function.

Framework

It would be beneficial to develop an improved geometrical objective, where an entire CAD model can be used as the objective. By developing such an approach, the geometrical optimisation of complex parts would be easier to implement and thereby faster to develop an optimum solution.

Bibliography

[1] Nazim Baluch, Zulkifli Mohamed Udin, and Che Sobry Abdullah. Advanced high strength steel in auto industry: an overview. *Engineering, Technology & Applied Science Research*, 4(4):686–689, 2014.

[2] Miklós Tisza. Recent development trends in sheet metal forming. *Internationl Journal of Microstructure and Materials Properties*, 8(1/2):125–140, 2013. doi: 10.1504/IJMMP.2013.052651.

[3] A. Andersson. Comparison of sheet metal forming simulation and try out tools in the design of a forming tool. *Journal of Engineering Design*, 15(6):551–561, 2004. doi: 10.1080/09544820410001697598.

[4] Karl Roll. Simulation of sheet metal forming - necessary developments in the future. *LS-DYNA Awenderforum*, A(1):59–68, 2008.

[5] A. Makinouchi, C. Teodosiu, and T. Nakagawa. Advance in fem simulation and its related technologies in sheet metal forming. *Annals of the CIRP*, 47(2):641–649, 1998. doi: 10.1016/S0007-8506(07)63246-6.

[6] Benny Endelt, Karl Brian Nielsen, and Joachim Danckert. New framework for on-line feedback control of a deep-drawing operation. *Journal of Materials Processing Technology*, 177:426–429, 2006. doi: 10.1016/j.jmatprotec.2006.04.026.

[7] Z. Marciniak, J.L. Duncan, and S.J. Hu. *Mechanics of Sheet Metal Forming*. Butterworth-Heinemann, Oxford, 2002. ISBN 0-7506-5300-0.

[8] P. Chandrasekaran and Dr. K. Manonmani. A review on springback effect in sheet metal forming process. *International Conference on Systems, Science, Control, Communication, Engineering and Technology*, 01:43–49, 2015.

[9] G. M. Sayeed Ahmed, Hakeemuddin Ahmed, Mohd Viquar Mohiuddin, and S. Md Safi Sajid. Experimental evaluation of springback in mild steel and its validation using ls-dyna. *Procedia Materials Science*, 6:1376–1385, 2014. doi: 10.1016/j.mspro.2014.07.117.

[10] K. Roll, T. Lemke, and K. Wiegand. Possibilities and strategies for simulations and compensation for springback. *AIP Conference Proceedings*, A(778):295–302, 2005. doi: 10.1063/1.2011236.

[11] Karl Brian Nielsen. *Sheet Metal Forming Simulation Using Explicit Finite Element Methods*. Department of Production, Aalborg University, 2000. ISBN 87-89767-69-6.

[12] Stuart P. Keeler. Determination of forming limits in automotive stampings. *SAE Transactions*, 74(Papers 650535—650936):1–9.

[13] Gorton M. Goodwin. Application of strain analysis to sheet metal forming problems in the press shop. *SAE Transactions*, 77(Section 1: Papers 680005–680246):380–387.

[14] H. Améziane-Hassani and K. W Neale. On the analysis of sheet metal wrinkling. *International Journal of Mechanical Sciences*, 33(1):13–30, 1991. doi: 10.1016/0020-7403(91)90024-W.

[15] M. H. Chen, L. Gao, D. W. Zuo, and M. Wang. Application of the forming limit stress diagram to forming limit prediction for the multi-step forming of auto panels. *Journal of Materials Processing Technology*, 187-188:173–177, 2007. doi: 10.1016/j.jmatprotec.2006.11.178.

[16] R Arrieux. Determination and use of the forming limit stress diagrams in sheet metal forming. *Journal of Material Processing Technology*, 53:47–56, 1995. doi: 10.1016/0924-0136(95)01960-M.

[17] V. Uthaisangsuk, U. Prahl, S. Münstermann, and W. Bleck. Experimental and numerical failure criterion for formability prediction in sheet metal forming. *Computational Materials Science*, 43:43–50, 2008. doi: 10.1016/j.commatsci.2007.07.036.

[18] Mehdi Safari, Seyed Jamal Hosseinipour, and Hamed Deilami Azodi. Experimental and numerical analysis of forming limit diagram (fld) and forming limit stress diagram (flsd). *Materials Sciences and Applications*, 2(5):497–503, 2011. doi: 10.4236/msa.2011.25067.

[19] R. Arrieux, M. Boivinb, and F. Le Maître. Determination of the forming limit stress curve for anisotropic sheets. *CIRP Annals*, 36(1), 1987. doi: 10.1016/S0007-8506(07)62584-0.

[20] P. D. Wa, A. Graf, S. R. MacEwen, D. J. Lloyd, K. Jain, and K. W. Neale. On formign limit stress diagram analysis. *International Journal of Solids and Structures*, 42:2225–2241, 2005. doi: 10.1016/j.ijsolstr.2004.09.010.

[21] Kamal Kolasangiani, Mahmoud Shariati, and Khalil Farhangdoost. Prediction of forming limit curves (fld, msfld and flsd) and necking time for ss304l sheet using finite element method and ductile fracture criteria. *Journal of Computational and applied research in mechanical engineering*, 4(2):121–132, 2015.

[22] A.KOCAŃDA and H. SADŁOWSKA. Automotive component development by means of hydroforming. *Archives of civil and mechanical engineering*, 8(3), 2008. doi: 10.1016/S1644-9665(12)60163-0.

[23] Sergey F. Golovashchenko. Method of designing and forming a sheet metal part, May 2008. Patent: US 2009/0272171 A1.

[24] Sergey F. Golovashchenko, Nicholas M. Bessonov, and Andrey M. Ilinich. Two-step method of forming complex shapes from sheet metal. *Journal of Materials Processing Technology*, 211(1):875–885, 2011. doi: 10.1016/j.jmatprotec.2010.01.004.

[25] Z. Zimniak. Problems of multi-step forming sheet metal process design. *Journal of Materials Processing Technology*, 106:152–158, 2000. doi: 10.1016/S0924-0136(00)00607-5.

[26] Taylan Altan and A. Erman Tekkaya. *Sheet Metal forming Fundamentals.* ASM International, Materials Park, OH 44073-0002, 2012. ISBN 978-1-61503-842-8. Chapter 8.

[27] Serope Kalpakjian and Steven R. Schmid. *Manufacturing, Engineering and Technology.* Pearson, 2014. ISBN 978-981-06-9406-7.

[28] Joachim Danckert. Reduction of the residual stresses in a deep-drawn cup by modifying the draw die profile. *CIRP Annals*, 44(1):259–262, 1995. doi: 10.1016/S0007-8506(07)62321-X.

[29] Joachim Danckert. *Analysis of Deep Drawing, Ironing and Backward Can Extrusion: with main emphasis on residual stresses and process robustness.* Department of Production, Aalborg University, 2006.

[30] G. S. Schajer. Hole-drilling residual stress measurements at 75: Origins, advances, opportunities. *Experimental Mechanics*, 50:245–253, 2010. doi: 10.1007/s11340-009-9285-y.

[31] Doral Banabic. *Sheet Metal Forming Processes: Constitutive Modelling and Numerical Simulation.* Springer-Verlag Berlin Heidelberg, 2010. ISBN 987-3-540-88112-4.

[32] A. Makinouchi. Sheet metal forming simulation in industry. *Journal of Materials Processing Technology*, 60(1):19–26, 1996. doi: 10.1016/0924-0136(96)02303-5.

[33] Muhammad Ali Ablat and Ala Qattawi. Numerical simulation of sheet metal forming: a review. *International Journal of Advanced Manufacturing Technology*, 89:1235–1250, 2017. doi: 10.1007/s00170-016-9103-5.

[34] M. J. Finn, P. C. Galbraith, L. Wu, J. O. Hallquist, L. Lum, and T.-L.-Lin. Use of a coupled explicit-implicit solver for calculating spring-back in automotive body panels. *Journal of Materials Processing Technology*, 50:395–409, 1995. doi: 10.1016/0924-0136(94)01401-L.

[35] LSTC. *LS-DYNA KEYWORD USER'S MANUAL - VOLUME II - Material Models.* Livermore, 2016.

[36] D. Banabic, H. Aretz, D.S. Comsa, and L. Paraianu. An improved analytical description of orthotropy in metallic sheets. *International Journal of Plasticity*, 21 (3):493–512, 2005. doi: 10.1016/j.ijplas.2004.04.003.

[37] Dorel Banabic, Dan Sorin Comsa, Matthias Sester, Mike Selig, Waldemar Kubli, Kjell Mattiasson, and Mats Sigvant. Influence of constitutive equations on the accuracy of prediction in sheet metal forming simulation. *Proceedings of NUMISHEET'08*, pages 37–42, 2008. ISBN 978-3-909386-80-2.

[38] Gasper Ganter, Tomaz Pepelnjak, and Karl Kuzman. Optimization of sheet metal forming processes by the use of numerical simulations. *Journal of Materials Processing Technology*, 130-131:54–59, 2002. doi: 10.1016/S0924-0136(02)00786-0.

[39] M. H. A. Bonte, A. H. van den Boogaard, and J. Huétink. An optimisation strategy for industrial metal forming processes: Modelling, screening and solving of optimisation problems in metal forming. *Structural and Multidisciplinary Optimization*, 35:571–586, 2008. doi: 10.1007/s00158-007-0206-3.

[40] J. P. Ponthot and J. P. Kleinermann. A cascade optimization methodology for automatic parameter identification and shape/process optimization in metal forming simulation. *Computer Methods in Applied Mechanics and Engineering*, 195 (41-43):5472–5508, 2006. doi: 10.1016/j.cma.2005.11.012.

[41] Benny Ørtoft Endelt and Karl Brian Nielsen. Identification of constitutive parameters for barlat's 2d criteria by inverse modeling. *NUMISHEET 2002, Proceedings of the 5th International Conference and Workshop on Numerical Simulation of 3D Sheet Forming Processes*, 2002.

[42] Raymond H. Myers, Douglas C. Montgomery, and Christine M. Anderson Cook. *Response Surface Methodology - Process and Product Optimization Using Designed Experiments*. John Wiley & Sons, Inc., Hoboken, New Jersey, 2009. ISBN 978-0-470-17446-3.

[43] David J. Benson. The history of ls-dyna. URL `https://www.d3view.com/wp-content/uploads/2007/06/benson.pdf`.

[44] Benny Endelt. *Least Square Optimization Techniques Applied on Sheet Metal Forming: Inverse Identification of Constitutive Parameters and Optimization of Process Parameters*. Department of Production, Aalborg University, 2003. ISBN 87-91200-18-0.

[45] Claes Rubin Klose, Dennis Bøjesen, Dimitra Alexouli, Georgi Nikolaev Nikolov, and Lisa Rydahl Bøystrup. *Simulation and Experimental Investigation of Roller Expanded Tube-Tubesheet Joint*. Department of Materials and Production, Aalborg University, Aalborg, Denmark, 2017.

[46] Alexander Bendix Krukow Barlo, Sebastian Blegebrønd Johansen, Rahim Ataollahi Eshkoor, and Morten Nør. *Analysis and Optimization of Manufacturing of Heat Exchangers - Production and Processes*. Department of Materials and Production, Aalborg University, Aalborg, Denmark, 2017.

[47] Miklós Tisza and Zsolt Lukács. Numerical simulation of multi-stage deep-drawing. *AIP Conference Proceedings*, 712(1):717–722, 2004. doi: 10.1063/1.1766611.

[48] M. Kawka, T. Kakita, and A. Makinouchi. Simulation of multi-step sheet metal forming processes by a static explicit fem code. *Journal of Materials Processing Technology*, 80-81:54–59, 1998. doi: 10.1016/S0924-0136(98)00133-2.

[49] LSTC. *LS-DYNA KEYWORD USER'S MANUAL - VOLUME I*. Livermore, 2002.

[50] Ding Tang, Dayong Li, and Yinghong Peng. Optimization to the tube-fin contact status of the tube expansion process. *Journal of Materials Processing Technology*, 211(4):573–577, 2011. doi: 10.1016/j.jmatprotec.2010.11.010.

[51] Yao Wang, Karl Brian Nielsen, Lihui Lang, and Benny Endelt. Investigation into bulging-pressing compound forming for sheet metal parts with very small radii. *The International Journal of Advanced Manufacturing Technology*, 95:445–457, 2017. doi: 10.1007/s00170-017-1207-z.

[52] S. H. Zhang, M. R. Jensen, J. Danckert, K. B. Nielsen, D. C. Kang, and L. H. Lang. Analysis of the hydromechanical deep drawing of cylindrical cups. *Journal of Materials Processing Technology*, 103:367–373, 2000. doi: 10.1016/S0924-0136(99)00439-2.

[53] M. Elyasi, M. Bakhshi-Jooybari, and A. Gorji. Mechanism of improvement of die corner filling in a new hydroforming die for stepped tubes. *Materials and Design*, 30:3824–3830, 2009. doi: 10.1016/j.matdes.2009.03.036.

[54] M. Elyasi, M. Bakhshi-Jooybari, A. Gorji, S. J. Hosseinipour, and S. Nourouzi. New die design for improvement of die corner filling in hydroforming of cylindrical stepped tubes. *Journal of Engineering Manufacture*, 223(7):821–827, 2009. doi: 10.1243/09544054JEM1344.

[55] Yao Wang, Lihui Lang, Zhiying Sun, and Peng Kan. Analysis of a bulging-pressing compound-forming process for the sheet metal part with a small round corner feature. *Chinese Journal of Engineering*, 39(7):1077–1086, 2017. doi: 10.13374/j.issn2095-9389.2017.07.014. In chinese.

[56] Joachim Danckert. Experimental investigation of square-cup deep-drawing. *Journal of Processing Technology*, 50:375–384, 1995. doi: 10.1016/0924-0136(94)01399-L.

[57] M. Gavas and M. Izciler. Effect of blank holder gap on deep drawing of square cups. *Materials and Design*, 28:1641–1646, 2007. doi: 10.1016/j.matdes.2006.03.024.

[58] S. H. Zhang, L. H. Lang, D. C. Kang, J. Danskert, and K. B. Nielsen. Hydromechanical deep-drawing of aluminum parabolic workpieces—experiments and numerical simulation. *International Journal of Machine Tools and Manufacture*, 40:1479–1492, 2000. doi: 10.1016/S0890-6955(00)00006-7.

[59] Lihui Lang, Joachim Danckert, and Karl Brian Nielsen. Study on hydromechanical deep drawing with uniform pressure onto the blank. *International Journal of Machine Tools and Manufacture*, 44:495–502, 2004. doi: 10.1016/j.ijmachtools.2003.10.028.

[60] J. N. Goodier and G. J. Schoessow. The holding power and hydraulic tightness of expanded tube joints. *Transactions of the ASME*, 65:489–496, 1943.

[61] E. D. Grimison and G. H. Lee. Experimental investigation of tube expanding. *Transactions of the ASME*, 65:497–505, 1943.

[62] A. Kalnins and D. P. Updike. Contact pressure in rolled tube-tubesheet joints. *Nuclear Engineering and Design*, 130:229–234, 1991. doi: 10.1016/0029-5493(91)90131-Z.

[63] H. Ma, H. J. Yu, C. F. Qian, Z. S. Liu, and J. X. Zhou. Experimental study of hydraulically expanded tube-to-tubesheet joints for shell-and-tube heat exchangers. *Procedia Engineering*, 130:263–274, 2015. doi: 10.1016/j.proeng.2015.12.220.

[64] Dimitra Alexouli, Dennis Bøjesen, Lisa Rydahl Bøystrup, Claes Rubin Klose, Georgi Nikolaev Nikolov, and Karl Brian Nielsen. 3D numerical model of tube-tubesheet joint roller expansion process. *Journal of Physics: Conference Series*, 896(1):012070, 2017. doi: 10.1088/1742-6596/896/1/012070.

[65] Søren Bøgelund Madsen, Bo Gervang, Claus Hessler Ibsen, and Anders Schmidt Kristensen. An improved numerical model of the tube-tubesheet joint rolling process. *Journal of Materials Processing Technology*, 2017.

[66] Thomas Borrvall. Mortar contact for implicit analysis. *LS-DYNA Forum*, 11, 2012.

[67] Yao Wang, Lihui Lang, Ehsan Sherkatghanad, Karl Brian Nielsen, and Chun Zhang. Design of an innovative multi-stage forming process for a complex aeronautical thin-walled part with very small radii. *Chinese Journal of Aeronautics*, 2018. doi: 10.1016/j.cja.2018.01.019. In Press, Corrected Proof.

[68] Yao Wang, Lihui Lang, Søren Lauridsen, and Peng Kan. Springback analysis and strategy for multi-stage thin-wall parts with complex geometries. *Journal of Central South University*, 24(7):1582–1593, 2017. doi: 10.1007/s11771-017-3563-0.

[69] Guy Norris and Mark Wagner. *Airbus A380 - Superjumbo of the 21st century.* Zenith Press, 400 First Avenue North, Suite 300, Minneapolis, MN 55401 USA, 2010. ISBN 978-0-7603-3838-4.

[70] P. A. Withey. Fatigue failure of the de Havilland Comet I. *Engineering Failure Analysis*, 4(2):147–154, 1997. doi: 10.1016/S1350-6307(97)00005-8.

[71] Hui Wang, Jie Zhou, Yan Luo, Peng Tang, and Youliang Chen. Forming of ellipse heads of large-scale austenitic stainless steel pressure vessel. *Procedia Engineering*, 18:837–842, 2014. doi: 10.1016/j.proeng.2014.10.085.

[72] Bradley N. Maker and Xinhai Zhu. Input parameters for springback simulationusing ls-dyna. *Livermore Software Technology Corporation*, June, 2001. URL `www.feainformation.com/forming_parameters2.pdf`.

[73] Takeshi Uemori, Tatsuo Okada, and Fusahito Yoshida. Simulation of springback in v-bending process by elasto-plastic finite element method with consideration of Bauschinger effect. *Metals and materials International*, 4(3):311–314, 1998.

[74] Takeshi Uemori, Tatsuo Okada, and Fusahito Yoshida. Fe analysis of springback in hat-bending with consideration of initial anisotropy and the Bauschinger effect. *Key Engineering Materials*, 177–180:497–502, 2000. doi: 10.4028/www.scientific.net/KEM.177-180.497.

[75] Jenn-Terng Gau and Gary L. Kinzel. A new model for springback prediction in which the Bauschinger effect is considered. *International Journal of Mechanical Sciences*, 45:1813–1832, 2001. doi: 10.1016/S0020-7403(01)00012-1.

[76] B. K. Chun, H. Y. Kim, and J. K. Lee. Modeling the Bauschinger effect for sheet metals, part II applications. *International Journal of Plasticity*, 18:597–616, 2002. doi: 10.1016/S0749-6419(01)00047-X.

[77] F. Yoshida and T. Uemori. A model of large-strain cyclic plasticity and its application to springback simulation. *International Journal of Mechanical Sciences*, 45(10):1687–1702, 2003. doi: 0.1016/j.ijmecsci.2003.10.013.

[78] Benny Endelt Kristensen and Karl Brian Nielsen. Least-squre formulation of the objective function, applied on hydro mechanical tube forming. *Proceedings of the 9th Internation Conference on Sheet Metal, SheMet*, pages 353–362, 2001. doi: 10.2514/6.2011-2146.

[79] Adballah Hage Hassan. Fundamentals of vibratory stress relief. *Asian Journal of Applied Sciences*, 7:317–324, 2014. doi: 10.3923/ajaps.2014.317.324.

[80] S. N. Shaikh. Vibratory residual stress relieving - a review. *IOSR Journal of Mechanical and Civil Engineering*, 5th, 2016. doi: 10.9790/1684-15008030301-04.

[81] R. T. McGoldrick and Harold E. Saunders. Some experiments in stress relieving castings and welded structures by vibration. *The Vibratory Stress Relief Library*, 1943. doi: 10.1111/j.1559-3584.1943.tb02307.x.

[82] Piotr Sędek and Marek Stanisław Węglowski. Application of mechanical vibration in the machine building technology. *Key Engineering Materials*, 504–506:1383–1388, 2012. doi: 10.4028/www.scientific.net/KEM.504-506.1383.

[83] C. A. Walker, A. J. Waddell, and D. J. Johnston. Vibratory stress relief - an investigation of the underlying processes. *The Vibratory Stress Relief Library*, 1994. doi: 10.1243/PIME_PROC_1995_209_228_02.

[84] M. C. Sun, Y. H. Sun, and R. K. Wang. Vibratory stress relieving of welded sheet steels of low alloy high strength steel. *Materials Letters*, 58:1396–1399, 2004. doi: 10.1016/j.matlet.2003.10.002.

[85] D. Rao, D. Wang, L.Chen, and C. Ni. The effectiveness evaluation of 314l stainless steel vibratory stress relief by dynamic stress. *International Journal of Fatigue*, 29: 192–196, 2007. doi: 10.1016/j.ijfatigue.2006.02.047.

[86] G. C. Luh and R. M. Hwang. Evaluating the effectiveness of vibratory stress relief by a modified hole-drilling method. *International Journal of Advanced Manufacturing Technology*, 14(11):815–823, 1998. doi: 10.1007/BF01350766.

[87] Jing Song and Yidu Zhang. Effect of vibratory stress relief on fatigue life of aluminum alloy 7075-T651. *Advances in Machanical Engineering*, 8(6) 1–9, 2016. doi: 10.1177/1687814016654379.

[88] Song Jing, Zhang Yidu, and Sun Ke. The numerical simulation for effect of vibratory stress relief on titanium alloy Ti-6Al-4V fatigue life. *Theory, Methodology, Tools and Applications for Modeling and Simulation of Complex Systems*, 16th: 530–539, 2016. doi: 10.1007/978-981-10-2669-0_57.

[89] S. Weiss, G. S. Baker, and R. D. Das Gupta. Vibrational residual stress relief in a plain carbon steel weldment. *WRC Bulletin*, 206:47–51, 1975.

[90] A. S. M. Y. Munsi, A. J. Waddell, and C. A. Walker. The effect of vibratory stress on the welding microstructure and residual stress distribution. *Proceedings of the Institution of Mechanical Engineers*, 215(Part L):99–111, 2001. doi: 10.1177/146442070121500204.

[91] M. Jafari Vardanjani, M. Ghayour, and R. Mokhtari Homami. Analysis of the vibrational stress relief for reducing the residual stresses caused by machining. *Experimental Techniques*, 40(2016):705–713, 2014. doi: 10.1007/s40799-016-00-713.

[92] X. C. Zhao, Y. D. Zhang, H. W. Zhang, and Q. W. Wu. Simulation of vibration stress relief after welding based on FEM. *Acta Metall. Sin.(Engl. Lett.)*, 21(4): 289–294, 2008. doi: 10.1016/S1006-7191(08)60051-4.

[93] X. C. Zhao, Y. D. Zhang, and Y. J. Ma. Finite element analysis of vibratory stress relief process. *Applied Mechanics and Materials*, 88–89:623–627, 2011. doi: 10.4028/ww.scientific.net/AMM.88-99.623.

[94] Jasbir Singh Arora. *Introduction To Optimum Design - Fourth edition.* Academic Press, Elsevier, 125 London Wall, London EC2Y 5AS, UK, 2017. ISBN 978-0-12-800806-5.

[95] Cynthia M. Tamasco, Masoud Rais-Rohani, and Arjaan Buijk. Sheet-stamping process simulation and optimization. *Collection of Technical Papers - AIAA/ASME/ASCE/AHS/ASC Structures, Structural Dynamics and Materials Conference*, 2011. doi: 10.2514/6.2011-2146.

Appendix

Paper: VSR Article

A

Numerical Model of Resonant Vibratory Stress Relieving Process on Plastic Deformed Hole Plate

C. R. Klose, D. Bøjesen and K. B. Nielsen

Department of Materials and Production, Aalborg University,
Fibigerstræde 16, DK-9220, Aalborg, Denmark

Keywords: Vibratory Stress Relief; Numerical Model; Plastic Deformation; Hole Plate; Residual Stresses.

Abstract

The method of vibratory stress relieving is of increasing interest in the recent years, due to the many potential benefits. This paper aims to investigate the vibratory stress relieving (VSR) treatment using FEM upon a well-documented case, Kirsch's plate with a hole under tensile loading. Here the plate is loaded until a level where residual stresses occur upon unloading, hereafter two different eigenfrequency modes are used for relieving the residual stresses. The two modes are bending and tension, where the plate is applied a small load periodic, which causes the vibrations to be resonant. For the two frequency modes the residual stresses were minimised in the region with the largest initial residual stresses, however, the bending mode only causes the relieving to be in the top and bottom of the plate. The stress relieving is caused when the resonant stress vibrations reaches the materials yielding in both tensile and compression, and formation of plastic strain occurs that redistributes the residual stresses. The study concludes that the future deployment of VSR treatment should be assisted by FEM to apply the correct supports to targeted relieve the desired regions.

Introduction

The method of vibratory stress relieving is experiencing increasing interest in the recent years, due to the desire for using this treatment for large structures, where a thermal treatment is close to impossible.
Vibratory stress relief (VSR) is a non-thermal stress relief method, in which a cyclic load is applied at a specific frequency to a component, to redistribute residual stress peaks and enhance dimensional stability [1]. Residual stresses are an undesirable outcome of casting, cold working or welding etc. which can contribute to accelerated corrosion cracking, influence strength, decrease fatigue life or cause distortion, when the component is put into service and loads are applied [2].
Employing VSR to reduce residual stresses as a substitute to conventional thermal treatment methods, have theoretical advantages such as: Inexpensive equipment and operating costs, decreased processing time, adjustable to a wide range of component sizes and decreased operating difficulty[2]. Compared to the cost of stress relief annealing, can saving approaching 90% be generated using VSR [3].

Since 1943 studies investigating the feasibility of using VSR have been conducted. Saunders et al.[4] presented experimental studies regarding several large welded structures, where the conclusions were indecisive of the stress reliving properties of VSR, but the confidence in the stability of the processed structures were increased. Walker et al.[5] demonstrated up to 40% reduction of peak residual stress magnitudes in cold-rolled mild steel by using VSR. The standard theory proposes that VSR works by combination of residual and amplitude stress exceeding the yield strength of the material, resulting in bulk plastic flow [5].

Studies have proved that utilizing VSR will have negligible to positive effect upon fatigue life of a range of materials, granted the estimated fatigue limit of the material is not exceeded [6, 7]. Song et al.[7] observed reduced and homogenized residual stress and stress concentrations, S-N curves from before and after VSR proved improvements of 7075-T651 aluminium fatigue life.

The application of finite element analysis of a cantilever beam showed that resonant and non-resonant vibrations relieved residual stresses, furthermore it was shown that the first ten cycles caused the largest residual stress to drop [8].
Finite element models of VSR used on welds and complex beam structures also showed positive result, if the correct amplitude stress and vibratory mode are selected [9, 10]. Zhao et al.[9] concluded that the vibration period do not have major effect on the stress reliving properties of VSR, furthermore a greater cyclic load is needed for non-resonant VSR, compared to resonant VSR.

The aim of this study is to investigate the feasibility of using FEM to perform the resonant VSR process, by using the well-known Kirsch's plate hole example for stress concentrations. The stress relieving will be demonstrated by two different frequency modes and compared to each other.

Hole Plate Model Parameters

The modelling approach for this paper is to model a plate where the the width and height is 40 mm, the thickness 1 mm and diameter of the hole located in the centre of the plate is 10 mm. The dimensions of the plate is selected, because the geometry becomes reliably stiff, and hereby the eigenfrequency is increased, which is lucrative to model with a explicit solver, since the process time will be fairly short. The numerical model is constructed in LS-DYNA, using fully integrated shell element modified for higher accuracy (Elform = -16)[11] with 7 integration points through the thickness, and the material model is 018_Power_Law_Plasticity, which is a isotropic plasticity model, that uses the power law hardening rule based on Hollomon's equation[12]. The plate is modelled as mild steel, the material parameters are presented in table 1.1.

Table 1.1. Material parameters of mild steel.

Mass density [ton/mm]	Young's modulus [MPa]	Poisson's ratio	Strength coefficient [MPa]	Hardening exponent	Initial yield stress [MPa]
7.850e-009	2.100e+005	0.3	530	0.26	230

The mesh located at the edge of the hole is made to provide optimal edge conditions, shown on figure 1.1, and in the remaining of the plate the mesh is perfect squares. The model consist of 6144 elements, measuring 0.5 mm in the square mesh, the maximum element size in the fitted mesh is 1.05 mm located in the mesh transition corner elements.

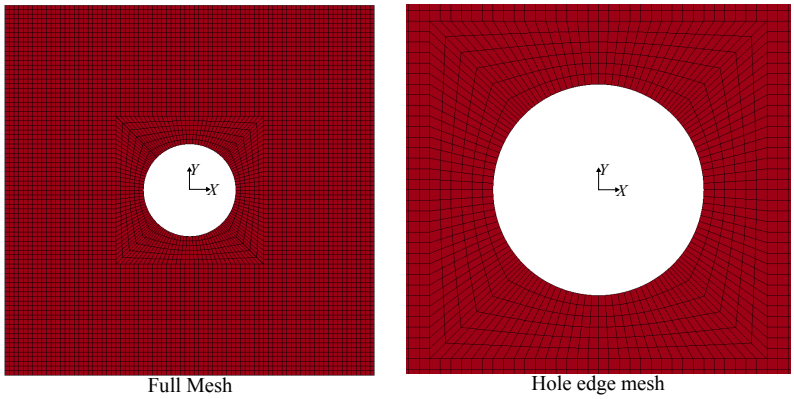

Figure 1.1. Left: Hole plate model with square mesh and hole edge optimal mesh. Right: Zoomed view of optimal hole edge mesh.

Modelling VSR

The purpose of modelling the VSR process is to investigate the ongoing phenomenons in the process, and determine their influence upon the result. Therefore Kirsch's solution to stresses around a hole is devised for the paper, where a infinite plate with a hole is uni-axial loaded. In order to induce residual stresses to this problem, the plate is loaded such the stress concentration exceeds the materials yield point and thereby plastically deforms the material in the vicinity of the hole, which would result in residual stresses after unloading of the plate. The residual stresses in the unloaded plate, can be seen on figure 1.2 (right).

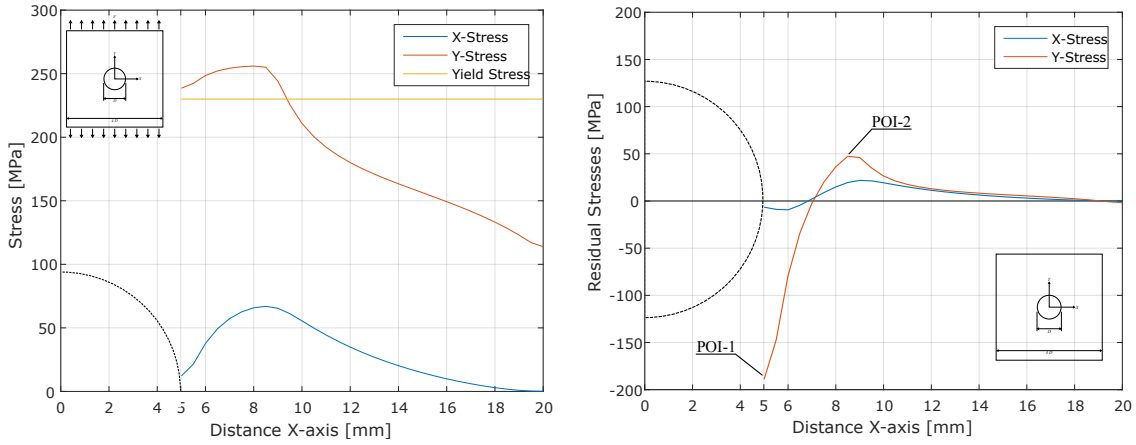

Figure 1.2. The loading situation for the plate, where the left graph shows the plate under maximum tensile loading. The right graph shows the residual stresses after unloading.

The aim of the VSR treatment is to remove or redistribute the stress concentrations, and therefore it is important to select the correct eigenfrequency mode for the structure. The

frequency modes are dependent on different variables, where the boundary conditions are used in this study to reach the desired eigenfrequency. The selected boundary conditions and frequency modes, can be seen in figure 1.3.

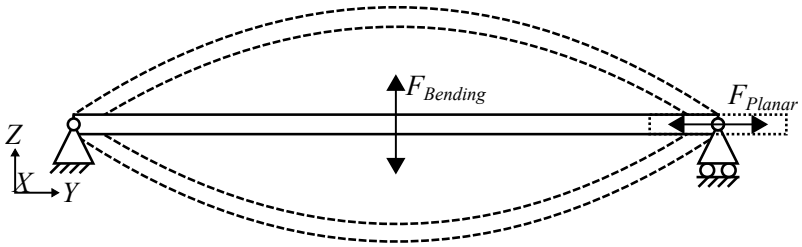

Figure 1.3. The lowest eigen frequency modes and the associated boundary conditions, for the VSR the models made in this paper.

The advantages of using these frequency modes are to achieve the largest stresses in the area which is desired to stress relief. The bending mode will force the middle of the plate to experience a bending situation, which will cause the largest bending stresses in the top and bottom of the plate. The planar mode will be similar to the plate loading, be where the largest stresses are in the vicinity of the hole.

Results

The simulation starts out with a loading situation, where the residual stresses are introduced to the plate, depending on the stress level in the plate, the plates eigenfrequency will deviate. Therefore the eigenfrequency is found by applying an impulse at the loading point, as can be seen on figure 1.3, and then calculated based on the wave propagation, see figure 1.4.

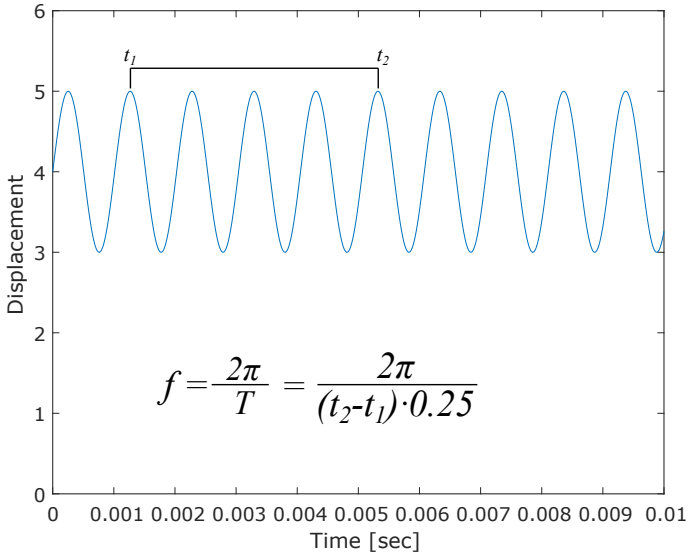

Figure 1.4. An example of the determination of the frequency for the numerical models.

The plate containing residual stresses are then applied a sinusoidal load corresponding to the found eigenfrequency, which can be seen on figure 1.5. The advantage of applying the

cyclic loading at the systems eigenfrequency, is that the displacement accumulates into a level at which the materials yield strength is reached, as can be seen in figure 1.5, where the displacement reaches a steady amplitude.

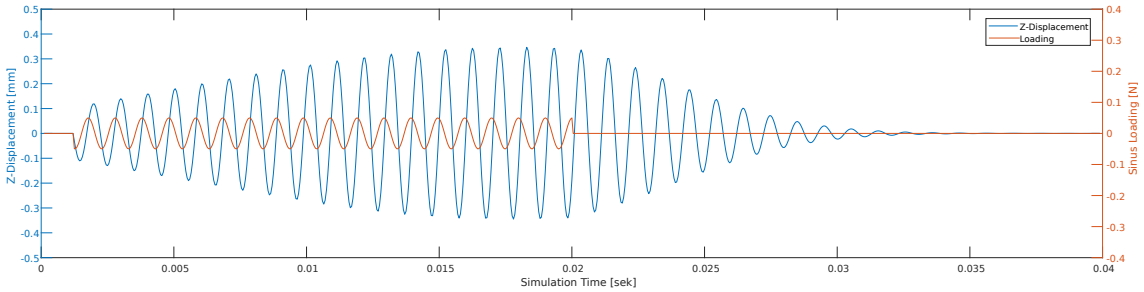

Figure 1.5. The blue line, shows the Z-displacement for the parts of the plate, that experiences the largest displacements. The orange line, shows the sinusoidal loading for the model.

When the cyclic loading is terminated, the system is applied damping, which relaxes the system into a quasi static state, where the residual stresses after the VSR treatment can be evaluated.

This study will focus on the largest tensile residual stresses and the largest compressive residual stresses. An example of the VSR process for the bending frequency mode can be seen on figure 1.6 and 1.7, for POI-1 and POI-2, see figure 1.2. On the two figures, three point through the thickness are monitored through the simulation time, which are the top, middle and bottom integration point. For the top and bottom integration point an averaged stress level is plotted as-well, which indicated residual stress through the cyclic loading. For both figures, the VSR process minimises the residual stresses for the top and bottom integrations points, while the middle integration point remains at the same level. The plastic strain development is plotted as-well and can be assigned the cause for the stress relieving.

It can be observed that the minimisation of the averaged residual stress levels occurs when the cyclic stress reaches the materials yielding point. When the cyclic stress reaches both the tensile and compressive yield stress the residual stress approaches 0 MPa.

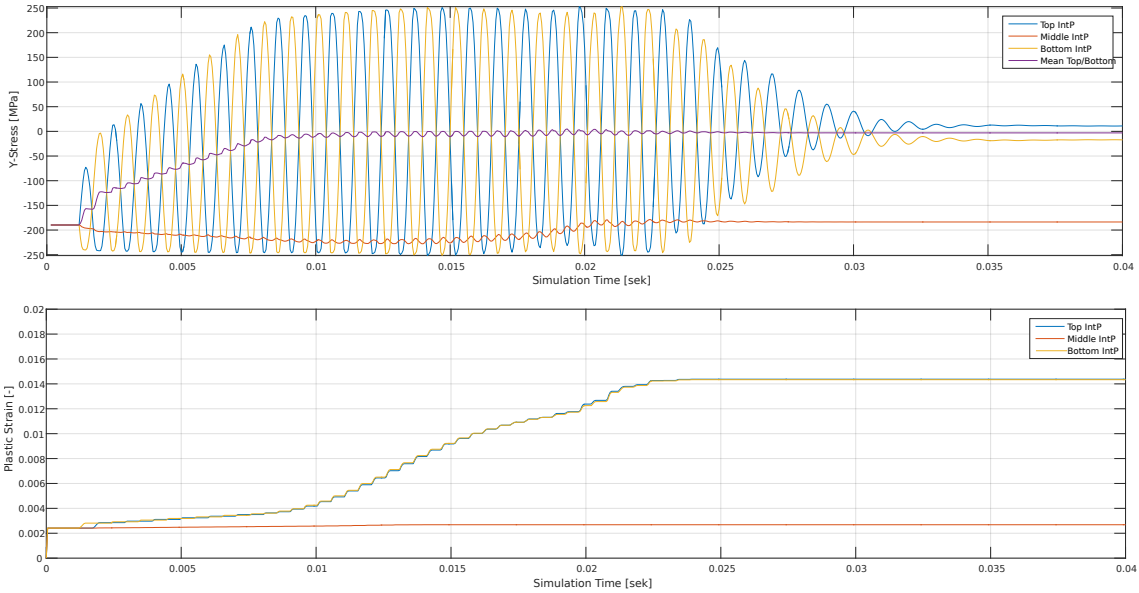

Figure 1.6. The element in the simulation which experiences the largest compressive Y-residual stresses, POI-1, where these graphs are for the bending mode. The top graph is Y-stresses in the top, middle and bottom of the plate, together with an averaging of the top and bottom points. The bottom graph is the associated plastic strain.

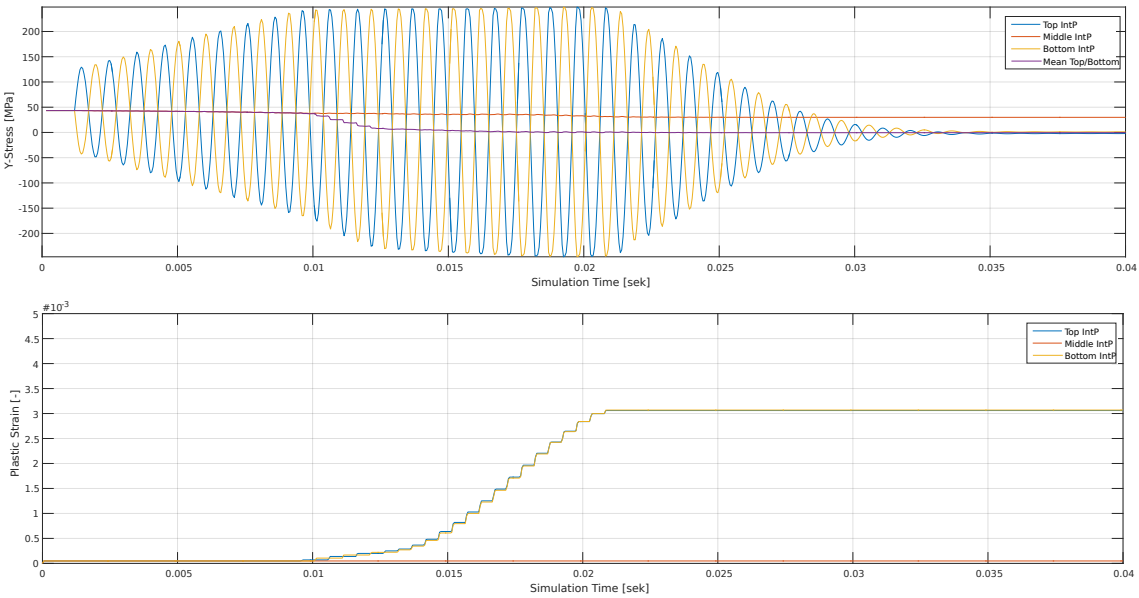

Figure 1.7. The element in the simulation which experiences the largest tensile Y-residual stresses, POI-2, where these graphs are for the bending mode. The top graph is the Y-stresses is the top, middle and bottom of the plate, together with an averaging of the top and bottom points. The bottom graph is the associated plastic strain.

For the planar mode, the integration points through the thickness experiences the same stresses, which is similar to a uni-axial tensile test, therefore the stresses observed for each integration point is similar.
This relieving of residual stresses through the thickness is also evaluated in table 1.2, where

the minimising of residual stresses, are mostly occurring in the outermost parts, which is in agreement with the bending stresses. For the planar frequency mode, the minimisation is consistent throughout the thickness.

Table 1.2. The residual stress level for the two points, through the thickness, of interest from figure 1.2 and the residual stresses for the points after VSR.

		POI-1			POI-2		
Position	IntP	Initial [MPa]	Bending [MPa]	Planar [MPa]	Initial [MPa]	Bending [MPa]	Planar [MPa]
Top	1	-188	-17.14	0.26	43,6	1.10	19.86
	2	-188	16.58	0.26	43,6	19.70	19.86
	3	-188	-62.19	0.26	43,6	28.82	19.86
Middel	4	-188	-183.70	0.26	43,6	29.93	19.86
	5	-188	-31.50	0.26	43,6	31.05	19.86
	6	-188	-25.21	0.26	43,6	24.82	19.86
Bottom	7	-188	10.95	0.26	43,6	-2.14	19.86

The minimisation of residual stresses are general for the section shown in figure 1.2, where the residual stresses can be seen in figure 1.8 and 1.9, where the VSR process, has minimised the stresses in this section. It should be noted that the stress relieving of the Y-Stresses for the bending frequency is only achieved for the top and bottom integration point, whereas middle point is at the same level as initially. This is however not the case for the X-Stresses, where the stress relieving is achieved throughout the thickness.

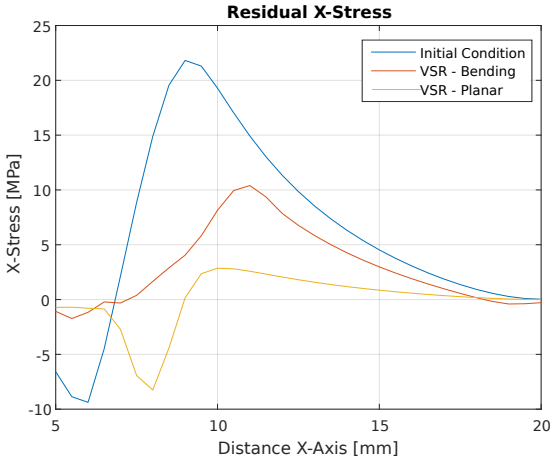

Figure 1.8. The residual X-stress before and after VSR in the section from the hole.

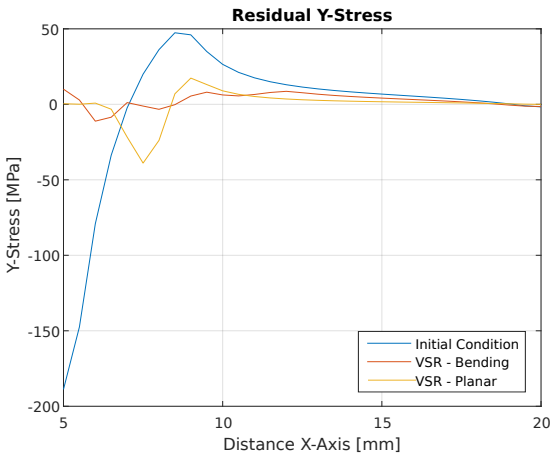

Figure 1.9. The residual Y-stress before and after VSR in the section from the hole.

The cause for the VSR is the formation of plastic strain, which either redistributes the residual stresses or even removes it. The plastic strain formation can be seen in figure 1.10, which is increased from the initial loading situation. Here it is noteworthy, that the planar mode does not increase the plastic strain level for POI-2, but it develops the most in the vicinity of the hole.

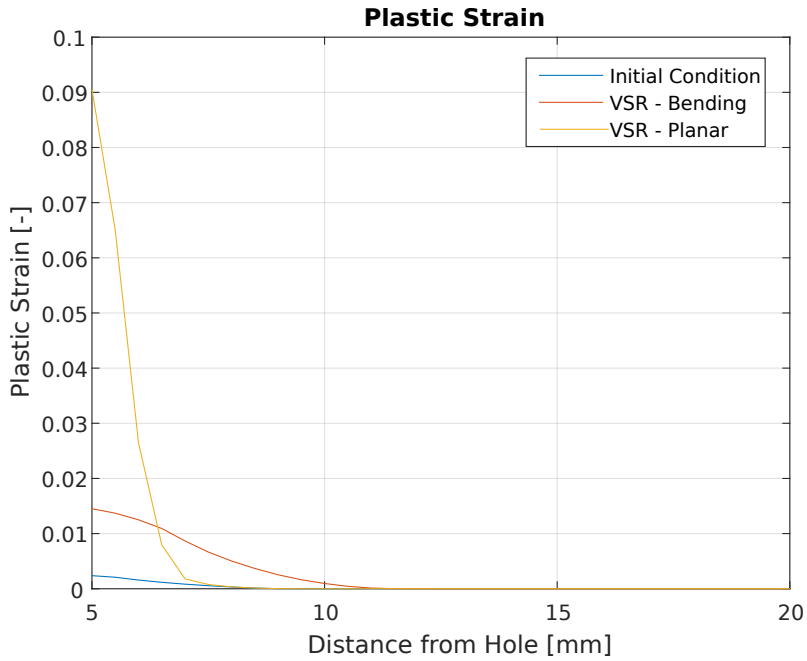

Figure 1.10. Effective Plastic Strain from the hole to the edge, for the initial condition and for the two VSR treatment modes.

Discussion

Based on this study, where a simulated plate with a hole is stress relieved, the VSR process shows to have a minimising effect on the residual stress. The relieving occurs when the tensile and compressive stress, during the cyclic loading, reaches the yield stress of the material, and thereby initiates the plastic flow, that causes the residual stresses to redistribute or even be removed. For the bending frequency mode the residual stress relieving had a larger effect in the outermost points through the thickness, which is caused by the selected frequency mode where the bending stress profile influenced the stress relieving. For the planar frequency mode the stress relieving is achieved throughout the thickness, and seems to relief more of the residual stresses than the bending frequency mode.

The performed study focus on the ability to observe influence form the VSR process using commercial finite element tools, in this case LS-DYNA, to minimise the largest residual stresses. The application of FEM in the use of this process, seem to be a necessary approach in the forward going studies regarding this process, when the component becomes more complex. For larger complex constructions the selected frequency modes are extremely important, since poor selection would cause the VSR process to introduce more residual stresses in other regions. Therefore the application of FEM would improve the understanding of stress relieving and the selection of structural supports during VSR, and thereby targeted apply the VSR process.

Conclusion

This study shows that the stress relieving process of VSR has an effect upon the plate hole problem, where the outermost points through the thickness minimises the residual

stress by plastically deforming the area with the largest residual stresses.

- The stress relieving occurs when the tensile and compressive stress during the cyclic loading exceeds the materials yield strength.
- The selection of frequency mode for the VSR process is very important in order to minimise the residual stresses.

In a case where the plate is constrained as a cantilever and loaded at the tip, the lowest eigenfrequency (in bending) would cause server plastic deformation at the boundary, even before reaching any beneficial reduction of residual stress at the symmetric section.

The application of FEM in determining the correct eigen frequency is extremely important in terms of relieving the desired residual stresses.

Bibliography

[1] Adballah Hage Hassan. Fundamentals of vibratory stress relief. *Asian Journal of Applied Sciences*, 7:317–324, 2014.

[2] S. N. Shaikh. Vibratory residual stress relieving - a review. *IOSR Journal of Mechanical and Civil Engineering*, 5th, 2016.

[3] Piotr Sędek and Marek Stanisław Węglowski. Application of mechanical vibration in the machine building technology. *Key Engineering Materials*, 504–506:1383–1388, 2012.

[4] R. T. McGoldrick and Harold E. Saunders. Some experiments in stress relieving castings and welded structures by vibration. *The Vibratory Stress Relief Library*, 1943.

[5] C. A. Walker, A. J. Waddell, and D. J. Johnston. Vibratory stress relief - an investigation of the underlying processes. *The Vibratory Stress Relief Library*, 1994.

[6] Song Jing, Zhang Yidu, and Sun Ke. The numerical simulation for effect of vibratory stress relief on titanium alloy Ti-6Al-4V fatigue life. *Theory, Methodology, Tools and Applications for Modeling and Simulation of Complex Systems*, 16th:530–539, 2016.

[7] Jing Song and Yidu Zhang. Effect of vibratory stress relief on fatigue life of aluminum alloy 7075-T651. *Advances in Machanical Engineering*, 8(6) 1–9, 2016.

[8] X. C. Zhao, Y. D. Zhang, and Y. J. Ma. Finite element analysis of vibratory stress relief process. *Applied Mechanics and Materials*, 88–89:623–627, 2011.

[9] X. C. Zhao, Y. D. Zhang, H. W. Zhang, and Q. W. Wu. Simulation of vibration stress relief after welding based on FEM. *Acta Metall. Sin.(Engl. Lett.)*, 21(4):289–294, 2008.

[10] Jianke Fu, Xiaohui Huang, and Liang Xu. Numerical simulation for technological parameters of vibratory stress relief in large welding structures. *Applied Mechanics and Materials*, 217–219:2046–2050, 2012.

[11] Livermore Software Technology Corporation (LSTC). *LS-DYNA KEYWORD USER'S MANUAL VOLUME I.* LSTC, LS-DYNA R10.0 edition, 2017.

[12] Livermore Software Technology Corporation (LSTC). *LS-DYNA KEYWORD USER'S MANUAL VOLUME II - Material Models.* LSTC, LS-DYNA R10.0 0 edition, 2017.

LS-PrePost: Blockmesher B

Blackmesher is an advanced mesh generation tool in LS-PrePost. Blackmesher is built as a successor to the mesh generation tools whcih can be found in LS-Ingrid, an should therefore use the same formulation methods. Blackmesher grants the user the ability to somewhat precisely control the layout of the mesh in a part, in contrary to the auto mesh generation tools that only allow the user to specify limited parameters in to auto mesh generation script. At this time is a number of bugs still present in Blockmesher which limits the complexity of the parts that can be generated. The advantage of using Blockmesher in the ability to save the mesh generation as a script, which allows auto generation of parts based on parameters that can be changed with e.i. a JAVA script.

B.1 Blockmesher Guide

This is a guide of how Blockmesher was used in this project, blockmesher can also be used in other ways. In this project was blockmesher used to generate mesh on surfaces, surfaces can be generated in two ways, from .IGES files or in LS-PrePost, both methods was used in the project, but the LS-PrePost method will be presented. .IGES files can be generated in CAD software such as SolidWork.

Generation of surfaces

The punch in the final step will be used as an example, in this guide. The punch can be simplified to straight sides and curves sides, furthermore is the punch axis symmetric.

The straight sides and the curved sides, can be generated from intersection points, the coordinate of these points are calculated in a script, which can be edit during the tool optimisation, this is shown on figure B.1. The lines are then revolved around the origo z-axis, to form surfaces, shown on figure B.1.

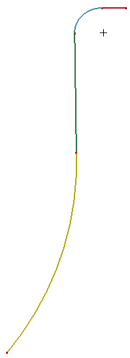

Figure B.1. Lines generated from intersection points.

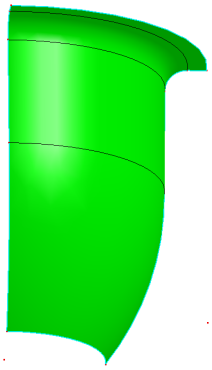

Figure B.2. surfaces revolved from lines.

Mesh Generation

After the surfaces are prepared, can the Blockmesher tool be used. Blockmesher uses blocks to control the mesh generation, in each block are the element density defined along with the size of the blocks. The blocks can be defined as shells or as solids. An illustration of the blocks and elements in Blockmesher can be seen on figure B.3, which are defined with the tool shown on figure B.3.

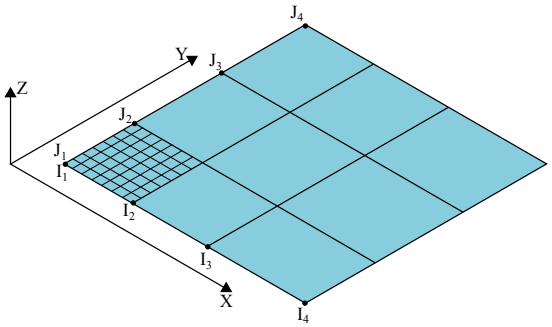

Figure B.3. Blockmesher indexing formulation.

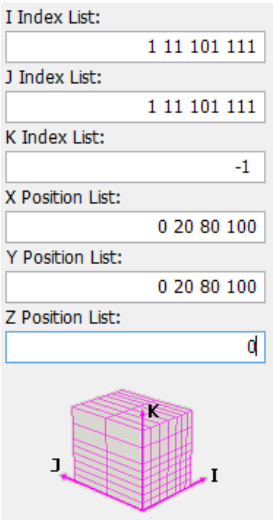

Figure B.4. Tool which are used to define the blocks

The number of blocks generated should fit the number of surfaces, as one block are used for one half of a surface.
The generated multi-block can be seen on figure B.5, which have five blocks in each length, this is done to have a mesh which is axis symmetric in the final part.

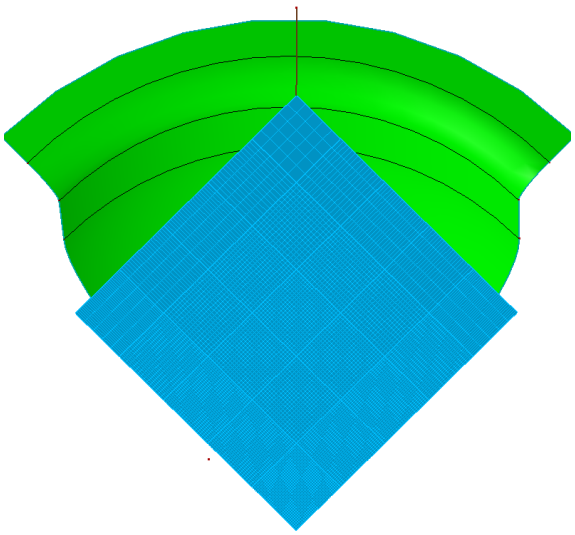

Figure B.5. Generated blocks.

A number of blocks, that are not used, are then deleted, shown on figure B.6. The remaining block are projected onto a angled centre line that ensure the final mesh doe not have a gap in the middle, shown on figure B.6

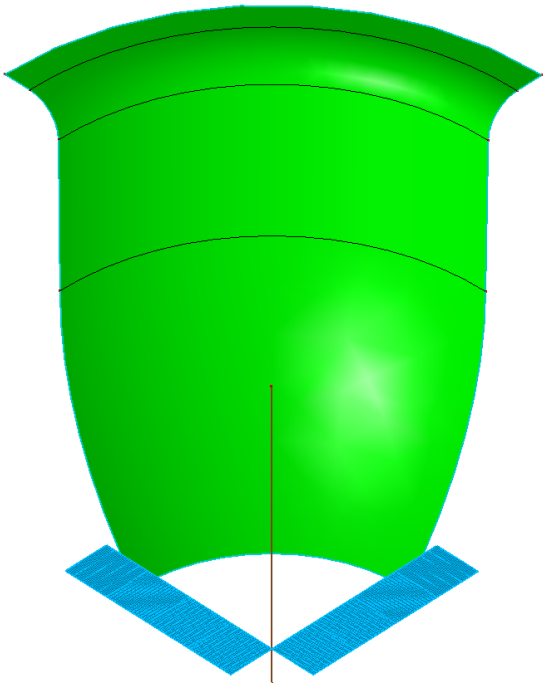

Figure B.6. Remaining blocks where the blocks which are not used are deleted.

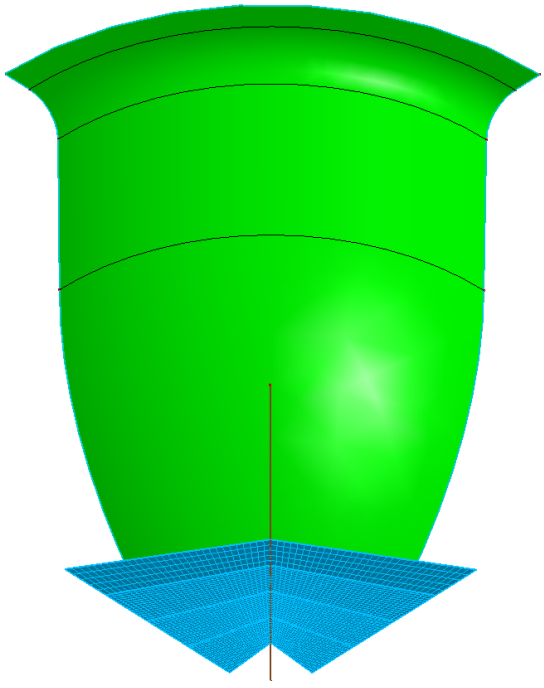

Figure B.7. Blocks are projected onto the centre line.

The blocks are projected onto the surfaces, shown on figure ,B.8, a number of bugs can occur during this stage. The projection bugs can be reworked by projecting the edges and

corners of the blocks onto the edge lines and corner points of the surface.

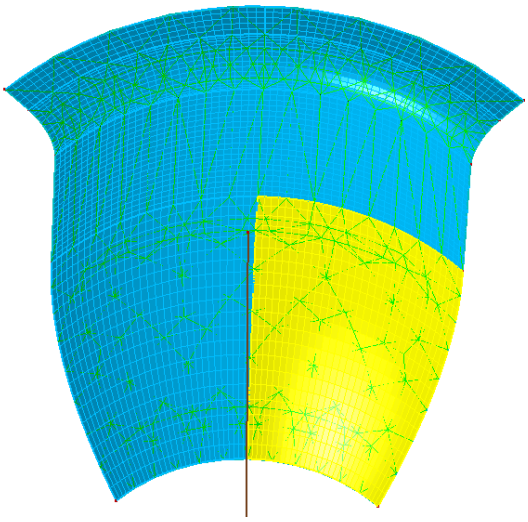

Figure B.8. Blocks projected onto the punch surfaces.

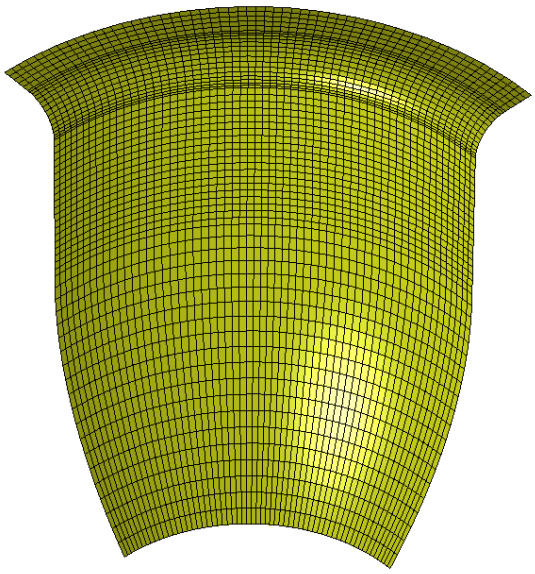

Figure B.9. Finished generated punch mesh.

The final generated mesh can be seen on figure B.9, it should be noted how mesh is axis symmetric, and the boarder between the different mesh zones meet perfectly, furthermore is all the element quad elements.

B.1.1 Blockmesher scripting

The commands used in the blockmesher tool and the general LS-PrePost interface, can be saved to an .cfile. LS-PrePost can then be initiated with the .cfile as input, followed by saving the built part and exiting LS-PrePost automatically.

The script used to make: Punch 14 in the Vesta Aircoil copper fin case, shown on the previous figures, can be seen on the next page.

```
cemptymodel
pnt param  0 6.5 0.0 10.09
pnt param  0 7.2 0.0 10.09
pnt param  0 5.2 0.0 8.09
pnt param  0 5.15 0.0 6.09
pnt param  0 3.2 0.0 0.6579999999999999
pnt param  0 2.0 0.0 0.09
pnt param  0 0.0 0.0 0.09
pnt param  0 7.2 0.0 8.09
pnt param  0 -3.8499999999999996 0.0 6.09
pnt param  0 2.0 0.0 -1.41
// ------------------------------
//  ↑ Points calc. in JAVA ↑
// ------------------------------
// ------------------------------
//       Make surfaces
// ------------------------------
pnt param  0 6 6 0.09
line pntpnt  0 0 2 1v 2
cirarc centerstartend 8v 2 3
line pntpnt  0 0 2 3v 4
cirarc centerstartend 9v 4 5
revolve  4 4e 2 3 1 none 0.0 90 0 0 0 0 0 0 0 1
line pntpnt  0 0 2 7v 11
// ---------------------------------
// Blockmesher
// ---------------------------------
bmcreate multiple i 1 31 51 71 86 91 j 1 31 51 71 86 91 k -1 x 0 1 2 3 4 5 y 0 1 2 3
4 5 z 0
bmdeletei i 2 6  j 2 6  k -1
bmdeletei i 1 2  j 1 2  k -1
bmproject i -2  j 2 6  k -1 line 18 xyz
bmproject i 2 6  j -2  k -1 line 18 xyz
bmproject i 1 2  j -6  k -1 line 5 xyz
bmproject i -6  j 1 2  k -1 line 5 xyz
bmproject i -1  j -6  k -1 point -2.88658e-15 6.5 10.09 xyz
bmproject i -6  j -1  k -1 point 6.5 0 10.09 xyz
bmproject i 5 6  j 1 2  k -1 surface 1 xyz
bmproject i 1 2  j 5 6  k -1 surface 1 xyz
bmproject i 1 2  j 4 5  k -1 surface 2 xyz
bmproject i 4 5  j 1 2  k -1 surface 2 xyz
bmproject i 1 2  j 3 4  k -1 surface 3 xyz
bmproject i 3 4  j 1 2  k -1 surface 3 xyz
bmproject i 2 3  j 1 2  k -1 surface 4 xyz
bmproject i 1 2  j 2 3  k -1 surface 4 xyz
bmaccept partid 14
// ------------------------------
//      Cleanup of parts
// ------------------------------
assembly del shape 1
renumber clean
renumber offset 0
renumber setkind PART 13
renumber renumkind 270
renumber keyword 1
renum occupant models
renumber clean
renumber offset 0
renumber setkind NODE 1399999
renumber setkind SHELL_ELEM 1399999
renumber renumkind 170 134
renumber keyword
renum occupant models
partdata assignapply 0 14 14 0 0 -1 -1 0 14
// ---------------------------------
//     Save the partid
// ------------------------------
save keywordabsolute 0
save keywordbylongfmt 0
save outversion 6
save keyword "Punch14.k"
exit
```

Optimisation Inputs

C

In this Appendix, the inputs for setting up the optimisation will be presented and described.
The optimisation is performed on an external cluster, which is accessed by a linux terminal. The optimisation package is constructed by Benny Endelt for his Ph. D Thesis [44], and is coded in java. The files needed for setting up the optimisation are listed beneath:

- *lsopti.in*
- *ObjectFunction.java*
- *nativein*

Each files will be presented in the following sections, and an additional section, where the data extraction will be presented.

C.1 lsopti.in

This files purpose is to determine the settings for the optimisation, where a blank version can be seen on figure C.1. The inputs to this file is given on the right side of the equal sign, where the inputs are given in the following types: double variable, integer variable, String variable or Boolean variable. A detailed description of the different inputs are given in [44], where the following will mainly focus on the inputs which are varied in the project.

```
parameters =
scale parameters = false
poor scaling = false
active = all
delta =
equal delta = 0
tr method = 2 25
tr initial = 0
tr fraction = 2
tr control = 1.5 2 0.2 .65 2
NonMonoton = false 1 1
free step = 0
Bound Method = false
tr lower =
tr upper =
max iterations = 100
epsilon = 1e-5 1e-5 0
newton method = TSSM m
hessian update = 2
reset hessian = 0
hessian scaling = 2
;; hybrid = 1 0.01
broyden secant = false 0 5
number of processors = 1
;; set dir = Sim1 Sim2 etc
;; NodeName = sf1 sf2 sf3  etc
;; MountPoint = /mnt/Sun2 etc
jacobian = false
print residual = false
;; history file = hist.dh
end
```

Figure C.1. The input file for the optimisation, lsopti.in.

The first line is the ***parameters***, where the initial parameters for the optimisation are given as a double variable. The number of design parameters in the optimisation has to match the number of initial parameters.
The ***scale parameters*** and ***poor scaling***, can be use if the parameters in the optimisation has large difference in magnitude, where for the first input the scaling of the individual parameters can be set, and for the second all the parameters are scaled.
The ***active*** function can used to defined if some of the parameters in the optimisation are not to be varied, where they can be set to be inactive.
The ***delta*** and ***equal delta***, is used for determine the step length for the finite difference approximations.
The ***tr method***, ***tr initial***, ***tr fraction*** and ***tr control***, are all related to the trust-region, where the first determines which type of trust-region method, the second is the initial size, and the third can be used for determining the initial size, based on the pure newton step. And the fourth input is some controls which are used in an update strategy for the trust-region, which will not be further elaborated.
The ***NonMonotone*** is a setting, where the objective function is allowed to increase for one step, in order to get out of a local minimum.
The ***free step*** is a possibility for making free steps for the x-number of initial iterations, where there are no restriction on the objective function.
The ***Bound Method*** is related to applying bound on the parameters, which is related to the ***tr lower*** and ***tr upper***, where the lower and upper bounds can be prescribed.
The ***max iterations*** and ***epsilon*** are the stopping criterias, for which the optimisation is terminated.

The ***newton method*** defines the optimisation algorithm, where a few are listed underneath:

- **gauss** = Gauss Newton Method
- **hessian** = The scaled factorised Broyden like method
- **hessian r** = The scaled factorised Broyden like method within the convex Broyden Class
- **TSSM** = The totally structured Secant Method
- **TSSM r** = The totally structured Secant Method within the convex Broyden Class

The *hessian update*, *reset hessian* and *hessian scaling* are all hessian strategies, where the first is used for the Broyden factor, the second is a resetting of the hessian and the third is a scaling strategy.
The *broyden secant* is used for the broyden secant method.
The *number of processors* are defining the number of processors which are prescribed for the specific optimisation, where the finite difference approximations can be distributed and run simultaneously.
The *jacobian* is either true or false, where true refers to the analytical jacobian defined in the *ObjectFunction.java*, and a false sets a requirement for making an finite difference approximation.

C.2 ObjectFunction.java

The interface with the optimisation tool, developed by Benny Endelt [44], is established through a problem file, where the non-linear least square formulation dictates that a "empirical" and "estimated" data is formulated. This problem file is named: ObjectFunction.java, which can be seen on figure C.2. The script is divided into some different classes, where this projects has utilised the following classes:

- FittedData
- PrintBar
- FormatString
- EmpiricalData

The **FittedData**, is estimated data which most often is the data acquired from the simulation. The **PrintBar** is a class which constructs the text file, at which the new set of parameters are to be implemented in the simulation. This part utilises the syntax required by LS-DYNA. The **FormatString** is used for the **PrintBar** class, where the new parameters are rewritten to the format that LS-DYNA requires. Finally, the **EmpiricalData** is used as the comparing part of the residual vector. This part is by Benny Endelt [44], often used for the empirical data when fitting experimental results with an simulated one.

```
1  import java.text.DecimalFormat;
2  import java.util.*;
3  import java.io.*;
4  import bek.opti.ObjectUtility;// Default file for Least square optimization package
5
6
7  public class ObjectFunction extends ObjectUtility{
8      private double P[]=new double[0];
9      private String dir="";
10
11     public ObjectFunction(){}
12
13   public void FittedData(){
14       P=GetParameters();    // Get current parameters
15       dir=GetDirectory();   // Set the directory of the problem
16       PrintPar(P);
17       NativeCall(dir,1000);   //Run LS-DYNA by the nativein file
18
19
20       double A[]=new double[0];
21  // Code for the residual vector
22
23       SetFittedData(A); // Set Data In ObjectUtility.class
24    }
25    private void PrintPar(double P[]){       //Changes the parameters settings in the
     keyword file
26         String S[]=new String[3];
27         S[0]="*KEYWORD";
28         S[1]="*PARAMETER";
29      S[2]=" Rd1 ," +FormatString(P[0]);
30         ToFile(S,dir+"PARAMETER");
31    }
32
33    private String FormatString(double value){
34         DecimalFormat E = new DecimalFormat("0.00000");
35         if (value<0)
36         value=-value;
37         String s=(E.format(value));
38           return s;
39    }
40
41    public void EmpiricalData(){
42        dir=GetDirectory();
43    double d[] = ReadFile(dir+"A.ini");
44
45        double A[]=new double[d.length];
46  // The empirical Data
47
48           SetEmpiricalData(A);   // Set Data In ObjectUtility.class
49    }
50
51
52    public static void main(String args[]){
53        new ObjectFunction();
54    }
55  } // end ObjectFunction.java
56
```

Figure C.2. A empty version of the java script: ObjectFunction.java.

C.3 nativein

The nativein file is a shell script, which is initiated by the Java script, by the command `NativeCall(dir,1000)` which can be seen on figure C.2, line 17. This command initiates the nativein file, where an example of such can be seen beneath. When the file is initiated, the first line is run and waits for the continuing until this command is done.
On the first line, a `cat` function is performed, this is a linux command that concatenation (i.e., stringing together) the two files `PARAMETER` and `Master.k`. The `PARAMETER`-file is the file which contains the parameters to the LS-DYNA model, this file is created by

the `PrintBar` class, see figure C.2 line 16 and 25-31. The `Master.k` is the parameterised keyword file for LS-DYNA, but with out the parameter settings. These two files are stringed together, and a new file is created `Master1.k`.
On the second line, the numerical model with the new parameter setting are run. The `dyna_s` function is the selected solver, in this case a single precession, the `i` is given the desired keyword to run, the `ncpu` gives the number of CPU desired to locate for this calculation, where by adding a minus in front, then the cluster regulates the number of CPU's available. And finally, the `memory` is used for allocating the memory for the solver. The third is running another shell script, where the desired output from the optimisation is determined. This shell script will be presented in the following section.

```
cat PARAMETER Master.k > Master1.k
dyna_s i=Master1.k ncpu=-8 memory=20M
sh Cutter.sh
```

C.4 Cutter.sh

The cutter file is a shell script, where the data from the ASCII file is cut out, and stored in a file, which is then loaded into the ObjectFunction.java script. An example of the code can be seen in the following.

```
tail -y1 "filename" | head -y2 > nod.data
cut -c x1-x2 nod.data > final.data
```

Based on this exemplified code, an example of how this code works in the file can be seen on figure C.3.

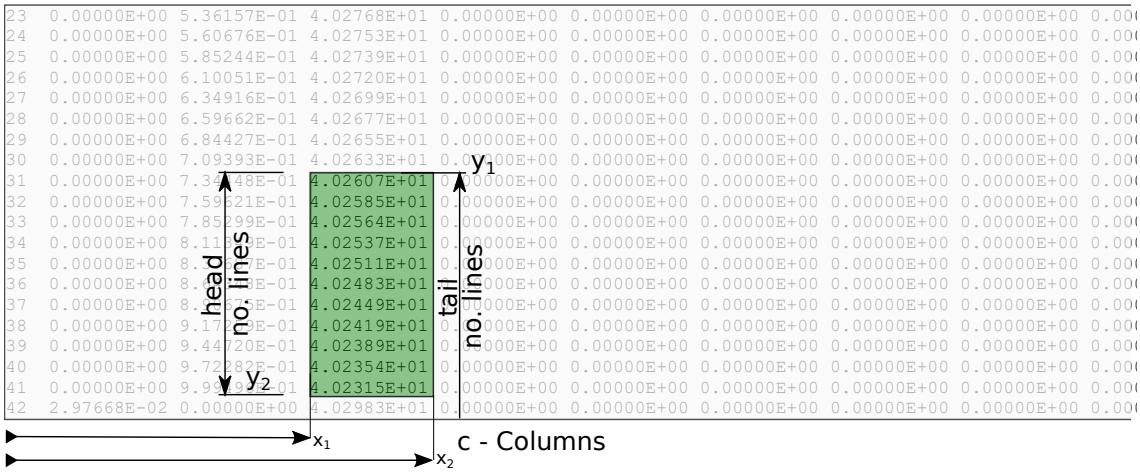

Figure C.3. An example of the way the Cutter.sh shell script works.

Fins Manufacturing at Vestas Aircoil A/S

D

The following Appendix chapter contains some additional information about the Numerical Model and the Optimisation, from Chapter 5. The keywords and the additional files can be found in the appended zip-file. The content of this Appendix chapter are listed beneath:

- Simulation Documentation
- Keyword Documentation: First Model
- Keyword Documentation: Second Model
- Optimisation Documentation

D.1 Simulation Documentation

A video of the simulation can be found via the following link or QR code:

`https://youtu.be/CUNLs4OWCF4`

Figure D.1. QR with link to simulation video on youtube.

The parts in the numerical model can be seen in table D.1, and each forming operation can be seen in the following figures: D.2, D.3, D.4, D.5, D.6, D.7, D.8 and D.9.

Table D.1. A list of the different parts in the numerical model, and the associated no. of elements.

Part	id	Number of Elements
Blank	1	2268
Blank Holder	2	2800
Punch 3	3	3125
Die 4	4	3430
Punch 5	5	3875
Die 6	6	3850
Punch 7	7	3875
Die 8	8	4550
Punch 9	9	3875
Die 10	10	8155
Punch 11	11	10150
Die 12	12	7830
Die 13	13	5005
Punch 0	21	3125
Blank Holder 2	22	910
Second Model		
Trimmed Blank	1	1844
Blank Holder	2	2800
Blank Holder 22	22	910
Blank Holder 3	23	1750
Die 12	12	7830
Die 15	15	5250
Punch 11	11	10010
Punch 14	14	3600

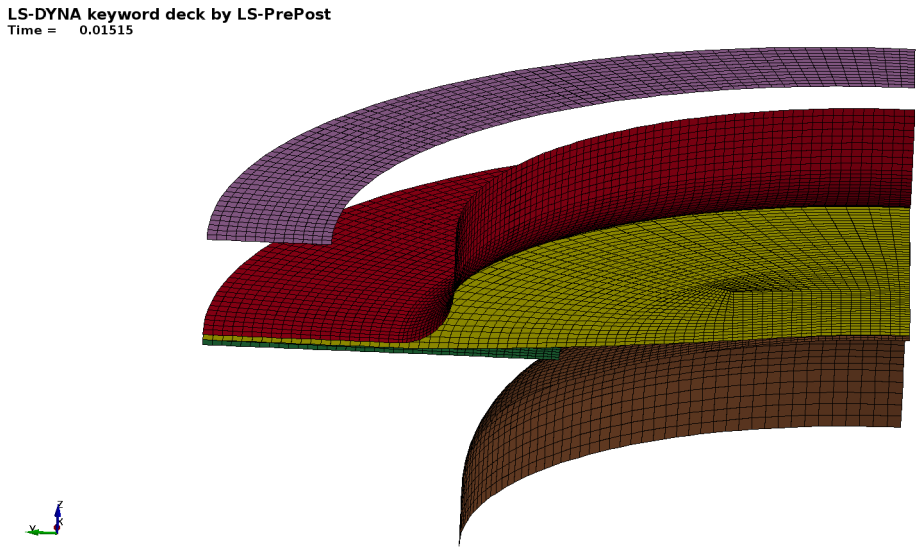

Figure D.2. The first forming step, where the red part is the die 4, yellow: the blank, Green: Blank Holder, Brown: Punch 0 and purple is the Blank Holder 2.

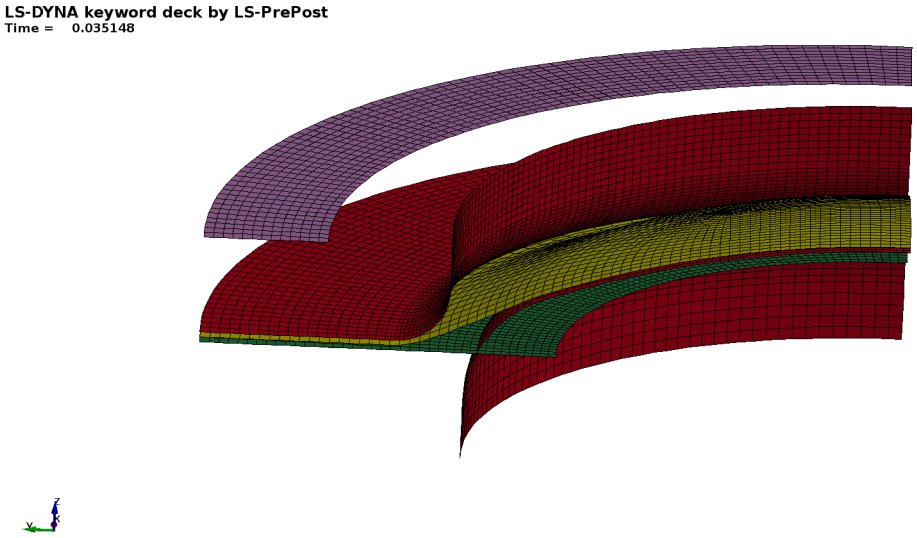

Figure D.3. The second forming step, where the red part is the die 4, yellow: the blank, Green: Blank Holder, Red is Punch 3, and purple is the blank holder 2.

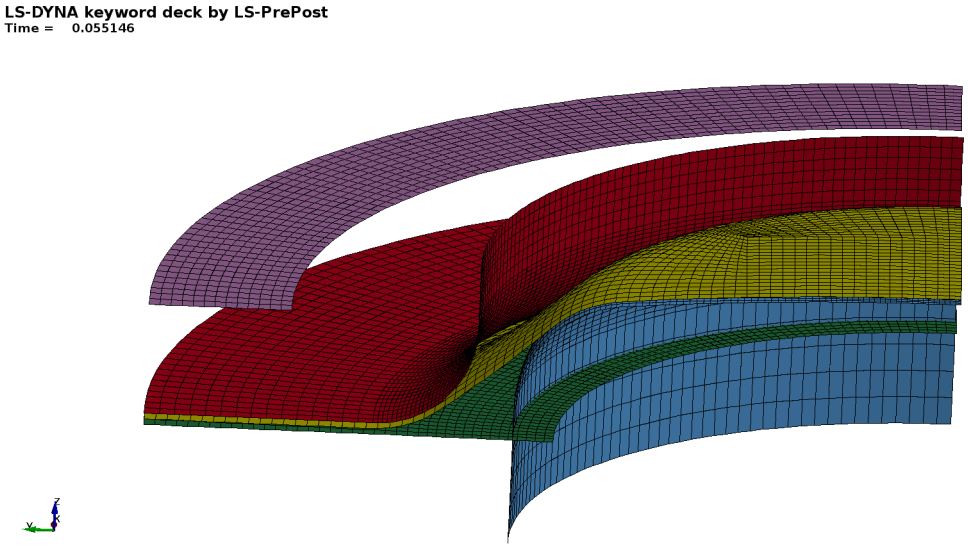

Figure D.4. The third forming step, where the red part is the die 6, yellow: the blank, Green: Blank Holder, blue is Punch 5, and purple is the blank holder 2.

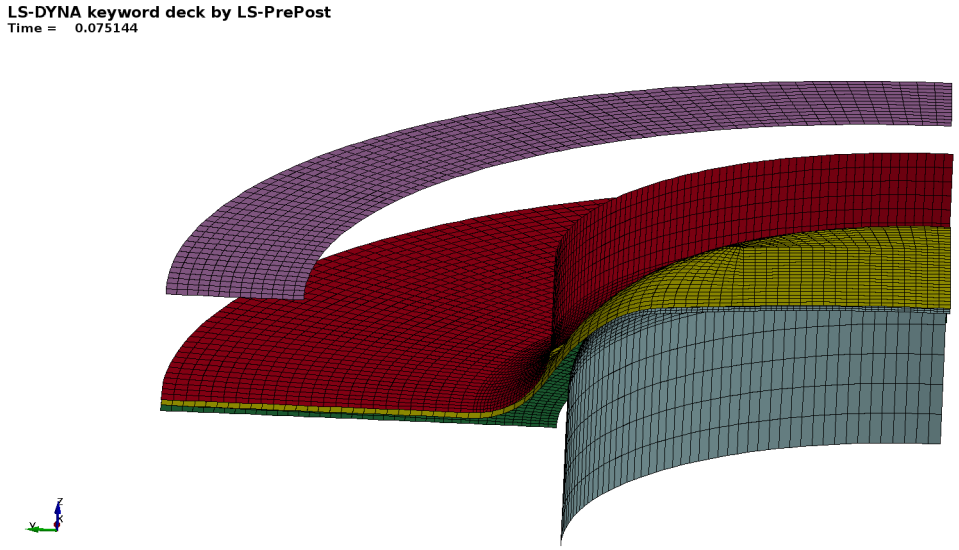

Figure D.5. The fourth forming step, where the red part is the die 8, yellow: the blank, Green: Blank Holder, blue is Punch 7, and purple is the blank holder 2.

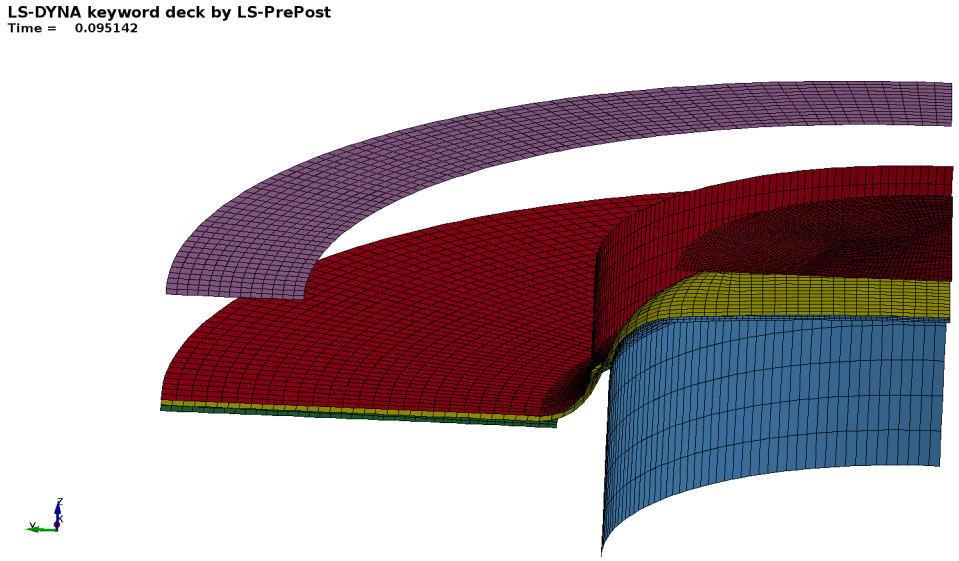

Figure D.6. The fifth forming step, where the red part is the die 10, yellow: the blank, Green: Blank Holder, blue is Punch 9, and purple is the blank holder 2.

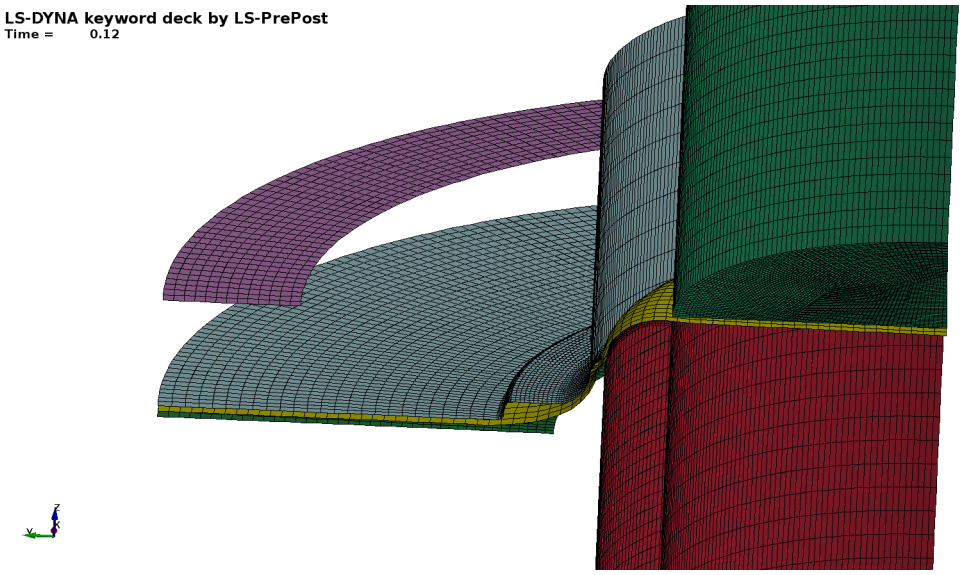

Figure D.7. Halfway of the sixth forming step, and the final operation of the first model, where the red part is the punch 11, yellow: the blank, Green: Blank Holder, blue: Die 12, green: Die 13, and purple: blank holder 2.

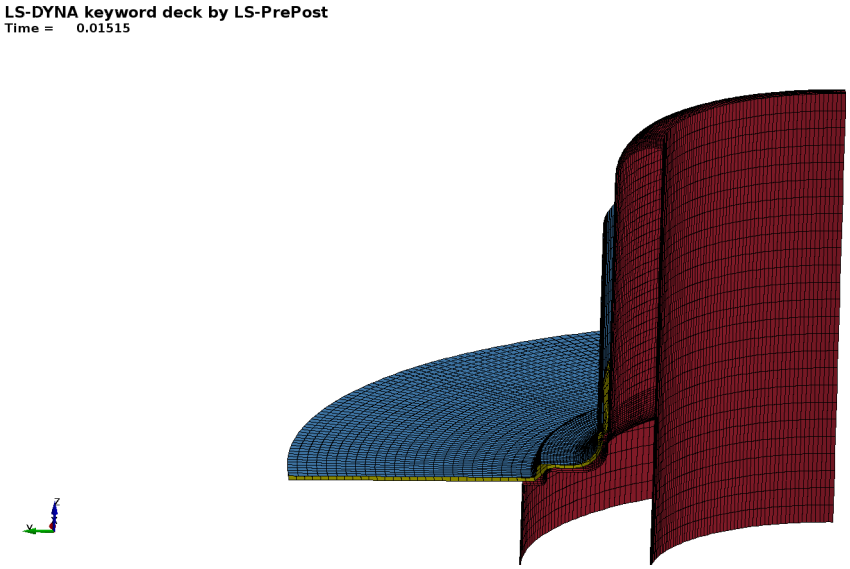

Figure D.8. The first forming step in the second model, but the sixth overall, right after the trimming, where the Blue: Die 12, Yellow: Trimmed Blank and Red: Punch 11.

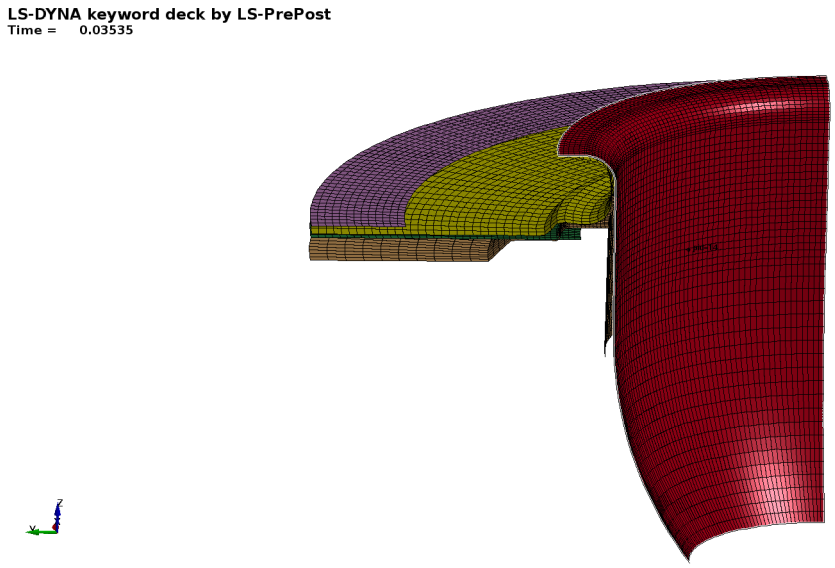

Figure D.9. The final seventh forming operations, which is used for the optimisation, where the yellow: Trimmed Blank, Purple: Blank holder, Green: Blank Holder, Brown: Die 15 and red: Punch 14

D.2 Keyword documentation: First Model

The first model consists of all the forming steps until the trimming operation. This section presents some cut-outs from the final keyword for the first model, and where all the comments are based on [49, 35].:

Control

In the following, the control parameters different from default will be described.

On figure D.10, the Control Shell function is shown, where the `istupd` is changed from 0 to 1, which makes the model include "membrane straining causes thickness change (important for sheet metal forming or whenever membrane stretching is important)" throughout the simulation. This is utilised for initially investigating the FLD effects on this model, and the thickness changes.

```
1   *CONTROL_SHELL
2   $#  wrpang     esort     irnxx    istupd    theory       bwc     miter      proj
3         20.0         0        -1         1         2         2         1         0
4   $# rotascl    intgrd    lamsht    cstyp6    tshell
5          1.0         0         0         1         0
6   $# psstupd   sidt4tu     cntco    itsflg    irquad
7           0         0         0         0         2
8   $#  nfail1    nfail4   psnfail    keepcs     delfr   drcpsid    drcprm
9           0         0         0         0         0         0       1.0
```

Figure D.10. A cut-out of the control card for shells.

On figure D.11, the termination time for the numerical model can be seen, `endtim`, which is determined based in experience with the model, and the influence from the kinetic

energy.

```
1   *CONTROL_TERMINATION
2   $#  endtim    endcyc     dtmin    endeng    endmas
3         0.12         0       0.0       0.01.000000E8
```

Figure D.11. A cut-out of the control card for the termination.

On figure D.12, the time step size for mass scaled solutions, `dt2ms`, which is set to the current value based on the minimal timestep for having stable contact conditions. And the minus makes it possible for the simulation to change the current timestep during the simulation.

```
1   *CONTROL_TIMESTEP
2   $#  dtinit    tssfac      isdo    tslimt     dt2ms      lctm     erode     ms1st
3         0.0       0.9         0       0.0-5.4330E-8         0         0         0
4   $#  dt2msf   dt2mslc     imscl    unused    unused     rmscl
5         0.0         0         0                           0.0
```

Figure D.12. A cut-out of the control card for the timestep.

Database

In this section, some of the selected database outputs will be presented.

On figure D.13, the settings for the d3plots can be seen, where number of dumps are determined in `npltc` to 200.

```
1   *DATABASE_BINARY_D3PLOT
2   $#      dt      lcdt      beam     npltc    psetid
3         0.0         0         0       200         0
4   $#   ioopt
5           0
```

Figure D.13. A cut-out for the database card for the d3plot.

Boundary Conditions

In this section, the boundary conditions applied to the non-rigid parts will be presented.

On figure D.14, the global boundary conditions are prescribed. Where `tc` is the translational constrain(1: x-axis, 2: y-axis), `rc` is the rotational constrain(5: y and z rotations, 6:z and x rotations), and `dir` gives the direction of the global plane constraints (1: x-direction, 2: y-direction)

```
1   *CONSTRAINED_GLOBAL
2   $#      tc        rc       dir         x         y         z
3           1         5         1       0.0       0.0       0.0
4           2         6         2       0.0       0.0       0.0
```

Figure D.14. A cut-out of the constrained global card.

On figure D.15, the constraints for the round part of the blank, where the nodes are described in a node set called 1, which is assign in `nsid` = 1, and are assign the boundary conditions: `dofx` and `dofy`.

```
*BOUNDARY_SPC_SET_ID
$#      id                                                              heading
          0Edge
$#    nsid       cid      dofx      dofy      dofz     dofrx     dofry     dofrz
         1         0         1         1         0         0         0         0
```

Figure D.15. A cut-out of the boundary SPC card.

Contacts

In this section, the few of the contacts used in this model is described. The general selected contact model is a forming surface to surface, which is very robust for forming simulations, which is penalty based.

On figure D.16, the contact model for the contact between Blank and Blank Holder is presented, where the `fs` is the static friction, which for all the contact models are set to 0.1, `fd` is the dynamic friction, which for all contact models are set to 0.1, similarly the viscous contact damping, `vdc`, is set to 70 %.

```
*CONTACT_FORMING_SURFACE_TO_SURFACE_ID
$#     cid                                                              title
         1Blank - Blank Holder
$#    ssid      msid     sstyp     mstyp    sboxid    mboxid       spr       mpr
         1         2         3         3         0         0         0         0
$#      fs        fd        dc        vc       vdc    penchk        bt        dt
       0.1       0.1       0.0       0.0      70.0         0       0.01.00000E20
$#     sfs       sfm       sst       mst      sfst      sfmt       fsf       vsf
       1.0       1.0       0.0       0.0       1.0       1.0       1.0       1.0
```

Figure D.16. A cut-out for a contact model.

On figure D.17, one of the contact model for the punch's are presented, where the difference from this model to the previously showed one, is the determined birth and death time, `bt` and `dt`, for the contact model, where this model is only prescribed to be used when this forming operations is to be performed.

```
*CONTACT_FORMING_SURFACE_TO_SURFACE_ID
$#     cid                                                              title
         2Blank - Punch 3
$#    ssid      msid     sstyp     mstyp    sboxid    mboxid       spr       mpr
         1         3         3         3         0         0         0         0
$#      fs        fd        dc        vc       vdc    penchk        bt        dt
       0.1       0.1       0.0       0.0      70.0         0      0.02      0.04
$#     sfs       sfm       sst       mst      sfst      sfmt       fsf       vsf
       1.0       1.0       0.0       0.0       1.0       1.0       1.0       1.0
```

Figure D.17. A cut-out for a contact model.

Loads and Motion

The following section, will contain the loads applied in the model, and describe how the motion is prescribed.

On figure D.18, the defined curve function for the blank holder is presented. Since the blank holder acts as a preloaded spring, then the function describes the preload at 100 N, and the increment in spring force to be 3 N/mm

```
*DEFINE_CURVE_FUNCTION_TITLE
Blank Holder force
$#    lcid      sidr       sfa       sfo      offa      offo    dattyp
         4         0       1.0       1.0       0.0       0.0         0
$#                                                                 function
100 +DZRB(4)*3
```

Figure D.18. A cut-out of the curve function.

On figure D.19, the previously defined curve is applied to the blank holder, by using the load rigid body function, which has part id 2, `pid`, the load is acting the z-direction, `dof`: 3, and the previously curve is assigned here, in the `lcid`.

```
*LOAD_RIGID_BODY
$#     pid       dof      lcid        sf       cid        m1        m2        m3
         2         3         4       1.0         0         0         0         0
```

Figure D.19. A cut-out of the load for the blank holder.

On figure D.20, the method used for describing the die's downward and upward movement is presented. The distance for the movement is set to 3, `dist`, and the starting time, `tstart`, time for reaching the position, `tend`, and the prescribed rise time, `trise`. These setting are prescribed for two curve smooth function, which gives a sinus curve for the movement by describing the velocity in the curve. These two curves are the described in another curve-function, where the two are subtracted, such the downwards velocity is positive and the upward velocity is negative.

```
*DEFINE_CURVE_SMOOTH_TITLE
Die 6 down
$#    lcid      sidr      dist    tstart      tend     trise        v0
         5         0       3.0      0.04     0.055     0.004       0.0
*DEFINE_CURVE_SMOOTH_TITLE
Die 6 up
$#    lcid      sidr      dist    tstart      tend     trise        v0
         7         0       3.0    0.0551      0.06     0.002       0.0
*DEFINE_CURVE_FUNCTION_TITLE
Die 6
$#    lcid      sidr       sfa       sfo      offa      offo    dattyp
         9         0       1.0       1.0       0.0       0.0         0
$#                                                                 function
LC5-LC7
```

Figure D.20. A cut-out of the defining curve for die 6.

On figure D.21, a representation of the prescribing of the curve function to the boundary prescribed motion rigid, where the previously described curve for die 6, is applied in line 6-9, where the part id, `pid`: 6, the direction for the prescribed motion in the z-direction, `dof`:3, the load curve, `lcid`:9, scaling factor, `sf`:-1.

```
1  *BOUNDARY_PRESCRIBED_MOTION_RIGID_ID
2  $#      id                                                              heading
3            0Die 4
4  $#     pid       dof       vad      lcid        sf       vid     death     birth
5            4         3         0         3      -1.0         01.00000E28       0.0
6  $#      id                                                              heading
7            0Die 6
8  $#     pid       dof       vad      lcid        sf       vid     death     birth
9            6         3         0         9      -1.0         01.00000E28       0.0
10 $#      id                                                              heading
11           0Die 8
12 $#     pid       dof       vad      lcid        sf       vid     death     birth
13           8         3         0        10      -1.0         01.00000E28       0.0
14 $#      id                                                              heading
15           0Die 10
16 $#     pid       dof       vad      lcid        sf       vid     death     birth
17          10         3         0        15      -1.0         01.00000E28       0.0
18 $#      id                                                              heading
19           0Die 12
20 $#     pid       dof       vad      lcid        sf       vid     death     birth
21          12         3         0        16      -1.0         01.00000E28       0.0
22 $#      id                                                              heading
23           0Die 13
24 $#     pid       dof       vad      lcid        sf       vid     death     birth
25          13         3         0        16      -1.0         01.00000E28       0.0
```

Figure D.21. A cut-out for all the prescribed motion for the rigid parts.

Parts

The following section presented the part handling, the material models, and the element formulation used.

On figure D.22, the way that all the different parts are positioned are described, where the part id, `pid`, and the z axis displacement, `xmov`, is described for the presented parts. This method shows what position each part is positioned in. Where all parts are constructed to be positioned to be at origo initially, and then move when the model is initiated.

```
1  *PART_MOVE
2  $#   pid            xmov            ymov            zmov     cid    iset
3         21             0.0             0.0            -2.4       0       0
4         13             0.0             0.0            1.68       0       0
5         11             0.0             0.0           -1.19       0       0
6         22             0.0             0.0       -1.11802       0       0
7          2             0.0             0.0            -1.3       0       0
8          1             0.0             0.0            -1.3       0       0
9          3             0.0             0.0           -0.87       0       0
10         5             0.0             0.0            -0.6       0       0
11         7             0.0             0.0            -0.9       0       0
12         9             0.0             0.0           -1.05       0       0
```

Figure D.22. A cut-out of the part move function.

On figure D.23, is the material model prescribed for the blank, which is Material Model no. 18: "This is an isotropic plasticity model with rate effects which uses a power law

hardening rule.", For this model the inputs are: Density, `ro`, Young's Modulus, `e`, Poissons Ratio, `pr`, Strength Coefficient, `k`, Hardening exponent, `n`.

```
*MAT_POWER_LAW_PLASTICITY_TITLE
Cobber-Blank
$#     mid        ro         e        pr         k         n       src       srp
         18.96000E-9  118000.0       0.3     315.0      0.54       0.0       0.0
$#    sigy        vp      epsf
       0.0       0.0       0.0
```

Figure D.23. A cut-out of the material model used for the blank.

On figure D.24, the element formulation for the blank is shown. For this the `elform` 2 is used which is Belytschko-Tsay formulation, which is very efficient and cheap, and 7 integration points are used through the thickness(`nip`). Finally, the shell thickness is prescribed as 0.18 mm, which is prescribed for `t1, t2, t3, t4`.

```
*SECTION_SHELL_TITLE
Blank
$#   secid    elform      shrf       nip     propt   qr/irid     icomp     setyp
         1         2       1.0         7       1.0         0         0         1
$#      t1        t2        t3        t4      nloc     marea      idof    edgset
      0.18      0.18      0.18      0.18       0.0       0.0       0.0         0
```

Figure D.24. A cut-out for the section shell card for the blank.

On figure D.25, an example of the material model prescribed for all the tooling parts are presented. Here a rigid material model is selected, which is recommended for tools. The inputs for the rigid tool part is: Density, `ro`, Young's Modulus, `e`, Poissons Ratio, `pr`, Constraints applied in the global direction, `cmo`=1, First constraint parameters(Translation), `con1` (4=x,y-direction), Second constraint parameter (Rotational), `con2` (7=x,y,z-rotation).

```
*MAT_RIGID_TITLE
Blank Holder
$#     mid        ro         e        pr         n    couple         m     alias
         27.90000E-9  210000.0       0.3       0.0       0.0       0.0
$#     cmo      con1      con2
       1.0         4         7
$#lco or a1        a2        a3        v1        v2        v3
       0.0       0.0       0.0       0.0       0.0       0.0
```

Figure D.25. A cut-out of the rigid material model for the tooling parts.

On figure D.26, the element formulation for the tooling parts can be seen. This one is similar to the one for the blank, however, here the number of integration points are by default set to one, when using rigid materials. Furthermore, the rigid parts are applied a thickness of 0.5 mm, which is selected based on experience, so the tooling parts are assigned a "mass".

```
1   *SECTION_SHELL_TITLE
2   Blank Holder
3   $#   secid    elform      shrf       nip     propt   qr/irid     icomp     setyp
4            2         2       1.0         1       1.0         0         0         1
5   $#      t1        t2        t3        t4      nloc     marea      idof    edgset
6          0.5       0.5       0.5       0.5       0.0       0.0       0.0         0
```

Figure D.26. A cut-out for the section shell card for the rigid parts.

Creating the dynain file

In the following section, the inputs used for creating the dynain file is presented. This dynain file is used for the second model as the input for the current model.
On figure D.27, the first 6 lines are creating the part list, which contain part id 1, `pid1`, and this part list is used for the interface springback lsdyna, function, which creates a dynain file containing the strains for each element.

```
1   *SET_PART_LIST_TITLE
2   Blank
3   $#     sid       da1       da2       da3       da4    solver
4            1       0.0       0.0       0.0       0.0MECH
5   $#    pid1      pid2      pid3      pid4      pid5      pid6      pid7      pid8
6            1         0         0         0         0         0         0         0
7   *INTERFACE_SPRINGBACK_LSDYNA
8   $#    psid      nshv     ftype         _    ftensr    nthhsv         _   intstrn
9            1         0         0         0         0         0         0         0
```

Figure D.27. A cut-out from the creation of the dynain-file.

D.3 Keyword documentation: Second Model

For the second model, most of the same inputs are used, only different parts, see table D.1, which are listed beneath:

- Parts
- Boundary Conditions
- Control
- Contacts
- Loads and Motion

The parts, see table D.1, which are included in the model, are moved as can be seen in figure D.28.

```
1   *PART_MOVE
2   $#   pid           xmov           ymov           zmov     cid    iset
3         11            0.0            0.0          -1.19       0       0
4          2            0.0            0.0           -3.0       0       0
5         12            0.0            0.0           -3.0       0       0
```

Figure D.28. A cut-out of the part-move for the second model.

Trimming

In the following, the trimming method used in LS-DYNA will be presented.

On figure D.29, the inputs to the trimming functions are given. Generally, line 1-6 are giving the area at which the trimming should be performed, and the part set list is to determine which part is to be trimmed, and this part-list is the prescribed trimming in Control Trimming.
The input for the DEFINE_CURVE_TRIM_NEW is: the trimming curve type, `TCTYPE`=1 (Curve data in XYZ format), Element removal option, `TFLG`=1 (Remove material inside curve), Tolerance limiting size for small elements created during trimming, `TCTOL`, finally the X and Y coordinates for the trimming curve, `CX` and `CY`.

```
1  *DEFINE_CURVE_TRIM_NEW_TITLE
2  Trimline
3  $#    tcid    tctype      tflg      tdir     tctol      toln    nseed1    nseed2
4         112         1         1         0      0.25       1.0      4254      4371
5  $#                cx                cy
6                 CoordX             CoordY
7  *SET_PART_LIST_TITLE
8  trimer
9  $#     sid       da1       da2       da3       da4    solver
10          66       0.0       0.0       0.0       0.0MECH
11 $#    pid1      pid2      pid3      pid4      pid5      pid6      pid7      pid8
12          1         0         0         0         0         0         0         0
13 *CONTROL_FORMING_TRIMMING
14        66
```

Figure D.29. A cut-out for the trimming cards.

Database

In the following, the database settings, which are used for the optimisation are presented here.

On figure D.30, the database card for the NODOUT file is presented, together with the selected sampling rate, `dt`.

```
1  *DATABASE_NODOUT
2  $#      dt    binary      lcur     ioopt   option1   option2
3  1.00000E-4         0         0         1       0.0         0
```

Figure D.30. A cut-out of the NODOUT creation.

On figure D.31, the selected nodes which are to be stored in the output NODOUT file, are selected.

```
1  *DATABASE_HISTORY_NODE
2  $#     id1       id2       id3       id4       id5       id6       id7       id8
3     2301859      1539      1558      1577      1596      1615      1634      1653
4        1691         0         0         0         0         0         0         0
```

Figure D.31. A cut-out for the nodes, which are to be used in store in the NODOUT file.

Parameters

In the following, the implemented parameter are shown.

On figure D.32, the parameters implemented by the `*PARAMETER` function, and the use of the parameters in the define curve function, where the parameters are implemented.

```
1   *PARAMETER
2    Rd ,8.50000
3    ...
4    *DEFINE_CURVE_SMOOTH_TITLE
5   Punch 14 down
6   $#     lcid      sidr      dist    tstart      tend     trise        v0
7             5         0        &d      0.02     0.035     0.004       0.0
8   *DEFINE_CURVE_SMOOTH_TITLE
9   Punch 14 Up
10  $#     lcid      sidr      dist    tstart      tend     trise        v0
11            6         0        &d    0.0351      0.04     0.004       0.0
```

Figure D.32. A cut-out of the applied parameter d.

D.4 Optimisation Documentation

In this section, the summary from the optimisation will be presented. Here a summary can be seen in table D.2, and on figure D.33 shows the cost functions for each iteration, and figure D.34 and D.35 shows the parameters for each iteration.

Table D.2. The summary for the optimisation run for the Fins case.

Object Function		Function Evaluations			Trust-Region	
Initial	Optimum	Total	Evaluation	Jacobian	Increase	Decrease
0.369	0.142	21	12	12	4	6

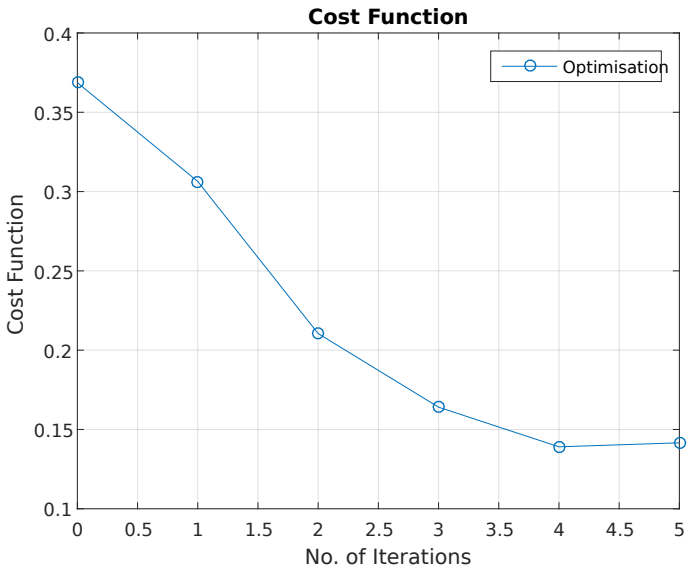

Figure D.33. The cost function for the tool optimisation.

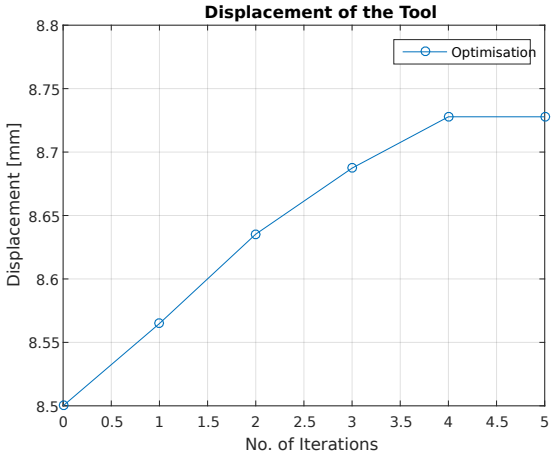

Figure D.34. The displacement for each iteration.

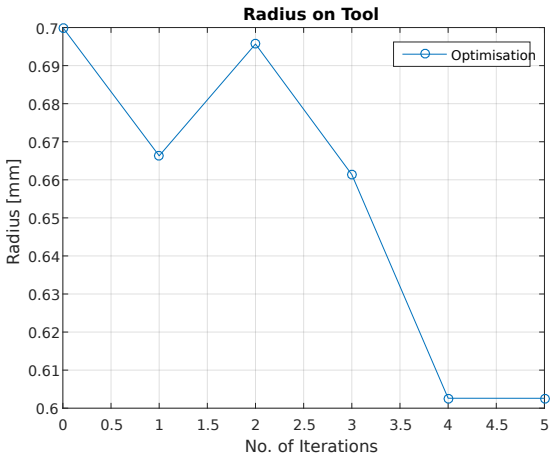

Figure D.35. The radius for each iteration.

Small Radius Cup

E

In the following, this Appendix will present some additional information of the Bulging-Pressure Compound forming, Chapter 6. The content for this Appendix can be seen beneath:

- Process Preparation
- Simulation Documentation
- Keyword Documentation
- Optimisation Documentation

E.1 Process Preparation

In preparation of modelling the bulging-pressing compound forming process, was the drawing on figure E.1 made, among others, with the measurements presented by Wang et al. [51].

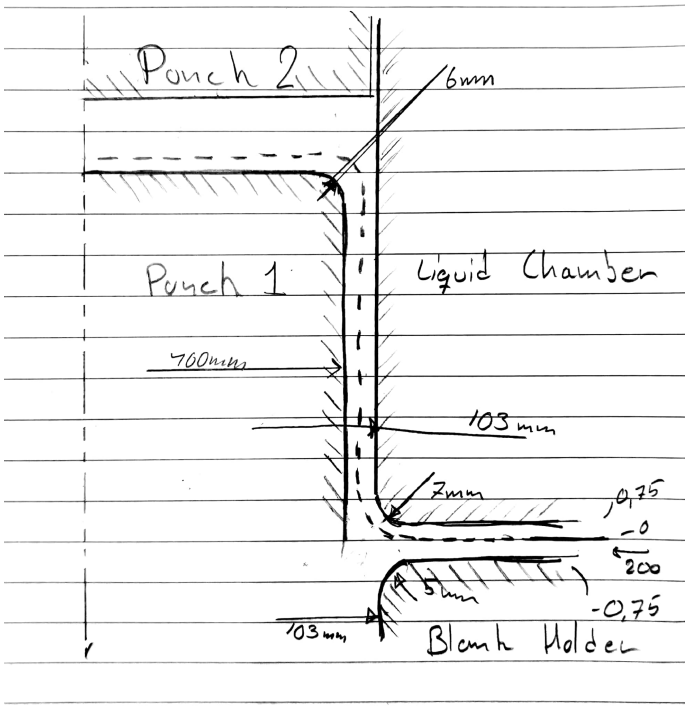

Figure E.1. text

E.2 Simulation Documentation

The simulations files can be found in the attached zip archive.
A video of the simulation can be found via the following link or QR code:

`https://youtu.be/ZEwuO01M6oE`

Figure E.2. QR with link to simulation video on youtube.

This section contains photos of the simulation, where different stages can be seen (figure E.3, E.4 and E.5) along with a comparison of the radius before and after bulging-pressing compound forming operation (figure E.6 and E.7).

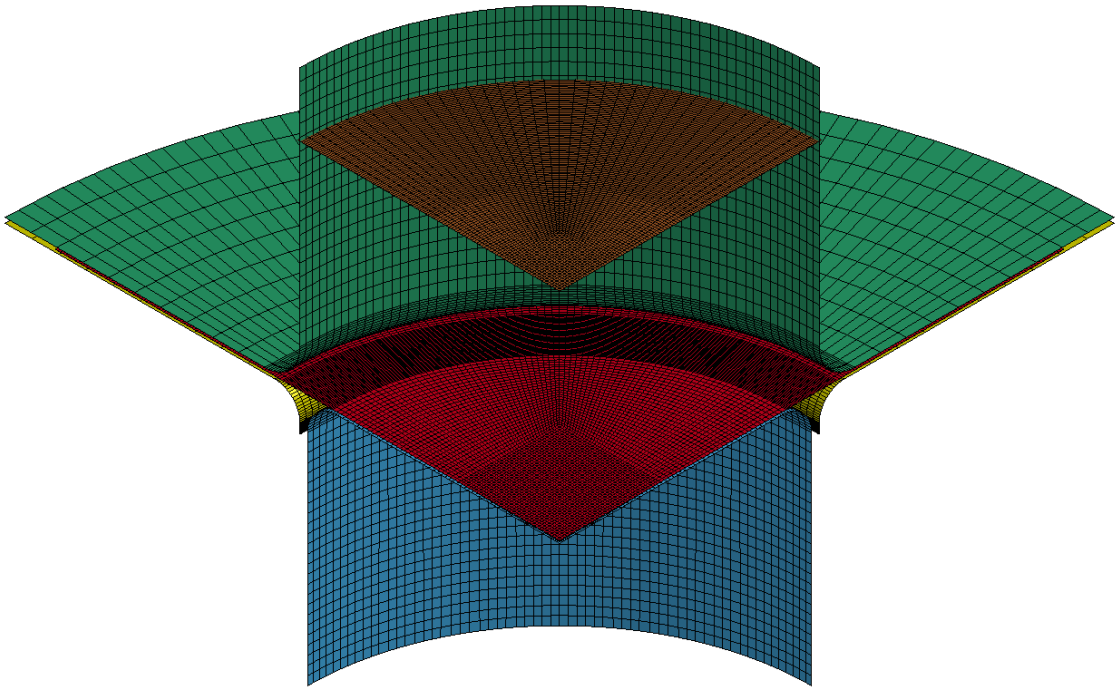

Figure E.3. Model at the initial starting position.

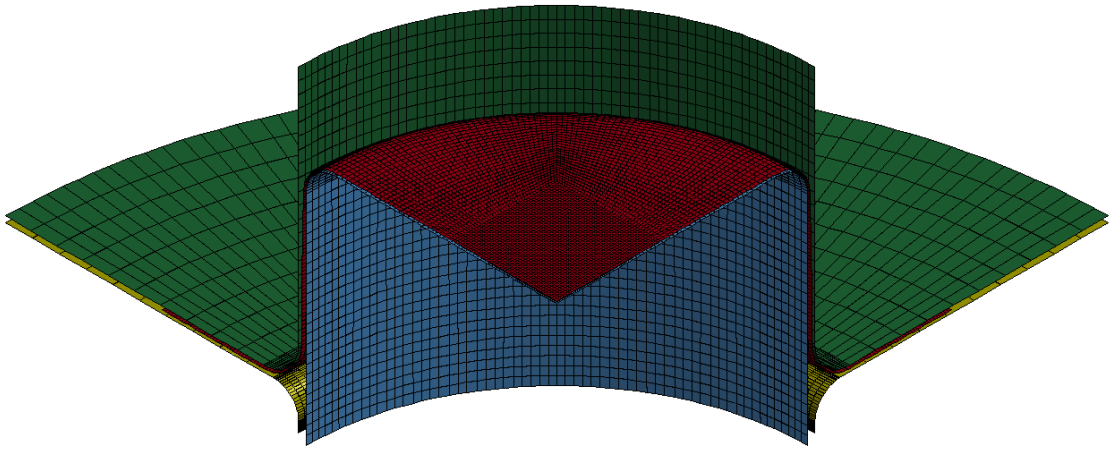

Figure E.4. Simulation at the end of the hydromechanical deep drawing operation.

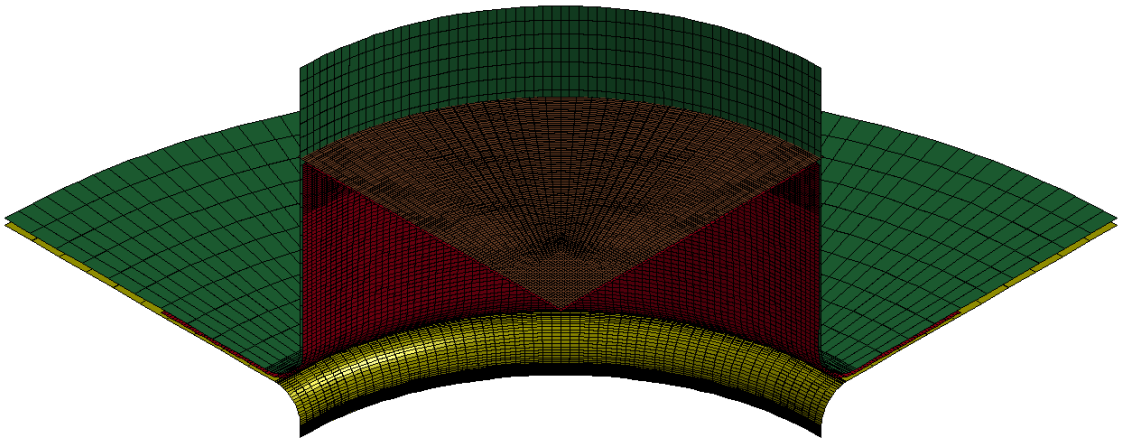

Figure E.5. Simulation at the end of the bulging-pressing compound forming operation.

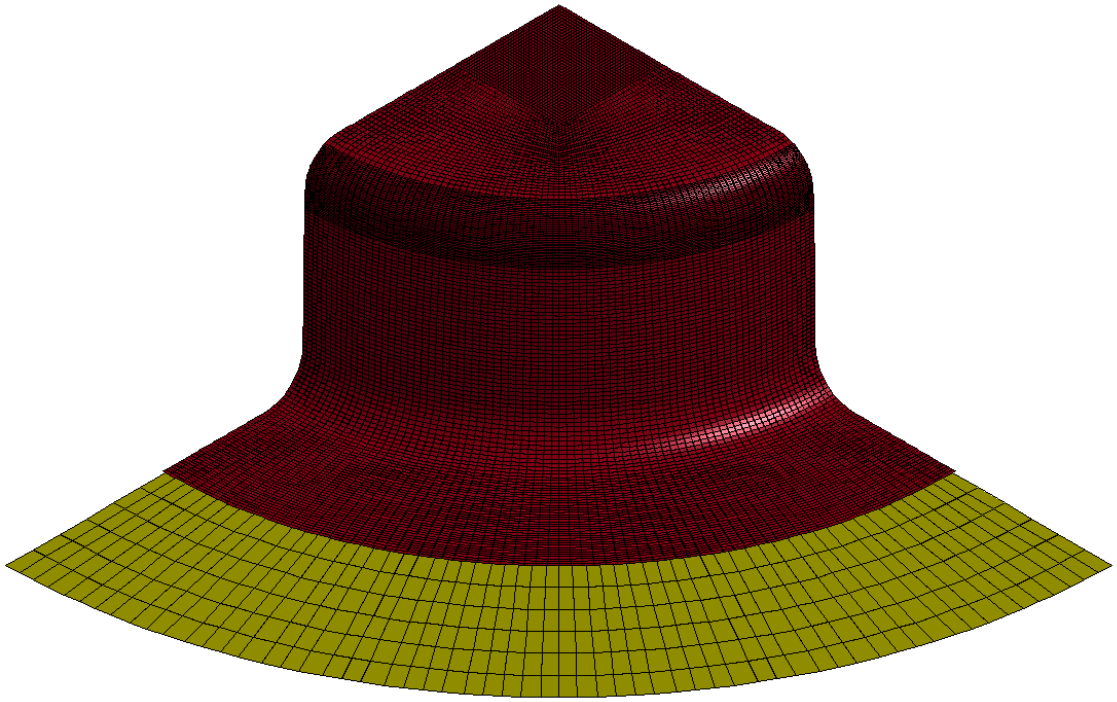

Figure E.6. Cup where the corner radius can be seen before the bulging-pressing compound forming operation.

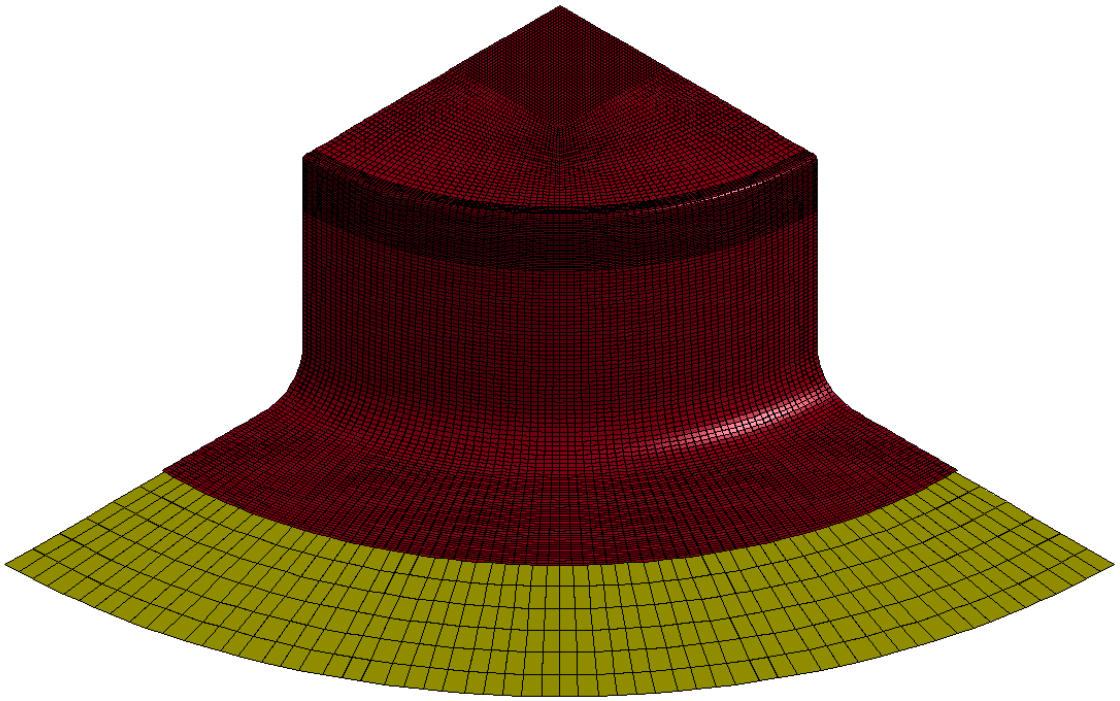

Figure E.7. Cup where the corner radius can be seen after the bulging-pressing compound forming operation.

E.3 Keyword Documentation

Parameter

The parameters of the simulation is defined by the parameter keyword, shown on E.8. The value of the parameters are used in other keyword via the id *Rd1,Rd2* etc.

```
1   *PARAMETER
2    Rd1 ,29.879,Rd2, 5.426,Rd3, 0.979,Rd4, 0.994
3    Rd5, 3.082,Rd6, 0.002
```

Figure E.8. Keyword defining the parameters.

Simulation time step size for mass scaling was set to -1×10^{-7} sec, as shown on figure E.9, the value was selected based on model stability.

```
1   *CONTROL_TIMESTEP
2   $#  dtinit    tssfac      isdo    tslimt     dt2ms      lctm     erode     ms1st
3          0.0       0.9         0       0.0-1.0000E-7         0         0         0
4   $#  dt2msf   dt2mslc     imscl    unused    unused     rmscl
5          0.0         0         0                           0.0
```

Figure E.9. Time step control keyword.

Termination time (figure E.10) was set to 0.021 sec, which allows 0.01 sec for each forming

process, and 0.001 sec for springback.

```
1   *CONTROL_TERMINATION
2   $#  endtim    endcyc     dtmin    endeng    endmas
3        0.021         0       0.0       0.01.000000E8
```

Figure E.10. Termination time control keyword.

Springback was done implicit (figure E.11), time step size was set to allow fast convergence.

```
1   *CONTROL_IMPLICIT_GENERAL
2   $#  imflag       dt0    imform      nsbs       igs     cnstn      form    zero_v
3           -7     0.001         2         1         2         0         0         0
```

Figure E.11. Implicit control keyword.

Database

The databases listed below, was enabled to dump data that could be used by the optimisation. Or to inspect the simulation result.

60 d3plot dump was used to evaluate the simulation visually, defined by the keyword shown on figure E.12. The d3plot was furthermore used to make the position plot, presented in the report.

```
1   *DATABASE_BINARY_D3PLOT
2   $#      dt      lcdt      beam     npltc    psetid
3          0.0         0         0        60         0
4   $#   ioopt
5           0
```

Figure E.12. Keyword controlling d3plot dump rate.

The elemental data was used as a object in the objective function, the element data was set to only dump once at the end of the simulation, by the entry *dt*, shown on figure E.13. Data was only dumped once to limit the size of the file containing the ASCII data.

```
1   *DATABASE_ELOUT
2   $#      dt    binary      lcur     ioopt   option1   option2   option3   option4
3        0.021         0         0         1         0         0         0         0
```

Figure E.13. Keyword controlling element data dump rate.

The elements's data that was saved, was selected with the keyword shown on figure E.14. two element lists was selected id 1 and 2, which contains the element along the X axis, Y axis.

```
1   *DATABASE_HISTORY_SHELL_SET
2   $#     id1       id2       id3       id4       id5       id6       id7       id8
3             1         2         0         0         0         0         0         0
```

Figure E.14. Keyword selecting the element list which element data are saved.

The element lists are defined with the shell list keyword (figure E.15), the id of the element list's id are specified with the *sid* entry. A list is made for the X axis elements and the Y axis and corner elements.

```
1   *SET_SHELL_LIST_TITLE
2   Element List X
3   $#     sid       da1       da2       da3       da4
4             1       0.0       0.0       0.0       0.0
5   $#    eid1      eid2      eid3      eid4      eid5      eid6      eid7      eid8
6                     %%%% Element list side X %%%%
```

Figure E.15. Keyword containing the id of elements, to be used by other keywords.

Node data dump rate was specified with the keyword shown on figure E.16, like element data is the keyword set to only dump once at the end of the simulation.

```
1   *DATABASE_NODOUT
2   $#       dt    binary      lcur     ioopt   option1   option2
3        0.021         0         0         1       0.0         0
```

Figure E.16. Dump rate of the node data, are controlled by this keyword.

With keyword shown on figure E.17, are the node list which node data is saved selected.

```
1   *DATABASE_HISTORY_NODE_SET
2   $#     id1       id2       id3       id4       id5       id6       id7       id8
3             2         0         0         0         0         0         0         0
```

Figure E.17. Node list with nodes that are saved data for.

Boundary Conditions

Movement of the punch 1 used in the hydromechanical deep drawing operation are moved a prescribe amount up a down. On figure E.18 can the keyword controlling this be seen, the part (punch 1) is selected with the entry *pid*, the movement direction is selected with entry *dof* and the curve with the movement is selected with the entry *lcid*.

```
1   *BOUNDARY_PRESCRIBED_MOTION_RIGID_ID
2   $#      id                                                          heading
3             0Punch1
4   $#     pid       dof       vad      lcid        sf       vid     death     birth
5             2         3         0         3       1.0         01.00000E28       0.0
```

Figure E.18. Keyword used to move rigid bodies.

In the punch 1 case is the movement defined with a s-curve (keyword figure E.19), where the start, end and rise time are specified with entries *tstart, tend* and *trise*. The specific movement distance is defined with the entry *dist* which is this case is the parameter `&d1`.

```
1   *DEFINE_CURVE_SMOOTH_TITLE
2   Punch1
3   $#    lcid      sidr      dist    tstart      tend     trise        v0
4            3        0&d1              0.0      0.01     0.003       0.0
```

Figure E.19. S-cruve with a defined start, end and rise time.

The symmetry boundaries along the X and Y axis, are specified with the keyword shown on figure E.20. In the direction normal to the global Y is the model constrained in Y-translation and Z and X rotation. And in global x is the constrains x-translation and Z and Y rotation.

```
1   *CONSTRAINED_GLOBAL
2   $#      tc        rc       dir         x         y         z
3            2         6         2       0.0       0.0       0.0
4            1         5         1       0.0       0.0       0.0
```

Figure E.20. Node list with nodes that are saved data for.

Load

The blank holder force was applied with the load rigid body keyword shown on figure E.21, where the part is specified (*pid*), the force direction (*dof*), load curve (*lcid*) and scale factor (*sf*). The scale factor was in this case ued to control the holder force.

```
1   *LOAD_RIGID_BODY
2   $#     pid       dof      lcid        sf       cid        m1        m2        m3
3            3         3         4   20000.0         0         0         0         0
```

Figure E.21. Rigid body motion keyword used model the blank holder force.

The hydraulic pressure was applied using the load mask method, the keyword for this can be seen on figure E.22. The part the pressure is applied to is specified with *pid*, the load curve with *lcid*. the pressure is only applied to elements within the specified area, which is selected with *lcidm* and the normal vector *vid2*.

```
1   *LOAD_MASK
2   $#     pid      lcid      vid1       off     boxid     lcidm      vid2     inout
3            1         1         0       0.0         0         2         1         0
4   $#  icycle
5           10
6            1         6         0       0.0         0         2         1         0
7           10
```

Figure E.22. Load mask keyword, used for a updating pressure area.

Two load curves was used, one for each operation. On figure E.23 can the load curve for the hydromechanical deep drawing operation be seen, the maximum pressure is controlled be the scaling.

```
1   *DEFINE_CURVE_TITLE
2   Hydro1
3   $#    lcid      sidr       sfa       sfo      offa      offo    dattyp     lcint
4             1         0       1.0       1.0       0.0       0.0         0         0
5   $#                a1                  o1
6                    0.0                 0.0
7                  0.001                 1.0
8                  0.009                 1.0
9                   0.01                 0.0
```

Figure E.23. Hydraulic pressure curve keyword for the hydromechanical deep drawing operation.

The load curve for the bulging-pressing compound forming operation was defined with the load curve shown on figure E.24. The hydraulic pressure of this operation was controlled by the parameters `&d3, &d4, &d5` and `&d6`. The scaling was set to -1 to make the pressure work in the same direction as the element normal, instead of opposite of the normal.

```
 1   *DEFINE_CURVE_TITLE
 2   Hydro2
 3   $#    lcid      sidr       sfa       sfo      offa      offo    dattyp     lcint
 4             6         0       1.0      -1.0       0.0       0.0         0         0
 5   $#                a1                  o1
 6                    0.0                 0.0
 7                   0.01                 0.0
 8                  0.012&d3
 9                  0.015&d4
10                  0.018&d5
11                   0.02&d6
12                 0.0201                 0.0
13                  0.021                 0.0
```

Figure E.24. Hydraulic pressure curve keyword for the bulging-pressing compound forming operation.

The hydraulic pressure area are defined using the same keyword, define curve shown on figure E.25, where the area defined by the area within coordinate points as shown on figure E.26.

```
1   *DEFINE_CURVE_TITLE
2   Hydro1_area
3   $#    lcid      sidr       sfa       sfo      offa      offo    dattyp     lcint
4             2         0       1.0       1.0       0.0       0.0         1         0
5   $#                a1                  o1
6                  %%%% 1/4 Circle corr 50 points. %%%%
```

Figure E.25. Define curve are used ti define the area the pressure at applied in.

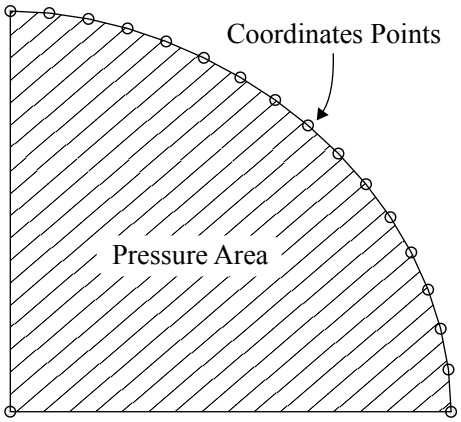

Figure E.26. Pressure area defined by coordinate points.

Contact

All contacts was modelled with the model contact_forming_surface_to_surface (figure E.27), where the two contacts parts are selected with *ssid* and *msid*, one keyword was made the each set of contacts. The friction static and dynamic, *fs* and *fd*, was set to 0.1 and viscous damping *vdc* was set to 70%.

```
*CONTACT_FORMING_SURFACE_TO_SURFACE_ID
$#     cid                                                                title
         1Blank-Punch1
$#    ssid      msid     sstyp     mstyp    sboxid    mboxid       spr       mpr
           1         2         3         3         0         0         0         0
$#      fs        fd        dc        vc       vdc    penchk        bt        dt
        0.1       0.1       0.0       0.0      70.0         0       0.0      0.01
$#     sfs       sfm       sst       mst      sfst      sfmt       fsf       vsf
        1.0       1.0       0.0       0.0       1.0       1.0       1.0       1.0
```

Figure E.27. Contact_forming_surface_to_surface keyword.

Element formulation and material model

Element formulation was specified with the keyword shown on figure E.28. For the blank was element formulation -16 used based on the implicit time period, for the tool parts was element formulation 2 used. The shell thickness is likewise defined in this keyword, which was 1.5 mm for the blank and 1 mm for the tools.

```
*SECTION_SHELL_TITLE
Blank
$#   secid    elform      shrf       nip     propt   qr/irid     icomp     setyp
           1       -16       1.0         5       1.0         0         0         1
$#      t1        t2        t3        t4      nloc     marea      idof    edgset
       1.5       1.5       1.5       1.5       0.0       0.0       0.0         0
```

Figure E.28. Shell element formulation keyword.

The anisotropic material model Hill 3R (figure E.29) was used on the blank, the inputs are: Mass density (*ro*), Young's modulus (*e*), Poisson's ratio ν (*pr*), Hardening rule (*hr*), Strength coefficient for exponential harding (*P1*) and Hardening exponent n (*P2*).

The anisotropic Lankford parameters are likewise specified: *R00, R45* and *R90*.

```
*MAT_HILL_3R_TITLE
Blank
$#     mid        ro         e        pr        hr        p1        p2
         12.70000E-9   71000.0       0.3       2.0     306.0      0.24
$#     r00       r45       r90      lcid        e0
         0.7      0.65       0.6         0       0.0
$#    aopt
         3.0
$#  unused    unused    unused        a1        a2        a3
                                     1.0       0.0       0.0
$#      v1        v2        v3        d1        d2        d3      beta
        0.0       1.0       0.0       0.0       1.0       0.0      45.0
```

Figure E.29. Hill 3R anisotropic material model keyword.

The tool parts was applied the rigid material model, shown on figure E.30, the input for the model are: Mass density (ro), Young's modulus (e), Poisson's ratio ν (pr).

```
*MAT_RIGID_TITLE
Punch1
$#     mid        ro         e        pr         n    couple         m     alias
         27.85000E-9  210000.0       0.3       0.0       0.0       0.0
$#     cmo      con1      con2
         1.0         4         7
$#lco or a1        a2        a3        v1        v2        v3
         0.0       0.0       0.0       0.0       0.0       0.0
```

Figure E.30. Rigid material model, used for tool parts.

E.4 Optimisation Documentation

The optimisation data of the small radii case are presented in table E.1 and E.2. Convergence of the cost function and the parameters are plotted in the figure E.31, E.32, E.33, E.34, E.35 and E.36. The resulting pressure curve is shown on figure E.38.

Table E.1. Shows the parameters, cost function and smallest edge radius for the initial setting, and for the different optimisations which has been performed.

Run	P1 [mm]	P2 [mm]	P3 [MPa]	P4 [MPa]	P5 [MPa]	P6 [MPa]	Cost Function	Radius [mm]
Initial	20.0	3.0	10.0	10.0	10.0	10.0	2427.61	3.93
First	23.22	4.80	9.14	8.62	29.57	199.41	726.40	0.70
Second	23.11	4.60	9.40	2 0.87	21.93	23.14	657.13	0.84
Third	23.09	4.56	9.24	28.37	26.24	56.35	664.39	0.64

Table E.2. Shows the optimisation data for each of the optimisation runs, which are the number of function evaluations and the type, together with the trust region increases, decreases and initial size, and finally the number of iterations.

Run	Function Evaluation			Trust Region			Iterations
	Total	Cost	Jacobian	Increase	Decrease	Initial size	
First	82	22	60	6	12	372.21	10
Second	42	12	30	2	7	40.00	5
Third	69	21	48	4	13	104.58	8

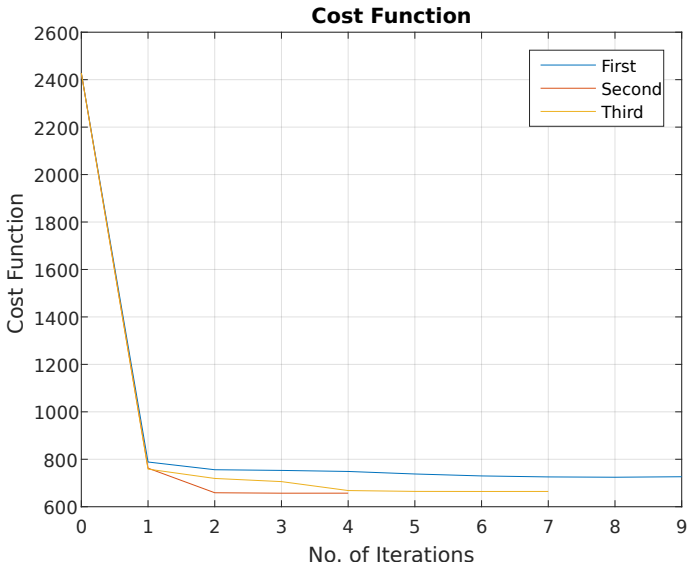

Figure E.31. The cost function for each iteration.

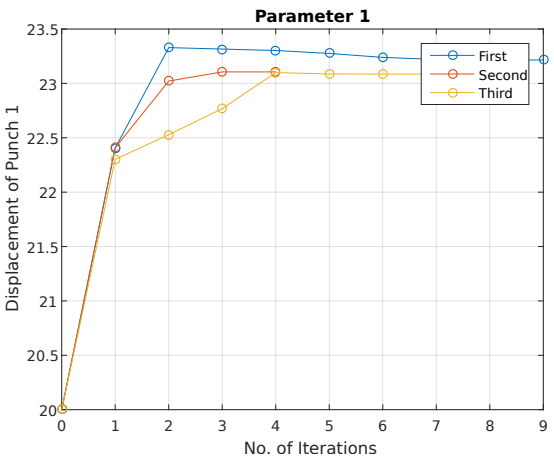

Figure E.32. The displacement of Punch 1 for each iteration.

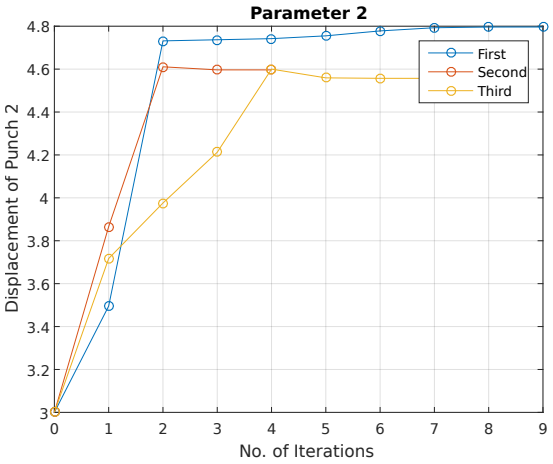

Figure E.33. The displacement of Punch 2 for each iteration.

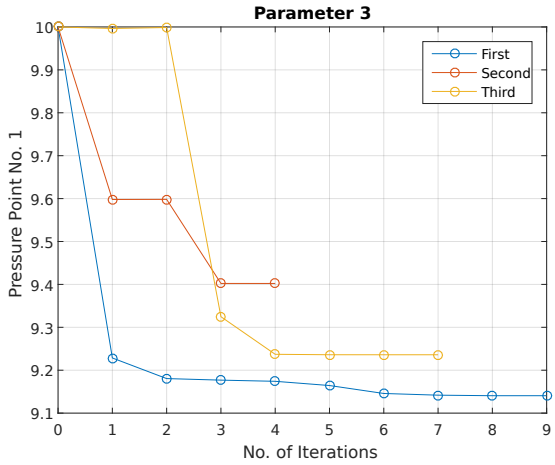

Figure E.34. Pressure point 1 for each iteration.

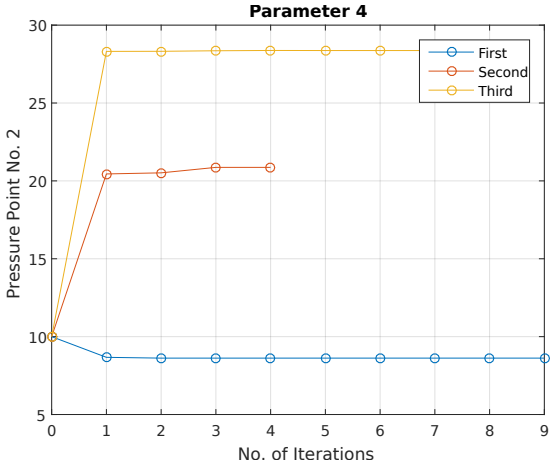

Figure E.35. Pressure point 2 for each iteration.

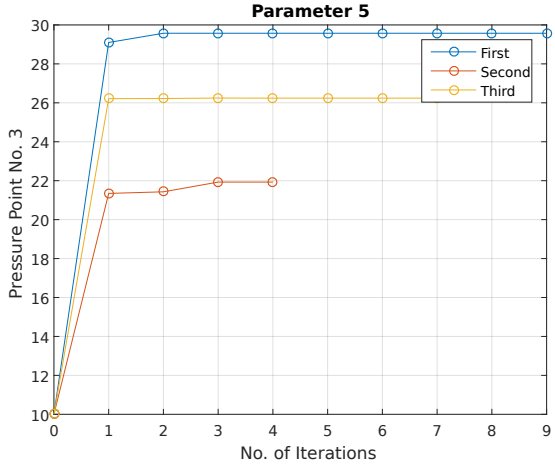

Figure E.36. Pressure point 3 for each iteration.

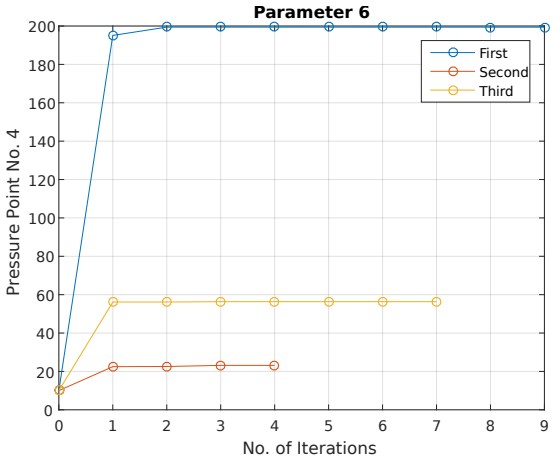

Figure E.37. Pressure point 4 for each iteration.

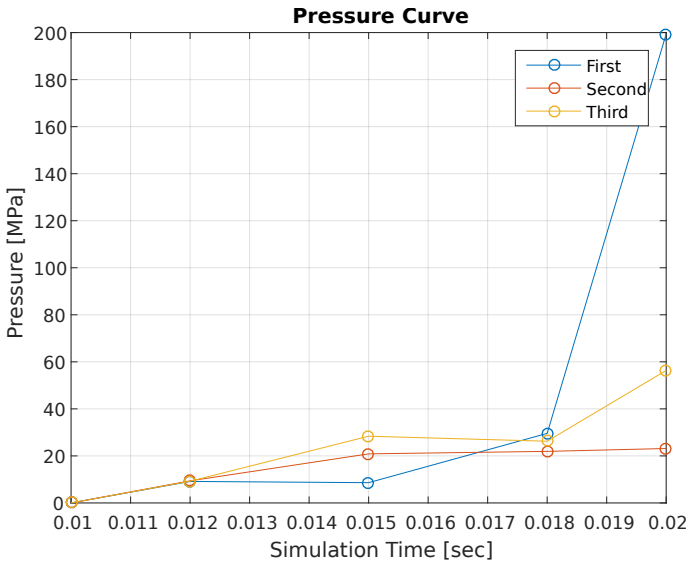

Figure E.38. The optimum pressure curve for each optimisation run.

Small Radii - Lunar Rover Test Piece F

In the following, this Appendix will present some additional information of the Bulging-Pressure Compound forming for the Lunar Rover test piece, Chapter 7. The content for this Appendix can be seen beneath:

- Process Preparation
- Simulation Documentation
- Keyword Documentation
- Optimisation Documentation

F.1 Process Preparation

In preparation of modelling of the processes was the drawings on figure F.1 made, the drawings was part of deciding the measurements of the punches and die.

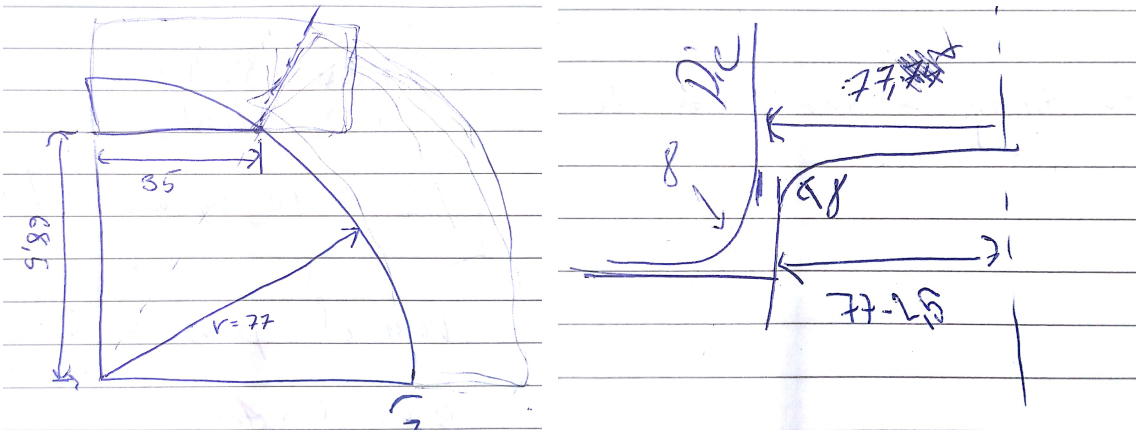

Figure F.1. Drawings of the die, punches and blank with measurements.

F.2 Simulation Documentation

The simulations files can be found in the attached zip archive.
A video of the simulation can be found via the following link or QR code:

https://youtu.be/mM0vfmQH_AA

Figure F.2. QR with link to simulation video on youtube.

This section contains additional photos of the the lunar rover test piece simulation. On figure F.3 can the simulation be seen at the final stage of the hydromechanical deep drawing operation. On figure F.4 can the final stage of the bulging-pressing compound forming operation be seen. On figure F.5 can the blank and blankholder be seen at the end of the simulation after springback. On figure F.6 can the final cup be seen from the top with the liquid chamber.

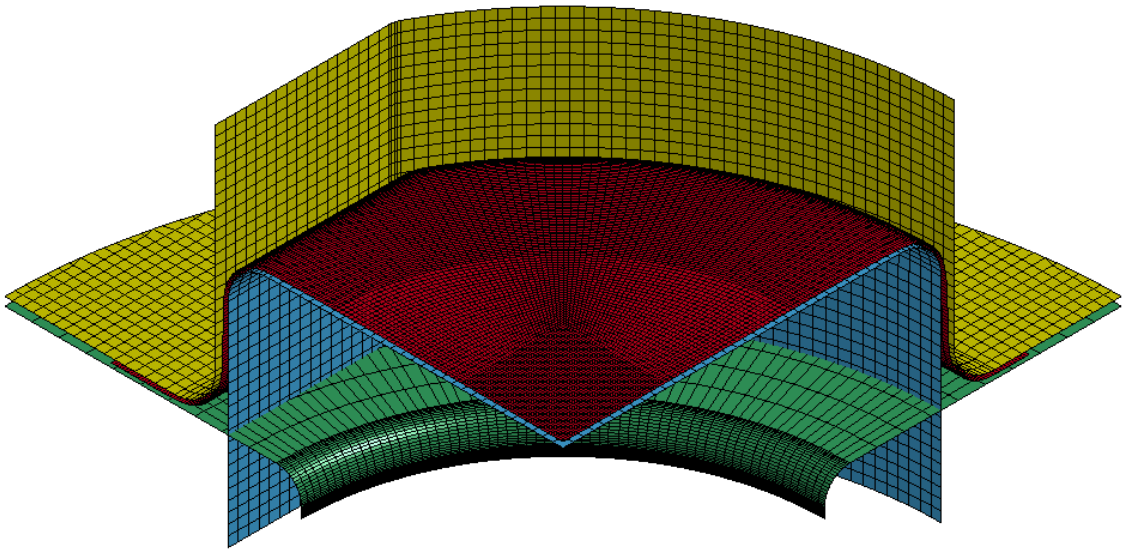

Figure F.3. End of hydromechanical deep drawing operation.

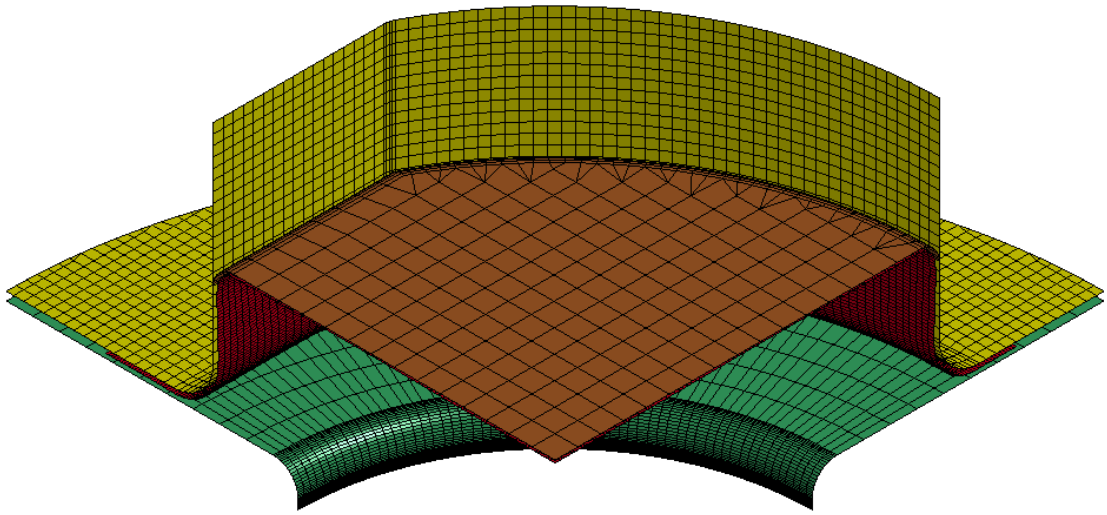

Figure F.4. End of bulging-pressing compound forming operation.

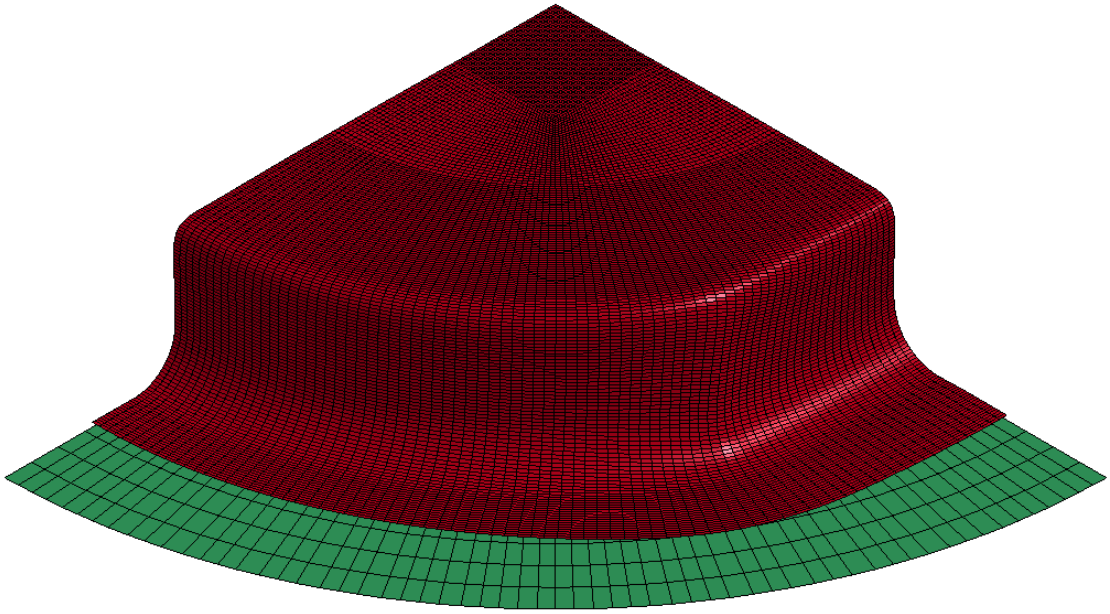

Figure F.5. The final part.

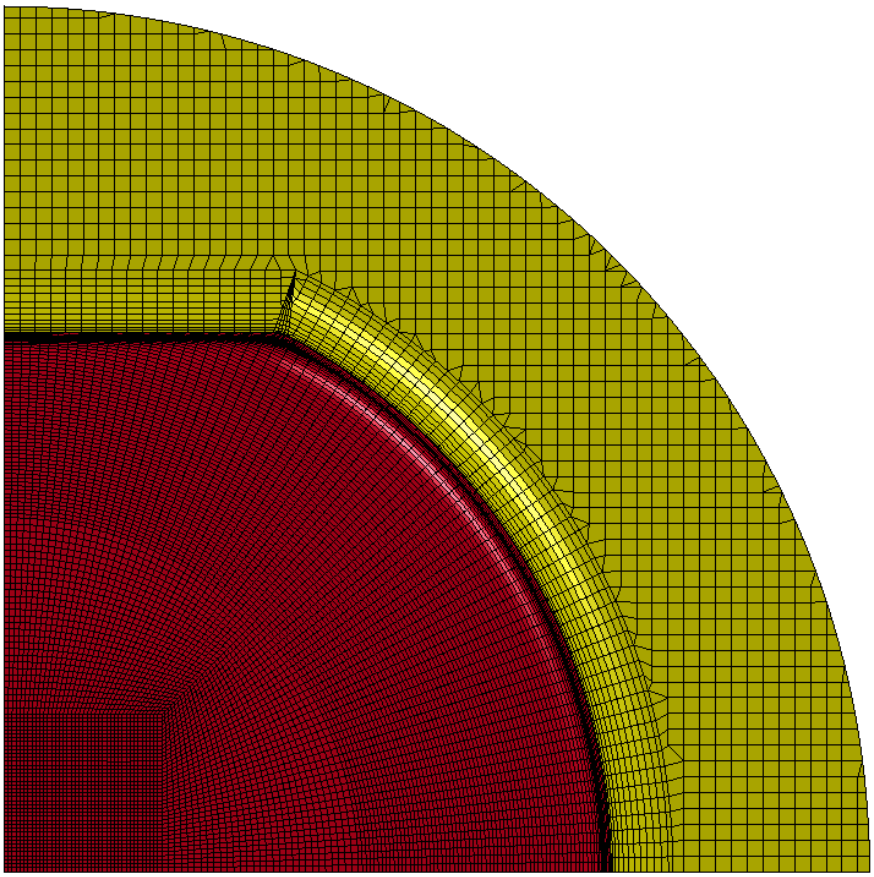

Figure F.6. The final part from the top, and the liquid chamber in yellow.

In table F.1 can the names of the parts, id and the no of elements of each parts be seen.

Table F.1. Parts, id and number of elements

Part	Id	No. Ele.
Blank	1	14320
Punch 1	2	2787
Blankholder	3	3000
Liquid chamber	4	3321
Punch 2	5	2787
Total		26215

F.3 Keyword Documentation

Due to the similarity with the small radii bulging-pressing compound forming case, can the keyword documentation be seen in Appendix E.3. In the lunar rover test piece simulation was the area where the hydraulic pressure change to reflect the part shape, the new area can be seen on figure F.7.

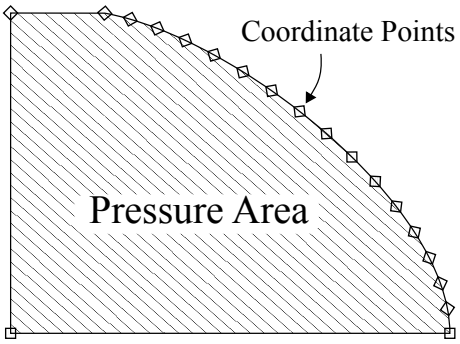

Figure F.7. Pressure area defined by coordinate points.

Furthermore was the maximum pressure in the hydromechanical deep drawing operation defined as a parameter which can be seen on figure F.8. Where the maximum pressure, is defined by the parameters `&d6` at the *sfo* entry.

```
*DEFINE_CURVE_TITLE
Hydro1
$#    lcid      sidr       sfa       sfo      offa      offo    dattyp     lcint
         1         0       1.0       &d6       0.0       0.0         0         0
$#                a1                  o1
                 0.0                 0.0
               0.001                 1.0
               0.009                 1.0
                0.01                 0.0
```

Figure F.8. Hydraulic pressure curve keyword.

F.4 Optimisation Documentation

for the lunar rover test piece optimisation the Total Structured Secant Method (TSSM) was used, the initial trust region was set to 1000. The optimastion data for the two elements sets is documented in table F.2, along with parameter development plots for the simulation with the corner node set, in the following figures; F.9, F.10, F.11, F.12, F.13, F.14, F.15 and F.16.

Table F.2. The summary for the optimisation run for the Fins case.

Run	Object Function		Function Evaluations			Trust-Region	
	Initial	Optimum	Total	Evaluation	Jacobian	Increase	Decrease
Corner set	34995.377	16.565	79	19	60	7	9
Edge set	34993.923	17.644	58	16	42	3	9

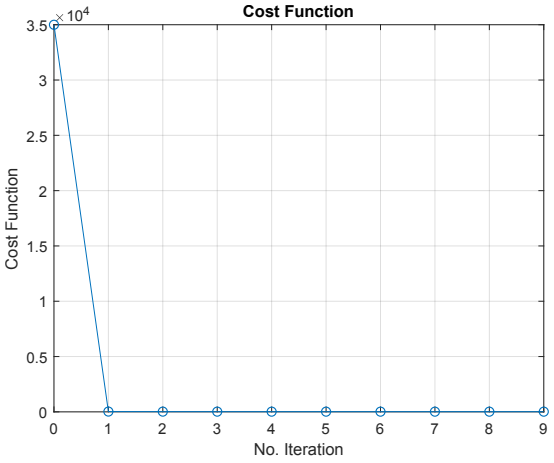

Figure F.9. The cost function for the lunar rover test piece

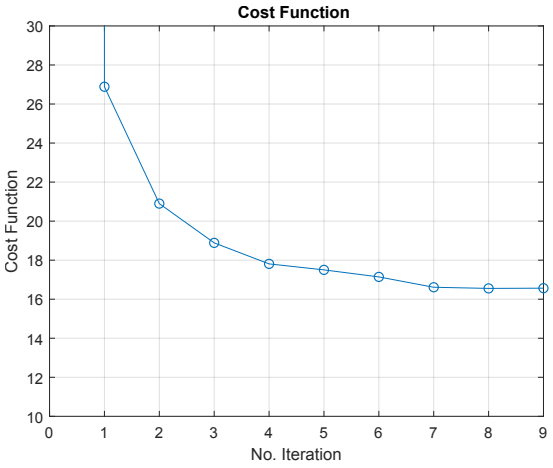

Figure F.10. Scaled version of figure F.9

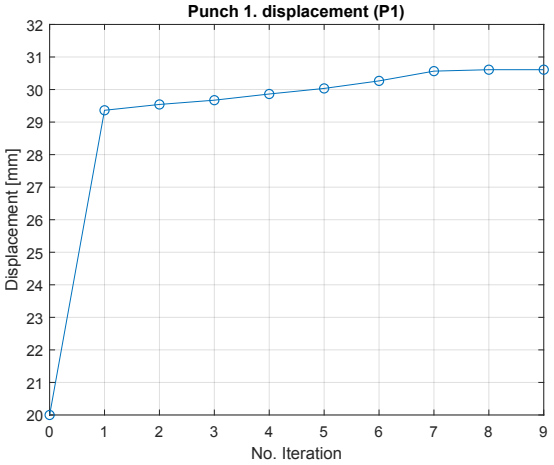

Figure F.11. Displacement of punch 1. in each iteration.

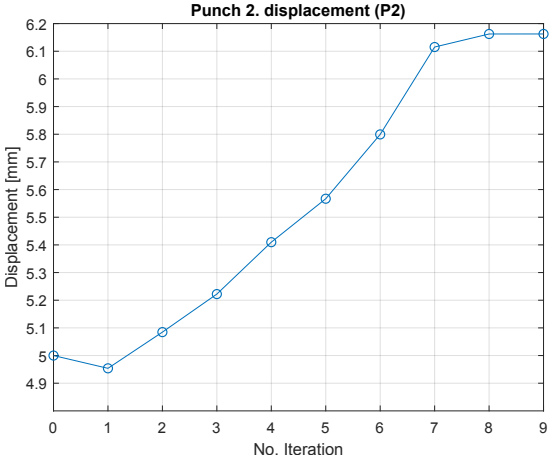

Figure F.12. Iteration development of displacement of punch 2.

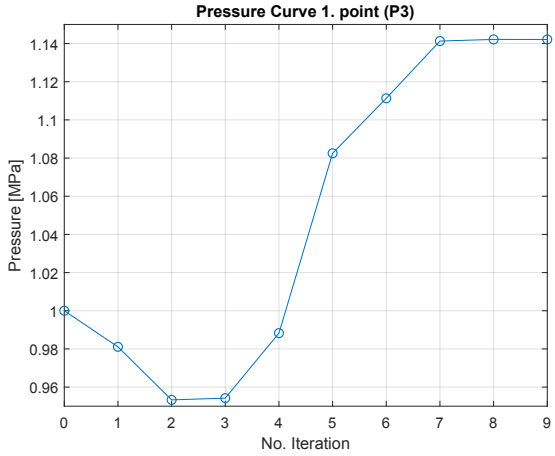

Figure F.13. 1. pressure point of second forming operation.

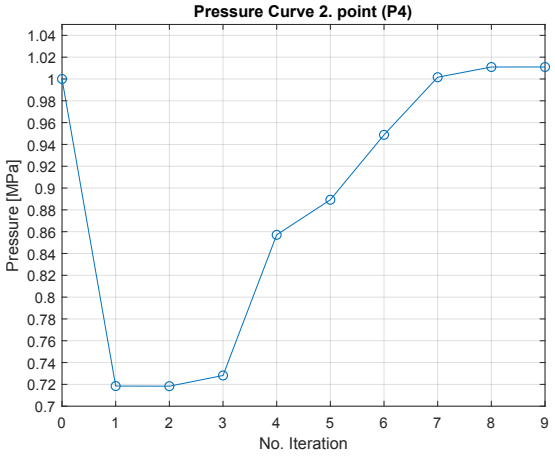

Figure F.14. 2. pressure point of second forming operation.

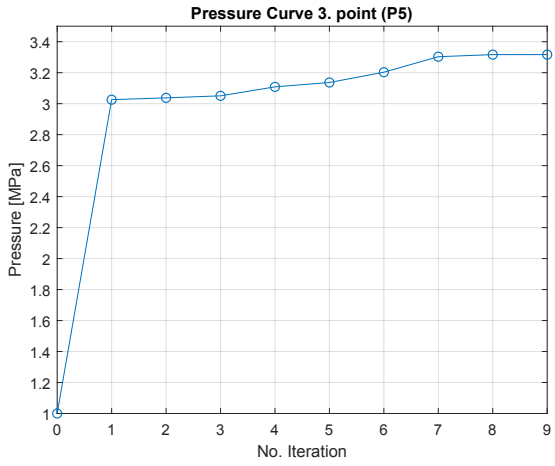

Figure F.15. 3. pressure point of second forming operation.

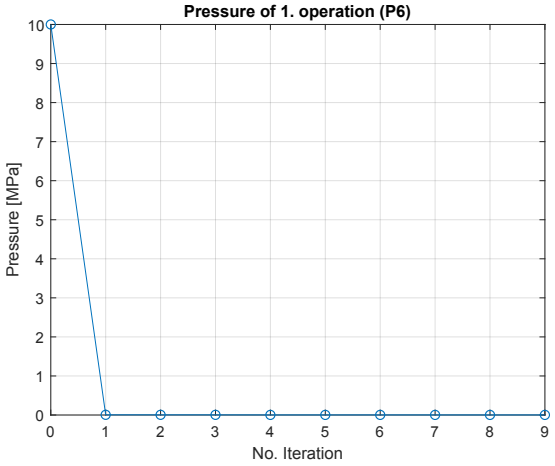

Figure F.16. Pressure of first forming operation, in each iteration.

Hydraulic Expanded Tube-Tubesheet Joint

G

In the following, this Appendix will present some additional information of the Hydraulic Expanded Tube-Tubesheet joint, Chapter 8. The content for this Appendix can be seen beneath:

- Simulation Documentation
- Keyword Documentation
- Optimisation Documentation

G.1 Simulation Documentation

The simulations files can be found in the attached zip archive.
A video of the simulation can be found via the following link or QR code:

`https://youtu.be/JE8adosYziw`

Figure G.1. QR with link to simulation video on youtube.

In this section, the numerical model for the tube-tubesheet case. The model can be seen on figure G.2, and the number of elements can be seen in table G.1.

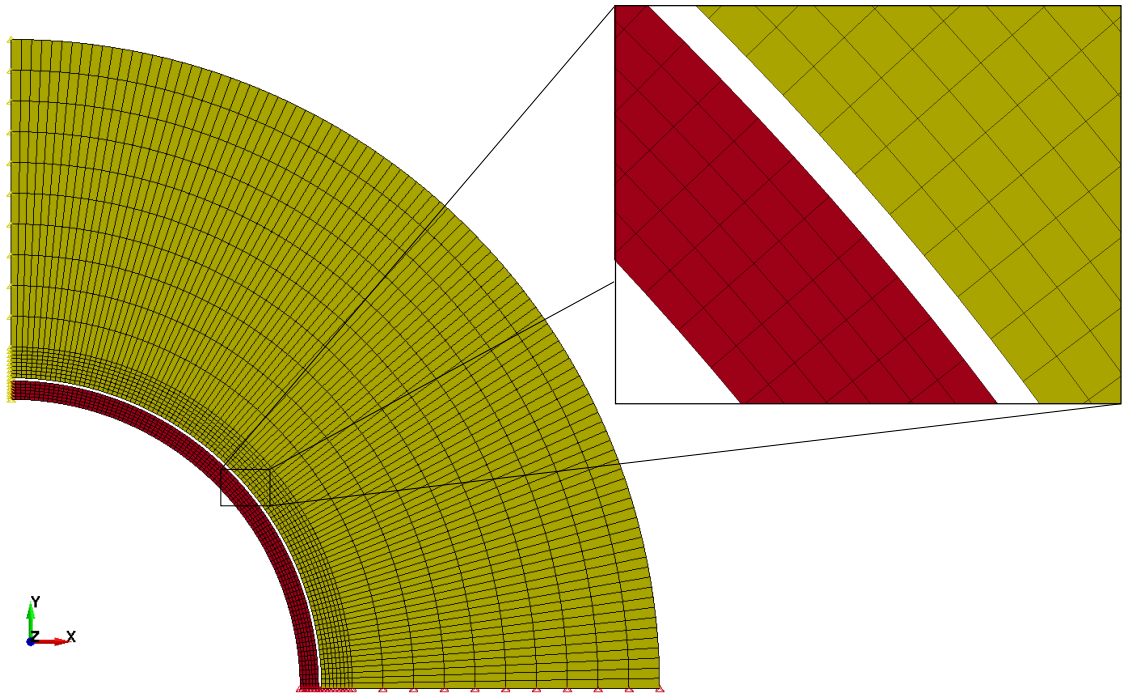

Figure G.2. The numerical model of the tube-tubesheet case, where the yellow part is the tubesheet and the red is the tube.

Table G.1. The number of solid elements in the tube and tubesheet.

		No. Solid Elements			
Part	id	Total	Circumferential	Radial	Axial
Tube	1	600	100	6	1
Tubesheet	2	1800	100	18	1

G.2 Keyword documentation

The following section will present the parts used in the keyword for this model, where all text is based on [49, 35]. The parts are cut out of the final keyword, and are commented underneath.

Parameter

The parameterisation of the numerical model for the later optimisation, see figure G.3, where the design parameter *d1* is set to 200.00

```
*PARAMETER
 Rd1 ,200.00
```

Figure G.3. Parameter cut out from the tube-tubesheet keyword.

Control

The following control cards, will only contact the ones which are changed from default.

See Figure G.4, where the entire model is checked for an initial penetration as a safe precaution, by setting *islchk* to 2, and the contact surface maximum penetration check multiplier is set to 10, in order to increase the allowed amount of contact penetration before the contact model is shut off.

```
*CONTROL_CONTACT
$#  slsfac    rwpnal    islchk    shlthk    penopt    thkchg     orien    enmass
       0.1       0.0         2         0         1         0         1         0
$#  usrstr    usrfrc     nsbcs    interm     xpene     ssthk      ecdt   tiedprj
         0         0         0         0      10.0         0         0         0
$#   sfric     dfric       edc       vfc        th     th_sf    pen_sf
       0.0       0.0       0.0       0.0       0.0       0.0       0.0
$#  ignore    frceng   skiprwg    outseg   spotstp   spotdel   spothin
         0         0         0         0         0         0       0.0
$#    isym    nserod    rwgaps    rwgdth     rwksf      icov    swradf    ithoff
         0         0         1       0.0       1.0         0       0.0         0
$#  shledg    pstiff    ithcnt    tdcnof     ftall    unused    shltrw
         0         0         0         0         0                 0.0
```

Figure G.4. Control contact cut out from the tube-tubesheet keyword.

See Figure G.5, where the *hgen* is changed to 2, in order to include the hourglass energy in the global energy balance.

```
*CONTROL_ENERGY
$#    hgen      rwen    slnten     rylen
         2         2         1         1
```

Figure G.5. Control Energy cut out from the tube-tubesheet keyword.

See figure G.6, here the implicit definition of the model is prescribed, by setting *imflag* to one, and the Initial time step size for implicit analysis is 1e-5

```
*CONTROL_IMPLICIT_GENERAL
$#  imflag       dt0    imform      nsbs       igs     cnstn      form    zero_v
         1 1.00000E-5         2         1         2         0         0         0
```

Figure G.6. Control Implicit cut out from the tube-tubesheet keyword.

See figure G.7, where the termination time for the simulation is set to 0.022 sec.

```
*CONTROL_TERMINATION
$#  endtim    endcyc     dtmin    endeng    endmas
     0.022         0       0.0       0.01.000000E8
```

Figure G.7. Control Termination cut out from the tube-tubesheet keyword.

Database

In this section, the desired output are prescribed, where the desired one from the optimisation is the resultant interface force, *RCFORC*, see figure G.8. Here the timeinterval between outputs are given in *dt*

```
*DATABASE_RCFORC
$#      dt    binary      lcur     ioopt
1.00000E-6         0         0         1
```

Figure G.8. Database RCFORC cut out from the tube-tubesheet keyword.

Also the binary d3plot is selected as-well, see figure G.9, where a total number of outputs are prescribed to 60, in the *npltc*.

```
*DATABASE_BINARY_D3PLOT
$#      dt      lcdt      beam     npltc    psetid
       0.0         0         0        60         0
$#   ioopt
         0
```

Figure G.9. Database d3plot cut out from the tube-tubesheet keyword.

Boundary Conditions

For the following, the boundary conditions for the numerical model is presented. Here the method of using the BOUNDARY_SPC_SET is selected due to the implicit solver, where the CONSTRAINT_GLOBAL showed poor performance. The Boundary SPC and the node set can be seen on figure G.10.

```
*BOUNDARY_SPC_SET_ID
$#      id                                                              heading
         0Tube Edge X
$#    nsid       cid      dofx      dofy      dofz     dofrx     dofry     dofrz
         2         0         0         1         0         0         0         0
*SET_NODE_LIST_TITLE
Tube Along X
$#     sid       da1       da2       da3       da4    solver
         2       0.0       0.0       0.0       0.0MECH
$#    nid1      nid2      nid3      nid4      nid5      nid6      nid7      nid8

                    $$$ Nodes Along the X edge $$$

*BOUNDARY_SPC_SET_ID
$#      id                                                              heading
         0Tube Edge Y
$#    nsid       cid      dofx      dofy      dofz     dofrx     dofry     dofrz
         3         0         1         0         0         0         0         0
*SET_NODE_LIST_TITLE
Tube ALong Y
$#     sid       da1       da2       da3       da4    solver
         3       0.0       0.0       0.0       0.0MECH
$#    nid1      nid2      nid3      nid4      nid5      nid6      nid7      nid8
                    $$$ Nodes Along the Y edge $$
*BOUNDARY_SPC_SET_ID
$#      id                                                              heading
         4BottomPlane
$#    nsid       cid      dofx      dofy      dofz     dofrx     dofry     dofrz
         4         0         0         0         1         1         1         0
*SET_NODE_LIST_TITLE
BottomPlane
$#     sid       da1       da2       da3       da4    solver
         4       0.0       0.0       0.0       0.0MECH
$#    nid1      nid2      nid3      nid4      nid5      nid6      nid7      nid8

                $$$ All the nodes in the bottom plane $$$

*BOUNDARY_SPC_SET_ID
$#      id                                                              heading
         5TopPlane
$#    nsid       cid      dofx      dofy      dofz     dofrx     dofry     dofrz
         5         0         0         0         1         1         1         0
*SET_NODE_LIST_TITLE
TopPlane
$#     sid       da1       da2       da3       da4    solver
         5       0.0       0.0       0.0       0.0MECH
$#    nid1      nid2      nid3      nid4      nid5      nid6      nid7      nid8

                    $$$ All the nodes in the top plane $$$
```

Figure G.10. Boundary SPC and Node set cut out from the tube-tubesheet keyword.

Load

The applied pressure on the inner tube wall is applied by the function shown on figure G.11, where the *ssid* describes the segment, the *lcid* is the load curve id, which is shown on figure G.12, and the scale factor *sf* is the parameterised parameter for the optimisation.

```
*LOAD_SEGMENT_SET_ID
$#      id                                                              heading
         0Pressure Applied
$#    ssid      lcid        sf        at
         1         1       &d1       0.0
```

Figure G.11. Load Segment cut out from the tube-tubesheet keyword.

On figure G.12, the load curve for the parameterised applied pressure can be seen.

```
*DEFINE_CURVE_TITLE
Pressure Curve
$#    lcid      sidr       sfa       sfo      offa      offo    dattyp     lcint
         1         0       1.0       1.0       0.0       0.0         0         0
$#                a1                  o1
               0.0                 0.0
             0.015                 1.0
             0.018                 1.0
             0.019                 0.0
              0.02                 0.0
```

Figure G.12. Define Curve cut out from the tube-tubesheet keyword.

Contact

The selected contact model is a implicit lagrange based contact model, which is known as MORTAR. Where the Mortar name is due to its sticky behaviour when contact is obtained. For the contact model the contact is prescribed for the two parts, tubesheet 2, and the tube 1. The static friction is set to 0.1 in *fs*, and the dynamic friction is negligtible for the MORTAR contact, *fd*. The viscous contact damping, *vdc*, is set to 70, based on experience and recommendations. These setting can be seen on figure G.13.

```
*CONTACT_AUTOMATIC_SURFACE_TO_SURFACE_MORTAR_ID
$#     cid                                                              title
         1Tube-Tubesheet
$#    ssid      msid     sstyp     mstyp    sboxid    mboxid       spr       mpr
         2         1         3         3         0         0         0         0
$#      fs        fd        dc        vc       vdc    penchk        bt        dt
       0.1       0.1       0.0       0.0      70.0         0       0.0 1.00000E20
$#     sfs       sfm       sst       mst      sfst      sfmt       fsf       vsf
       1.0       1.0       0.0       0.0       1.0       1.0       1.0       1.0
$#    soft    sofscl    lcidab    maxpar     sbopt     depth     bsort    frcfrq
         0       0.1         0     1.025       2.0         2         0         1
$#  penmax    thkopt    shlthk     snlog      isym     i2d3d    sldthk    sldstf
       0.0         0         0         0         0         0       0.0       0.0
$#    igap    ignodprfac/mpadtstif/mpar2   unused     unused    flangl   cid_rcf
         1         0       0.0       0.0                           0.0         0
```

Figure G.13. Contact Model cut out from the tube-tubesheet keyword.

Tube and Tubesheet: Element formulation, Material Model and Hourglass Control

For the two parts, tube and tubesheet, the same element formulation, material model and hourglass control is used, and therefore these will be presented as one in the following.

The prescribed element formulation can be seen on figure G.14, where the constant stress solid element formulation is selected, *elform*: 1, which is a very robust, implemented for implicit analysis and is cheap to use.

```
*SECTION_SOLID_TITLE
Tube
$#   secid    elform       aet
         1         1         0
```

Figure G.14. Section Solid cut out from the tube-tubesheet keyword.

The material model, can be seen on figure G.15, is no 3, which is a isotropic and kinematic hardening plasticity model, which is very cost effective and can be used for solid elements. The inputs are: *RO*, mass density, *E*, Young's Modulus, *PR*, Poisson's Ratio, *SIGY*, Yield Stress and *ETAN*, Tangent Modulus.

```
*MAT_PLASTIC_KINEMATIC_TITLE
Tube
$#     mid        ro         e        pr      sigy      etan      beta
         17.85000E-9  193000.0       0.3     325.0    2200.0       0.0
$#     src       srp        fs        vp
       0.0       0.0       0.0       0.0
```

Figure G.15. Material Model cut out from the tube-tubesheet keyword.

The hourglass control applied for the tube and tubesheet can be seen on figure G.16, where Belytschko-Bindeman [1993] assumed strain co-rotational stiffness form for 2D and 3D solid elements only, is used. By setting *ihq* to 6.

```
*HOURGLASS
$#    hgid       ihq        qm       ibq        q1        q2    qb/vdc        qw
         1         6       0.1         0       1.5      0.06       0.1       0.1
```

Figure G.16. Hourglass cut out from the tube-tubesheet keyword.

Sensor Control

The sensor is used to improve the robustness of the numerical model, where the pressure and contact is shut off, when a given switching condition is violated. The defined Sensor control can be seen on figure G.17. Where the SENSOR_DEFINE_NODE is defining the node at which the violation criteria is measured, and the SENSOR_SWITCH is given the coordinate value for the switching condition, at 21.15 mm.

```
*SENSOR_CONTROL
$#  cntlid      type    typeid   timeoff      nrep
         1PRESSURE           1         0         0
$# initstt      sit1      sit2      sit3      sit4      sit5      sit6      sit7
ON                1         0         0         0         0         0         0
*SENSOR_CONTROL
$#  cntlid      type    typeid   timeoff      nrep
         2CONTACT            1         0         0
$# initstt      sit1      sit2      sit3      sit4      sit5      sit6      sit7
ON                1         0         0         0         0         0         0
*SENSOR_DEFINE_NODE
$#  sensid     node1     node2       vid       crd     ctype
         1    203636         0X                0COORD
*SENSOR_SWITCH
$#  switid      type    sensid     logic     value   filtrid    timwin
         1Sensor             1GT             21.15         0       0.0
```

Figure G.17. Sensor Control cut out from the tube-tubesheet keyword.

G.3 Optimisation Documentation

For the tube-tubesheet optimisations The Totally Structured Secant Method was used with a predefined trust-region at 500.00. The results from five optimisations are summarised in table G.2, and are the convergence are shown for each of the optimisations in the following figures.

Table G.2. The summary from the optimisation for five tube-tubesheet runs.

Yield Stress [MPa]		Objective Func.		Parameter		Function Evaluations			Trust-Region	
Tube	Tubesheet	Ini.	Opti.	Ini.	Opti.	Tot.	Eval.	Jacob.	Inc.	Dec.
325	325	0.00697	6.55e-4	200	304.48	37	28	9	3	11
325	260	0.02592	0.00167	180	249.68	60	47	13	5	21
325	390	0.00318	5.73e-4	220	324.91	34	27	7	2	13
260	325	0.00231	9.15e-4	200	267.84	39	31	8	3	15
390	325	0.01283	9.50e-4	220	309.14	49	38	11	4	16

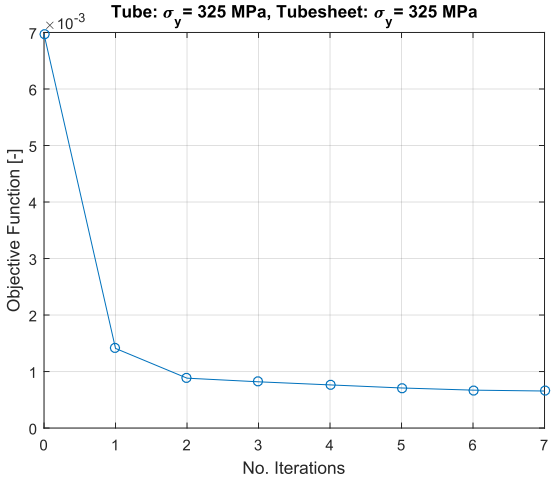

Figure G.18. Objective function for the setting: tube σ_y=325 MPa and tubesheet σ_y=325 MPa, for each iteration.

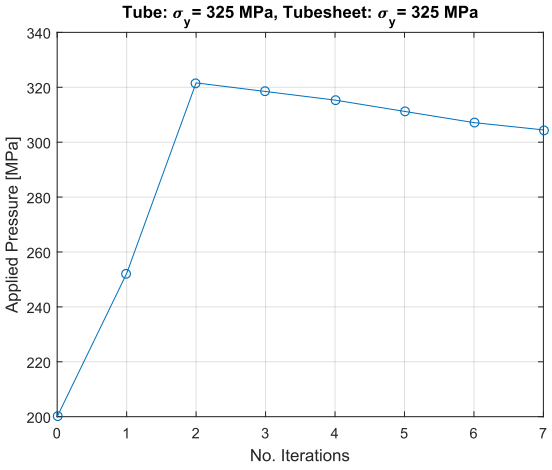

Figure G.19. Parameters for the setting: tube σ_y=325 MPa and tubesheet σ_y=325 MPa, for each iteration.

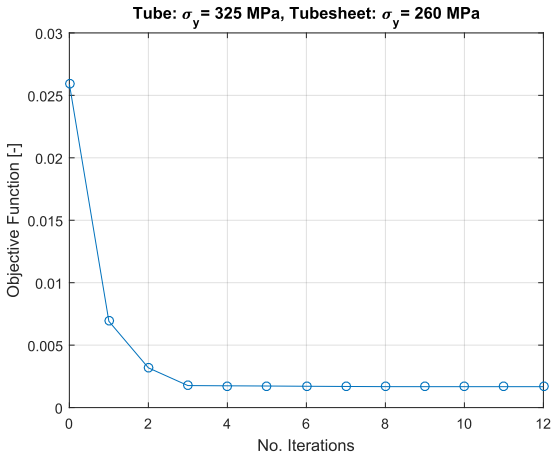

Figure G.20. Objective function for the setting: tube σ_y=325 MPa and tubesheet σ_y=260 MPa, for each iteration.

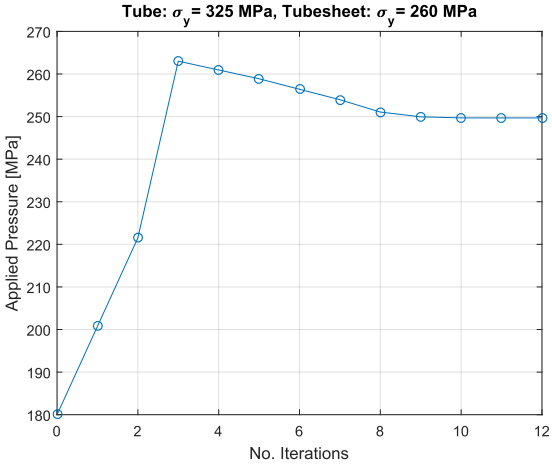

Figure G.21. Parameters for the setting: tube σ_y=325 MPa and tubesheet σ_y=260 MPa, for each iteration.

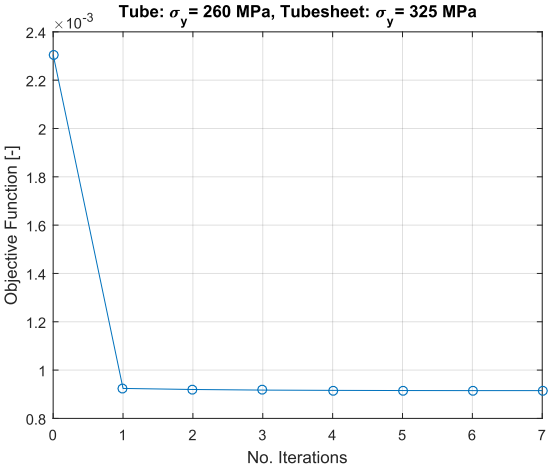

Figure G.22. Objective function for the setting: tube σ_y=260 MPa and tubesheet σ_y=325 MPa, for each iteration.

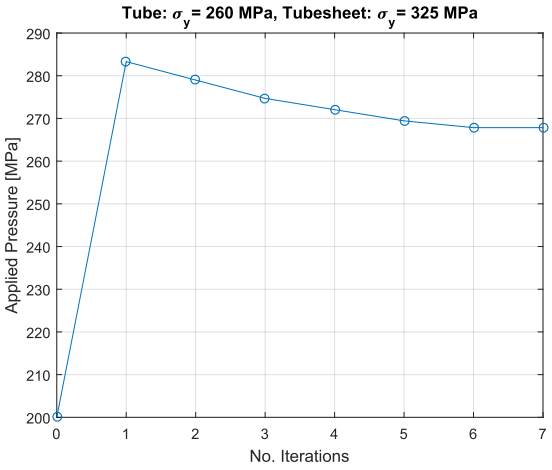

Figure G.23. Parameters for the setting: tube σ_y=260 MPa and tubesheet σ_y=325 MPa, for each iteration.

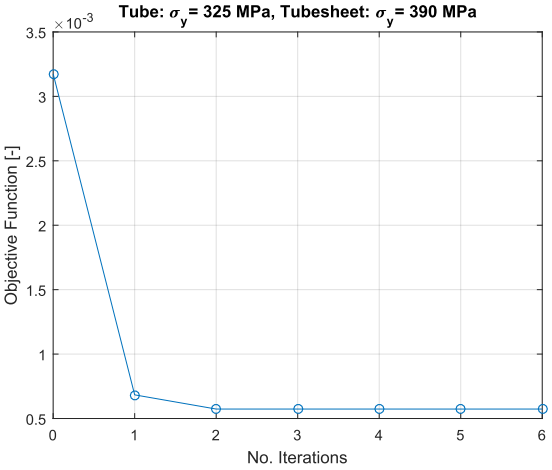

Figure G.24. Objective function for the setting: tube σ_y=325 MPa and tubesheet σ_y=390 MPa, for each iteration.

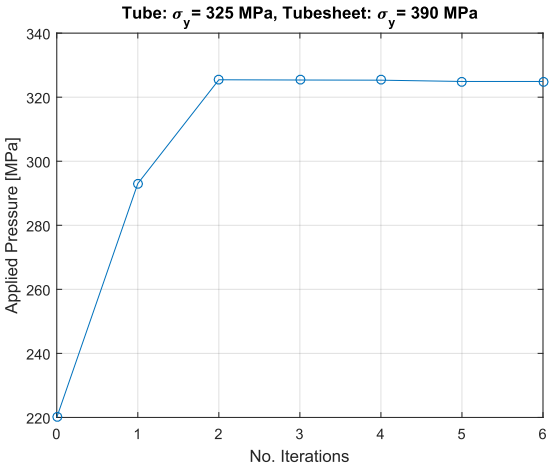

Figure G.25. Parameters for the setting: tube σ_y=325 MPa and tubesheet σ_y=390 MPa, for each iteration.

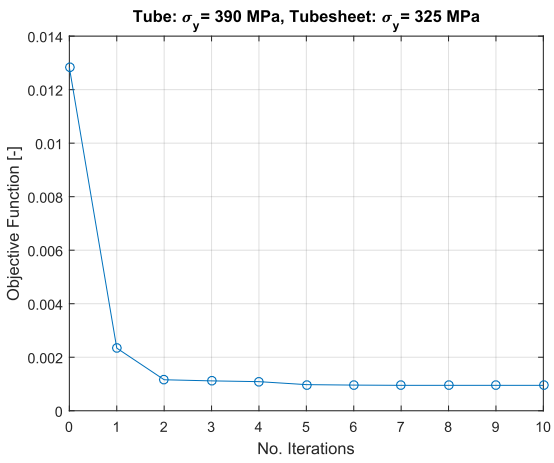

Figure G.26. Objective function for the setting: tube σ_y=390 MPa and tubesheet σ_y=325 MPa, for each iteration.

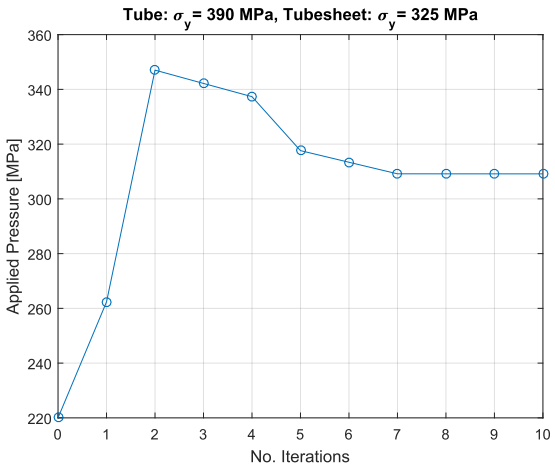

Figure G.27. Parameters for the setting: tube σ_y=390 MPa and tubesheet σ_y=325 MPa, for each iteration.

Optimisation Summary for the Clearance Effects

In the following, the same settings as for the previous presented are used, and the summary can be found in table G.3, and the following figures are show the convergence of these.

Table G.3. The summary from the optimisation for two clearance effect runs

Clearance	Objective Func.		Parameter [mm]		Function Evaluations			Trust-Region	
	Ini.	Opti.	Ini.	Opti.	Tot.	Eval.	Jacob.	Inc.	Dec.
0.05	5.29e-3	5.88e-4	200	303.55	60	47	13	5	21
0.15	0.5	7.43e-4	200	298.30	26	20	6	3	8

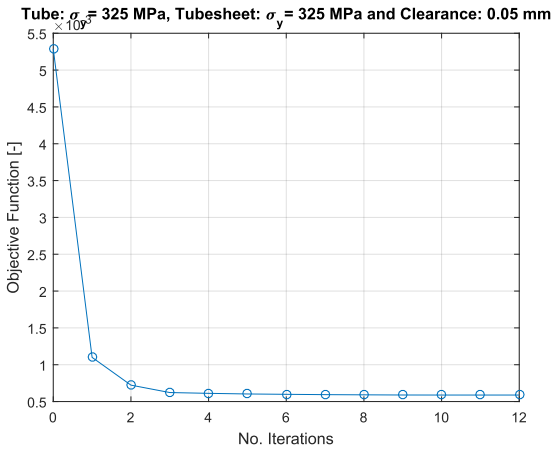

Figure G.28. Objective function for the setting: tube σ_y=325 MPa, tubesheet σ_y=325 MPa and clearance: c=0.05 mm, for each iteration.

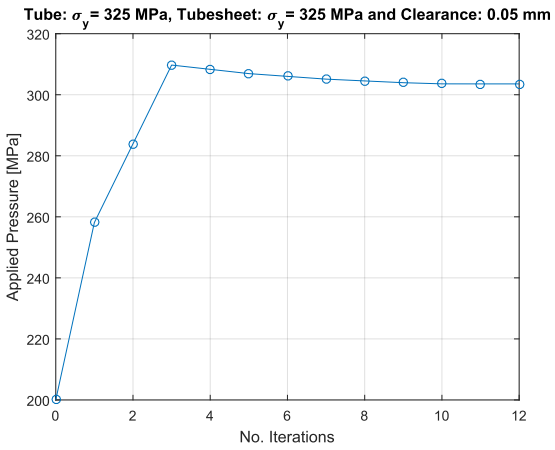

Figure G.29. Parameters for the setting: tube σ_y=325 MPa, tubesheet σ_y=325 MPa and clearance: c=0.05 mm, for each iteration.

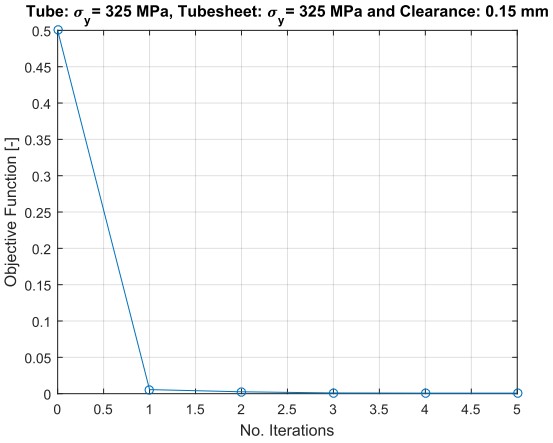

Figure G.30. Objective function for the setting: tube σ_y=325 MPa, tubesheet σ_y=325 MPa and clearance: c=0.15 mm, for each iteration.

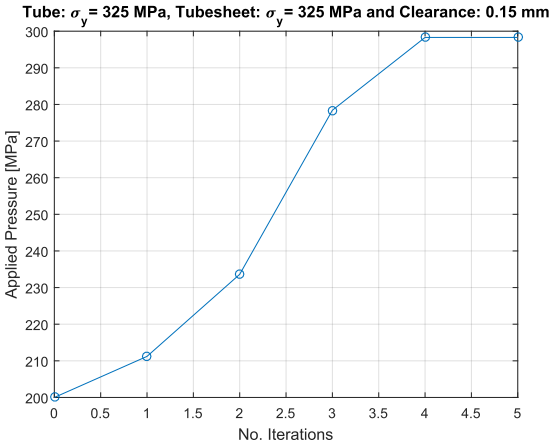

Figure G.31. Parameters for the setting: tube σ_y=325 MPa, tubesheet σ_y=325 MPa and clearance: c=0.15 mm, for each iteration.

Airbus A380 Door Frame Corner H

In the following, this Appendix will present some additional information of the Springback optimisation for the Airbus Door Corner Piece, Chapter 9. The content for this Appendix can be seen beneath:

- Process Preparation
- Simulation Documentation
- Keyword Documentation
- Optimisation Documentation

H.1 Process Preparation

During the initial study of the corner part manufacturing was a number of sketch made, on figure H.1 can some of the drawings be seen.

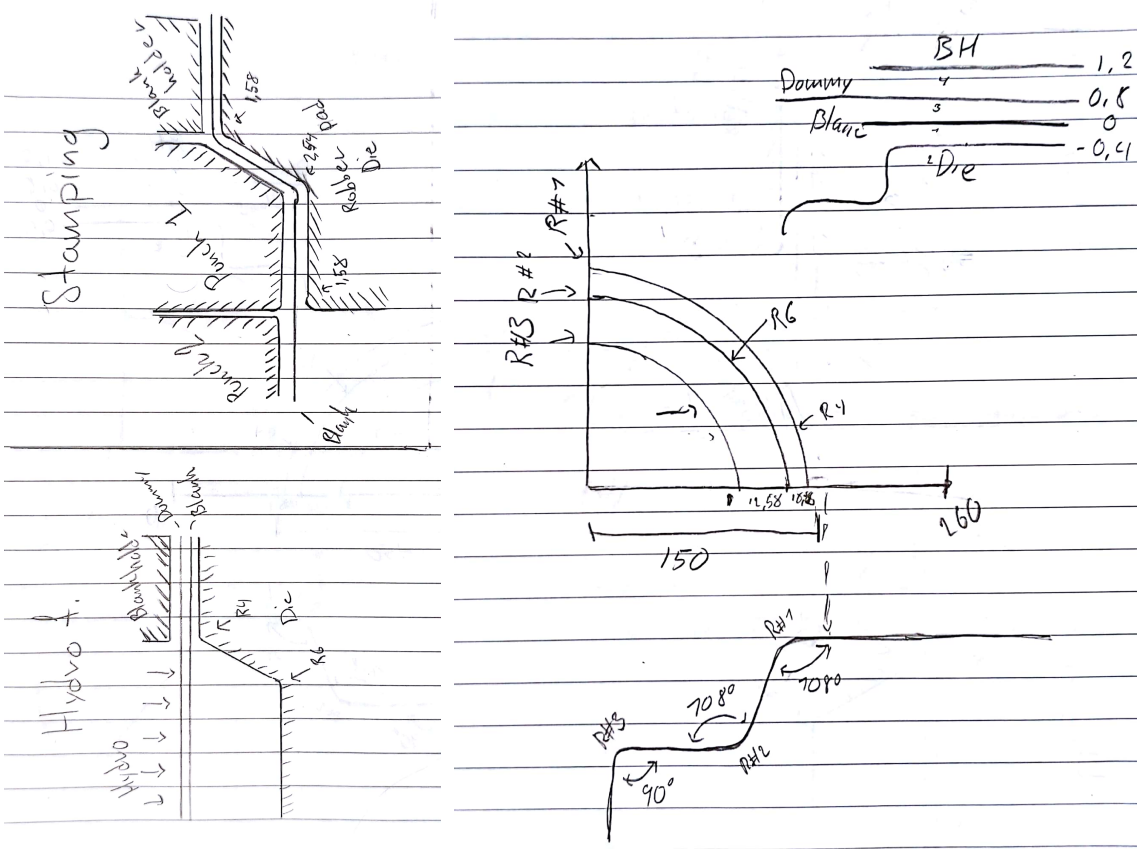

Figure H.1. Drawing of the process and final product, made in preparation of modelling.

H.2 Simulation Documentation

The simulations files can be found in the attached zip archive.
A video of the simulation can be found via the following link or QR code:

`https://youtu.be/SKldEctjrDU`

Figure H.2. QR with link to simulation video on youtube.

The Airbus springback simulation, is in this case documented with photos and model

data. The simulation is shown in different stages below, on figure H.3 the hydroforming parts, on figure H.4 the stamping parts, on figure H.5 the final stage of the hydroforming operations and on figure H.6.

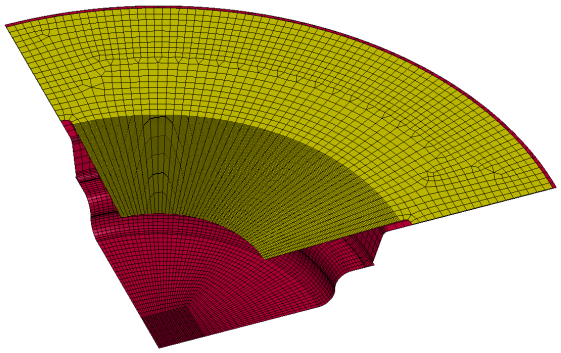

Figure H.3. Blank and hydroforming die. Blankholder and dummy are not shown.

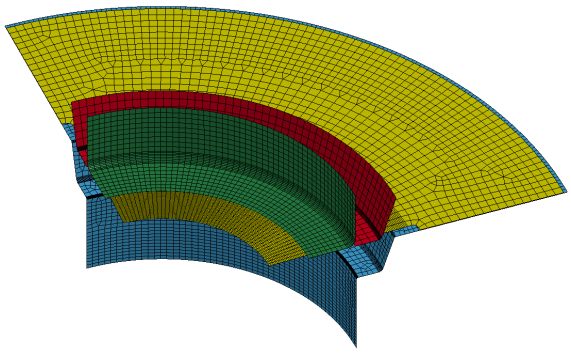

Figure H.4. Blank, stamping die, punch1 and punch2. Blankholder is not shown.

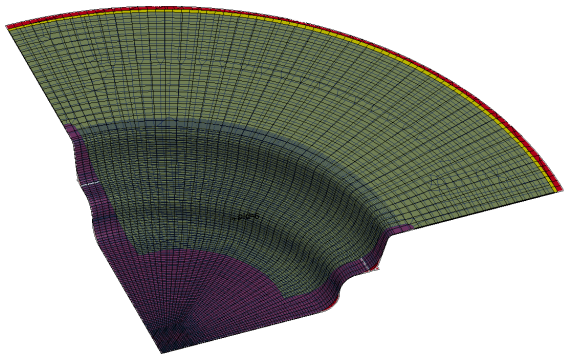

Figure H.5. End of hydroforming operation, with transparent dummy.

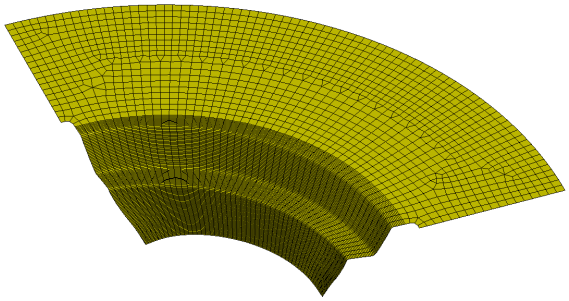

Figure H.6. Formed Blank after springback.

The parts, id and number of elements are documented in table H.1.

Table H.1. Model parts, id and number of elements.

Part	id	No. Ele.
Blank	1	6252
Die	2	6788
Blankholder	3	1338
Punch 1	4	850
Punch 2	5	1300
Hydro. die	6	6176
Dummy	7	5200
Total		27904

H.3 Keyword Documentation

In the following section will important keywords be presented, the keywords are cut out of the master keyword and model, which can be found in the attached ZIP archive.

Parameter

The hydroforming maximum pressure parameter was defined using the keyword shown on figure H.7, the parameter id is defined in the hydroforming pressure load curve.

```
1   *KEYWORD
2   *PARAMETER
3    Rd ,35.51776
```

Figure H.7. Parameter keyword, controlling the hydroforming pressure.

Control

The control keyword that was changed from default, is presented. The termination time, figure H.8, was set to 0.04 sec based on the explicit springback. Springback was defined using the keyword shown on figure H.9, where timestep was set to 5×10^{-5} sec and *imform=2* was selected for implicit springback analysis after termination, the number of springback steps was set to 10.

```
*CONTROL_TERMINATION
$#  endtim    endcyc     dtmin    endeng    endmas
      0.04         0       0.0       0.01.000000E8
```

Figure H.8. Termination time keyword.

```
*CONTROL_IMPLICIT_GENERAL
$#  imflag       dt0    imform      nsbs       igs     cnstn      form    zero_v
          25.00000E-5         2        10         1         0         0         0
```

Figure H.9. Implicit springback analysis keyword.

Database

Data logging from the simulation was selected with the database keywords, d3plot was set to 60 dumps in total as shown on figure H.10. The node coordinates was used in the optimisation, dump rate was set to 1×10^{-4} sec, shown on figure H.11 only the last dump was used. The node list that was dumped data for was selected with the keyword, shown on figure H.12.

```
*DATABASE_BINARY_D3PLOT
$#      dt      lcdt      beam     npltc    psetid
       0.0         0         0        60         0
$#   ioopt
         0
```

Figure H.10. D3plot dump keyword, 60 dumps is selected.

```
*DATABASE_NODOUT
$#      dt    binary      lcur     ioopt   option1   option2
1.00000E-4         0         0         1       0.0         0
```

Figure H.11. Dump rate of nodout is selected.

```
*DATABASE_HISTORY_NODE_SET
$#     id1       id2       id3       id4       id5       id6       id7       id8
         5         0         0         0         0         0         0         0
```

Figure H.12. Node list to dump is selected.

Boundary Conditions

Three types of boundary conditions was used: Prescribed motion rigid (figure H.13), SPC (figure H.15) and SPC birth/death (figure H.16).

Prescribed motion body, was used to move punch 1 and punch 2 up and down. The size of the motion and timing, was selected with the s-curve keyword (figure H.14), where start-, end- and rise-time are adjusted.

```
*BOUNDARY_PRESCRIBED_MOTION_RIGID_ID
$#      id                                                              heading
          0Punch1
$#     pid       dof       vad      lcid        sf       vid     death     birth
          4         3         0        11      -1.0         01.00000E28       0.0
$#      id                                                              heading
          0Punch2
$#     pid       dof       vad      lcid        sf       vid     death     birth
          5         3         0         9      -1.0         01.00000E28       0.0
```

Figure H.13. Motion of rigid bodies can be controlled.

```
*DEFINE_CURVE_SMOOTH_TITLE
Punch1
$#    lcid      sidr      dist    tstart      tend     trise        v0
          3         0     24.87      0.01      0.02     0.001       0.0
```

Figure H.14. S-curve for rigid body motions.

Boundary SPC, was used to lock the sides of the Blank and dummy, the locked nodes are selected in a node list. The specific DOF are selected with the *dofx, dofy, dofz, dofrx, dofry* and *dofrz* entries.

```
*BOUNDARY_SPC_SET_ID
$#      id                                                              heading
          0Dummy-X
$#    nsid       cid      dofx      dofy      dofz     dofrx     dofry     dofrz
          2         0         0         1         0         1         0         1
*SET_NODE_LIST_TITLE
Dummy-X
$#     sid       da1       da2       da3       da4    solver
          2       0.0       0.0       0.0       0.0MECH
$#    nid1      nid2      nid3      nid4      nid5      nid6      nid7      nid8
                      %%%% Node list Dummy x %%%%
```

Figure H.15. Node list locking.

Boundary SPC Birth/Death, was used to lock the dummy after the hydroforming operation, and the blank flange during the springback analysis. The nodes that are locked are specified with a node list, and the *Birth* and *Death* specify when the boundary and turned on and off.

```
*BOUNDARY_SPC_SET_BIRTH_DEATH_ID
$#      id                                                              heading
          0Blankflange
$#    nsid       cid      dofx      dofy      dofz     dofrx     dofry     dofrz
          7         0         0         0         1         0         0         0
$#   birth     death
    0.01051.00000E20
*SET_NODE_LIST_TITLE
Blankflange
$#     sid       da1       da2       da3       da4    solver
          7       0.0       0.0       0.0       0.0MECH
          %%%% Node list Blankflange %%%%%
```

Figure H.16. Node list locking with start and end time.

Loads

The load keyword, segment set (figure H.17), was used to prescribe the hydraulic pressure during the hydroforming operation. The segment that the pressure is applied to is selected with the *ssid* entry (dummy), and the maximum pressure by the *sf* entry whcih is this case is the parameter *&d*. The pressure load curve (keyword shown on figure H.18)is selected with the *lcid* entry.

```
1   *LOAD_SEGMENT_SET_ID
2   $#      id                                                          heading
3            0Pressure
4   $#    ssid      lcid        sf        at
5             1         5&d               0.0
```

Figure H.17. Element segment where load is applied

```
 1   *DEFINE_CURVE_TITLE
 2   Hydro
 3   $#    lcid      sidr       sfa       sfo      offa      offo    dattyp     lcint
 4             5         0       1.0       1.0       0.0       0.0         0         0
 5   $#                a1                  o1
 6                    0.0                 0.0
 7       9.9999997474e-05                 0.0
 8                  0.007                 1.0
 9                  0.008                 1.0
10                  0.009                 0.0
11                   0.05                 0.0
```

Figure H.18. Time and size, of a curve which can be used for different things.

The load rigid body keyword was used to control the blank holder force, shown on figure H.19, where the load curve, load direction, part and scale factor are specified.

```
1   *LOAD_RIGID_BODY
2   $#     pid       dof      lcid        sf       cid        m1        m2        m3
3             3         3         2   -7500.0         0         0         0         0
```

Figure H.19. Long on a rigid body, controlled with a curve and scale factor.

Contacts

Contact is the simulation was controlled with the keyword shown on figure H.20. The parts for which the keyword in defining contact are selected with the entry *ssid* and *msid* where the part is id used. For turning the contacts on and of are the entries *bt* and *dt* adjusted. Seven contacts was defined in total.

```
*CONTACT_FORMING_SURFACE_TO_SURFACE_ID
$#     cid                                                                title
         1Blank-Die
$#    ssid      msid     sstyp     mstyp    sboxid    mboxid       spr       mpr
         1         2         3         3         0         0         0         0
$#      fs        fd        dc        vc       vdc    penchk        bt        dt
       0.1       0.1       0.0       0.0      70.0         0       0.0      0.04
$#     sfs       sfm       sst       mst      sfst      sfmt       fsf       vsf
       1.0       1.0       0.0       0.0       1.0       1.0       1.0       1.0
```

Figure H.20. Contact keyword.

Material and Element formulation

The element formulation is specify with the keyword shown on figure H.21. The number of integrations points trough the thickness is likewise selected in this keyword.

```
*SECTION_SHELL_TITLE
Blank
$#   secid    elform      shrf       nip     propt   qr/irid     icomp     setyp
         1       -16       1.0         7       1.0         0         0         1
$#      t1        t2        t3        t4      nloc     marea      idof    edgset
       0.8       0.8       0.8       0.8       0.0       0.0       0.0         0
```

Figure H.21. Shell formulation selection and specification.

The part materials are specified with the material keywords. The blank and dummy was prescribed with the keyword shown on figure H.22. The tool pars was prescribed rigid material shown on figure H.23.

```
*MAT_POWER_LAW_PLASTICITY_TITLE
Blank
$#     mid        ro         e        pr         k         n       src       srp
         17.85000E-9  198000.0      0.28    1372.0      0.44       0.0       0.0
$#    sigy        vp      epsf
     270.0       0.0       0.0
```

Figure H.22. Part material definition

```
*MAT_RIGID_TITLE
Die
$#     mid        ro         e        pr         n    couple         m     alias
         27.85000E-9  210000.0       0.3       0.0       0.0       0.0
$#     cmo      con1      con2
       1.0         7         7
$#lco or a1        a2        a3        v1        v2        v3
       0.0       0.0       0.0       0.0       0.0       0.0
```

Figure H.23. Rigid material used for the tool parts.

Other

Part damping was specified with the keyword shown on figure H.24, the scale and when it was turned on was controlled with the *lcid* entry which is a curve, and part with *pid*.

```
*DAMPING_PART_MASS
$#     pid      lcid        sf      flag
         1         7    5000.0         0
```

Figure H.24. Part mass damping used to stop swinging of the blank after stamping.

The part for whcih springback analysis was conducted was defined with the keyword shown on figure H.25, where the blank is specified.

```
*INTERFACE_SPRINGBACK_SEAMLESS
$#    psid      nshv     ftype          _     ftensr    nthhsv          _    intstrn
         1         0         0          0          0         0          0          0
```

Figure H.25. Springback analysis definition.

H.4 Optimisation Documentation

Optimisation results of the Airbus case, the parameter data for each iteration is presented in table H.2. Convergence of the cost function and parameters are shown on the following figures (H.26, H.27, H.28, H.29, H.30).

Table H.2. Parameters and cost function convergence.

Iteration	P1	Radius	P3	Pressure	Cost function
0	1.0	5.0	1.0	100.0	123.98
1	4.9999E-4	10.8153	0.8277	35.5319	96.68
2	4.9790E-4	10.8141	0.8255	35.5217	96.36
3	4.9742E-4	10.8138	0.8256	35.5178	96.05
4	4.9740E-4	10.8137	0.8256	35.5177	96.21

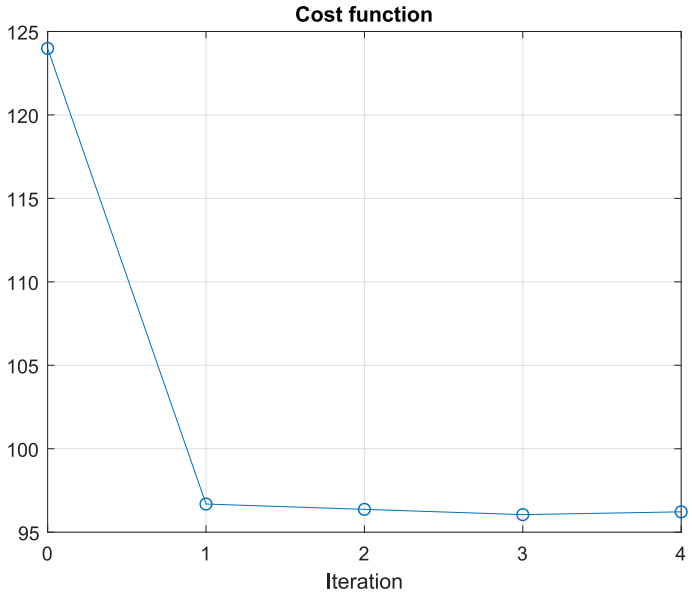

Figure H.26. Plot of the cost function convergence.

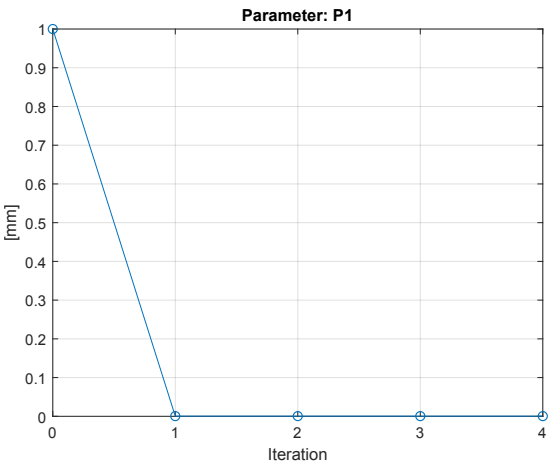

Figure H.27. Convergence plot of the distance P1.

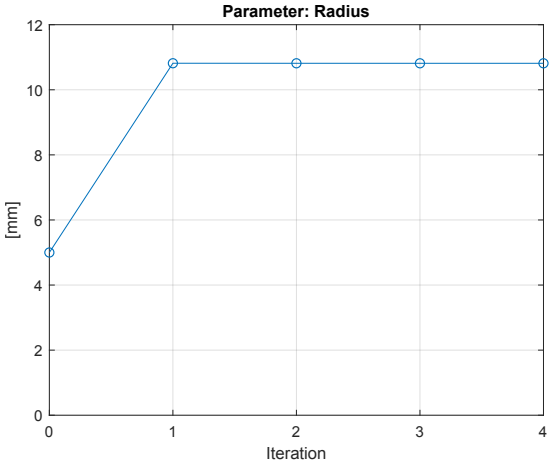

Figure H.28. Convergence of the hydroforming die radius.

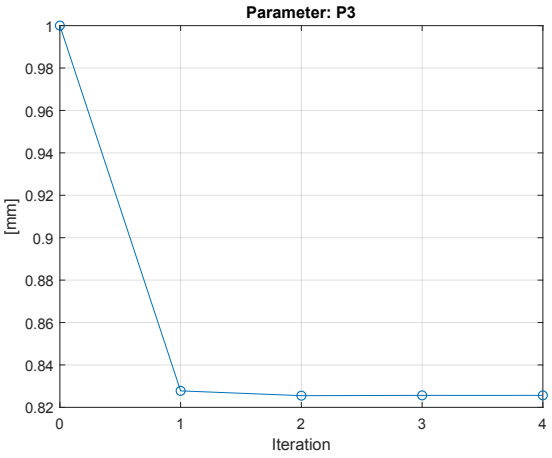

Figure H.29. Distance P3 convergence plot.

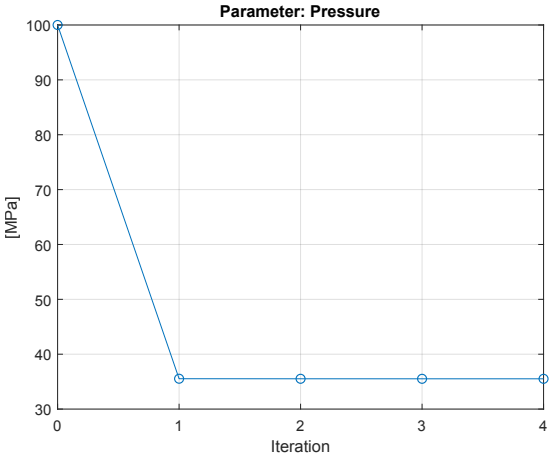

Figure H.30. Pressure convergence development.

H.5 Airbus Blank and Stamping Drawing

Drawing of the blank and stamping parts with measurements. The blank shown on figure H.31 is the original used as a base for the blank used in the simulation.

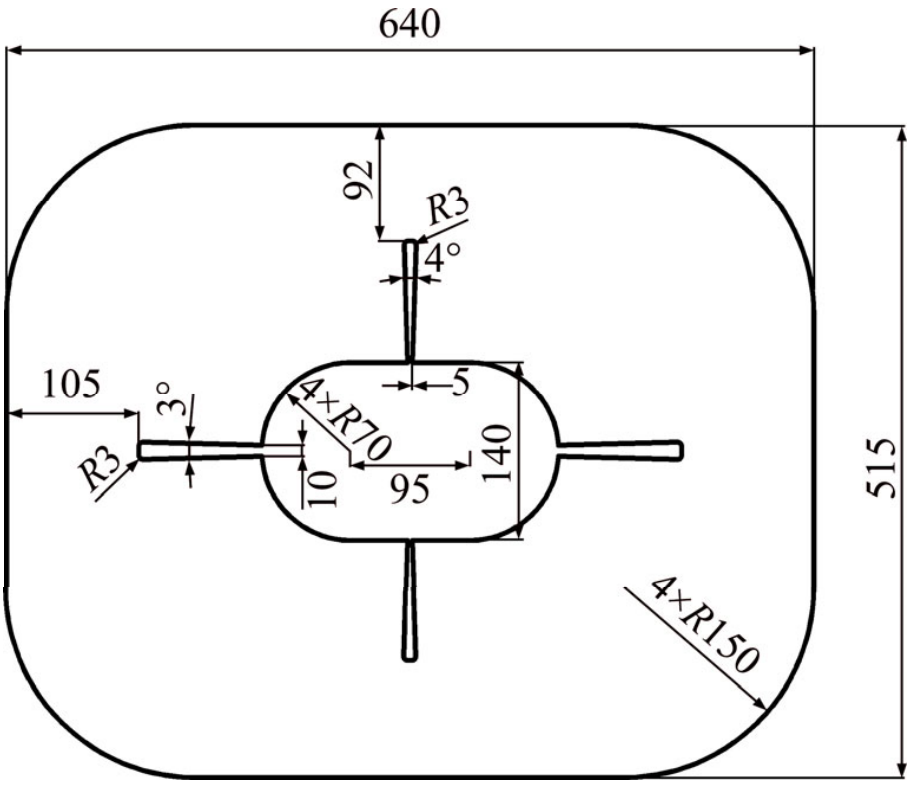

Figure H.31. Blanks measurements from Wang et al. [67]

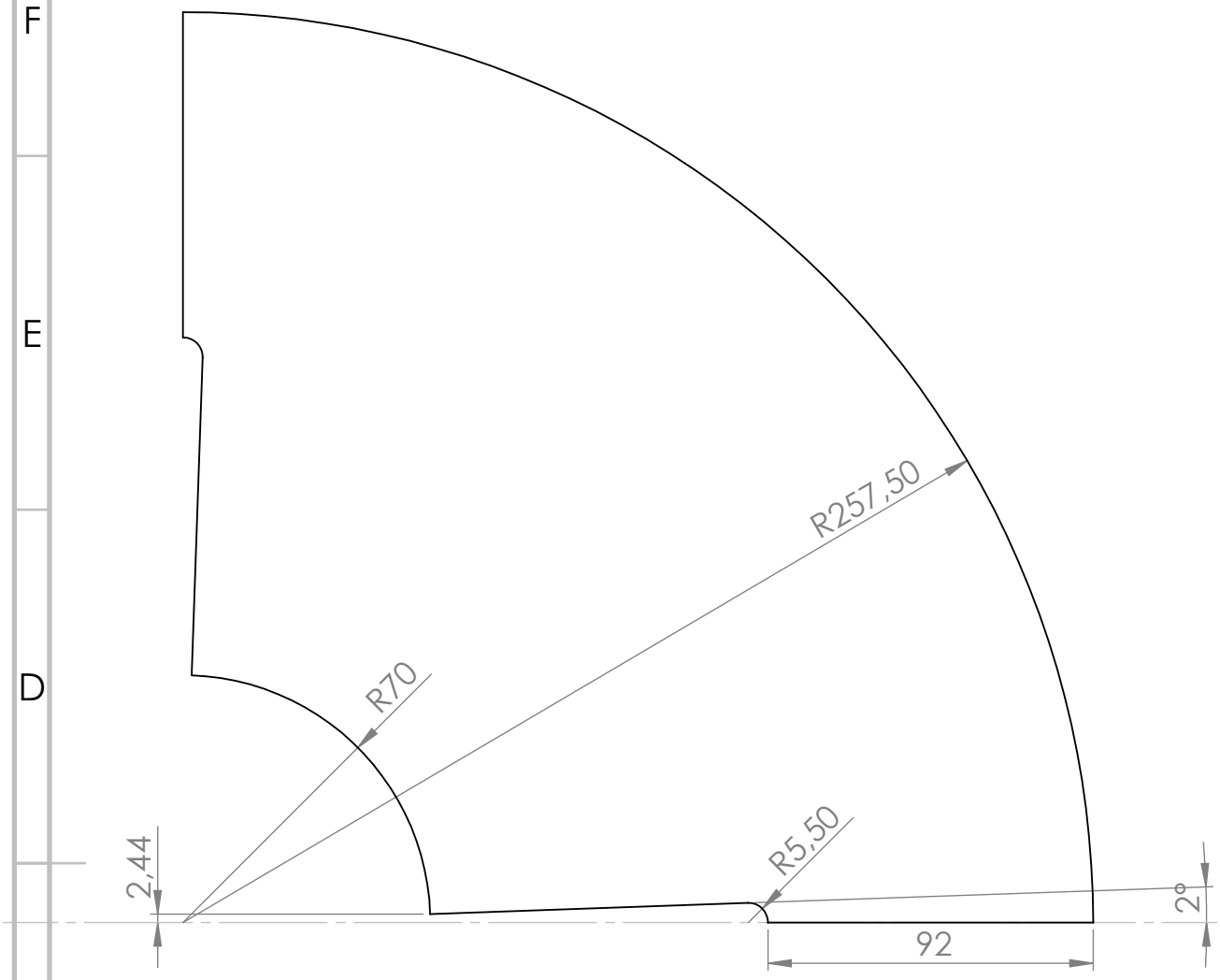

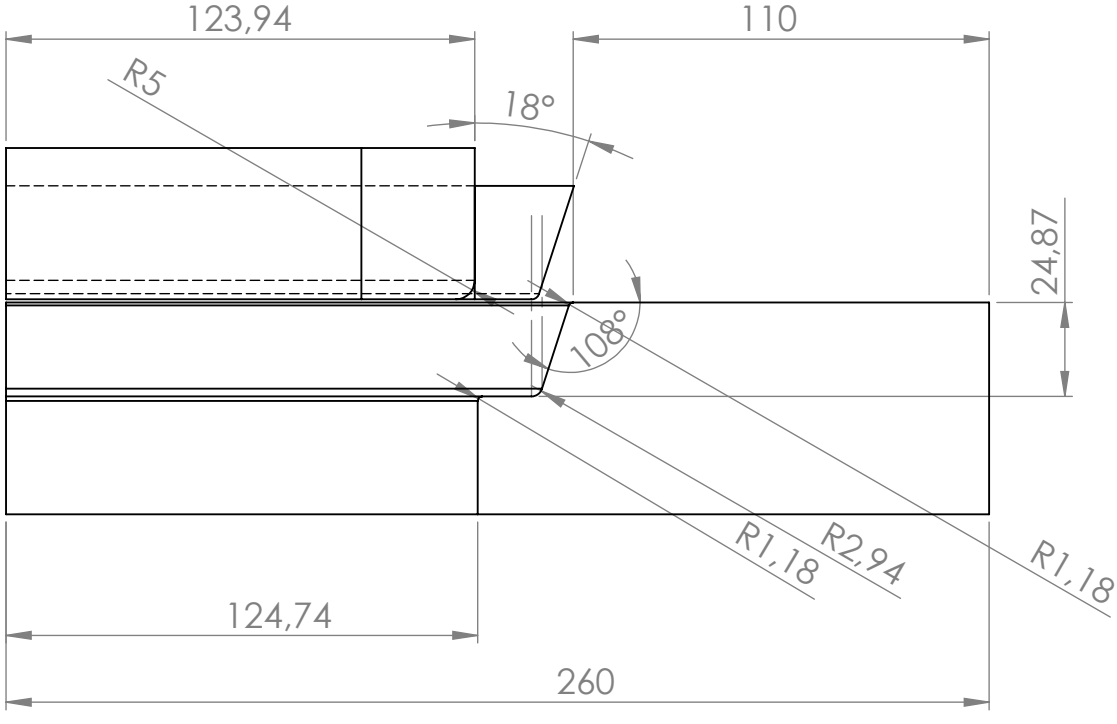

Blank and stamping parts dimentions in [mm]

VSR - Deep Drawn Cup

I

In the following, this Appendix will present some additional information of the VSR treatment of a Deep drawn cup, Chapter 10. The content for this Appendix can be seen beneath:

- Simulation Documentation
- Keyword Documentation
  - Deep Drawing
  - VSR Model

I.1 Simulation Documentation

The simulations files can be found in the attached zip archive.
A video of the simulation can be found via the following link or QR code:

`https://youtu.be/Y7EZKMy5Ohc`

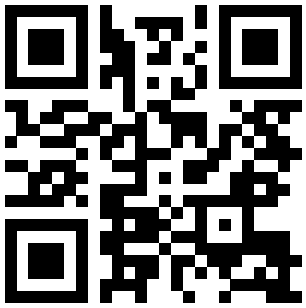

Figure I.1. QR with link to simulation video on youtube.

In the following, the two numerical models for this case. The first is the deep drawing operation, and the second is the VSR treatment.

I.1.1 Deep Drawing

On figure I.2 and I.3, some cut out of selected timesteps can be seen, and the parts in this model can be seen in table I.1.

Table I.1. The parts for the deep drawing operation, and the number of elements, together with the color for the parts on figure I.2 and I.3.

Parts	ID	No. Elements	Color on figures
Blank	1	1988	Yellow
Punch 1	2	8674	Green
Punch 2	3	6920	Red
Die 1	4	4935	Red
Die 2	5	5480	Yellow
Blank Holder	7	1422	Blue

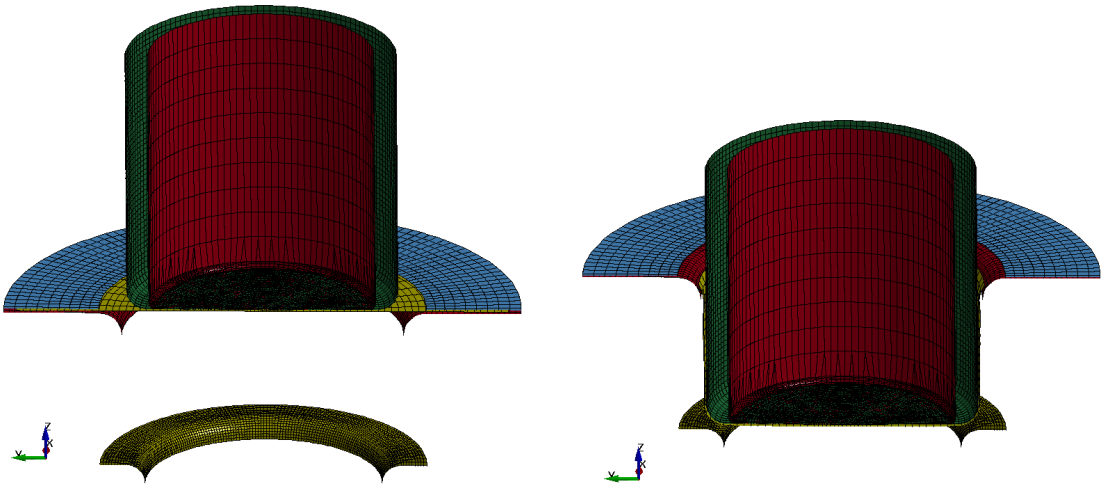

Figure I.2. To the left, is the initial situation. To the right, after first forming step.

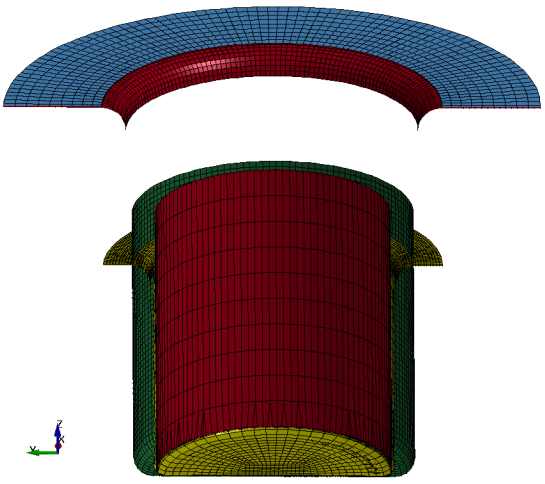

Figure I.3. After the final forming operation.

I.1.2 VSR Model

On figure I.4, the VSR model can be seen, and the only part which are included in this model is the blank from table I.1.

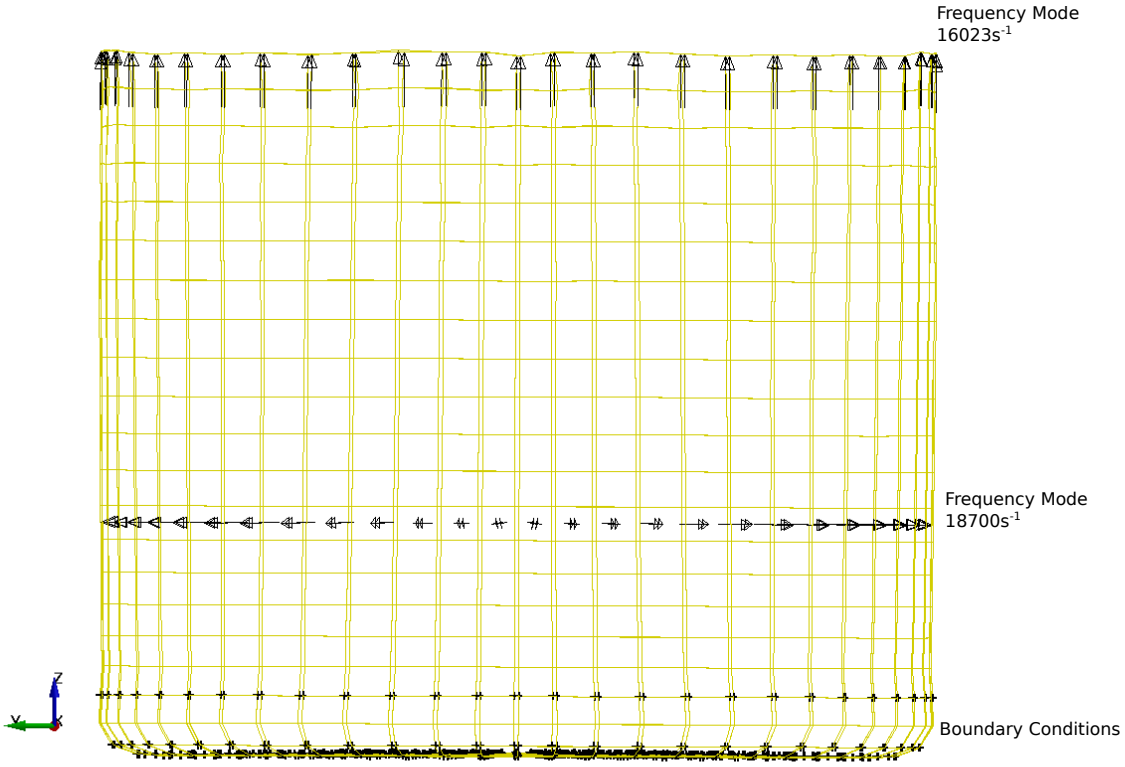

Figure I.4. The formed cup, and the selected boundary conditions, and the node/elements which are applied loads for each frequency mode.

I.2 Keyword Documentation

In the following, the keyword documentation for the two model will be presented.

I.2.1 Deep Drawing

Control

In the following, the control parameters different from default will be described.

On figure I.5, the Control Shell function is shown, where the `istupd` is changed from 0 to 1, which makes the model include "membrane straining causes thickness change (important for sheet metal forming or whenever membrane stretching is important)" throughout the simulation.

```
*CONTROL_SHELL
$#  wrpang     esort     irnxx    istupd    theory       bwc     miter      proj
      20.0         0        -1         1         2         2         1         0
$# rotascl    intgrd    lamsht    cstyp6    tshell
       1.0         0         0         1         0
$# psstupd   sidt4tu     cntco    itsflg    irquad
         0         0         0         0         2
$#  nfail1    nfail4   psnfail    keepcs     delfr   drcpsid    drcprm
         0         0         0         0         0         0       1.0
```

Figure I.5. A cut-out of the control shell card.

On figure I.6, the control card for hourglass energy is shown, where the hourglass viscousity type is Flanagan-Belytschko integration, by setting `ihq` to 2.

```
*CONTROL_HOURGLASS
$#     ihq        qh
         2       0.1
```

Figure I.6. A cut-out of the control hourglass card.

See Figure I.7, where the *hgen* is changed to 2, in order to include the hourglass energy in the global energy balance.

```
*CONTROL_ENERGY
$#    hgen      rwen    slnten     rylen
         2         2         1         1
```

Figure I.7. A cut-out of the control energy card.

See figure I.8, where the termination time for the simulation is set to 0.015 sec.

```
*CONTROL_TERMINATION
$#  endtim    endcyc     dtmin    endeng    endmas
     0.015         0       0.0       0.01.000000E8
```

Figure I.8. A cut-out of the control termination card.

On figure I.9, the time step size for mass scaled solutions, `dt2ms`, which is set to zeros, which means that no mass scaling is done.

```
*CONTROL_TIMESTEP
$#  dtinit    tssfac      isdo    tslimt     dt2ms      lctm     erode     ms1st
       0.0       0.9         0       0.0       0.0         0         0         0
```

Figure I.9. A cut-out of the control timestep card

On figure I.10, the control card for setting the implicit solver is activated, by changing `imflag` to -3, the it uses curve no. 3, see figure I.11, such when the curve value one, then

the implicit solver is active. Furthermore, the timestep for the implicit solver is set to `dt0` 1×10^{-4} sec.

```
*CONTROL_IMPLICIT_GENERAL
$#  imflag       dt0    imform      nsbs       igs     cnstn      form    zero_v
         -31.00000E-4         1         1         2         0         0         0
```

Figure I.10. A cut-out of the control implicit card.

On figure I.11, the curve for the implicit solver can be seen.

```
*DEFINE_CURVE_TITLE
Imp
$#    lcid      sidr       sfa       sfo      offa      offo    dattyp     lcint
         3         0       1.0       1.0       0.0       0.0         0         0
$#                a1                  o1
                 0.0                 0.0
              0.0109                 0.0
               0.011                 1.0
                 0.2                 1.0
```

Figure I.11. A cut-out of the define curve.

Database

In this section, some of the selected database outputs will be presented.

On figure I.12, the settings for the d3plots can be seen, where number of dumps are determined in `npltc` to 100.

```
*DATABASE_BINARY_D3PLOT
$#      dt      lcdt      beam     npltc    psetid
       0.0         0         0       100         0
```

Figure I.12. A cut-out of the database d3plot card

Contacts

In the following, some examples of the contacts models which are being used will be presented. For this model, the used contact models are penalty based.

On figure I.13, the contact model for punch1 & blank and punch2 & blank can be seen. Both contacts, the `fs` is the static friction, which for all the contact models are set to 0.1, `fd` is the dynamic friction, which for all contact models are set to 0.1, similarly the viscous contact damping, `vdc`, is set to 70 %. Here it is notable, that the death time for the contact models are different, see `dt`, this is because, when each forming operation is done, then the contact is shut off.

```
*CONTACT_FORMING_SURFACE_TO_SURFACE_ID
$#     cid                                                                title
         1Blank -Punch1
$#    ssid      msid     sstyp     mstyp    sboxid    mboxid       spr       mpr
           1         2         3         3         0         0         2         0
$#      fs        fd        dc        vc       vdc    penchk        bt        dt
        0.1       0.1       0.0       0.0      70.0         0       0.0     0.006
$#     sfs       sfm       sst       mst      sfst      sfmt       fsf       vsf
        1.0       1.0       0.0       0.0       1.0       1.0       1.0       1.0
*CONTACT_FORMING_SURFACE_TO_SURFACE_ID
$#     cid                                                                title
         2Blank -Punch 2
$#    ssid      msid     sstyp     mstyp    sboxid    mboxid       spr       mpr
           1         3         3         3         0         0         2         0
$#      fs        fd        dc        vc       vdc    penchk        bt        dt
        0.1       0.1       0.0       0.0      70.0         0       0.0     0.011
$#     sfs       sfm       sst       mst      sfst      sfmt       fsf       vsf
        1.0       1.0       0.0       0.0       1.0       1.0       1.0       1.0
```

Figure I.13. A cut-out of two contact models.

Loads and Motion

In the following, the loads and prescribed motions will be presented.

On figure I.14, the defined curve for the blank holder is presented. This will be used in the loading, where this curve represents a constant loading condition.

```
*DEFINE_CURVE_TITLE
Blank Holder Curve
$#    lcid      sidr       sfa       sfo      offa      offo    dattyp     lcint
           1         0       1.0       1.0       0.0       0.0         0         0
$#                 a1                  o1
                  0.0                 1.0
                  1.0                 1.0
```

Figure I.14. A cut-out of the defined curve for the blank holder.

On figure I.15, the loading condition is prescribed to the blank holder. The load is acting in the z-direction, `dof`=3, and load curve no. 1 is used, `lcid`=1, and the load is $-50\,\mathrm{kN}$, see `sf`.

```
*LOAD_RIGID_BODY
$#     pid       dof      lcid        sf       cid        m1        m2        m3
         7         3         1  -50000.0         0         0         0         0
```

Figure I.15. A cut-out of the load for the blank holder.

On figure I.16, the S-shaped velocity curve is described. The distance for the movement is set to 250, `dist`, and the starting time, `tstart`, time for reaching the position, `tend`, and the prescribed rise time, `trise`.

```
*DEFINE_CURVE_SMOOTH_TITLE
Displacement
$#    lcid      sidr      dist    tstart      tend     trise        v0
         2         0     250.0       0.0      0.02     0.005       0.0
```

Figure I.16. A cut-out of the defined curve smooth.

On figure I.17, punch1 and punch2 are prescribed the curve from figure I.16, `lcid`=2, and which are done in the z-direction, `dof`=3, and they are moving in the downwards, `sf`=-1.

```
*BOUNDARY_PRESCRIBED_MOTION_RIGID_ID
$#      id                                                          heading
          0Punch1
$#     pid       dof       vad      lcid        sf       vid     death     birth
         2         3         0         2      -1.0         01.00000E28       0.0
$#      id                                                          heading
          0Punch2
$#     pid       dof       vad      lcid        sf       vid     death     birth
         3         3         0         2      -1.0         01.00000E28       0.0
```

Figure I.17. A cut-out of the prescribed rigid motion.

Parts

In the following, the information about the parts be presented.

On figure I.18, the part move function is used, where part 5, `pid`=5, is moved −60 mm in the z-direction, `zmov`=-60.0.

```
*PART_MOVE
$#   pid            xmov            ymov            zmov     cid    iset
       5             0.0             0.0          -60.0       0       0
```

Figure I.18. A cut-out of the part move.

On figure I.19, is the material model prescribed for the blank, which is Material Model no. 18: "This is an isotropic plasticity model with rate effects which uses a power law hardening rule.", For this model the inputs are: Density, `ro`, Young's Modulus, `e`, Poissons Ratio, `pr`, Strength Coefficient, `k`, Hardening exponent, `n`.

```
*MAT_POWER_LAW_PLASTICITY_TITLE
Blank 304
$#     mid        ro         e        pr         k         n       src       srp
         17.85000E-9  196000.0       0.3    1367.0      0.42       0.0       0.0
$#    sigy        vp      epsf
        0.0       0.0       0.0
```

Figure I.19. A cut-out of the material model for the blank.

On figure I.20, the element formulation for the blank is shown. For this the `elform` 2 is used which is Belytschko-Tsay formulation, which is very efficient and cheap, and 7

integration points are used through the thickness(`nip`). Finally, the shell thickness is prescribed as 1.5 mm, which is prescribed for `t1, t2, t3, t4`.

```
*SECTION_SHELL_TITLE
Blank
$#   secid    elform      shrf       nip     propt   qr/irid     icomp     setyp
         1         2       1.0         7       1.0         0         0         1
$#      t1        t2        t3        t4      nloc     marea      idof    edgset
       1.5       1.5       1.5       1.5       0.0       0.0       0.0         0
```

Figure I.20. A cut-out of the section shell.

On figure I.21, an example of the material model prescribed for all the tooling parts are presented. Here a rigid material model is selected, which is recommended for tools. The inputs for the rigid tool part is: Density, `ro`, Young's Modulus, `e`, Poissons Ratio, `pr`, Constraints applied in the global direction, `cmo`=1, First constraint parameters(Translation), `con1` (4=x,y-direction), Second constraint parameter (Rotational), `con2` (7=x,y,z-rotation).

```
*MAT_RIGID_TITLE
Punch1
$#     mid        ro         e        pr         n    couple         m     alias
           27.85000E-9  210000.0       0.3       0.0       0.0       0.0
$#     cmo      con1      con2
       1.0         4         7
$#lco or a1        a2        a3        v1        v2        v3
       0.0       0.0       0.0       0.0       0.0       0.0
```

Figure I.21. A cut-out of a rigid material model.

On figure I.22, the element formulation for the tooling parts can be seen. This one is similar to the one for the blank, however, here the number of integration points are by default set to one, even though it says 7, when using rigid materials. Furthermore, the rigid parts are applied a thickness of 1 mm, which is selected based on experience, so the tooling parts are assigned a "mass".

```
*SECTION_SHELL_TITLE
Punch1
$#   secid    elform      shrf       nip     propt   qr/irid     icomp     setyp
         2         2       1.0         7       1.0         0         0         1
$#      t1        t2        t3        t4      nloc     marea      idof    edgset
       1.0       1.0       1.0       1.0       0.0       0.0       0.0         0
```

Figure I.22. A cut-out of the section shell for the rigid parts.

Creating the dynain file

In the following section, the inputs used for creating the dynain file is presented. This dynain file is used for the second model as the input for the current model.
On figure I.23, the first 6 lines are creating the part list, which contain part id 1, `pid1`, and this part list is used for the interface springback lsdyna, function, which creates a dynain file containing the strains for each element.

```
1  *INTERFACE_SPRINGBACK_LSDYNA
2  $#     psid      nshv     ftype          _     ftensr    nthhsv          _    intstrn
3            1         0         0          0          0         0          0          0
4            *SET_PART_LIST
5  $#      sid       da1       da2       da3       da4    solver
6            1       0.0       0.0       0.0       0.0MECH
7  $#     pid1      pid2      pid3      pid4      pid5      pid6      pid7      pid8
8            1         0         0         0         0         0         0         0
```

Figure I.23. A cut-out of the creation for the dynain file.

I.2.2 VSR Model

In this section, the VSR model will be described, but since the model contains some of the same features from the Deep drawing Model. The things which will not be presented again are listed underneath.

- Material Mode and Element Formulation
- Database
- Control - Hourglass and Energy

Control

The following will contain the control cards used for the VSR Model.

On figure I.24, the termination time, `endtim`=0.51 sec and the timestep for mass scaling `dt2ms`$=-1 \times 10^{-8}$ sec.

```
1  *CONTROL_TERMINATION
2  $#  endtim    endcyc     dtmin    endeng    endmas
3         0.51         0       0.0       0.01.000000E8
4  *CONTROL_TIMESTEP
5  $#  dtinit    tssfac      isdo    tslimt     dt2ms      lctm     erode     ms1st
6           0.0       0.9         0       0.0-1.0000E-8         0         0         0
7  $#  dt2msf   dt2mslc     imscl    unused    unused     rmscl
8           0.0         0         0                           0.0
```

Figure I.24. A cut-out of the control card for the termination and timestep.

On figure I.25, the setting used for the implicit solver can be seen. Here it can be seen that the implicit solver is switched on after at the defined time, due to the `imflag`=-8, which refers to the defined curve. Furthermore, the timestep used for the implicit solver is set to 0.001 sec, `dt0`.

```
1  *CONTROL_IMPLICIT_GENERAL
2  $#  imflag       dt0    imform      nsbs       igs     cnstn      form    zero_v
3           -8     0.001         2         1         2         0         0         0
4  *DEFINE_CURVE_TITLE
5  Implicit
6  $#    lcid      sidr       sfa       sfo      offa      offo    dattyp     lcint
7             8         0       1.0       1.0       0.0       0.0         0         0
8  $#                a1                  o1
9                   0.0                 0.0
10                  0.5                 0.0
11                0.5001                1.0
12                  5.0                 1.0
```

Figure I.25. A cut-out of the control card for the implicit solver.

Boundary Conditions

In the following, the boundary conditions applied for the VSR model is described.

On figure I.26, the applied boundary condition can be seen, where the nodeset shown on figure I.4 for the Boundary Condition are used here as `nsid`=4. These nodes are locked in x, y and z translation, by `dofx`=1, `dofy`=1 and `dofz`=1.

```
1  *BOUNDARY_SPC_SET_ID
2  $#      id                                                              heading
3             0LockNodes
4  $#    nsid       cid      dofx      dofy      dofz     dofrx     dofry     dofrz
5             4         0         1         1         1         0         0         0
```

Figure I.26. A cut-out of the boundary conditions applied for the model.

Loads

In the following, the loads applied for the two frequency modes will be presented. The node and elements applied these loads can be seen on figure I.4.

On figure I.27, the first 1-9 lines are relating to the frequency mode for $16\,023\,\mathrm{s}^{-1}$ and line 10-20 are for the frequency mode $18\,700\,\mathrm{s}^{-1}$. Generally, the only difference between these two are the method they are applied on. For line 1-9, the load is acting in the z-direction, `dof`=3, and the magnitude of the load is determine by the scale factor, `sf`. The loadcurve is applied in `lcid`, where the curve function can be seen in line 9. This is a sinus function, which is shut off at time 0.4 sec, which is determined by the load curve no 9, `LC9`. The function has the variable `time`, which is the current time step.
The settings are similar for the loads applied for the shell elements, where the loading in acting in the direction of the shell normal. The curve in line 20, is similar to the other one, only the eigenvalue is different.

```
*LOAD_NODE_SET
$#    nsid       dof      lcid        sf       cid        m1        m2        m3
         1         3         5      30.0         0         0         0         0
*DEFINE_CURVE_FUNCTION_TITLE
Relieving
$#    lcid      sidr       sfa       sfo      offa      offo    dattyp
         5         0       1.0       1.0       0.0       0.0         0
$#                                                                  function
LC9*sin(2*pi*16023*time)
*LOAD_SHELL_SET_ID
$#      id                                                           heading
         0Shell Load
$#    esid      lcid        sf        at
         2        11       0.0       0.0
*DEFINE_CURVE_FUNCTION_TITLE
Relieving Second God MODE
$#    lcid      sidr       sfa       sfo      offa      offo    dattyp
        11         0       1.0       1.0       0.0       0.0         0
$#                                                                  function
LC9*sin(2*pi*18700*time)
```

Figure I.27. A cut-out for the loads.

Damping

In the following, the damping settings will be presented.

On figure I.28, the damping setting are presented, where mass damping is used, and applied for the blank, `pid`=1, and curve 12 is applied, `lcid`=12, together with the mass damping at 50, `sf`. The mass damping is applied after the loading is terminated and before the implicit solver is initiated. This is done in order to fade out the vibrations in the cup, and to limit the amount of kinetic energy.

```
*DAMPING_PART_MASS
$#     pid      lcid        sf      flag
         1        12      50.0         0
*DEFINE_CURVE_TITLE
Damping
$#    lcid      sidr       sfa       sfo      offa      offo    dattyp     lcint
        12         0       1.0       1.0       0.0       0.0         0         0
$#                a1                  o1
                 0.0                 0.0
                0.44                 0.0
                0.45                 1.0
                0.47                 1.0
                0.48                 0.0
                 2.0                 0.0
```

Figure I.28. A cut-out of the mass damping.